Islanding Detection and Control of an Islanded Electronically-Coupled Distributed Generation Unit

by

Houshang Karimi

A thesis submitted in conformity with the requirements

for the degree of Doctor of Philosophy

Department of Electrical and Computer Engineering
University of Toronto

Your file Votre référence
ISBN: 978-0-494-39821-0
Our file Notre référence
ISBN: 978-0-494-39821-0

Islanding Detection and Control of an Islanded Electronically-Coupled Distributed Generation Unit

Houshang Karimi

Doctor of Philosophy

Graduate Department of Electrical and Computer Engineering

University of Toronto

2008

Abstract

This thesis presents a control strategy for islanded (autonomous) operation of an electronically-coupled Distributed Generation (DG) unit and its local load. In a grid-connected mode of operation, the grid dominantly dictates frequency and voltage at the Point of Common Coupling (PCC) and the DG unit controls its exchanged real and reactive power components with the grid, using the conventional control strategy based on dq-current components. Subsequent to an islanding detection and confirmation, the dq-current controller is disabled and the proposed robust controller is activated. The proposed controller utilizes (i) an internal oscillator for frequency control and (ii) a feedback control system to regulate the island voltage. Despite load parameters uncertainties and unbalanced load conditions, the proposed controller guarantees robust stability and pre-specified performance criteria, e.g. fast transient response and zero steady-state error.

To provide smooth transition from a grid-connected mode to an autonomous (islanded) mode, a fast and accurate islanding detection method is also proposed and investigated in this thesis. The islanding detection method is based on injecting a negative-sequence current through the Voltage Sourced Converter (VSC) controller of a DG unit and detecting and quantifying the corresponding negative-sequence voltage at the PCC, as the islanding indicator, by means of a Unified Three-phase Signal Processor (UTSP). Performances of the islanding detection method and the proposed robust controller are demonstrated based on digital time-domain simulation studies in the PSCAD/EMTDC software, and validated based on a laboratory scale experimental setup.

Dedication

To Nazli, for her companionship and patience, and to Ramtin, who has brought us joy and happiness.

Acknowledgements

I would like to express my special thanks to my supervisor, Professor R. Iravani, for his invaluable advice, his guidance, and his financial support all throughout my Ph.D. program. Also, financial supports from the University of Toronto through the University of Toronto Open Fellowship and Edward S. Rogers Sr. Graduate Scholarship are gratefully acknowledged.

I am also greatly indebted to Professor Edward J. Davison for his help on the development of my thesis and for his helpful collaboration and dedication in many of the control theory parts of my thesis as well as his useful advice and contribution to this thesis.

My thanks also go to Professor F. P. Dawson, and Professor A. Prodic for their review of the thesis and useful suggestions, and to Professor P. Lehn for attending my departmental defense and for his useful comments.

I am grateful to Professor Jin Jiang for his careful review of my thesis and for attending my final oral examination as the External Examiner.

Table of Contents

List of Tables

List of Figures

List of Abbreviations

DG:	Distributed Generation
dq:	direct-quadrature
DR:	Distributed Resource
EPLL:	Enhanced PLL
LTI:	Linear Time Invariant
MIMO:	Multiple-Input Multiple-Output
MISO:	Multiple-Input Single-Output
NDZ:	Non-Detection Zone
PCC:	Point of Common Coupling
PI:	Proportional-Integral
PLL:	Phase-Locked Loop
PWM:	Pulse Width Modulated
RSP:	Robust Servomechanism Problem
SCR:	Short-Circuit-Ratio
SISO:	Single-Input Single-Output
SNR:	Signal-to-Noise-Ratio
SPWM:	Sinusoidal Pulse Width Modulation
THD:	Total Harmonic Distortion
UL:	Underwriters Laboratories, Inc.
UPS:	Uninterruptible Power Supply
UTSP:	Unified Three-phase Signal Processor
VSC:	Voltage-Sourced Converter

List of Symbols

e: error signal

f_{sw}: switching frequency

i: AC current

s: Laplace transform variable

t: continuous time

u: input signal

v: voltage

x: state variable

y: output signal

θ: phase angle

ω_o: center frequency

ω_c: cut-off frequency

Chapter 1

Introduction

1.1 Statement of the Problem

Distributed Generation (DG) systems such as photovoltaic, wind farm, fuel cell, micro turbine, and internal combustion engine units are increasingly used to address environmental problems, improve power quality, and increase capacity of the electric grid. A DG unit is often connected in parallel with a host distribution network and supplies power to the utility system and local loads. A DG unit usually uses a Voltage-Sourced Converter (VSC) as its interface medium as shown in Figure 1.1. Under normal conditions, both the DG unit and its local load operate in a grid-connected mode. In a grid-connected mode, the conventional control strategy for the interface VSC is based on the current-controlled strategy [1] in which the grid dominantly dictates frequency and voltage at the Point of Common Coupling (PCC) and the interface VSC controls its exchanged real and reactive power components with the grid, using dq-current components.

A utility power system is often subjected to preplanned or accidental switching events. These events may result in an intentional or accidental *islanding* operation of a DG unit. When the DG unit and its local load are disconnected from the grid by opening switch CB, Figure 1.1, an islanded system is created. Under the current utility practice and the existing standards [2,3], accidental islanding is not permitted and, upon islanding detection, DG units are required to be disconnected and shut down for the following reasons [4-6]:

- Subsequent to an islanding event, frequency and voltage of the island may drift and the island can become unstable. Voltage and/or frequency excursions can cause damage to the

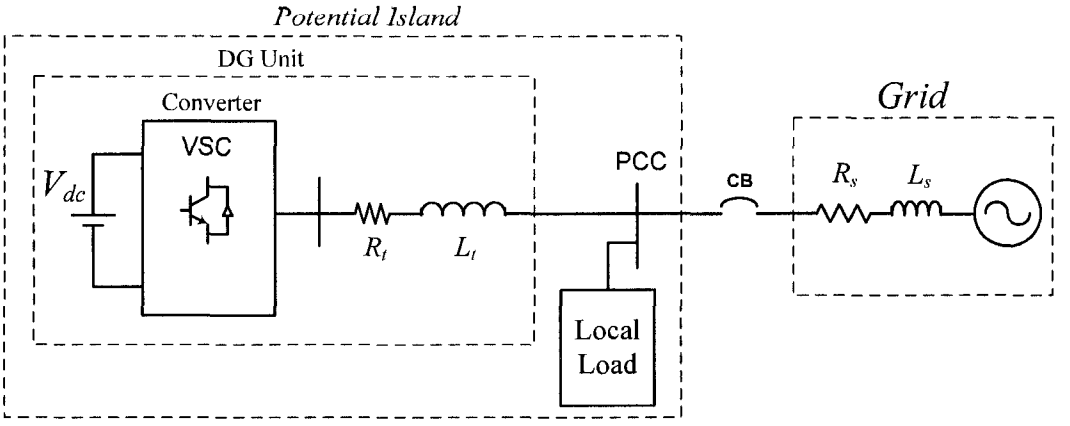

Figure 1.1: Schematic diagram of a grid-interfaced DG unit

local load [7].

- An energized island may adversely impact restoration of normal service by the utility, e.g. automatic reclosing.
- Reclosing onto an island may result in re-tripping the line or damage to the DG unit, or other pieces of equipment [8].
- Islanding may create a hazard for the utility line-workers by causing a portion of the grid to remain energized when it is assumed to be disconnected from all energy sources [9].

With the gradual increase in the depth of penetration of DG units, the economical considerations, the reliability requirements, and the continuity of supply indicate that subsequent to islanding detection of a DG unit and its local load, the island should remain operational and operate as an *autonomous* system. However, there are several technical challenges associated with the operation and control of autonomous islands. A technical challenge to enable an island to remain operational in both grid-connected and islanded modes is to equip the coupling VSC of the DG unit with controllers that can accommodate both modes of operation and the transition process between the two modes. When the DG unit, including its local load, is islanded, due to power mismatch between the load and the DG unit, without voltage and frequency controls, the voltage magnitude and the island frequency deviate from their rated values. Thus, voltage and frequency of the load can vary significantly if the DG unit does not provide voltage and frequency control. Therefore, to achieve autonomous operation of the island with no power uninterruptible, the islanding event must be

rapidly detected and a new control strategy that can regulate voltage magnitude and frequency of the island should be activated.

Accurate and fast detection of the islanding phenomenon is another challenge, which is a prerequisite to achieve uninterruptible autonomous operation for the island. To permit smooth transition from the grid-connected to the islanded mode of operation, and to maintain stability and power quality of the island, fast and accurate islanding detection is required. Most of the currently used and/or proposed islanding detection methods are relatively slow, i.e. operate within half a second to two seconds following an islanding event [10], and thus cannot lead to autonomous operation of an island. Nevertheless, these methods are adequately fast when used as anti-islanding methods.

The main objective of this thesis is to design a control strategy to provide autonomous operation for an islanded system. It should be noted that the controller must accommodate unbalanced load scenarios and uncertain load parameters. In addition, since the continuity of supply (no power interruption) is required, transition from the grid-connected mode to the islanded mode should be carried out smoothly. Therefore, a fast and accurate islanding detection method should also be developed.

1.2 Existing Methods of Islanding Detection

This section outlines various existing islanding detection methods. Based on the literature review, islanding detection methods may be divided into three categories: *passive resident methods*, *active resident methods*, and *communication-based methods*. In this section, we briefly overview the most important methods of islanding detection in each of these categories. Principles of operation, merits, drawbacks, and also the non-detection zones (NDZ) of such methods have been discussed in [11]. For a given islanding detection method, the NDZ is a region (or space), specified by the system parameters, in which the islanding detection fails to detect an islanding event [8].

1.2.1 Passive Resident Methods

A passive resident method relies on the detection of an abnormality in the electrical parameters at the PCC. The three major passive methods, resident in the converter, are based on [11-13]:

1. over/under voltage and over/under frequency protection (OVP/UVP and OFP/UFP),

2. phase jump detection (PJD) or power factor detection,

3. detection of voltage harmonics.

Any passive resident method has a NDZ, i.e. in a closely matched-power condition between the DG unit and the local load, the passive method fails to detect islanding. The reason is that under a matched-power condition, the monitored signals, e.g. voltage, frequency or their derivatives, do not deviate noticeably and consequently do not exceed their threshold values within reasonable time intervals. However, a smaller NDZ can be achieved by reducing the threshold values for the monitored signals. This is at the price of causing more nuisance/false trips. Nevertheless, the passive methods are structurally simple and can be implemented at low cost.

1.2.2 Active Resident Methods

An active resident method attempts to artificially create an abnormal condition in the PCC voltage that can be detected subsequent to an islanding event. Several active resident methods have been discussed in [11] and include

1. slip mode frequency shift (SMS) or phase-locked loop slip [14],

2. frequency bias or active frequency drift (AFD) [15],

3. Sandia frequency shift (SFS) and Sandia voltage shift (SVS) [4],

4. frequency jump or Zebra method [11].

An active detection scheme is expected to have no NDZ, since it intentionally creates a mismatched-power condition subsequent to the islanding event. However, when the system is already in a mismatched-power condition, the injected signal by the VSC could coincidentally create a matched-power condition. As a result, an island can be formed and the active method may fail to detect it.

Power quality degradation, stability concern, and multi-DG interactions are the other issues associated with active islanding detection methods [16].

1.2.3 Communications-Based Methods

A communication-based method involves transmission of data between a DG unit and the host utility system. The data is used by the DG system to determine when to cease operation. The three main methods of this category are based on the use of

1. power line carrier (PLC) communications [17,18],
2. signal produced by disconnect [11],
3. supervisory control and data acquisition (SCADA) [11].

All communication-based methods are fast and have no NDZ, except for the PLC method which fails when some types of loads replicate the carrier signal. For example, an electric motor subjected to mechanical vibrations could produce harmonic voltages [17] which may coincide with those of the carrier signal.

The main limitations of a communication-based scheme are the cost and complexity. The reason is that a transmitter, capable of sending signals through the distribution system to all DG units, is relatively expensive. The other concern is the possible interference of the communication signal with those of other power line communication applications, e.g. automatic meter reading [11] schemes.

1.3 Rationale for a New Islanding Detection Method

Based on the literature review carried out in Section 1.2, the lack of an islanding detection method as the first step for stable, autonomous operation of the islanded system is obvious. In this thesis, we propose an islanding detection method that:

- is faster than the available methods,
- has no NDZ, and minimum power quality impact,
- is insensitive to distortions, e.g. noise and harmonics,
- is robust to perturbation in system parameters and characteristics.

The proposed islanding detection method is based on local measurements (without communications) and provides the capability for smooth transition from a grid-connected mode to an islanded mode of operation.

1.4 Existing Control Strategies for Autonomous Operation of Islanded Systems

This section reviews the existing control schemes for autonomous operation of an islanded system in the context of microgrids and uninterruptible power supply (UPS) systems.

1.4.1 Microgrid Control Strategies

A microgrid is an integrated energy system consisting of loads, distribution grid, and DG units which can operate in (i) a grid-connected mode, (ii) an islanded (autonomous) mode, and (iii) transition between the two modes [19]. Under normal conditions, a microgrid operates in a grid-connected mode and the grid dominantly dictates frequency and voltage of the microgrid. In the grid-connected mode, each DG unit of the microgrid controls its exchanged real and reactive power components with the grid based on the dq-current control strategy. However, subsequent to an islanding event, the islanded microgrid should activate new control strategies to provide voltage and frequency regulation.

An augmented *dq*-current control strategy for multiple DG units in an islanded microgrid, based on frequency/power and voltage/reactive-power droop characteristics of each DG unit, has been extensively reported [19-24]. In this approach, each DG unit is equipped with two droop characteristics: (i) frequency as a linear function of real power, and (ii) voltage magnitude as a linear function of reactive power. Based on these droop characteristic, frequency is dominantly controlled by real power flow, and voltage magnitude is regulated by reactive power flow of the DG unit. This approach does not directly incorporate load dynamics in the control loop. Thus, large and/or fast load changes can result in either poor dynamic response or even voltage/frequency instability.

A control strategy to regulate voltage and frequency of a single DG islanded system is pro-

posed in [25]. This method assumes intentional islanding and a high band-width for its current control loop, i.e. the interface converter is modelled by an ideal current source. This method could fail if the load dynamics are faster than that of the current source. A robust control scheme for a microgrid, based on H_∞ optimal control [26,27], is proposed in [28] to provide robust performance in the presence of variations of power factor correction (PFC) capacitor. PFC capacitance is the only uncertain parameter which appears in the microgrid model. Moreover, the H_∞ norm is effective for providing robust stability and may not guarantee voltage tracking capability under parametric uncertainty.

1.4.2 UPS Control Strategies

Uninterruptible power supply (UPS) systems are widely used in commercial and industrial applications such as computers, communication systems, medical equipment, and semiconductor manufacturing systems. Voltage control, low total harmonic distortion (THD), zero output impedance, desirable transient response, and robustness with respect to nonlinear and uncertain loads are the main performance characteristics for a UPS system [29]. If a UPS system is expected to operate under unbalanced conditions, the design of a robust controller that fulfills the requirements is a challenging task [29].

Several robust control strategies have been proposed for UPS systems in the technical literatures [30-39]. The sliding mode control (SMC) provides a fast transient response and a superb performance against load parameters uncertainties [31,32,40]. However, the main limitation of the SMC is the so-called chattering phenomenon [41] which can be reduced by the use of high performance switches and increase in the switching frequency [40].

Recent advance in microprocessors and digital signal processors have made the digital control tractable in industrial applications. As a result, the deadbeat control strategies have been applied to regulate the output voltage of a UPS system [33-37]. Based on a deadbeat control, a closed-loop system shows fast transient response and, to a certain degree, can provide robust stability with respect to parameters uncertainties. Although the method has been successfully implemented for single-phase and three-phase UPS systems, it is (i) highly sensitive to model uncertainties, (ii) sensitive to noise on the measured variables, and (iii) based on estimation of system parameters [42,43].

To overcome disadvantages of the deadbeat control, multi-loop controllers [38,39] which are structurally simple and easy to implement are proposed. A multi-loop control strategy is based on an inner current loop to provide a high bandwidth for stability and fast dynamic response, and an outer voltage loop to produce sinusoidal output voltage with minimum steady-state error and minimum harmonics. However, this approach suffers from the switching noise and distortions since it proposes a wide-band controller [39]. Therefore, particular care must be taken in digital implementation of the controller, e.g. reducing the band-width of the controller.

The aforementioned control strategies cannot robustly provide the desired performance specifications over a wide range of parameters uncertainties. Therefore, to ensure a prespecified degree of robustness, the H_∞ optimal control approach of [26,27] for sinusoidal reference tracking of a single-phase UPS inverter is proposed in [44]. As mentioned in Section 1.4.1, the H_∞ optimal control is not suitable for obtaining a guaranteed robust performance. Hence, the approach of [44] may not guarantee voltage tracking feature of the closed-loop system under parameter perturbations.

To reduce the drawbacks of the H_∞ control, a robust controller can be shaped using the μ-synthesis approach of [45]. Robust controller design for a single-phase UPS inverter, based on the μ-synthesis, is discussed in [46]. The proposed method considers perturbations in both input DC voltage and load as static and dynamic uncertainties, respectively. By applying the μ-synthesis, a feedback controller that simultaneously achieves robust stability and robust tracking performance is obtained. The main drawback associated with the μ-formulation is a high-order controller due to the loop-shaping requirements. As an example, the proposed controller of [46] is a 28^{th} order controller, which is reduced to a 12^{th} order controller after applying the optimal Hankel-norm model reduction method.

In this thesis, a control strategy for autonomous operation of an islanded system, based on the dynamic model of the island, is proposed. The robust control techniques such as robust servomechanism problem (RSP) [47] and parametric tools [48] are used to design and analyze the proposed controller. The proposed controller is robust with respect to load parameters uncertainties and accommodates unbalanced load conditions.

1.5 Thesis Objective

The main objective of this research is to propose a control strategy to provide autonomous operation for a single DG islanded system. The proposed controller must be

1. robust with respect to load parameters uncertainties,
2. capable of coping with unbalanced load conditions,
3. immune to measurement and switching noise,
4. able to reject disturbances such as harmonics,
5. structurally simple for efficient implementation in digital hardware/software environments.

In addition, to guarantee smooth transition from a grid-connected mode to an islanded mode of operation, a fast and accurate islanding detection method should also be developed. The proposed islanding detection method must

1. be faster than the available methods,
2. have no NDZ, and minimum power quality impact,
3. be insensitive to distortions, e.g. noise and harmonics,
4. be robust to perturbation in system parameters and characteristics.

1.6 Thesis Structure

Chapter 2 develops a mathematical model and investigates the stability performance of a Unified Three-phase Signal Processor (UTSP). The UTSP is based on a new approach to decompose a set of three-phase signals into its constituting symmetrical components. The UTSP also estimates frequency, magnitudes and phase-angles of the sequence components. The UTSP provides real-time estimation of instantaneous symmetrical components and their attributes also in a variable frequency environment. In the context of this research, the UTSP system is used as the core unit of an active islanding detection method, which is also proposed in this thesis.

Chapter 3 evaluates the performance of the UTSP of Chapter 2. Several simulation case studies are performed in the Matlab/Simulink environment to show that the UTSP system is capable of estimating the sequence components and the parameters of a set of three-phase signal which can be polluted with noise and harmonics. Chapter 3 verifies that the UTSP system can be employed as the main building block of an active islanding detection method.

Chapter 4 proposes a new islanding detection method, using the UTSP as its main building block, for a DG unit which is coupled to a utility grid through a three-phase VSC. The proposed islanding detection method is based on injecting a negative-sequence current through the VSC controller and detecting and quantifying the corresponding negative-sequence voltage at the PCC of the VSC by means of the UTSP system. Performance of the proposed islanding detection method under UL1741 anti-islanding test [3] is evaluated, and its sensitivity to noise, grid short-circuit ratio, grid voltage imbalance, and deviations in the UL1741 test parameters are presented.

Autonomous operation of an islanded single DG system which is under balanced conditions is investigated in Chapter 5. The objective is to design a robust controller for the DG unit to regulate voltage magnitude and frequency of the island, despite unknown load parameters. To provide a fixed frequency for the island, a crystal oscillator is used in the control system of the DG unit. To robustly regulate voltage magnitude at the PCC, a feedback control system, based on a dynamic model of the islanded system, in a rotating reference frame (dq-frame), is designed. The proposed islanding detection method of Chapter 4 is employed to detect the islanding event for this purpose.

Chapter 6 investigates autonomous operation of an islanded single DG system which is under unbalanced load conditions. The chapter presents a robust controller for the DG unit to provide a set of balanced voltages at the load terminals, despite an unbalanced load with uncertain parameters. Similar to the control strategy of Chapter 5, the designed controller utilizes an internal oscillator to control the island frequency, and employs the proposed islanding detection method of Chapter 4 to permit transition capability from the grid-connected to the islanded mode of operation. Summary and conclusions of the thesis are presented in Chapter 7.

Chapter 2

Unified Three-phase Signal Processor (UTSP) for Islanding Detection

This chapter develops a mathematical model and proposes a stability performance of a Unified Three-phase Signal Processor (UTSP). The UTSP is a new system for decomposing a set of three-phase signals into its constituting symmetrical components. The UTSP also estimates frequency, magnitudes and phase-angles of the sequence components. The UTSP is useful for real-time estimation of instantaneous symmetrical components and their attributes in a variable frequency environment.

In the first section, dynamical equations of the UTSP are developed. The governing equations of the UTSP are derived based on defining an instantaneous cost function and minimizing the function by means of a gradient descent algorithm. In the second section, a stability analysis of the UTSP, similar to the classic analysis for Phase-Locked Loop (PLL) [49], is performed. The UTSP is an autonomous forced nonlinear system and nonlinear analysis of such a system requires the theory of Input to State Stability (ISS) [50]. As of now, there are no systematic approaches to investigate stability of this group of nonlinear systems, and we do not discuss nonlinear analysis of the UTSP in this thesis. This chapter also presents a method for adjusting parameters of the UTSP.

2.1 Introduction

Most signals in the power systems are in the form of three-phase sinusoidal signals. A set of three-phase signals is *balanced* when the three signals have equal magnitudes and 120 degrees phase-displacements, otherwise they are *unbalanced.* The theory of symmetrical components [51] indicates that an unbalanced set of three-phase signals can be uniquely decomposed into three sets of three-phase signals: (1) a set of balanced signals with 120 degrees phase-shifts called the positive-sequence, (2) a set of balanced signals with -120 degrees phase-shifts called the negative-sequence, and (3) a third set with zero degree phase-shifts called the zero-sequence.

Assuming that the power system operates at a fixed and known frequency, and under a steady-state sinusoidal condition, each sequence component is determined by its magnitude and its phase-angle. Thus, a total of six parameters for the three sequence components are conventionally used to characterize them in the steady-state sinusoidal operation.

Symmetrical components find their applications in a variety of power system problems such as power systems protection, fault detection and classification, reactive power compensation, unbalance compensation, system modeling and identification [52-56]. Particularly, the concept of symmetrical components can be employed in the fast growing technologies of distributed generation (DG) systems to resolve protection issues such as islanding.

The theory of symmetrical components was first introduced in [51] for complex phasors. It is formulated in terms of a linear matrix transformation involving the unity complex phasor $a = e^{j\frac{2\pi}{3}}$. The concept of symmetrical components for time-domain signals was then presented in [57]. The extension, however, also uses the complex phasor $a = e^{j\frac{2\pi}{3}}$ and results in the instantaneous symmetrical components which are complex quantities; the real and imaginary parts of which are used for the analysis purposes [58]. The complex phasor $a = e^{j\frac{2\pi}{3}}$ can be considered as a phase-shift operator of $\frac{2\pi}{3}$ radian (in the complex plane) when it operates on a complex phasor. Its operation on a real time-domain signal is, however, somehow ambiguous and an obstacle in understanding the nature of instantaneous symmetrical components. For example, the method presented in [59] uses the instantaneous symmetrical components as the basis for load balancing and power factor correction. The method of [59] defines the power factor based on the phase difference between the instantaneous positive-sequence components of voltage and current signals. Then, it calculates the

phase-angles in the complex plane. Although the authors of [59] have justified their approach, it still remains unclear as the calculated phase-angles are not proved to be identical with those of the actual time-domain sequence components [60].

To alternatively define the instantaneous symmetrical components, some authors interpreted the unity complex phasor $a = e^{j\frac{2\pi}{3}}$ as a $\frac{2\pi}{3}$ radian phase-shift in time-domain. This definition is more suitable than the previous one as it does not involve complex quantities in time-domain signals. Such a 120 degrees time-domain phase-shift is then transformed to a 90-degree phase-shift operator for easier realization and is implemented using either an enhanced PLL [61], a linear first-order all-pass filter [62], or a state observer [63]. Signal processing techniques such as stochastic estimation theory [64], adaptive linear combiner [65] and weighted least-squares estimation [66] are intrinsically similar to other methods which have been employed to realize the phase-shift in time-domain and subsequently to estimate the instantaneous symmetrical components.

This chapter presents a Unified Three-phase Signal Processor (UTSP) for decomposing a set of three-phase signals into its constituting instantaneous positive-, negative-, and zero-sequence components [60]. The proposed UTSP system operates based on estimating magnitudes, phase-angles and frequency of the sequence components, and synthesizing the signals in the time-domain. Since the UTSP provides real-time estimation of the magnitudes and phase-angles of the sequence components, the steady-state and dynamic phasors associated with the symmetrical components are also provided by the UTSP [60]. In other words, the UTSP estimates the sequence components both in frequency-domain (as phasors) and in time-domain (as sinusoidal signals). The summation of the three sequence components forms the fundamental components in both frequency and time domains.

Stability analysis of the UTSP system is carried out, similar to the classic analysis for PLL, based on linearizing the dynamical system and obtaining the associated eigenvalues of the linearized system. The analysis concludes that the linearized system is asymptotically stable. Some guidelines regarding design of parameters of the UTSP system are also discussed in this chapter.

2.2 Mathematical Model of the UTSP

Consider the set of three-phase signals $u(t) = [u_a(t)\ u_b(t)\ u_c(t)]^T$ associated with a measured set of three-phase voltages or currents. $u(t)$ can be unbalanced and/or contain distortions, e.g. harmonics and noise. We particularly assume that $u(t)$ has a fundamental component

$$u_1(t) = \begin{bmatrix} A_1 \sin(\omega_0 t + \delta_1) \\ A_2 \sin(\omega_0 t + \delta_2) \\ A_3 \sin(\omega_0 t + \delta_3) \end{bmatrix} \tag{2.1}$$

which comprises three symmetrical components as $u_1(t) = u_p(t) + u_n(t) + u_z(t)$ in which

$$u_p = \begin{bmatrix} A_p \sin(\omega_0 t + \delta_{p0}) \\ A_p \sin(\omega_0 t + \delta_{p0} - \frac{2\pi}{3}) \\ A_p \sin(\omega_0 t + \delta_{p0} + \frac{2\pi}{3}) \end{bmatrix},\ u_n = \begin{bmatrix} A_n \sin(\omega_0 t + \delta_{n0}) \\ A_n \sin(\omega_0 t + \delta_{n0} + \frac{2\pi}{3}) \\ A_n \sin(\omega_0 t + \delta_{n0} - \frac{2\pi}{3}) \end{bmatrix},$$

$$u_z = \begin{bmatrix} A_z \sin(\omega_0 t + \delta_{z0}) \\ A_z \sin(\omega_0 t + \delta_{z0}) \\ A_z \sin(\omega_0 t + \delta_{z0}) \end{bmatrix}. \tag{2.2}$$

The objective is to identify a system that receives the input signal $u(t)$ and estimates the sequence components defined in (2.2) and estimates their attributes including magnitudes, phase-angles and frequency.

Assume that $y(t, \Theta) = [y_a(t, \Theta)\ \ y_b(t, \Theta)\ \ y_c(t, \Theta)]^T$ is the "desired" output of our "desired" system which is expressed in terms of Θ as a suitable vector of parameters to be estimated. In other words, the output signal y is considered to be an estimate of the fundamental component of the input signals, i.e. u_1, and the vector of parameters Θ includes the estimates of magnitudes A_x, phase-angles δ_{x0}, $x = p, n, z$, and frequency ω_0 of the sequence components of u_1. Based on the concept of symmetrical components, the output signal y can also be written as a combination of its constituting positive-, negative- and zero-sequence components as follows:

$$y = y_p + y_n + y_z = V_p S_p + V_n S_n + V_z S_z \tag{2.3}$$

where V_p, V_n and V_z are the magnitudes of the positive-, negative- and zero-sequence components of the output signal y, respectively, and S_p, S_n, and S_z are vectors defined as

$$S_p = \begin{bmatrix} \sin\phi_p \\ \sin(\phi_p - \frac{2\pi}{3}) \\ \sin(\phi_p - \frac{4\pi}{3}) \end{bmatrix}, \quad S_n = \begin{bmatrix} \sin\phi_n \\ \sin(\phi_n + \frac{2\pi}{3}) \\ \sin(\phi_n + \frac{4\pi}{3}) \end{bmatrix}, \quad S_z = \begin{bmatrix} \sin\phi_z \\ \sin\phi_z \\ \sin\phi_z \end{bmatrix}. \tag{2.4}$$

In (2.4), ϕ_p, ϕ_n and ϕ_z are phase-angles of positive-, negative- and zero-sequence components of the output signal y, respectively. We also define the following vectors:

$$C_p = \begin{bmatrix} \cos\phi_p \\ \cos(\phi_p - \frac{2\pi}{3}) \\ \cos(\phi_p - \frac{4\pi}{3}) \end{bmatrix}, \quad C_n = \begin{bmatrix} \cos\phi_n \\ \cos(\phi_n + \frac{2\pi}{3}) \\ \cos(\phi_n + \frac{4\pi}{3}) \end{bmatrix}, \quad C_z = \begin{bmatrix} \cos\phi_z \\ \cos\phi_z \\ \cos\phi_z \end{bmatrix}. \tag{2.5}$$

Notice that ϕ_x and δ_x, $x = p, n, z$, are connected through the estimated frequency ω as follows:

$$\phi_x(t) = \int_0^t \omega(\tau)d\tau + \delta_x(t) \qquad x = p, n, z \tag{2.6}$$

where $\delta_x, x = p, n, z$ are the estimates of constant phase-angles $\delta_{x0}, x = p, n, z$, respectively. For an $n \times n$ real matrix A and a real $n \times 1$ vector X, we have

$$\frac{\partial}{\partial X}(X^T AX) = AX + A^T X, \tag{2.7}$$

and if A is a real symmetric matrix, then

$$\frac{\partial}{\partial X}(X^T AX) = 2AX. \tag{2.8}$$

We use the gradient descent method to derive differential equations for the vector of parameters $\Theta = \begin{bmatrix} \theta_1 & \dots & \theta_7 \end{bmatrix}^T = \begin{bmatrix} V_p & V_n & V_z & \Delta\omega & \delta_p & \delta_n & \delta_z \end{bmatrix}^T$. The gradient descent algorithm provides a method of adjusting unknown parameters Θ so that a properly defined cost function J tends to its minimum point. The method is based on the idea of moving the unknown parameter to the opposite direction of the variations of the cost function with respect to that parameter [67]. Its

general formulization is as follows.

$$\dot{\Theta}(t) = -\mu \frac{\partial}{\partial \Theta} J(t, \Theta). \tag{2.9}$$

In (2.9), the $n \times n$ matrix μ is defined as $\text{diag}\{\mu_1, \cdots, \mu_n\}$ which μ_i, $i = 1 \cdots n$ are positive real constant numbers.

A well-defined cost function for our analysis can be the "instantaneous distance" between the input signal $u(t)$ and the output signal $y(t, \Theta)$ as

$$\begin{aligned} J(t, \Theta) &= \tfrac{1}{2}\|u(t) - y(t, \Theta)\|^2 \triangleq \tfrac{1}{2}\|e(t, \Theta)\|^2 = \tfrac{1}{2} e^T e \\ &= \tfrac{1}{2}[(u_a - y_a)^2 + (u_b - y_b)^2 + (u_c - y_c)^2] \\ &= \tfrac{1}{2}[e_a^2 + e_b^2 + e_c^2]. \end{aligned} \tag{2.10}$$

Now, we derive the governing differential equations of the desired system (UTSP) using the gradient decent method as defined in (2.9) based on the cost function of (2.10) and the output signal as characterized in (2.3). First, we calculate gradient of cost function J with respect to parameter θ_i, i=1,2, ... 7, i.e. $\frac{\partial}{\partial \theta_i} J(t, \Theta)$, using (2.8) and *The Chain-Rule Theorem* [68] as follows.

$$\frac{\partial J}{\partial \theta_i} = \frac{\partial (\frac{1}{2} e^T e)}{\partial \theta_i} = (\frac{\partial (\frac{1}{2} e^T e)}{\partial e})^T . \frac{\partial e}{\partial \theta_i} = e^T . \frac{\partial (u - y)}{\partial \theta_i} = -e^T . \frac{\partial y}{\partial \theta_i} \qquad i = 1, 2, ...7 \tag{2.11}$$

Therefore,

$$\frac{\partial y}{\partial V_x} = \frac{\partial}{\partial V_x}(V_p S_p + V_n S_n + V_z S_z) = S_x \quad for \quad x = p, n, z \tag{2.12}$$

$$\frac{\partial y}{\partial \Delta\omega} = \sum_{x=p,n,z} V_x \frac{\partial S_x}{\partial \Delta\omega} = \sum_{x=p,n,z} V_x \frac{\partial S_x}{\partial \phi_x} . \frac{\partial \phi_x}{\partial \Delta\omega} = t \sum_{x=p,n,z} V_x C_x \tag{2.13}$$

$$\frac{\partial y}{\partial \delta_x} = \frac{\partial}{\partial \delta_x} \sum_{k=p,n,z} (V_k S_k) = \sum_{k=p,n,z} (V_k \frac{\partial S_k}{\partial \delta_x}) = \sum_{k=p,n,z} V_k (\frac{\partial S_k}{\partial \phi_x} \frac{\partial \phi_x}{\partial \delta_x}) = V_x C_x \quad for\ x = p, n, z \tag{2.14}$$

Substituting for $\frac{\partial J}{\partial \theta_i}$ from (2.12)-(2.14) in (2.11) and (2.9), the governing differential equations

of the desired system (or the UTSP) are

$$\begin{cases} \dot{V}_p &= \mu_1 e^T.S_p \\ \dot{V}_n &= \mu_2 e^T.S_n \\ \dot{V}_z &= \mu_3 e^T.S_z \\ \dot{\Delta\omega} &= \mu_4 e^T.(V_pC_p + V_nC_n + V_zC_z) \\ \dot{\phi}_p &= \omega + \mu_5 e^T.C_p \\ \dot{\phi}_n &= \omega + \mu_6 e^T.C_n \\ \dot{\phi}_z &= \omega + \mu_7 e^T.C_z \end{cases} \tag{2.15}$$

In (2.15), the fourth equation is a simplified version of the one directly obtained from the gradient descent method. The simplification is in removing a factor of time t as if it is absorbed in the parameter μ_4. This simplification turns the system into a time-invariant (autonomous) system. Dynamical equations (2.15) indicate that the UTSP is an autonomous and forced nonlinear system with seven state variables.

A block diagram representation of the UTSP system corresponding to (2.15) is shown in Figure 2.1. The three top integrating units estimate amplitudes V_p, V_n and V_z, respectively. The four bottom integrating units estimate phase-angles ϕ_z, ϕ_n and ϕ_p, and frequency ω. Each Sine-Cosine Generating (SCG) unit generates two vectors S_x, C_x, $x = p, n, z$ which are used for estimating V_x, ϕ_x, $x = p, n, z$ and ω. Each dot-product (DP) unit provides the dot-product of its two input vectors and each scalar-product (SP) unit produces the scalar-product of its two inputs. The UTSP shown in Figure 2.1 receives a set of three-phase signals shown by $u(t)$ and provides the following:

1. frequency ω,
2. rate of change of frequency $\dot{\omega}$,
3. fundamental components in time-domain, i.e. y,
4. vector of error or distortions e, e.g. harmonics, inter-harmonics, transient disturbances,
5. amplitude of the positive-sequence component V_p,
6. amplitude of the negative-sequence component V_n,

7. amplitude of the zero-sequence component V_z,
8. phase-angle of the positive-sequence component ϕ_p,
9. phase-angle of the negative-sequence component ϕ_n,
10. phase-angle of the zero-sequence component ϕ_z,
11. instantaneous (time-domain) positive-sequence component $y_p = V_p S_p$,
12. instantaneous negative-sequence component $y_n = V_n S_n$,
13. instantaneous zero-sequence component $y_z = V_z S_z$,
14. steady-state (phasor-domain) positive-sequence component $Y_p = V_p \angle 0$,
15. steady-state negative-sequence component $Y_n = V_n \angle(\phi_n - \phi_p)$,
16. steady-state zero-sequence component $Y_z = V_z \angle(\phi_z - \phi_p)$,
17. fundamental components (phasor-domain) $Y = Y_p + Y_n + Y_z$.

If required, more information can be obtained through additional computations. For example, two UTSP units can be employed for a set of three-phase voltage and current measurements to compute instantaneous reactive currents and instantaneous real/reactive power components defined in electric power systems [69,70].

One may also adjust the parameters of the UTSP system to obtain appropriate performances for power systems applications, e.g. FACTS controllers, HVDC converters, and custom power controllers [60]. It should be noted that such a system with the capability of providing numerable parameters and signals is only controlled by parameters μ_i, $i = 1, 2, ..., 7$. These parameters determine the speed and the accuracy of the system outputs.

2.3 Stability Analysis of UTSP

This section is devoted to stability analysis of the proposed UTSP based on a classic engineering approach presented in the literatures such as [49]. The UTSP is an autonomous forced nonlinear

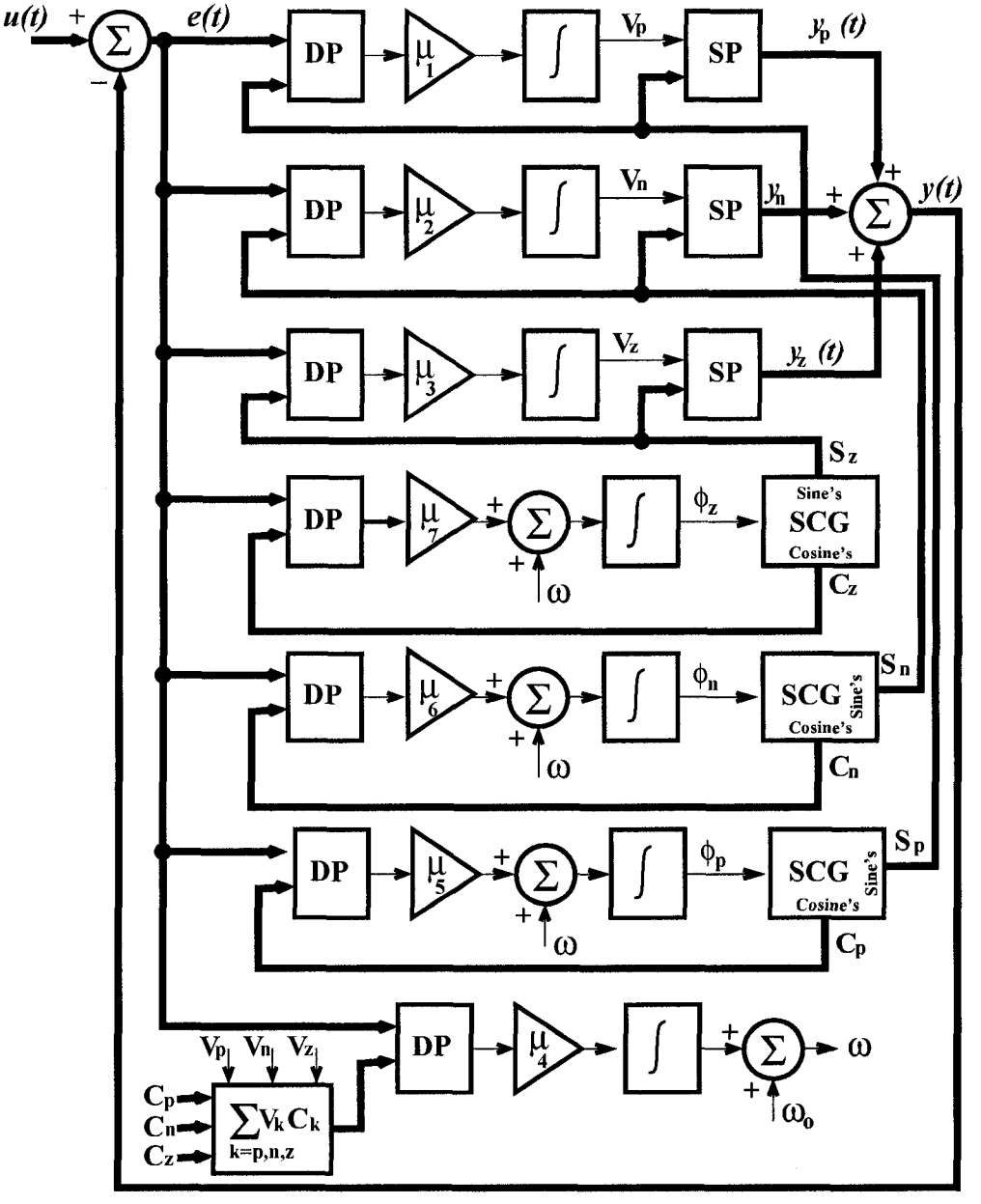

Figure 2.1: Block diagram of UTSP

system with seven states. Nonlinear analysis of such systems is a demanding task and requires the Input to State Stability (ISS) theory [50]. To prove nonlinear stability of the UTSP, we should find an ISS-Lyapunov function for the system (2.15). As of now, there has been no systematic method to find the ISS-Lyapunov function for such a system and therefore nonlinear analysis is not addressed here. In this section, stability of the UTSP system is justified by applying a pure sinusoidal three-phase signal as the input to the UTSP system and neglecting the oscillatory terms in the resultant dynamic [49]. It should be noted that the three-phase input signal, i.e. $u(t)$ of Figure 2.1, can be unbalanced. The stability approach adopted here is similar to the classic analysis for PLL [49] and is not a rigorous mathematical proof.

Let $u(t) = u_p(t) + u_n(t) + u_z(t)$ be the input signal to the UTSP which is a combination of positive-, negative- and zero-sequence components, i.e., $u_p(t)$, $u_n(t)$ and $u_z(t)$. Moreover, suppose $\phi_0(t) = \omega_0 t$ where ω_0 is the angular frequency and a constant real number. $u_p(t)$, $u_n(t)$ and $u_z(t)$ are defined as

$$u_p(t) = A_p \begin{bmatrix} \sin\phi_0 \\ \sin(\phi_0 - \frac{2\pi}{3}) \\ \sin(\phi_0 - \frac{4\pi}{3}) \end{bmatrix}, \quad u_n(t) = A_n \begin{bmatrix} \sin(\phi_0 + \delta_n) \\ \sin(\phi_0 + \delta_n + \frac{2\pi}{3}) \\ \sin(\phi_0 + \delta_n + \frac{4\pi}{3}) \end{bmatrix} \tag{2.16}$$

$$u_z(t) = A_z \begin{bmatrix} \sin(\phi_0 + \delta_z) \\ \sin(\phi_0 + \delta_z) \\ \sin(\phi_0 + \delta_z) \end{bmatrix}. \tag{2.17}$$

It is assumed that A_x, $x = p, n, z$, δ_n and δ_z are constant numbers and therefore $u_x(t)$, $x = p, n, z$ are pure sinusoidal signals. The estimated sequence components by the UTSP are $y_p(t)$, $y_n(t)$ and $y_z(t)$. Therefore, V_x, ϕ_p, ϕ_n and ϕ_z are estimation of A_x, $x = p, n, z$, ϕ_0, $(\phi_0 + \delta_n)$ and $(\phi_0 + \delta_z)$, respectively. The error vector is

$$
\begin{aligned}
e(t) = u(t) - y(t) \quad &= \begin{bmatrix} [A_p \sin\phi_0 - V_p \sin\phi_p] \\ [A_p \sin(\phi_0 - \frac{2\pi}{3}) - V_p \sin(\phi_p - \frac{2\pi}{3})] \\ [A_p \sin(\phi_0 - \frac{4\pi}{3}) - V_p \sin(\phi_p - \frac{4\pi}{3})] \end{bmatrix} \\
&+ \begin{bmatrix} [A_n \sin(\phi_0 + \delta_n) - V_n \sin\phi_n] \\ [A_n \sin(\phi_0 + \delta_n + \frac{2\pi}{3}) - V_n \sin(\phi_n + \frac{2\pi}{3})] \\ [A_n \sin(\phi_0 + \delta_n + \frac{4\pi}{3}) - V_n \sin(\phi_n + \frac{4\pi}{3})] \end{bmatrix} \\
&+ \begin{bmatrix} [A_z \sin(\phi_0 + \delta_z) - V_z \sin\phi_z] \\ [A_z \sin(\phi_0 + \delta_z) - V_z \sin\phi_z] \\ [A_z \sin(\phi_0 + \delta_z) - V_z \sin\phi_z] \end{bmatrix}
\end{aligned} \tag{2.18}
$$

First, we calculate the dot-product of the error vector $e(t)$ in S_x, $x = p, n, z$ as they are required for calculating the first three equations of (2.15).

$$
e^T.S_p = e^T.\begin{bmatrix} \sin\phi_p \\ \sin(\phi_p - \frac{2\pi}{3}) \\ \sin(\phi_p - \frac{4\pi}{3}) \end{bmatrix} = T_1 + T_2 + ... + T_9 \tag{2.19}
$$

where T_1, T_1, ..., T_9 are

$$
\begin{aligned}
T_1 &= [A_p \sin\phi_0 - V_p \sin\phi_p] \sin\phi_p \\
&= \tfrac{1}{2}A_p \cos(\phi_p - \phi_0) - \tfrac{1}{2}V_p - \tfrac{1}{2}A_p \cos(\phi_p + \phi_0) + \tfrac{1}{2}V_p \cos 2\phi_p, \\
T_2 &= [A_n \sin(\phi_0 + \delta_n) - V_n \sin\phi_n] \sin\phi_p \\
&= \tfrac{1}{2}A_n \cos(\phi_p - \phi_0 - \delta_n) - \tfrac{1}{2}V_n \cos(\phi_p - \phi_n) \\
&-\tfrac{1}{2}A_n \cos(\phi_p + \phi_0 + \delta_n) + \tfrac{1}{2}V_n \cos(\phi_p + \phi_n), \\
T_3 &= [A_z \sin(\phi_0 + \delta_z) - V_z \sin\phi_z] \sin\phi_p,
\end{aligned} \tag{2.20}
$$

$$
\begin{aligned}
T_4 &= [A_p \sin(\phi_0 - \tfrac{2\pi}{3}) - V_p \sin(\phi_p - \tfrac{2\pi}{3})] \sin(\phi_p - \tfrac{2\pi}{3}) \\
&= \tfrac{1}{2} A_p \cos(\phi_p - \phi_0) - \tfrac{1}{2} V_p \\
&\quad -\tfrac{1}{2} A_p \cos(\phi_p + \phi_0 - \tfrac{4\pi}{3}) + \tfrac{1}{2} V_p \cos(2\phi_p - \tfrac{4\pi}{3}), \\
T_5 &= [A_n \sin(\phi_0 + \delta_n + \tfrac{2\pi}{3}) - V_n \sin(\phi_n + \tfrac{2\pi}{3})] \sin(\phi_p - \tfrac{2\pi}{3}) \\
&= \tfrac{1}{2} A_n \cos(\phi_p - \phi_0 - \delta_n - \tfrac{4\pi}{3}) - \tfrac{1}{2} V_n \cos(\phi_p - \phi_n - \tfrac{4\pi}{3}) \\
&\quad -\tfrac{1}{2} A_n \cos(\phi_p + \phi_0 + \delta_n) + \tfrac{1}{2} V_n \cos(\phi_p + \phi_n), \\
T_6 &= [A_z \sin(\phi_0 + \delta_z) - V_z \sin \phi_z] \sin(\phi_p - \tfrac{2\pi}{3}),
\end{aligned}
\tag{2.21}
$$

$$
\begin{aligned}
T_7 &= [A_p \sin(\phi_0 - \tfrac{4\pi}{3}) - V_p \sin(\phi_p - \tfrac{4\pi}{3})] \sin(\phi_p - \tfrac{4\pi}{3}) \\
&= \tfrac{1}{2} A_p \cos(\phi_p - \phi_0) - \tfrac{1}{2} V_p \\
&\quad -\tfrac{1}{2} A_p \cos(\phi_p + \phi_0 + \tfrac{4\pi}{3}) + \tfrac{1}{2} V_p \cos(2\phi_p + \tfrac{4\pi}{3}), \\
T_8 &= [A_n \sin(\phi_0 + \delta_n + \tfrac{4\pi}{3}) - V_n \sin(\phi_n + \tfrac{4\pi}{3})] \sin(\phi_p - \tfrac{4\pi}{3}) \\
&= \tfrac{1}{2} A_n \cos(\phi_p - \phi_0 - \delta_n - \tfrac{2\pi}{3}) - \tfrac{1}{2} V_n \cos(\phi_p - \phi_n - \tfrac{2\pi}{3}) \\
&\quad -\tfrac{1}{2} A_n \cos(\phi_p + \phi_0 + \delta_n) + \tfrac{1}{2} V_n \cos(\phi_p + \phi_n), \\
T_9 &= [A_z \sin(\phi_0 + \delta_z) - V_z \sin \phi_z] \sin(\phi_p - \tfrac{4\pi}{3}).
\end{aligned}
\tag{2.22}
$$

Therefore

$$
\begin{aligned}
e^T.S_p = \textstyle\sum_{i=1}^{9} T_i &= \tfrac{3}{2}[A_p \cos(\phi_p - \phi_0) - V_p] - \overbrace{\frac{3}{2}[A_n \cos(\phi_p + \phi_0 + \delta_n) - V_n \cos(\phi_p + \phi_n)]}^{dft} \\
&\simeq -\tfrac{3}{2}(V_p - A_p).
\end{aligned}
\tag{2.23}
$$

In (2.23), the dft stands for "double frequency terms" which are filtered out by integrators of the UTSP system of Figure 2.1. Hence, we neglect the oscillatory dft in stability analysis. Similarly, we perform the same procedure to calculate $e^T.S_n$

$$
e^T.S_n = e^T. \begin{bmatrix} \sin \phi_n \\ \sin(\phi_n + \frac{2\pi}{3}) \\ \sin(\phi_n + \frac{4\pi}{3}) \end{bmatrix} = T_1 + T_2 + ... + T_9, \tag{2.24}
$$

where $T_1, T_1, ..., T_9$ are

$$\begin{aligned}
T_1 &= [A_p \sin\phi_0 - V_p \sin\phi_p] \sin\phi_n \\
&= \tfrac{1}{2}A_p \cos(\phi_n - \phi_0) - \tfrac{1}{2}V_p \cos(\phi_n - \phi_p) \\
&-\tfrac{1}{2}A_p \cos(\phi_n + \phi_0) + \tfrac{1}{2}V_p \cos(\phi_n + \phi_p), \\
T_2 &= [A_n \sin(\phi_0 + \delta_n) - V_n \sin\phi_n] \sin\phi_n \\
&= \tfrac{1}{2}A_n \cos(\phi_n - \phi_0 - \delta_n) - \tfrac{1}{2}V_n - \tfrac{1}{2}A_n \cos(\phi_n + \phi_0 + \delta_n), + \tfrac{1}{2}V_n \cos 2\phi_n \\
T_3 &= [A_z \sin(\phi_0 + \delta_z) - V_z \sin\phi_z] \sin\phi_n,
\end{aligned} \tag{2.25}$$

$$\begin{aligned}
T_4 &= [A_p \sin(\phi_0 - \tfrac{2\pi}{3}) - V_p \sin(\phi_p - \tfrac{2\pi}{3})] \sin(\phi_n + \tfrac{2\pi}{3}) \\
&= \tfrac{1}{2}A_p \cos(\phi_n - \phi_0 - \tfrac{2\pi}{3}) - \tfrac{1}{2}V_p \cos(\phi_n - \phi_p - \tfrac{2\pi}{3}) \\
&-\tfrac{1}{2}A_p \cos(\phi_n + \phi_0) + \tfrac{1}{2}V_p \cos(\phi_n + \phi_p), \\
T_5 &= [A_n \sin(\phi_0 + \delta_n + \tfrac{2\pi}{3}) - V_n \sin(\phi_n + \tfrac{2\pi}{3})] \sin(\phi_n + \tfrac{2\pi}{3}) \\
&= \tfrac{1}{2}A_n \cos(\phi_n - \phi_0 - \delta_n) - \tfrac{1}{2}V_n - \tfrac{1}{2}A_n \cos(\phi_n + \phi_0 + \delta_n - \tfrac{2\pi}{3}) \\
&+\tfrac{1}{2}V_n \cos(2\phi_n - \tfrac{2\pi}{3}), \\
T_6 &= [A_z \sin(\phi_0 + \delta_z) - V_z \sin\phi_z] \sin(\phi_n + \tfrac{2\pi}{3}),
\end{aligned} \tag{2.26}$$

$$\begin{aligned}
T_7 &= [A_p \sin(\phi_0 - \tfrac{4\pi}{3}) - V_p \sin(\phi_p - \tfrac{4\pi}{3})] \sin(\phi_n + \tfrac{4\pi}{3}) \\
&= \tfrac{1}{2}A_p \cos(\phi_n - \phi_0 + \tfrac{2\pi}{3}) - \tfrac{1}{2}V_p \cos(\phi_n - \phi_p + \tfrac{2\pi}{3}) \\
&-\tfrac{1}{2}A_p \cos(\phi_n + \phi_0) + \tfrac{1}{2}V_p \cos(\phi_n + \phi_p), \\
T_8 &= [A_n \sin(\phi_0 + \delta_n + \tfrac{4\pi}{3}) - V_n \sin(\phi_n + \tfrac{4\pi}{3})] \sin(\phi_n + \tfrac{4\pi}{3}) \\
&= \tfrac{1}{2}A_n \cos(\phi_n - \phi_0 - \delta_n) - \tfrac{1}{2}V_n - \tfrac{1}{2}A_n \cos(\phi_n + \phi_0 + \delta_n - \tfrac{4\pi}{3}) \\
&+\tfrac{1}{2}V_n \cos(2\phi_n - \tfrac{4\pi}{3}), \\
T_9 &= [A_z \sin(\phi_0 + \delta_z) - V_z \sin\phi_z] \sin(\phi_n + \tfrac{4\pi}{3}).
\end{aligned} \tag{2.27}$$

Therefore

$$\begin{aligned} e^T.S_n = \ & \sum_{i=1}^{9} T_i = \tfrac{3}{2}[A_n\cos(\phi_n-\phi_0-\delta_n)-V_n]\overbrace{-\frac{3}{2}[A_p\cos(\phi_n+\phi_0)-V_p\cos(\phi_n+\phi_p)]}^{dft} \\ & \simeq -\tfrac{3}{2}(V_n-A_n), \end{aligned} \tag{2.28}$$

and

$$\begin{aligned} e^T.S_z &= e^T.\begin{bmatrix}\sin\phi_z & \sin\phi_z & \sin\phi_z\end{bmatrix}^T \\ &= (e_a+e_b+e_c)\sin\phi_z = 3[A_z\sin(\phi_0+\delta_z)-V_z\sin\phi_z]\sin\phi_z \\ &= \tfrac{3}{2}[A_z\cos(\phi_z-\phi_0-\delta_z)-V_z] \\ &\underbrace{-\frac{3}{2}[A_z\cos(\phi_z+\phi_0+\delta_z)-V_z\cos 2\phi_z]}_{dft} \simeq -\tfrac{3}{2}(V_z-A_z). \end{aligned} \tag{2.29}$$

In (2.23), (2.28) and (2.29), we can assume that $\cos(\phi_p-\phi_0)=1$, $\cos(\phi_n-\phi_0-\delta_n)=1$ and $\cos(\phi_z-\phi_0-\delta_z)=1$, since ϕ_p, ϕ_n and ϕ_z are the estimates of ϕ_0, $\phi_0+\delta_n$ and $\phi_0+\delta_z$, respectively. Therefore, $(\phi_p-\phi_0)\simeq 0$, $(\phi_n-\phi_0-\delta_n)\simeq 0$ and $(\phi_z-\phi_0-\delta_z)\simeq 0$.

Now, we calculate the dot-product of the error vector $e(t)$ in C_x, $x=p,n,z$ since they are required for calculating the last four equations of (2.15).

$$e^T.C_p = e^T.\begin{bmatrix}\cos\phi_p \\ \cos(\phi_p-\frac{2\pi}{3}) \\ \cos(\phi_p-\frac{4\pi}{3})\end{bmatrix} = T_1+T_2+\ldots+T_9, \tag{2.30}$$

where T_1, T_1, ..., T_9 are

$$\begin{aligned} T_1 &= (A_p\sin\phi_0-V_p\sin\phi_p)\cos\phi_p \\ &= \tfrac{1}{2}A_p\sin(\phi_0-\phi_p)-\tfrac{1}{2}V_p\sin 2\phi_p+\tfrac{1}{2}A_p\sin(\phi_0+\phi_p), \\ T_2 &= [A_n\sin(\phi_0+\delta_n)-V_n\sin\phi_n]\cos\phi_p \\ &= \tfrac{1}{2}A_n\sin(\phi_0+\delta_n-\phi_p)-\tfrac{1}{2}V_n\sin(\phi_n-\phi_p)+\tfrac{1}{2}A_n\sin(\phi_0+\delta_n+\phi_p) \\ &\quad -\tfrac{1}{2}V_n\sin(\phi_n+\phi_p), \\ T_3 &= [A_z\sin(\phi_0+\delta_z)-V_z\sin\phi_z]\cos\phi_p, \end{aligned} \tag{2.31}$$

$$
\begin{aligned}
T_4 &= [A_p \sin(\phi_0 - \tfrac{2\pi}{3}) - V_p \sin(\phi_p - \tfrac{2\pi}{3})] \cos(\phi_p - \tfrac{2\pi}{3}) \\
&= \tfrac{1}{2} A_p \sin(\phi_0 - \phi_p) + \tfrac{1}{2} A_p \sin(\phi_0 + \phi_p - \tfrac{4\pi}{3}) - \tfrac{1}{2} V_p \sin(2\phi_p - \tfrac{4\pi}{3}), \\
T_5 &= [A_n \sin(\phi_0 + \delta_n - \tfrac{4\pi}{3}) - V_n \sin(\phi_n - \tfrac{4\pi}{3})] \cos(\phi_p - \tfrac{2\pi}{3}) \\
&= \tfrac{1}{2} A_n \sin(\phi_0 + \delta_n - \phi_p - \tfrac{2\pi}{3}) - \tfrac{1}{2} V_n \sin(\phi_n - \phi_p - \tfrac{2\pi}{3}) \\
&+ \tfrac{1}{2} A_n \sin(\phi_0 + \delta_n + \phi_p) - \tfrac{1}{2} V_n \sin(\phi_n + \phi_p), \\
T_6 &= [A_z \sin(\phi_0 + \delta_z) - V_z \sin \phi_z] \cos(\phi_p - \tfrac{2\pi}{3}),
\end{aligned}
\tag{2.32}
$$

$$
\begin{aligned}
T_7 &= [A_p \sin(\phi_0 - \tfrac{4\pi}{3}) - V_p \sin(\phi_p - \tfrac{4\pi}{3})] \cos(\phi_p - \tfrac{4\pi}{3}) \\
&= \tfrac{1}{2} A_p \sin(\phi_0 - \phi_p) + \tfrac{1}{2} A_p \sin(\phi_0 + \phi_p - \tfrac{2\pi}{3}) - \tfrac{1}{2} V_p \sin(2\phi_p - \tfrac{2\pi}{3}), \\
T_8 &= [A_n \sin(\phi_0 + \delta_n - \tfrac{2\pi}{3}) - V_n \sin(\phi_n - \tfrac{2\pi}{3})] \cos(\phi_p - \tfrac{4\pi}{3}) \\
&= \tfrac{1}{2} A_n \sin(\phi_0 + \delta_n - \phi_p - \tfrac{4\pi}{3}) - \tfrac{1}{2} V_n \sin(\phi_n - \phi_p - \tfrac{4\pi}{3}) \\
&+ \tfrac{1}{2} A_n \sin(\phi_0 + \delta_n + \phi_p) - \tfrac{1}{2} V_n \sin(\phi_n + \phi_p), \\
T_9 &= [A_z \sin(\phi_0 + \delta_z) - V_z \sin \phi_z] \cos(\phi_p - \tfrac{4\pi}{3}).
\end{aligned}
\tag{2.33}
$$

Thus,

$$
\begin{aligned}
e^T.C_p = \textstyle\sum_{i=1}^{9} T_i &= \tfrac{3}{2} A_p \sin(\phi_0 - \phi_p) + \overbrace{\frac{3}{2}[A_n \sin(\phi_0 + \delta_n + \phi_p) - V_n \sin(\phi_n + \phi_p)]}^{dft} \\
&\simeq -\tfrac{3}{2} A_p (\phi_p - \phi_0).
\end{aligned}
\tag{2.34}
$$

Similarly

$$
e^T.C_n = e^T. \begin{bmatrix} \cos \phi_n \\ \cos(\phi_n + \frac{2\pi}{3}) \\ \cos(\phi_n + \frac{4\pi}{3}) \end{bmatrix} = T_1 + T_2 + ... + T_9, \tag{2.35}
$$

where T_1, T_1, ..., T_9 are

$$\begin{aligned}
T_1 &= [A_p \sin\phi_0 - V_p \sin\phi_p]\cos\phi_n \\
&= \tfrac{1}{2}A_p \sin(\phi_0 - \phi_n) - \tfrac{1}{2}V_p \sin(\phi_p - \phi_n) \\
&+\tfrac{1}{2}A_p \sin(\phi_0 + \phi_n) - \tfrac{1}{2}V_p \sin(\phi_p + \phi_n), \\
T_2 &= [A_n \sin(\phi_0 + \delta_n) - V_n \sin\phi_n]\cos\phi_n \\
&= \tfrac{1}{2}A_n \sin(\phi_0 + \delta_n - \phi_n) + \tfrac{1}{2}A_n \sin(\phi_0 + \delta_n + \phi_n) - \tfrac{1}{2}V_n \sin 2\phi_n, \\
T_3 &= [A_z \sin(\phi_0 + \delta_z) - V_z \sin\phi_z]\cos\phi_n,
\end{aligned} \tag{2.36}$$

$$\begin{aligned}
T_4 &= [A_p \sin(\phi_0 - \tfrac{2\pi}{3}) - V_p \sin(\phi_p - \tfrac{2\pi}{3})]\cos(\phi_n + \tfrac{2\pi}{3}) \\
&= \tfrac{1}{2}A_p \sin(\phi_0 - \phi_n - \tfrac{4\pi}{3}) - \tfrac{1}{2}V_p \sin(\phi_p - \phi_n - \tfrac{4\pi}{3}) \\
&+\tfrac{1}{2}A_p \sin(\phi_0 + \phi_n) - \tfrac{1}{2}V_p \sin(\phi_p + \phi_n), \\
T_5 &= [A_n \sin(\phi_0 + \delta_n - \tfrac{4\pi}{3}) - V_n \sin(\phi_n - \tfrac{4\pi}{3})]\cos(\phi_n + \tfrac{2\pi}{3}) \\
&= \tfrac{1}{2}A_n \sin(\phi_0 + \delta_n - \phi_n) + \tfrac{1}{2}A_n \sin(\phi_0 + \delta_n + \phi_n - \tfrac{2\pi}{3}) \\
&-\tfrac{1}{2}V_n \sin(2\phi_n - \tfrac{2\pi}{3}), \\
T_6 &= [A_z \sin(\phi_0 + \delta_z) - V_z \sin\phi_z]\cos(\phi_n + \tfrac{2\pi}{3}),
\end{aligned} \tag{2.37}$$

$$\begin{aligned}
T_7 &= [A_p \sin(\phi_0 - \tfrac{4\pi}{3}) - V_p \sin(\phi_p - \tfrac{4\pi}{3})]\cos(\phi_n + \tfrac{4\pi}{3}) \\
&= \tfrac{1}{2}A_p \sin(\phi_0 - \phi_n - \tfrac{2\pi}{3}) - \tfrac{1}{2}V_p \sin(\phi_p - \phi_n - \tfrac{2\pi}{3}) \\
&+\tfrac{1}{2}A_p \sin(\phi_0 + \phi_n) - \tfrac{1}{2}V_p \sin(\phi_p + \phi_n), \\
T_8 &= [A_n \sin(\phi_0 + \delta_n - \tfrac{2\pi}{3}) - V_n \sin(\phi_n - \tfrac{2\pi}{3})]\cos(\phi_n + \tfrac{4\pi}{3}) \\
&= \tfrac{1}{2}A_n \sin(\phi_0 + \delta_n - \phi_n) + \tfrac{1}{2}A_n \sin(\phi_0 + \delta_n + \phi_n - \tfrac{4\pi}{3}) - \tfrac{1}{2}V_n \sin(2\phi_n - \tfrac{4\pi}{3}), \\
T_9 &= [A_z \sin(\phi_0 + \delta_z) - V_z \sin\phi_z]\cos(\phi_n + \tfrac{4\pi}{3}).
\end{aligned} \tag{2.38}$$

Therefore,

$$\begin{aligned}
e^T.C_n = \textstyle\sum_{i=1}^{9} T_i &= \tfrac{3}{2}A_n \sin(\phi_0 + \delta_n - \phi_n) + \overbrace{\frac{3}{2}[A_p \sin(\phi_0 + \phi_n) - V_p \sin(\phi_p + \phi_n)]}^{dft} \\
&\simeq -\tfrac{3}{2}A_n(\phi_n - \phi_0 - \delta_n).
\end{aligned} \tag{2.39}$$

Finally

$$\begin{aligned} e^T.C_z &= e^T.\begin{bmatrix}\cos\phi_z & \cos\phi_z & \cos\phi_z\end{bmatrix}^T \\ &= (e_a+e_b+e_c)\cos\phi_z = 3[A_z\sin(\phi_0+\delta_z)-V_z\sin\phi_z]\cos\phi_z \\ &= \tfrac{3}{2}A_z\sin(\phi_0+\delta_z-\phi_z)+\underbrace{\frac{3}{2}[A_z\sin(\phi_0+\delta_z+\phi_z)-V_z\sin 2\phi_z]}_{dft} \\ &\simeq -\tfrac{3}{2}A_z(\phi_z-\phi_0-\delta_z). \end{aligned} \tag{2.40}$$

In (2.34), (2.39) and (2.40), we can also assume that $sin(\phi_p-\phi_0) = (\phi_p-\phi_0)$, $sin(\phi_n-\phi_0-\delta_n) = (\phi_n-\phi_0-\delta_n)$ and $sin(\phi_z-\phi_0-\delta_z) = (\phi_z-\phi_0-\delta_z)$, since $(\phi_p-\phi_0)\simeq 0$, $(\phi_n-\phi_0-\delta_n)\simeq 0$ and $(\phi_z-\phi_0-\delta_z)\simeq 0$.

Defining $\alpha_x = V_x - A_x$, $x = p,n,z$ and $\beta_p = \phi_p-\phi_0$, $\beta_x = \phi_x-\phi_0-\delta_x$, $x = n,z$, and substituting for $e^T.S_x$ and $e^T.C_x$, $x = p,n,z$ from (2.23), (2.28), (2.29), (2.34), (2.39) and (2.40) in (2.15), we deduce the following dynamical equations

$$\begin{cases} \dot{\alpha}_p &= -\tfrac{3}{2}\mu_1\alpha_p, \\ \dot{\alpha}_n &= -\tfrac{3}{2}\mu_2\alpha_n, \\ \dot{\alpha}_z &= -\tfrac{3}{2}\mu_3\alpha_z, \\ \dot{\Delta\omega} &= -\tfrac{3}{2}\mu_4[(\alpha_p+A_p)A_p\beta_p+(\alpha_n+A_n)A_n\beta_n+(\alpha_z+A_z)A_z\beta_z], \\ \dot{\beta}_p &= \Delta\omega-\tfrac{3}{2}\mu_5A_p\beta_p, \\ \dot{\beta}_n &= \Delta\omega-\tfrac{3}{2}\mu_6A_n\beta_n, \\ \dot{\beta}_z &= \Delta\omega-\tfrac{3}{2}\mu_7A_z\beta_z. \end{cases} \tag{2.41}$$

Neglecting the nonlinear part of the fourth equation in (2.41), we obtain the linearized model for the UTSP as

$$\begin{cases} \dot{\alpha}_p &= -\frac{3}{2}\mu_1\alpha_p, \\ \dot{\alpha}_n &= -\frac{3}{2}\mu_2\alpha_n, \\ \dot{\alpha}_z &= -\frac{3}{2}\mu_3\alpha_z, \\ \dot{\Delta\omega} &= -\frac{3}{2}\mu_4[A_p^2\beta_p + A_n^2\beta_n + A_z^2\beta_z], \\ \dot{\beta}_p &= \Delta\omega - \frac{3}{2}\mu_5 A_p\beta_p, \\ \dot{\beta}_n &= \Delta\omega - \frac{3}{2}\mu_6 A_n\beta_n, \\ \dot{\beta}_z &= \Delta\omega - \frac{3}{2}\mu_7 A_z\beta_z. \end{cases} \tag{2.42}$$

Defining $X = \begin{bmatrix} \alpha_p & \alpha_n & \alpha_z & \Delta\omega & \beta_p & \beta_n & \beta_z \end{bmatrix}^T$, we can express (2.42) in the form of $\dot{X} = AX$, where

$$A = \begin{bmatrix} -\frac{3}{2}\mu_1 & 0 & 0 & 0 & 0 & 0 & 0 \\ 0 & -\frac{3}{2}\mu_2 & 0 & 0 & 0 & 0 & 0 \\ 0 & 0 & -\frac{3}{2}\mu_3 & 0 & 0 & 0 & 0 \\ 0 & 0 & 0 & 0 & -\frac{3}{2}\mu_4 A_p^2 & -\frac{3}{2}\mu_4 A_n^2 & -\frac{3}{2}\mu_4 A_z^2 \\ 0 & 0 & 0 & 1 & -\frac{3}{2}\mu_5 A_p & 0 & 0 \\ 0 & 0 & 0 & 1 & 0 & -\frac{3}{2}\mu_6 A_n & 0 \\ 0 & 0 & 0 & 1 & 0 & 0 & -\frac{3}{2}\mu_7 A_z \end{bmatrix} \tag{2.43}$$

Equation (2.42) represents a linear time-invariant system. There are various approaches to investigate asymptotic stability of a linear time-invariant system [71]. For example, for the continuous-time system

$$\dot{X} = AX \tag{2.44}$$

the necessary and sufficient condition for asymptotic stability of the origin of the system is that all eigenvalues of A have negative real parts, or zeros of the characteristic polynomial, (2.45), have negative real parts.

$$\Delta(s) = |sI - A| = s^n + a_1 s^{n-1} + ... + a_{n-1}s + a_n \tag{2.45}$$

In (2.45), $I_{n\times n}$ is the identity matrix and a_i, $i = 1, 2, ..., n$ are real numbers where n is the order of the system.

We use the Routh-Hurwitz stability criterion [71] to prove stability of the linearized model of

UTSP. Characteristic polynomial of matrix A can be expressed as

$$\Delta(s) = |sI - A| = (s + \frac{3}{2}\mu_1)(s + \frac{3}{2}\mu_2)(s + \frac{3}{2}\mu_3)|sI - A_1| \tag{2.46}$$

where A_1 is

$$A_1 = \begin{bmatrix} 0 & -\frac{3}{2}\mu_4 A_p^2 & -\frac{3}{2}\mu_4 A_n^2 & -\frac{3}{2}\mu_4 A_z^2 \\ 1 & -\frac{3}{2}\mu_5 A_p & 0 & 0 \\ 1 & 0 & -\frac{3}{2}\mu_6 A_n & 0 \\ 1 & 0 & 0 & -\frac{3}{2}\mu_7 A_z \end{bmatrix}. \tag{2.47}$$

Eigenvalues $s_1 = -\frac{3}{2}\mu_1$, $s_2 = -\frac{3}{2}\mu_2$ and $s_3 = -\frac{3}{2}\mu_3$ are stable since they are real negative numbers and lie in the strict left half s-plane. Therefore, we should prove that eigenvalues of matrix A_1 have negative real parts, i.e. the roots of $\Delta_1(s) = |sI - A_1|$ lie in the strict left half s-plane. $\Delta_1(s)$ is given by

$$\Delta_1(s) = s^4 + a_1 s^3 + a_2 s^2 + a_3 s^1 + a_4 s^0, \tag{2.48}$$

where a_i, $i = 1, 2, 3, 4$ are

$$\begin{aligned} a_1 &= \tfrac{3}{2}(\mu_5 A_p + \mu_6 A_n + \mu_7 A_z), \\ a_2 &= \tfrac{9}{4}(\mu_5\mu_6 A_p A_n + \mu_5\mu_7 A_p A_z + \mu_6\mu_7 A_n A_z) + \tfrac{3}{2}\mu_4\left(A_p^2 + A_n^2 + A_z^2\right), \\ a_3 &= \tfrac{9}{4}\mu_4\left[A_p^2(\mu_6 A_n + \mu_7 A_z) + A_n^2\left(\mu_5 A_p + \mu_7 A_z\right) + A_z^2\left(\mu_5 A_p + \mu_6 A_n\right)\right] \\ &\quad + \tfrac{27}{8}\mu_5\mu_6\mu_7 A_p A_n A_z, \\ a_4 &= \tfrac{27}{8}\mu_4 A_p A_n A_z\left(\mu_6\mu_7 A_p + \mu_5\mu_7 A_n + \mu_5\mu_6 A_z\right). \end{aligned} \tag{2.49}$$

Since all coefficients of $\Delta_1(s)$ are positive real numbers ($a_i > 0$, $i = 1, 2, 3, 4$), it meets the necessary conditions for the stability. Hence, we apply the Routh-Hurwitz stability criterion to the fourth-order polynomial $\Delta_1(s)$ to obtain the sufficient conditions for stability of the system as given by Table 2.1.

Based on the Routh-Hurwitz stability criterion, the necessary and sufficient conditions for

Table 2.1: Routh's stability criterion for polynomial (2.48)

s^4	1	a_2	a_4
s^3	a_1	a_3	0
s^2	$c_1 = a_1a_2 - a_3$	a_1a_4	0
s^1	$d_1 = a_1a_2a_3 - a_3^2 - a_1^2a_4$	0	0
s^0	a_4	0	0

asymptotic stability of the origin of the linearized system are

$$\begin{aligned} c_1 &= a_1a_2 - a_3 > 0 \\ d_1 &= a_1a_2a_3 - a_3^2 - a_1^2a_4 > 0 \end{aligned} \tag{2.50}$$

where

$$\begin{aligned} c_1 &= \tfrac{27}{4}\mu_5\mu_6\mu_7A_pA_nA_z + \tfrac{9}{4}\mu_4(\mu_5A_p^3 + \mu_6A_n^3 + \mu_7A_z^3) \\ &+\tfrac{27}{8}\mu_5^2A_p^2(\mu_6A_n + \mu_7A_z) + \tfrac{27}{8}\mu_6^2A_n^2(\mu_5A_p + \mu_7A_z) \\ &+\tfrac{27}{8}\mu_7^2A_z^2(\mu_5A_p + \mu_6A_n), \end{aligned} \tag{2.51}$$

and

$$\begin{aligned} d_1 &= \tfrac{81}{16}\mu_5^2A_p^4\mu_4^2A_n^2 + \tfrac{81}{16}\mu_5^2A_p^4\mu_4^2A_z^2 + \tfrac{81}{16}\mu_6^2A_n^4\mu_4^2A_p^2 \\ &+\tfrac{81}{16}\mu_6^2A_n^4\mu_4^2A_z^2 + \tfrac{81}{16}\mu_7^2A_z^4\mu_4^2A_p^2 + \tfrac{81}{16}\mu_7^2A_z^4\mu_4^2A_n^2 \\ &+\tfrac{243}{32}\mu_5^2A_p^4\mu_6^2A_n^2\mu_4 + \tfrac{243}{16}\mu_5^2A_p^4\mu_6A_n\mu_7A_z\mu_4 + \tfrac{243}{32}\mu_5^3A_p^3\mu_6A_n^3\mu_4 \\ &+\tfrac{243}{32}\mu_5^2A_p^2\mu_6A_n^3\mu_7A_z\mu_4 + \tfrac{729}{64}\mu_5^3A_p^3\mu_6^2A_n^2\mu_7A_z + \tfrac{243}{32}\mu_5^2A_p^4\mu_7^2A_z^2\mu_4 \\ &+\tfrac{243}{32}\mu_5^3A_p^3\mu_7A_z^3\mu_4 + \tfrac{243}{32}\mu_5^2A_p^2\mu_7A_z^3\mu_6A_n\mu_4 + \tfrac{729}{64}\mu_5^3A_p^3\mu_7^2A_z^2\mu_6A_n \\ &+\tfrac{243}{32}\mu_5A_p^3\mu_6^2A_n^2\mu_7A_z\mu_4 + \tfrac{243}{32}\mu_5A_p^3\mu_6A_n\mu_7^2A_z^2\mu_4 + \tfrac{243}{32}\mu_5A_p\mu_6A_n^3\mu_7^2A_z^2\mu_4 \\ &+\tfrac{243}{32}\mu_5A_p\mu_6^2A_n^2\mu_7A_z^3\mu_4 + \tfrac{729}{32}\mu_5^2A_p^2\mu_6^2A_n^2\mu_7^2A_z^2 + \tfrac{81}{16}\mu_5A_p^5\mu_4^2\mu_6A_n \\ &+\tfrac{81}{16}\mu_5A_p^3\mu_4^2\mu_7A_zA_n^2 + \tfrac{81}{16}\mu_5A_p^3\mu_4^2\mu_6A_nA_z^2 + \tfrac{81}{16}\mu_5A_p^5\mu_4^2\mu_7A_z \\ &+\tfrac{81}{16}\mu_5A_p\mu_4^2A_n^3\mu_6A_z^2 + \tfrac{81}{16}\mu_5A_p\mu_4^2A_z^3\mu_7A_n^2 + \tfrac{243}{32}\mu_6^3A_n^3\mu_5A_p^3\mu_4 \\ &+\tfrac{243}{32}\mu_6^2A_n^4\mu_5^2A_p^2\mu_4 + \tfrac{243}{16}\mu_6^2A_n^4\mu_5A_p\mu_7A_z\mu_4 + \tfrac{729}{64}\mu_6^3A_n^3\mu_5^2A_p^2\mu_7A_z \\ &+\tfrac{243}{32}\mu_6^2A_n^4\mu_7^2A_z^2\mu_4 + \tfrac{243}{32}\mu_6^3A_n^3\mu_7A_z^3\mu_4 + \tfrac{729}{64}\mu_6^3A_n^3\mu_7^2A_z^2\mu_5A_p \\ &+\tfrac{81}{16}\mu_6A_n^3\mu_4^2A_p^2\mu_7A_z + \tfrac{81}{16}\mu_6A_n^5\mu_4^2\mu_5A_p + \tfrac{81}{16}\mu_6A_n^5\mu_4^2\mu_7A_z \\ &+\tfrac{81}{16}\mu_6A_n\mu_4^2A_z^3\mu_7A_p^2 + \tfrac{243}{32}\mu_7^3A_z^3\mu_5A_p^3\mu_4 + \tfrac{243}{32}\mu_7^2A_z^4\mu_5^2A_p^2\mu_4 \\ &+\tfrac{243}{16}\mu_7^2A_z^4\mu_5A_p\mu_6A_n\mu_4 + \tfrac{729}{64}\mu_7^3A_z^3\mu_5^2A_p^2\mu_6A_n + \tfrac{243}{32}\mu_7^3A_z^3\mu_6A_n^3\mu_4 \\ &+\tfrac{243}{32}\mu_7^2A_z^4\mu_6^2A_n^2\mu_4 + \tfrac{729}{64}\mu_7^3A_z^3\mu_6^2A_n^2\mu_5A_p + \tfrac{81}{16}\mu_7A_z^5\mu_4^2\mu_5A_p \\ &+\tfrac{81}{16}\mu_7A_z^5\mu_4^2\mu_6A_n. \end{aligned} \tag{2.52}$$

Parameters μ_i, $i = 1, 2, ..., 7$ and A_x, $x = p, n, z$ are positive real numbers. Thus, c_1 and d_1 are positive real numbers and there is no change in signs of coefficients of the first column of Table 2.1. Therefore, all roots of (2.48) lie in the strict left half s-plane. This analysis concludes that the linearized model of the UTSP system, i.e. (2.42), is asymptotically stable. The linear stability analysis also confirms that the dynamics of magnitude estimation are linearly decoupled from the rest of the system. Moreover, based on the linearized model, the phase-angle estimation dynamics are inter-coupled and also coupled with the frequency estimation dynamics. This indicates that magnitude and phase-frequency changes have insignificant coupling effects on each other but phase and frequency changes exhibit stronger impacts on each other.

2.4 Design Guidelines

This section provides guidelines to the design of parameters of the UTSP system of Figure 2.1. The system is characterized by seven parameters $\mu_1, \cdots, \mu_7$ which determine its performance. A method for design of these parameters is presented here based on the concept of pole placement for the linearized system of (2.42). The linearized system has seven eigenvalues. The eigenvalues associated with the magnitudes are $s_i = -3\mu_i/2$, $i = 1, 2, 3$. The linear analysis confirms that the magnitude dynamics are linearly decoupled from each other and from the rest of the system. Thus, these three subsystems can be designed independently. Each μ_i, $i = 1, 2, 3$ results in a time-constant of $\tau_i = -1/s_i = 2/(3\mu_i)$. For example, a value of $\mu_i = 40$ results in a time-constant of 16.67 ms which is equal to one cycle of 60 Hz.

Contrary to the magnitude modes, the phase-angles and frequency modes are dynamically coupled. To proceed with analyzing the roots of polynomial $\Delta_1(s)$ given by (2.48), let's assume

$$\mu_5 A_p = \mu_6 A_n = \mu_7 A_z = \mu_8 \tag{2.53}$$

and define $A_p^2 + A_n^2 + A_z^2 = A^2$. Then, the coefficients of polynomial $\Delta_1(s)$ are: $a_1 = \frac{9}{2}\mu_8$, $a_2 = \frac{27}{4}\mu_8^2 + \frac{3}{2}A^2\mu_4$, $a_3 = \frac{9}{2}A^2\mu_4\mu_8 + \frac{27}{8}\mu_8^3$ and $a_4 = \frac{27}{8}\mu_4\mu_8^2A^2$. In this case, polynomial $\Delta_1(s)$ can be represented as $\Delta_1(s) = (s + \frac{3}{2}\mu_8)^2\Delta_2(s)$ in which

$$\Delta_2(s) = s^2 + \frac{3}{2}\mu_8 s + \frac{3}{2}\mu_4 A^2 = s^2 + 2\zeta\omega_n s + \omega_n^2, \tag{2.54}$$

where ζ and ω_n correspond to damping ratio and natural frequency, respectively. It is observed that $s_4 = s_5 = -\frac{3}{2}\mu_8$ are two roots of $\Delta_1(s)$ which are independent from μ_4 and the other two roots, called s_6 and s_7, are the roots of $\Delta_2(s)$.

Assume that μ_8 is fixed and we draw the root locus of $\Delta_2(s)$ when μ_4 varies from zero to infinity, Figure 2.2. For $\mu_4 = 0$, roots are located at $s_6 = 0$ and $s_7 = -\frac{3}{2}\mu_8$. As μ_4 increases, roots approach to each other and intersect at $s_6 = s_7 = -\frac{3}{4}\mu_8$ for $\mu_4 = \frac{3\mu_8^2}{8A^2}$ which corresponds to $\zeta = 1$. Further increasing the value of μ_4 generates two complex conjugate roots corresponding to $\zeta < 1$. A value of $0.5 \leq \zeta \leq 1$ is practically recommended. The design procedure may be arranged as follows.

1. Choose μ_1 to μ_3. These three parameters can independently be selected based on the required speed for the magnitudes dynamics. Note that μ_i corresponds to an eigenvalue of $s_i = -3\mu_i/2$ and a time-constant of $\tau_i = \frac{2}{3\mu_i}$ or a settling time of $T_i = 5\tau_i$ (for $i = 1, 2, 3$). A choice of $\mu_1 = \mu_2 = \mu_3 = 2\mu/3$ is recommended. A value of $\mu = 100$ leads to a settling time of 50 ms (about 3 cycles for power system applications).

2. Choose the damping ratio ζ and the natural frequency ω_n for the simplified phase/frequency dynamics of (2.54). Recommendations are $0.5 \leq \zeta \leq 1$ and $\zeta\omega_n = \mu$. Obtain μ_4 and μ_8 from $\zeta\omega_n = \frac{3}{4}\mu_8$ and $\omega_n^2 = \frac{3}{2}\mu_4 A^2$ (recommended values: $\mu_8 = 4\mu/3$ and $\mu_4 = \frac{2}{3A^2\zeta^2}\mu^2$).

3. Calculate μ_5 to μ_7 from (2.53).

Condition (2.53) indicates that μ_5, μ_6 and μ_7 are inversely proportional to the magnitudes of their corresponding sequence components. Notice that parameters A_p, A_n and A_z are unknown and an estimate of these parameters suffices to satisfy (2.53).

2.5 Summary and Conclusions

This chapter develops mathematical model and investigates stability analysis of a Unified Three-phase Signal Processor (UTSP). The UTSP is a new system for calculating the symmetrical components in time-domain and estimating their parameters including their magnitudes, phase-angles and frequency.

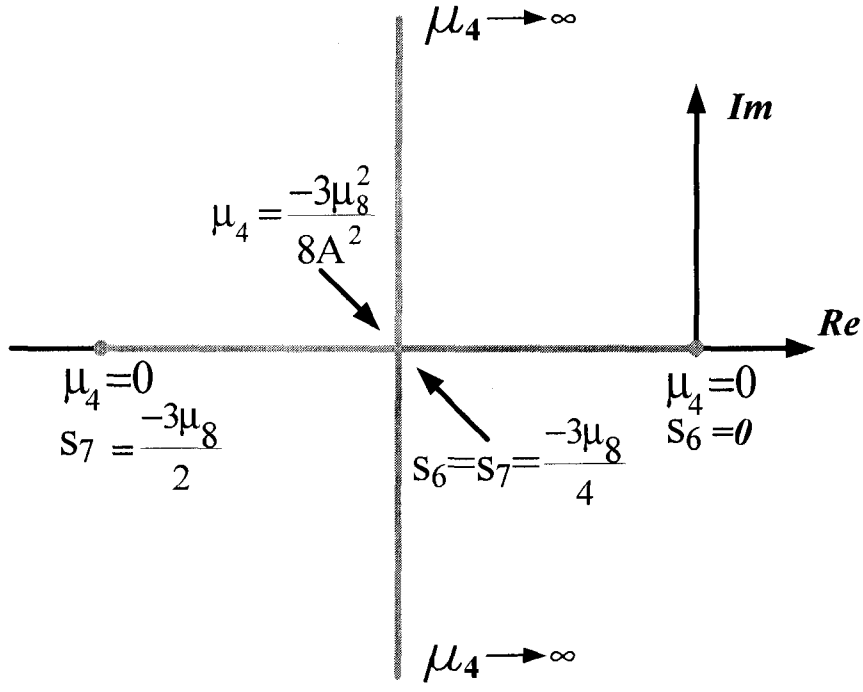

Figure 2.2: Root-locus of the simplified frequency/phase-angle dynamics when μ_4 varies

In the first section, dynamical equations of the UTSP are mathematically derived based on defining an instantaneous cost function and minimizing the function by means of a gradient descent algorithm. Based on minimizing the cost function, we deduce a mathematical model of the UTSP as an autonomous forced nonlinear system with seven states.

In the second section, stability of the UTSP is investigated using its linearized model and obtaining the associated eigenvalues. The analysis concludes that the linearized model of the UTSP system is asymptotically stable. The linear analysis also confirms that the magnitude estimation dynamics are linearly decoupled from rest of the UTSP system. On the other hand, the phase-angle estimation dynamics are inter-coupled and coupled with the frequency estimation dynamics. This means that magnitude and phase-frequency changes have small coupling on each other but phase and frequency changes have stronger impacts on each other. Finally, a method for adjusting the parameters of the UTSP is presented. The design method is based on the root locus of the linear model of the UTSP system.

Chapter 3

Performance Evaluation of UTSP

3.1 Introduction

This chapter evaluates the performance of the Unified Three-phase Signal Processor (UTSP) of Chapter 2. Several simulation case studies are performed in the Matlab/Simulink environment to show that the UTSP system is capable of estimating the sequence components and the parameters of a set of three-phase signal that are polluted with noise and distortions. Performance evaluation of the UTSP is carried out in two parts. Initiatory/basic performance, tracking features, and sensitivity of the UTSP system with respect to distortions, e.g. noise and harmonics, are performed in the first part. Then, the UTSP system is compared with the conventional dq0 phase-locked loop (PLL) [72-75] and the three-phase enhanced PLL (EPLL) of [76]. The comparisons are made in terms of structural complexity and performance of the three systems, e.g. transient response, level of noise immunity, distortion sensitivity, and sensitivity to unbalanced conditions. Finally, performance of the UTSP system is experimentally validated and the corresponding experimental results are given in Appendix A.

3.2 Performance Evaluations

In this section, several case studies are presented to evaluate performance of the proposed UTSP. Figure 2.1 shows a block diagram of the UTSP whose dynamical equations were derived in Chapter 2. A software model of UTSP of Figure 2.1 is developed in the Matlab/Simulink environment

and used to generate the results presented in this chapter. It is to be noted that the UTSP parameters μ_1 to μ_7 are designed using the algorithm presented in Chapter 2, Section 2.4.

For power system applications with the fundamental frequency of 60 Hz, the choice of $\mu_1 = \mu_2 = \mu_3 = 2\mu/3 = 67$ results in a settling time of about $t_s = 50$ ms for the magnitudes dynamics. To compute the rest of parameters, the damping ratio and the damping factor are selected as $\zeta = 0.707$ and $\zeta\omega_n = \mu = 100$. This results in $\mu_8 = 4\mu/3 = 133$ and $\mu_4 = 2\mu^2/(3A^2\zeta^2) \approx 10000$. Notice that $A^2 = A_p^2+A_n^2+A_z^2$ is uncertain and it must be approximated. It is assumed that the input signal is a set of unbalanced three-phase signals consisting of 1 pu positive-sequence, 0.5 pu negative-sequence, and 0.2 pu zero-sequence component. Thus, $A_p = 1$, $A_n = 0.5$ and $A_n = 0.2$ and therefore $A^2 = 1.29$. The remaining parameters are obtained as $\mu_5 = \mu_8/A_p \approx 133$, $\mu_6 = \mu_8/A_n \approx 266$ and $\mu_7 = \mu_8/A_z \approx 660$. The system of Figure 2.1 has a robust performance with respect to its parameters and the approximations have minimal impact on its performance. The studies confirm that the above set of parameters, for example, can practically operate for a wide range of input signal parameters.

3.2.1 Extraction of Sequence Components

Input to the UTSP is a set of 60 Hz, three-phase pure sinusoidal signals. It is a balanced signal with the amplitude of 1 pu in the time-interval of [0 0.1] s. The signal after t=0.1 s comprises 1 pu of the positive-sequence component, 0.5 pu of the negative-sequence component and 0.2 pu of the zero-sequence component. The constant phase angles of positive-, negative- and zero-sequence components are set to 0, 2 and 1 radian, respectively. The central frequency ω_0 of the VCO of Figure 2.1 is set to 120π rad/s. Figures 3.1 and 3.2 show the input signal, the estimated fundamental components of the input and the error signal, and the extracted sequence components, respectively. Precise extraction of the estimated signals is observed after a transient-time of about three cycles from Figure 3.1(c).

Estimated amplitudes and phase-angles of the sequence components are shown in Figures 3.3(a) and (b), respectively. These variables are also accurately estimated within about 50 ms. The estimated frequency is shown in Figure 3.3(c) which settles down to its actual value of 60 Hz within 2.5 cycles. It should be noted that the large transient error in the estimated frequency results from the fact that magnitudes of sequence components of the input signals intentionally undergo sudden

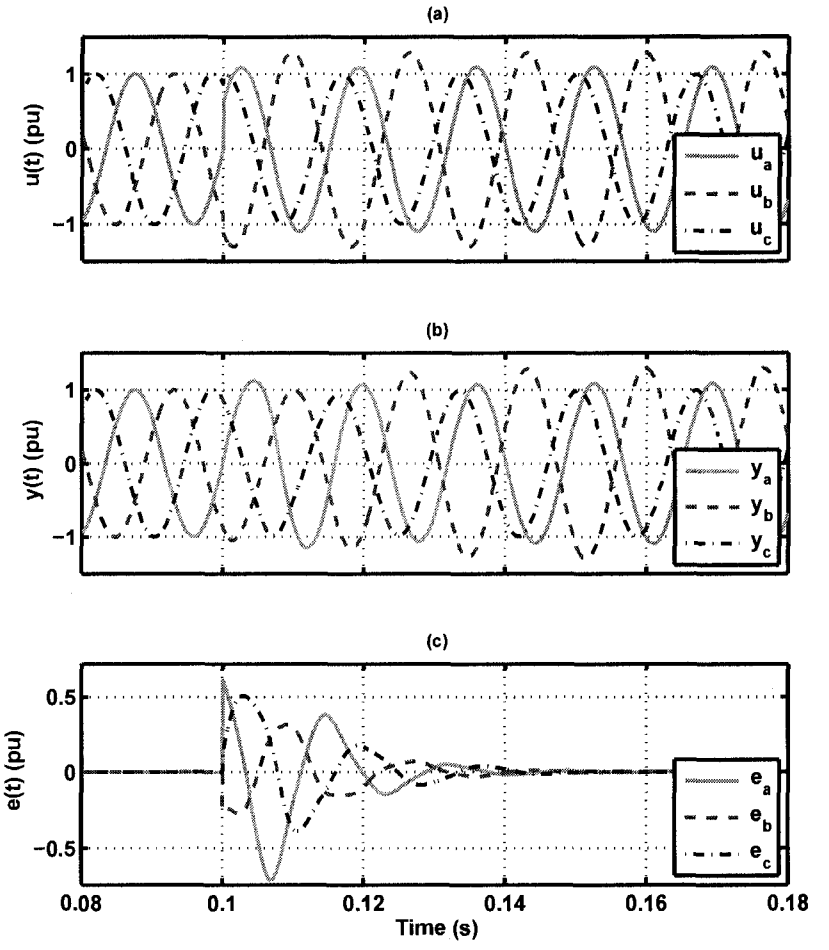

Figure 3.1: Performance of the UTSP system for a sudden change in the magnitudes of sequence components (a) input signals, (b) extracted fundamental components, and (c) error signals

changes. In a realistic system, however, such unbalanced conditions are not likely to occur, since there are always imperfections which prevent sudden changes in the sequence components.

3.2.2 Amplitude Tracking

In this study, the amplitude tracking feature of the UTSP system is studied. While the frequency of the input signal is constant and set at 60 Hz, the amplitudes of its sequence components undergo various step changes. Three different scenarios are considered. In each scenario, only the magnitude of one of the sequence components of the input signal is stepped up/down to a certain value. Performance of the UTSP system in response to the amplitude step changes of the input signal is demonstrated in Figure 3.4.

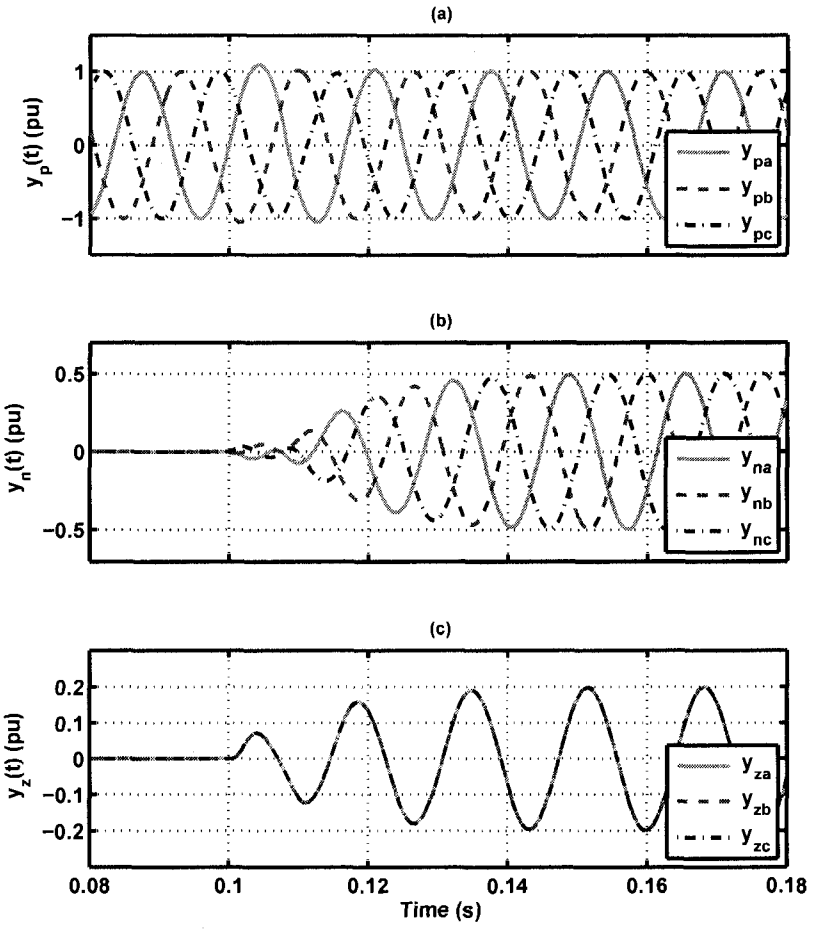

Figure 3.2: Performance of the UTSP system for a sudden change in the magnitudes of sequence components (a) extracted positive-sequence component, (b) extracted negative-sequence component, and (c) extracted zero-sequence component

Figure 3.4(a) shows positive-sequence amplitude tracking of the UTSP when the input is subjected to step changes of -100%, -60%, -20%, 20%, 60%, and 100% at t=0.1 s. The UTSP response to each step change reaches the steady-state within 40 ms. Performance of the UTSP and the results for negative- and zero-sequence amplitude tracking are shown in Figures 3.4(b) and (c), respectively. The step changes of negative- and zero-sequence components are 2%, 4%, 6%, 9% and 12%. Figure 3.4 also shows that the UTSP accurately tracks the step changes of the amplitudes in less than 40 ms.

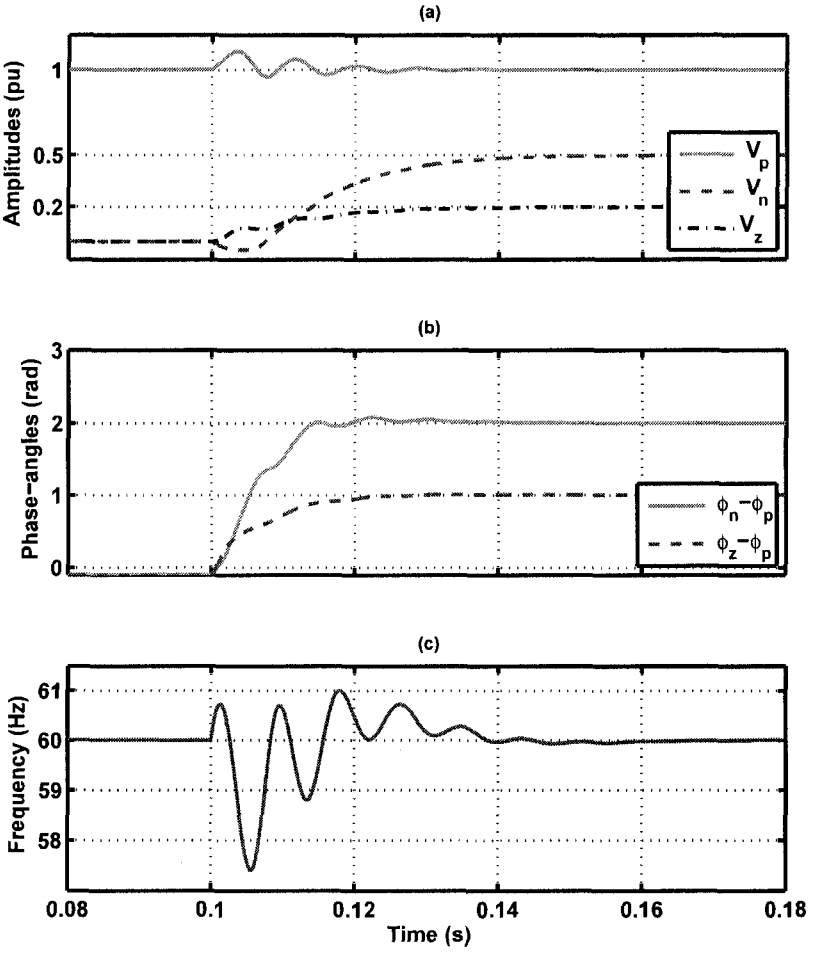

Figure 3.3: Performance of the UTSP system for a sudden change in the magnitudes of sequence components (a) estimated amplitudes of sequence components, (b) estimated phase-angles of sequence components with respect to the phase-angle of positive-sequence component, and (c) estimated frequency

3.2.3 Frequency Tracking

This study case verifies performance of the UTSP with respect to large as well as small step changes in the frequency of the input signal. The input to the UTSP is a set of balanced three-phase signals whose attributes are all constant values except its frequency which is subjected to the step changes at t=0.1 s. The frequency step changes are ±2, ±4, ±6, ±8, ±10, ±0.1, ±0.2, ±0.3, ±0.4, ±0.5 Hz about the central frequency of 60 Hz. The large and the small step changes of the input signal frequency are considered since some frequency estimation methods [77] present (i) a smaller error for a large step change, and (ii) a steady-state error to a small step change in

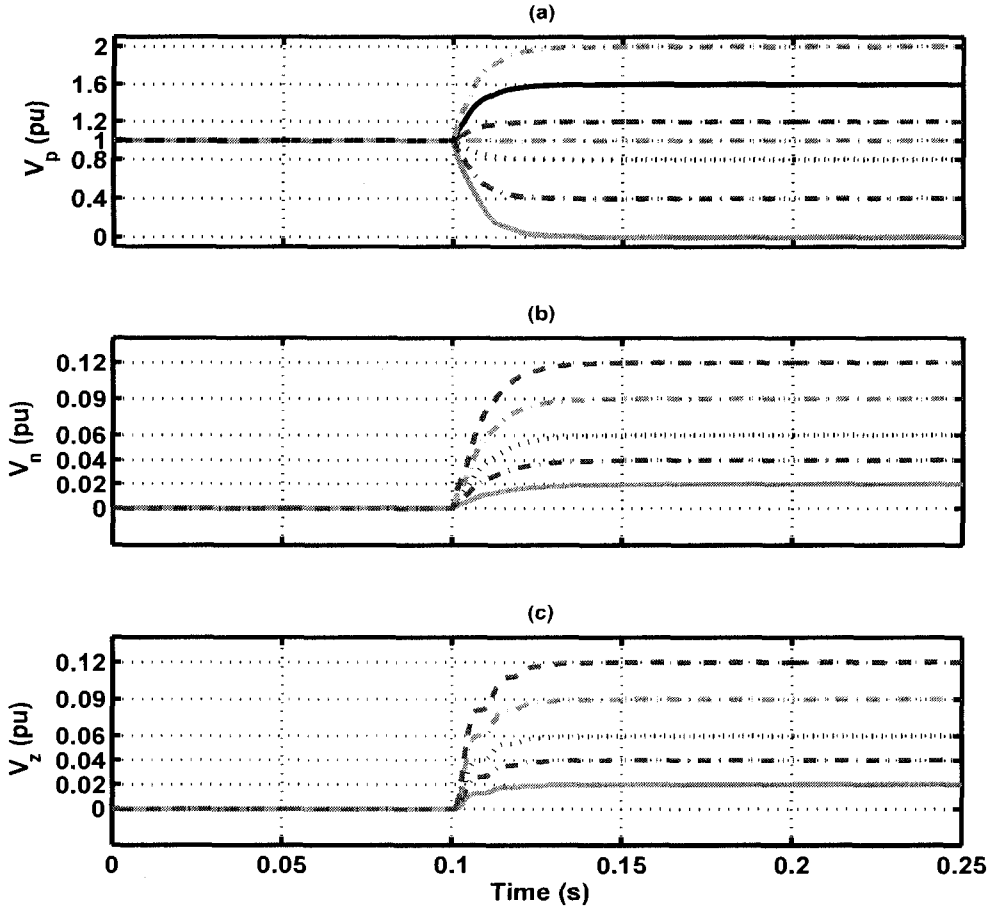

Figure 3.4: Amplitude tracking performance of the UTSP in response to step changes in sequence components of the input signal (a,b,c) estimated amplitudes of positive-, negative-, and zero-sequence components

the frequency. Figure 3.5 shows dynamic responses of the UTSP system to these frequency step changes. Figures 3.5(a) and (b) demonstrate that the UTSP system is capable of tracking large as well as small step changes of the input signal frequency with zero steady-state error and a transient response of about three cycles. The UTSP shows a desirable performance for estimating the frequency within the specified ranges.

3.2.4 Noise Immunity

Noise characteristics of the UTSP system are studied in this section. To conduct the study, an unbalanced set of three-phase signals which is polluted by a Gaussian white noise is applied to the

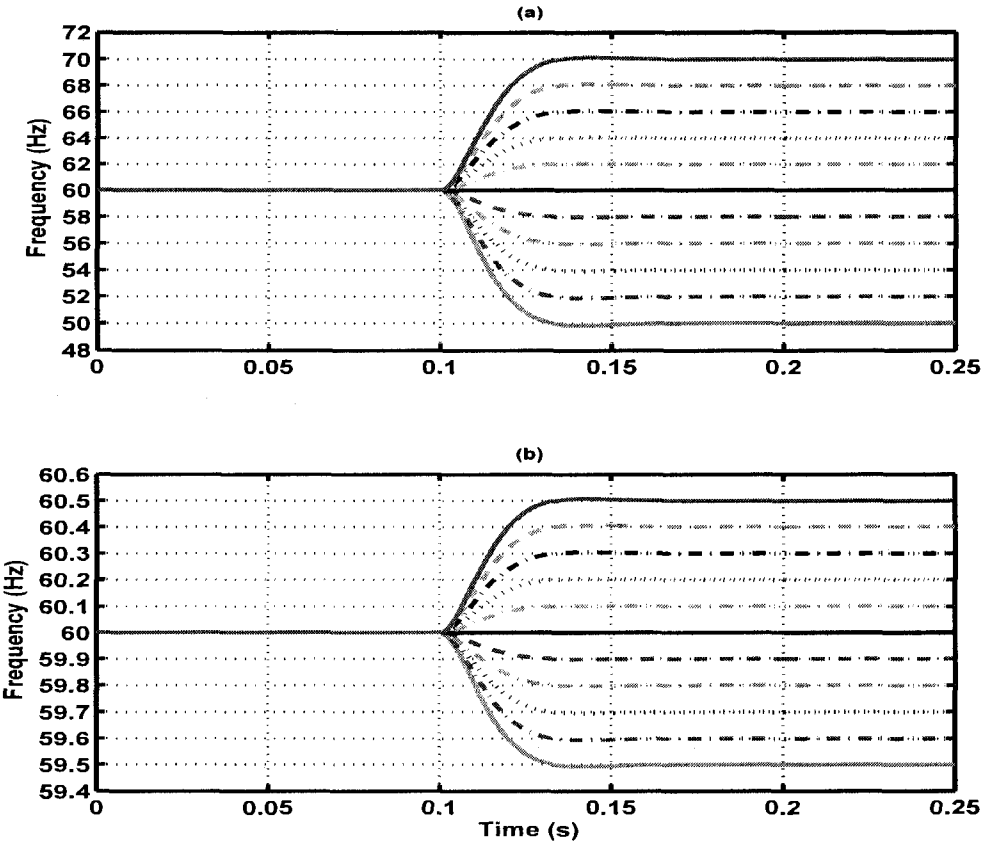

Figure 3.5: Frequency tracking performance of the UTSP in response to step changes in the input signal frequency (a) large steps, and (b) small steps

UTSP system. Phase-a of the input signals is given as

$$\begin{aligned} u_a(t) &= A_a \sin(\omega_0 t + \delta_a) + n(t) \\ &= \underbrace{A_p \sin(\omega_0 t + \delta_p)}_{u_{pa}} + \underbrace{A_n \sin(\omega_0 t + \delta_n)}_{u_{na}} + \underbrace{A_z \sin(\omega_0 t + \delta_z)}_{u_{za}} + n(t), \end{aligned} \tag{3.1}$$

where u_{pa}, u_{na}, and u_{za} are instantaneous positive-, negative-, and zero-sequence components of phase-a, respectively, and $n(t)$ is a Gaussian white noise with zero mean and variance of σ^2 = 0.05, A_p = 1 pu, A_n = 0.05 pu, A_z = 0.5 pu, $\delta_n - \delta_p$ = 1 rad, $\delta_z - \delta_p$ = 3 rad, and ω_0 = $2\pi 60$ rad/s. The noise power of σ^2 = 0.05 corresponds to a Signal-to-Noise-Ratio (SNR) of 10 dB which is a typical value for a highly polluted power system environment [78]. For a sinusoidal signal with magnitude A and noise variance σ^2, the Signal-to-Noise-Ratio (SNR) is defined as SNR=$10\log(\frac{A^2}{2\sigma^2})$ dB. The unbalanced three-phase signal has approximate magnitudes equal to

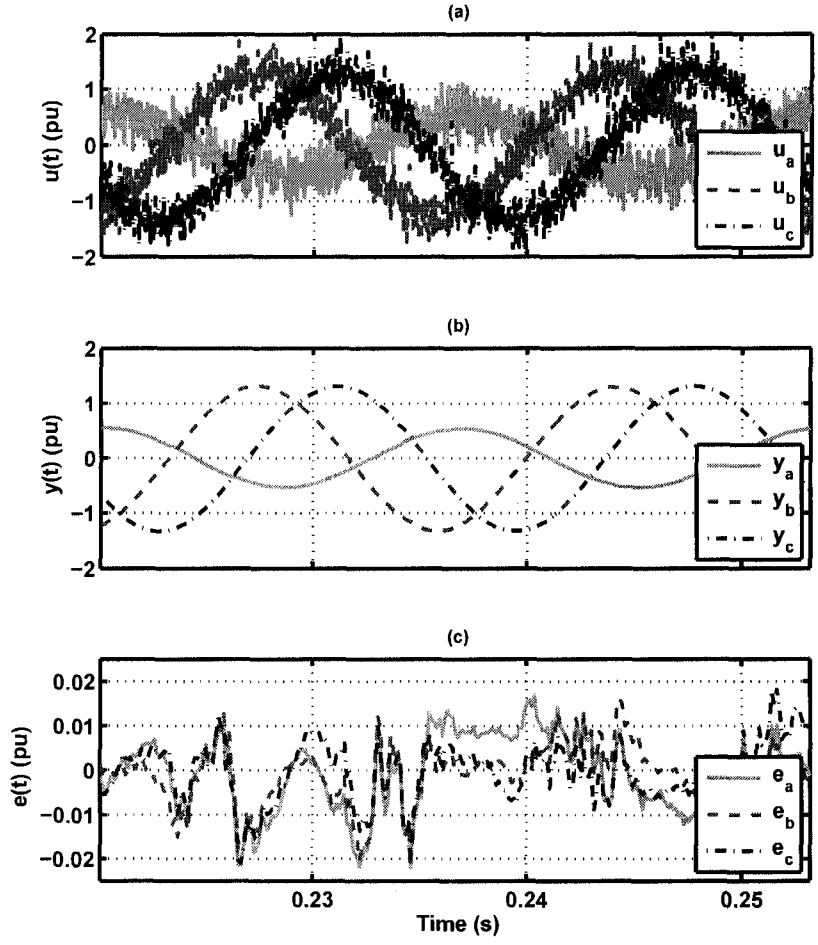

Figure 3.6: Performance of the UTSP system in the presence of noise (a) input signals with SNR_a=4.6 dB and SNR_b=SNR_c=12.3 dB, (b) extracted fundamental components by the UTSP system: SNR_a=17.8 dB, SNR_b=SNR_c=24.8 dB, and (c) error signals

A_a = 0.54 pu and A_b = A_c = 1.31 pu for phase-a, phase-b and phase-c, respectively. Thus, the SNRs for each phase are given as SNR_a=4.6 dB and SNR_b=SNR_c=12.3 dB.

Figures 3.6, 3.7 and 3.8 show input and output signals of the UTSP system for this study case. Figures 3.6(a), (b) and (c) show the input signals to the UTSP, estimated fundamental components, and the error signals, respectively. The SNRs of the extracted fundamental components are calculated as SNR_a=17.8 dB and SNR_b=SNR_c=24.8 dB. Figure 3.6 shows that the UTSP system filters the noise and improves the SNRs.

The estimated symmetrical components and their estimated magnitudes are shown in Fig-

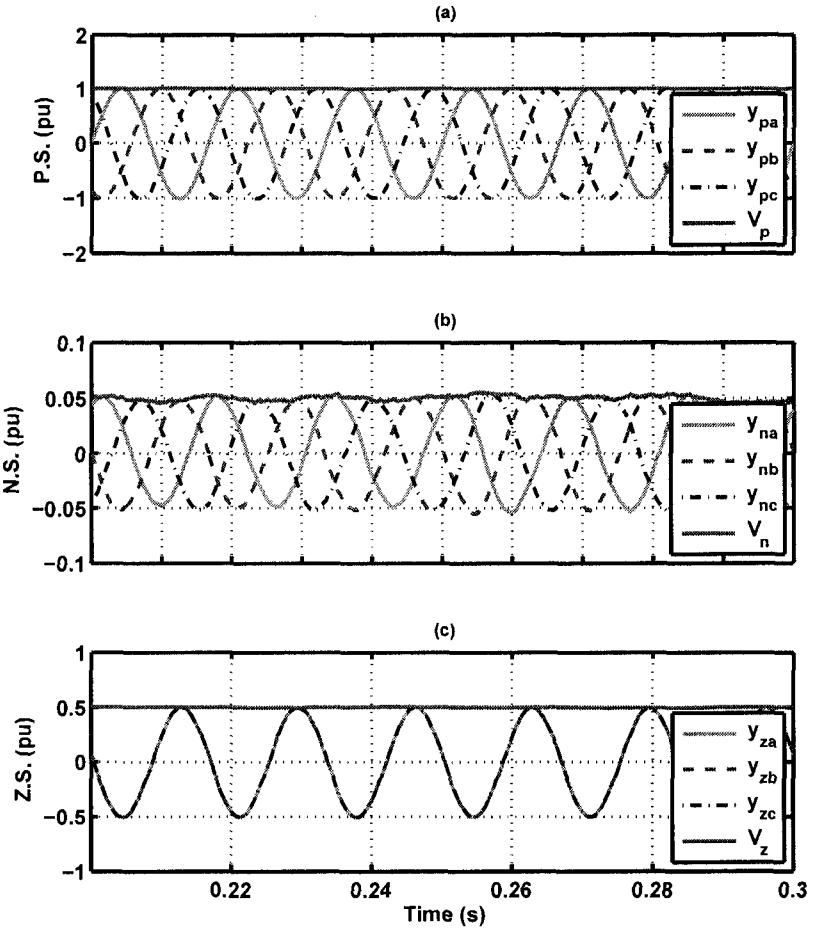

Figure 3.7: Instantaneous sequence components and their estimated magnitudes in the presence of noise (a) positive-sequence, (b) negative-sequence, and (c) zero-sequence

ure 3.7. Figure 3.7(b) clearly demonstrates that the UTSP is able to accurately estimate very small amount of the negative-sequence component of its input, even in the presence of noise. The estimated phase-angles of the negative- and zero-sequence components, and the estimated frequency are shown in Figure 3.8(a) and (b), respectively. Smooth and accurate estimates of these variables in the presence of noise are observed. However, a small component of the steady-state ripple error is introduced in the estimated magnitudes, phase-angles, and the estimated frequency, Figures 3.7 and 3.8.

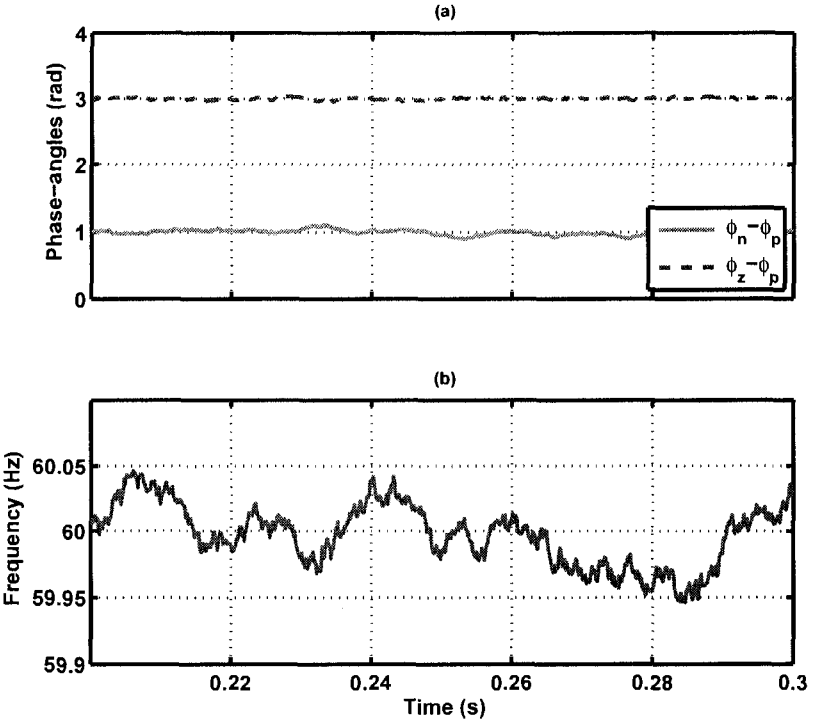

Figure 3.8: Performance of the UTSP system in the presence of noise (a) estimated phase-angles of sequence components with respect to the phase-angle of positive-sequence component and (b) estimated frequency

3.2.5 Effect of Harmonics

In this section, the effects of high-frequency and low-frequency harmonic components on the UTSP performance are studied. In the case of high-frequency harmonics, a set of three-phase Sinusoidal Pulse Width Modulated (SPWM) signals is applied to the UTSP system. The SPWM signals are generated by comparing a high-frequency triangular carrier with a set of three-phase sinusoidal modulating signals. Frequency of the triangular carrier is 33 times of the modulating signals, i.e. $f_s = 33 \times 60$ Hz. In addition, it is assumed that the modulating signals comprise 1 pu positive-, 0.4 pu negative-, and 0.2 pu zero-sequence components, and therefore the SPWM signals applied to the UTSP are unbalanced. The harmonics in the SPWM waveforms appear as sidebands, centered around the carrier frequency and its multiples, that is, around frequencies f_s, $2f_s$, $3f_s$ and so on [79].

The estimated fundamental components of the SPWM input and the error signals are shown in Figure 3.9(a) and Figures 3.9(b) to (d), respectively. The steady-state error signals $e(t)$, Fig-

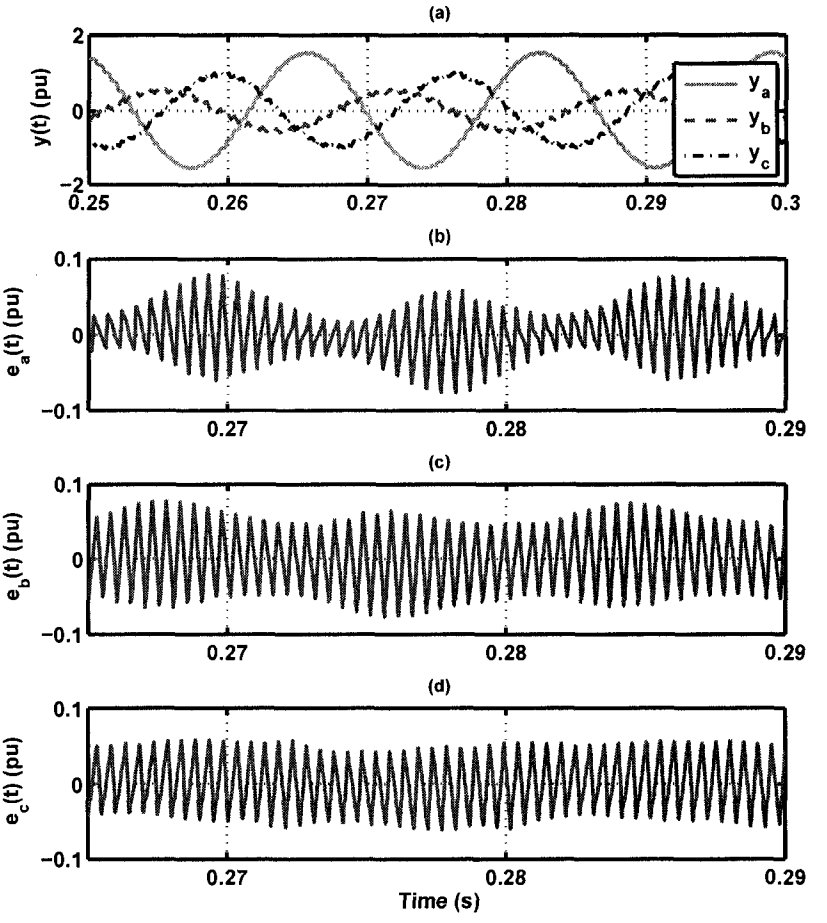

Figure 3.9: Performance of the UTSP system in the presence of high-frequency harmonics (a) extracted fundamental components by the UTSP system: THD_a=0.0243, THD_b=0.0929, and THD_c=0.0441 and (b,c,d) error signals

ures 3.9(b) to (d), result from the high-frequency harmonic components of the SPWM signals. Figure 3.10 shows the estimated symmetrical components of the fundamental component of the input signals. The estimated magnitudes of sequence components and the estimated fundamental frequency are shown in Figure 3.11. Figure 3.11 shows that the estimated amplitudes and the estimated frequency introduce a steady-state oscillatory error with the frequency of the carrier signal, i.e. 1980 Hz.

Total Harmonic Distortion (THD) and spectra of both the SPWM input signal and its estimated fundamental components by the UTSP are given in Table 3.1 and Figure 3.12, respectively. As it is observed, the UTSP system filters out the high-frequency harmonics and improves THDs of the SPWM input signals.

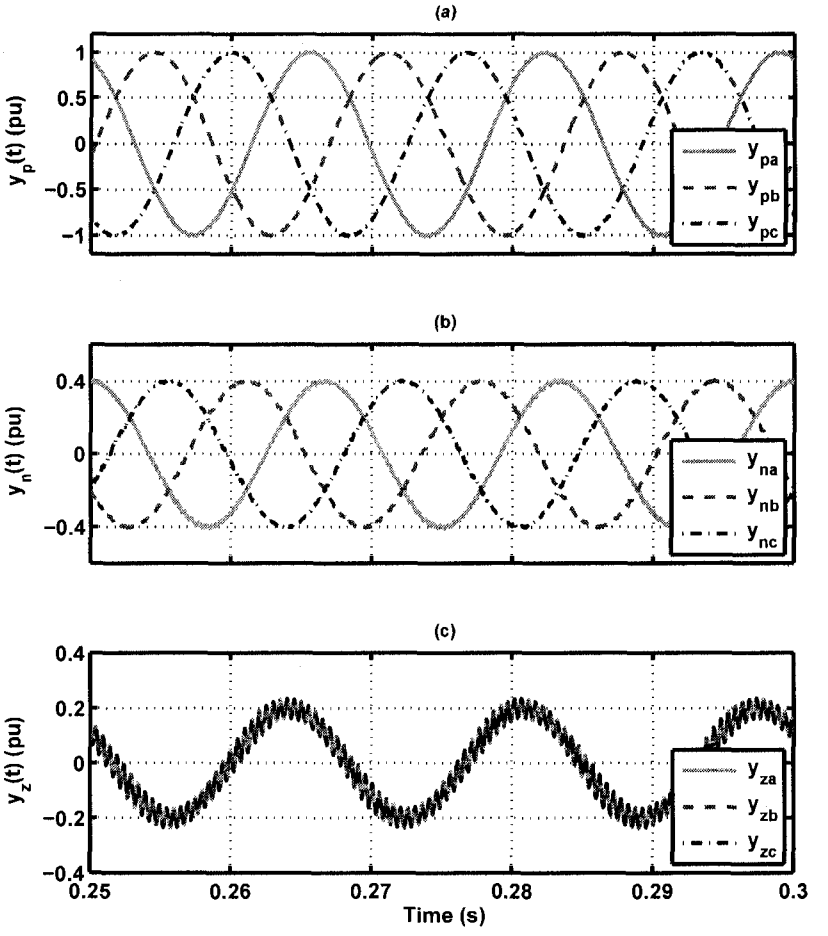

Figure 3.10: Instantaneous sequence components in the presence of high-frequency harmonics (a) positive-sequence, (b) negative-sequence, and (c) zero-sequence

The studies show that the estimated amplitudes of the sequence components and the estimated frequency include a small oscillatory (ripple) error if the input to the UTSP is polluted with harmonic components.

In the next case study, a set of balanced three-phase signals, distorted by low-frequency harmonics, are considered. To conduct the studies, the peak value of the oscillatory error in the estimated frequency and amplitude of the estimated positive-sequence component are considered as the indices for performance evaluation of the UTSP. The maximum values of the oscillatory error introduced in the estimated frequency and the estimated amplitude of positive-sequence component due to the second, third, and fifth harmonics are shown in Figure 3.13. For example, the ripple error due to 20 percent of the third harmonic and 10 percent of the fifth harmonic in the es-

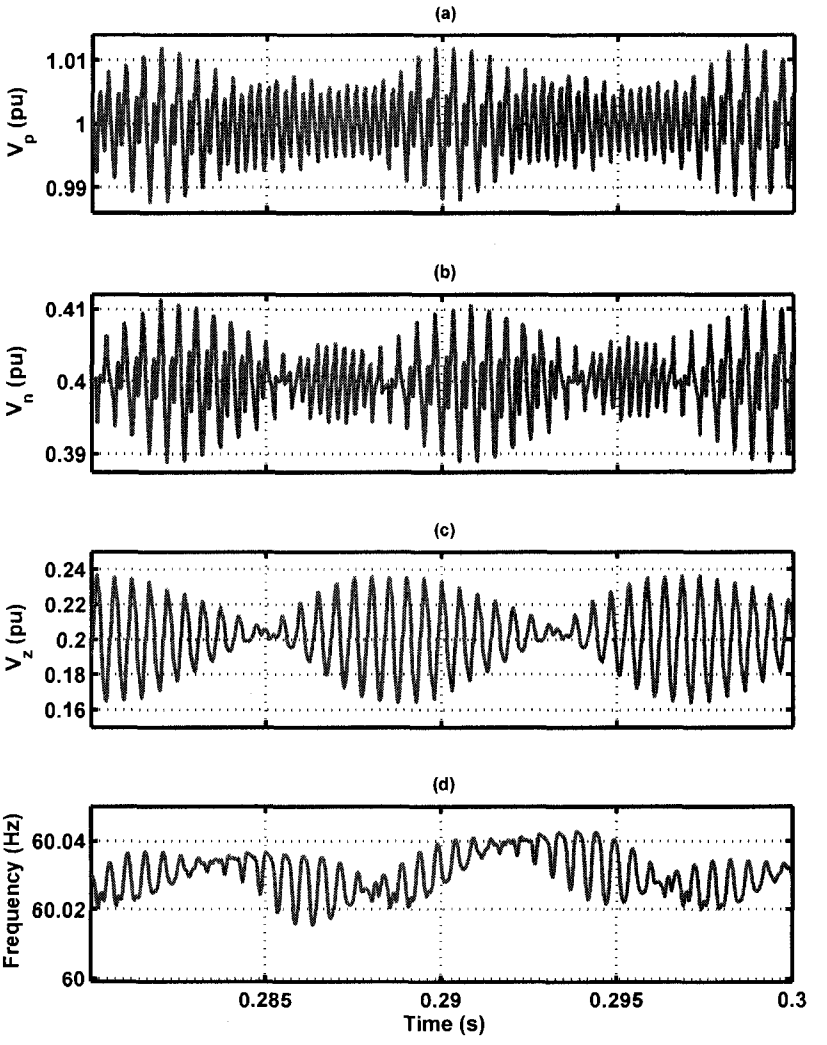

Figure 3.11: UTSP outputs in the presence of high-frequency harmonics (a,b,c) estimated magnitudes of positive-, negative-, and zero-sequence components, and (b) estimated frequency

timated frequency is equal to 2.85 mHz. This level of error is well within the acceptable range for power system applications [80]. Impacts of the harmonics of orders higher than five are practically negligible.

3.3 Comparison Between UTSP and dq0 PLL

The dq0 PLL [72-75] is a well-known tool for phase-angle and frequency estimations in three-phase systems. The UTSP system is an extension to the conventional dq0 PLL [60]. The UTSP

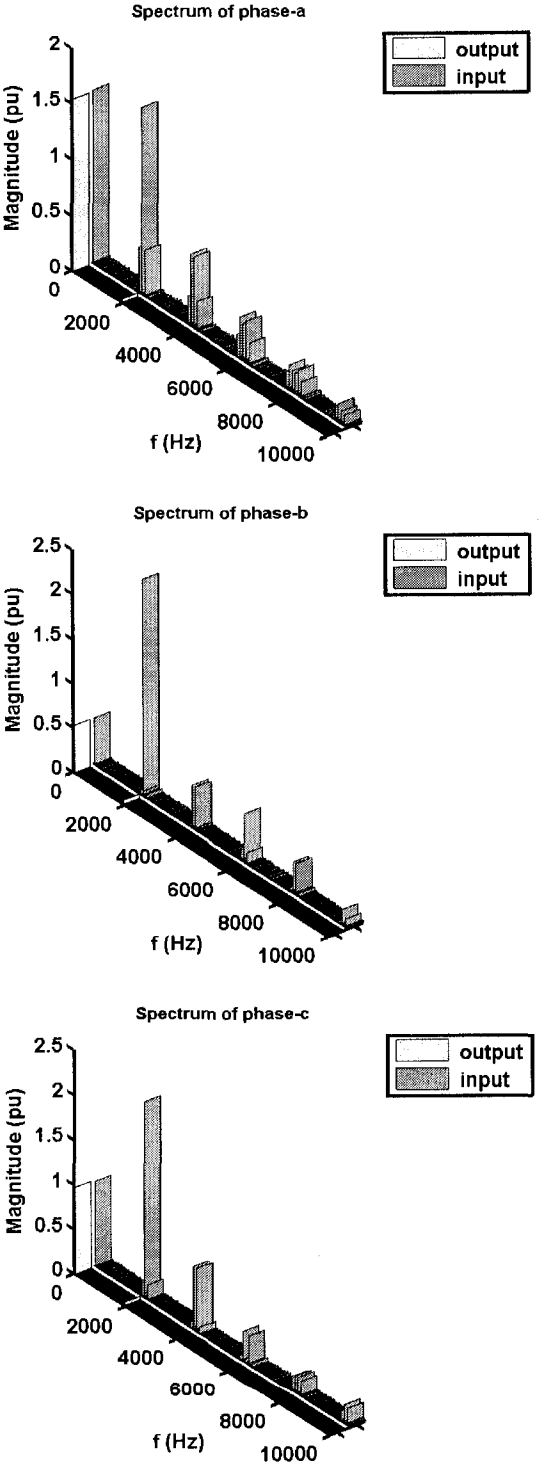

Figure 3.12: Spectra of the SPWM input signal and its estimated fundamental components

Table 3.1: THDs of input and its estimated fundamental components

	input SPWM signal	estimated fundamental component
phase-a	1.534	0.0243
phase-b	5.245	0.0929
phase-c	2.752	0.0441

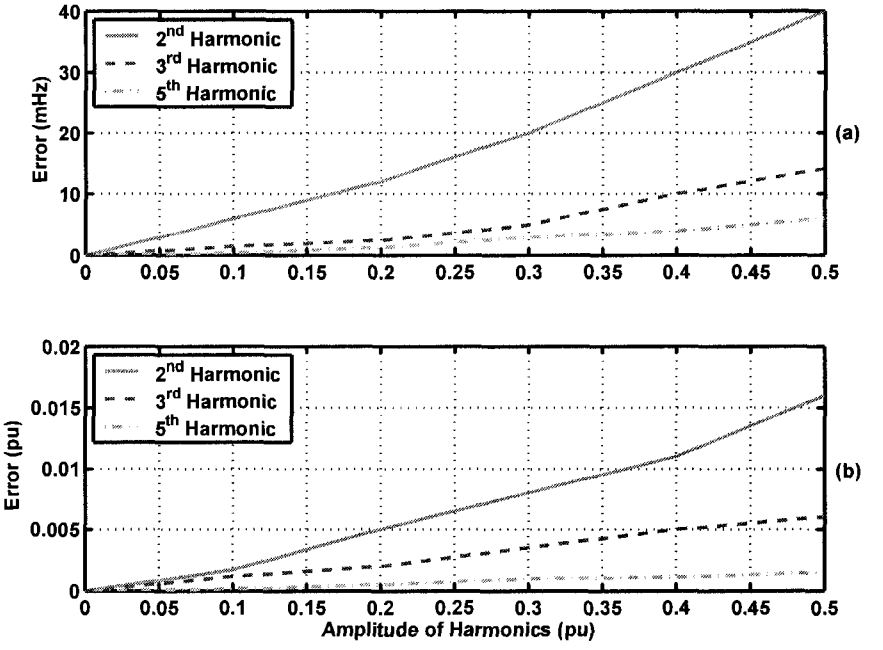

Figure 3.13: Performance of the UTSP in the presence of low frequency harmonics: magnitude of oscillatory (ripple) error in the estimated (a) frequency and (b) amplitude of positive-sequence component

system estimates a larger number of signals and parameters and, as will be shown, offers improved performance. Parameters of the dq0 PLL are selected such that its transient response to a frequency jump is almost the same as that of the UTSP system. This section presents three simulation case studies to compare performances of the UTSP system and the conventional PLL. Comparisons are made in terms of transient responses, impacts of harmonics, noise immunity, and unbalanced conditions imposed on the input signals.

In the first case, the input signal is a set of balanced three-phase signals with the amplitude of 1 pu. The input signal is distorted by a seventh harmonic with the magnitude of 0.1 pu and a random phase-angle. In order to compare the transient responses of the two systems, a frequency jump from 60 Hz to 64 Hz at t=0.3 s is also introduced in the input signal. The results are shown

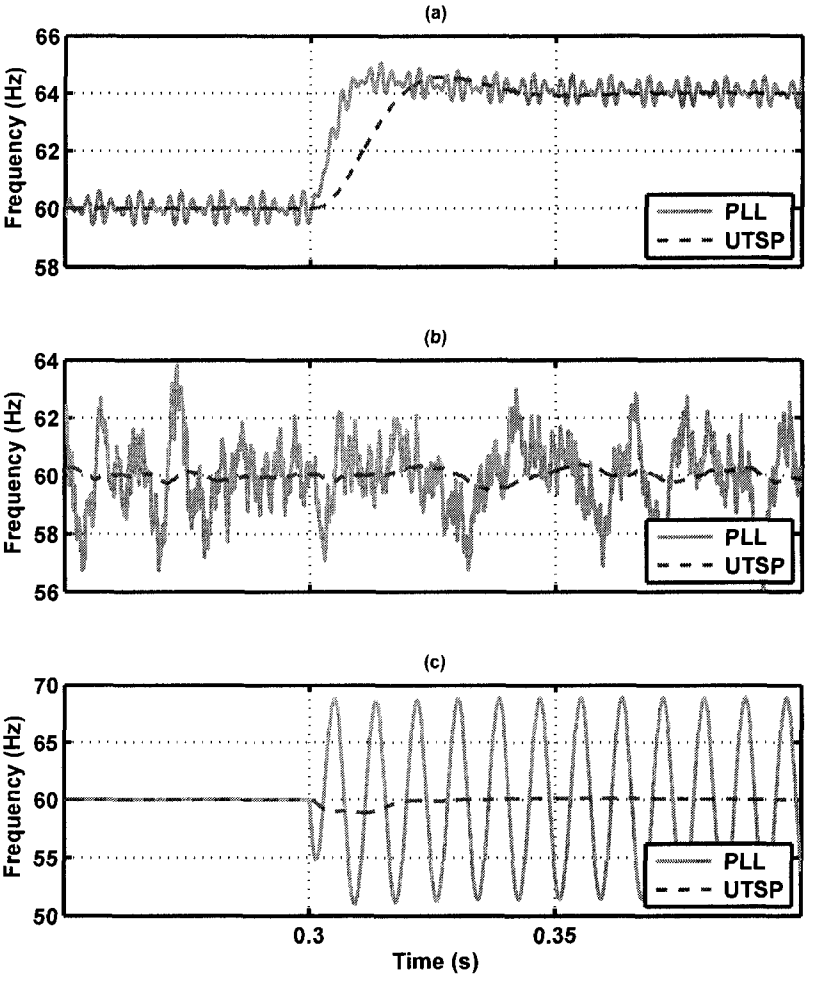

Figure 3.14: Performance comparison of the UTSP system and the conventional dq0 PLL: estimated frequency by UTSP and PLL for (a) presence of the 10% of the seventh harmonic and a jump of frequency at t=0.3 s, (b) input signal with SNR=10 dB, and (c) occurrence of an unbalanced condition at t=0.3 s

in Figure 3.14(a). For the same settling time, magnitude of the oscillatory (ripple) error in the estimated frequency by the UTSP system is several times less than that of the PLL. Notice that although the PLL is faster than the UTSP in terms of rise time, both have the same overshoot and settling time.

In the second case study, the input is a balanced pure sinusoidal set of signals, corrupted with a Gaussian white noise with zero mean and variance of 0.05, i.e. $\sigma^2 = 0.05$ or SNR=10 dB. Figure 3.14(b) shows the estimated frequencies by the UTSP and conventional PLL. Figure 3.14(b) indicates that as compared with the UTSP, the PLL presents about eight times as much oscillatory

(ripple) error.

In the third case study, an unbalanced condition is applied when both phase-a and phase-b of the input signals are stepped down from 1 pu to zero at t=0.3 s. The estimated frequencies by the UTSP system and the conventional PLL are shown in Figure 3.14(c). As expected, the PLL generates double-frequency ripples due to the presence of negative-sequence component. The UTSP system, on the other hand, does not exhibit any ripple error.

3.4 Comparison Between UTSP and EPLL

This section compares the UTSP and a three-phase Enhanced Phase-locked Loop (EPLL) system introduced in [76]. The comparison is made in terms of structural complexity and performance of the two systems, e.g. transient response, noise immunity, impact of harmonics, and impact of unbalanced conditions. The aim of this section is to show that the UTSP has a superior performance and a simpler structure than those of the three-phase EPLL system. It should be noted that parameters of the EPLL are selected such that fast transient response is obtained [76].

3.4.1 Structural Complexity

Figure 3.15 shows a block diagram of the three-phase EPLL system. The three-phase EPLL system [76] comprises (i) three single-phase EPLL units, (ii) a computational unit which calculates the instantaneous positive-sequence component based on the signals provided by the three single-phase EPLLs, and (iii) another single-phase EPLL which estimates parameters of the positive-sequence component. The single-phase EPLL presented in [81] consists of three integrators, i.e. it has three state variables. Therefore, the three-phase EPLL comprises twelve states. It should be noted that the three-phase EPLL of Figure 3.15 only provides positive-sequence component and its parameters, i.e. its magnitude, frequency and phase-angle.

The UTSP of Figure 2.1 has seven integrators or state variables. As discussed in Chapter 2, Section 2.2, the UTSP receives a set of three-phase signal, $u(t)$, and provides all sequence components and their attributes. Therefore, the UTSP system is structurally simpler than the three-phase EPLL, and nevertheless, produces more output signals and parameters than the three-phase EPLL.

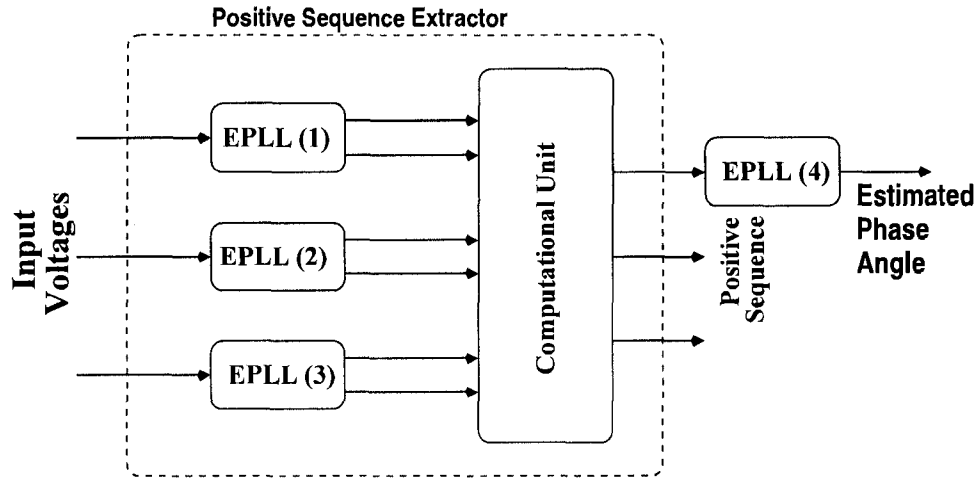

Figure 3.15: Block diagram of the EPLL

3.4.2 Transient Response

A balanced, distortion-free, three-phase input signal is applied to both EPLL and UTSP systems. At t=0.4 s, the input signal is subjected to frequency step changes of (i) 60 to 64 Hz and (ii) 60 to 60.4 Hz. Performance of the two systems in estimating and tracking the variations in the frequency of the input signal is illustrated in Figure 3.16. It is observed that the UTSP has a faster transient response than that of the EPLL. Transient response of the UTSP system to the frequency step changes of the input signal is 0.05 s, whereas it is about 0.25 s for the EPLL system.

3.4.3 Noise Immunity

Figure 3.17 compares the UTSP and the EPLL systems in terms of their immunity to noise. The input in all cases is a balanced pure sinusoidal set of signals, corrupted with a Gaussian white noise with zero mean at different variances. From the studies carried out in Section 3.2.4, we conclude that the input noise generates an oscillatory ripple error in both the estimated frequency and the estimated amplitudes of the sequence components. Figure 3.17 shows that the error introduced in the estimated frequency of the UTSP is less than that of the EPLL. However, the error of the estimated amplitude of positive-sequence component of the EPLL is slightly better than that of the UTSP.

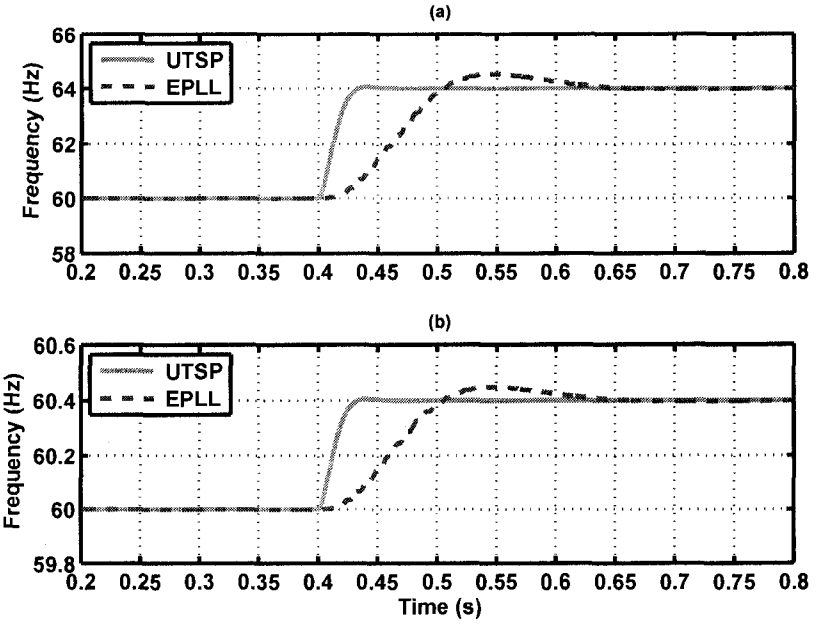

Figure 3.16: Frequency step response of the UTSP and the EPLL: (a) large step and (b) small step

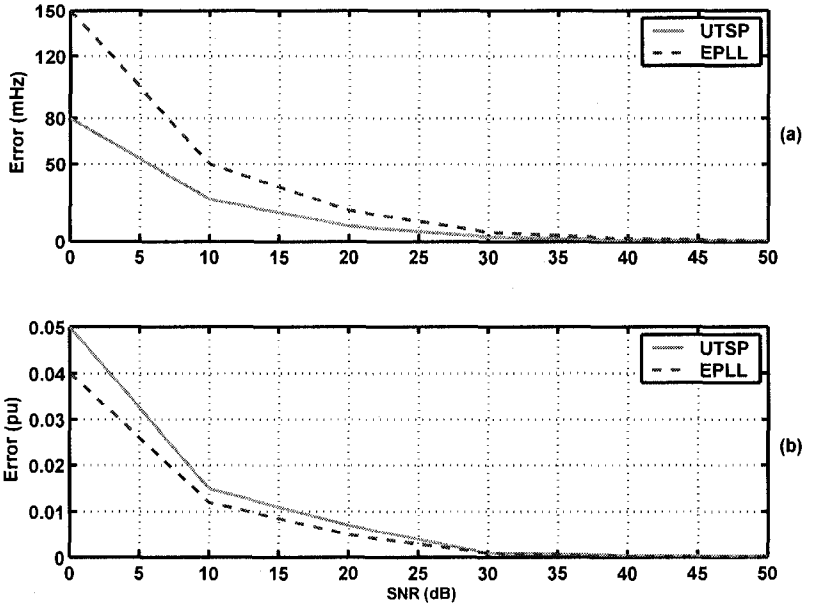

Figure 3.17: Comparison of the UTSP and the EPLL in terms of their level of immunity to noise, (a) magnitude of ripple error in the estimated frequency (b) magnitude of ripple error in the estimated amplitude of positive sequence component

3.4.4 Harmonics Sensitivity

Sensitivities of the UTSP and the EPLL to harmonics are compared in Figure 3.18. The input is a balanced pure sinusoidal set of three-phase signals corrupted by the second, third, and fifth

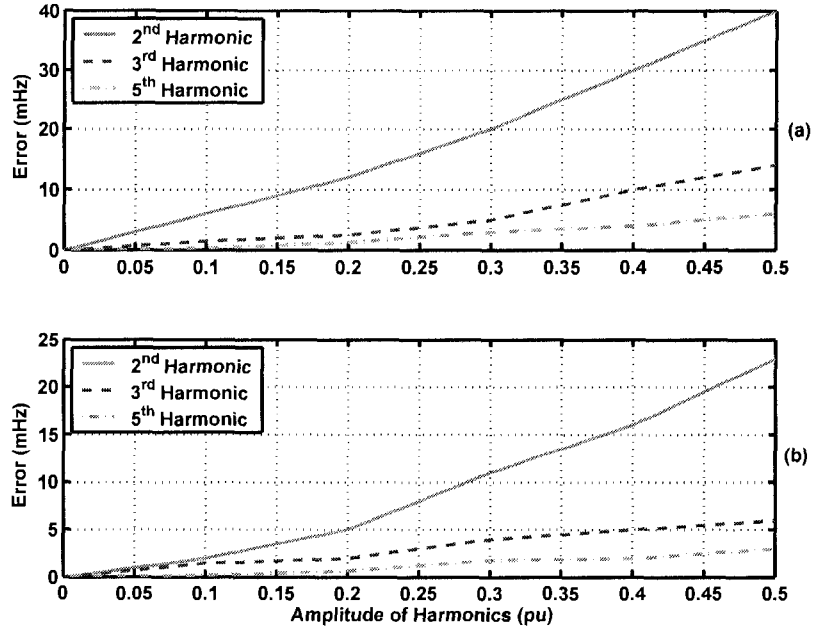

Figure 3.18: Steady-state error in the estimated frequency by: (a) UTSP (b) EPLL

harmonics. In Figure 3.18, the vertical axis is the error of the estimated frequency and the horizontal axis is the magnitude of each harmonic. Figure 3.18 shows that the EPLL system is less sensitive to the presence of harmonics. The UTSP and the EPLL systems can even operate in the presence of inter-harmonics since they are not window-based algorithms [77,82]. Figure 3.18 also indicates that the EPLL system provides a highly distortion-insensitive estimate of the frequency in the presence of harmonic pollution [76]. Although the error associated with the UTSP system in the presence of harmonics is about twice as much as that of the EPLL system, it is well within the acceptable range for power system applications [80].

3.4.5 Insensitivity to Unbalanced Conditions

Based on the studies carried out in Section 3.2.1 and [76], both the UTSP and the EPLL systems are insensitive to unbalanced conditions. Each system is able to adjust itself to unbalanced conditions with no steady-state error in the estimated frequency, phase-angle, and the magnitude of each sequence component.

3.5 Conclusions

This chapter investigated the performance of the Unified Three-phase Signal Processor (UTSP) discussed in Chapter 2. Several simulation case studies were performed in the Matlab/Simulink environment to illustrate that the UTSP is capable of estimating the symmetrical components in time-domain and their parameters including magnitudes, phase-angles and frequency. Moreover, the desired transient and steady-state performances of the UTSP including the tracking features, the noise characteristics, and insensitivity to harmonics were studied. Then, the UTSP system was compared with the dq0 PLL and the EPLL. The comparisons were made in terms of structural complexity, frequency tracking, noise immunity, distortion sensitivity, and unbalanced conditions. The results from these simulation studies show that the UTSP system is superior to the dq0 PLL [60] and EPLL.

Based on the studies carried out in this chapter, the main features of the UTSP can be summarized as follows.

- ***Extraction of Sequence Components***. This feature is demonstrated in Figures 3.1, 3.2, and 3.3. The UTSP system estimates sequence components of the input signal in about three cycles.

- ***Amplitude and Frequency Tracking***. Tracking features of the UTSP are studied in Sections 3.2.2 and 3.2.3. Precise extraction of the magnitudes of sequence components and frequency is observed after a transient-time of about three cycles, i.e., no steady-state error is observed in the estimated frequency or in the estimated magnitudes of sequence components.

- ***Noise Immunity***. Robustness of the UTSP system with respect to noise is demonstrated by several simulation studies, carried out in Section 3.2.4, e.g. Figures 3.6 to 3.8. The UTSP is able to estimate a very small negative-sequence component in the presence of noise. In the next chapter, we use this feature for islanding detection.

- ***Insensitivity to Harmonics***. Robustness of the UTSP system with respect to harmonics is shown in Figures 3.9 to 3.13. The steady-state oscillatory error is observed in the estimated frequency and magnitudes of sequence components due to the presence of harmonics.

Chapter 4

Islanding Detection Based on Negative-Sequence Current Injection

This chapter presents a new active islanding detection method for a Distributed Resource (DR) unit which is coupled to a utility grid through a three-phase Voltage-Sourced Converter (VSC). The method is based on injecting a negative-sequence current through the VSC controller and detecting and quantifying the corresponding negative-sequence voltage at the Point of Common Coupling (PCC) of the VSC by means of the Unified Three-phase Signal Processor (UTSP) introduced in Chapter 2.

According to the studies carried out in Chapter 3, the UTSP system provides high degree of immunity to noise, and thus enables islanding detection based on injecting a small (< 3%) negative-sequence current. The negative-sequence current is injected by a negative-sequence controller which is adopted as a complementary part of the conventional VSC current controller. Based on simulation studies in the PSCAD/EMTDC environment, performance of the islanding detection method under UL1741 anti-islanding standard test is evaluated, and its sensitivity to noise, grid short-circuit ratio, grid voltage imbalance, and deviations in the UL1741 test parameters are presented. The studies show that based on negative-sequence current injection of about 2 to 3%, islanding can be detected within 60 ms even for the worst case scenario, i.e. under the UL1741 standard test condition [3].

A laboratory test system is also implemented to experimentally provide proof of concept for the proposed islanding detection method. The experimental results of the test system are given in

Appendix A, Section A.3. The test results show that the proposed method provides the expected performance.

4.1 Introduction

In the context of Distributed Resource (DR) units, an island is formed when one or more DR units and a set of loads, usually at a distribution voltage level, are disconnected from the utility system and remain operational. Accidental formation of an island, e.g. due to a fault, may result in a multitude of issues [80,83], e.g. un-coordinated protection, inadequate grounding, and safety aspects. Thus, under the current utility practice, accidental islanding operation is not permitted and upon islanding detection, the DR units are required to be disconnected. Such a process is also known as anti-islanding [4]. If autonomous operation of an island is permitted [20], fast islanding detection is required for appropriate decision making to manage autonomous operation of the island. Thus, in either case, islanding detection is a requirement for utilization of DR units.

In the technical literature, there are several proposed/tested islanding detection methods which can be classified into (i) communication-based methods [18] and (ii) DR resident methods [11]. DR resident methods themselves are also divided into passive methods and active methods [8], [11], [14], [15], [84], [85]. Well-established over/under voltage and over/under frequency protection (OVP/UVP and OFP/UFP), and phase jump detection (PJD) are widely used/proposed as passive resident methods [11]. Active resident methods include slide-mode frequency shift (SMS) [14], active frequency drift (AFD) or frequency bias [15], and active frequency drift with positive feedback or Sandia Frequency Shift (SFS) [4]. These active techniques use positive feedbacks in their control loops to control reactive power and expedite under/over frequency threshold violation when the grid is not present to maintain the frequency.

In this chapter, an active islanding detection method for a DR unit which is interfaced to a distribution utility grid through a Voltage-Sourced Converter (VSC) is presented. The method is based on injecting a negative-sequence current through the VSC controllers, and quantifying the corresponding negative-sequence voltage, at the PCC of the DR unit, as the islanding detection signal. Detection and quantification of the PCC negative-sequence voltage is carried out by the UTSP system introduced in Chapter 2 which provides high degree of immunity to noise and thus

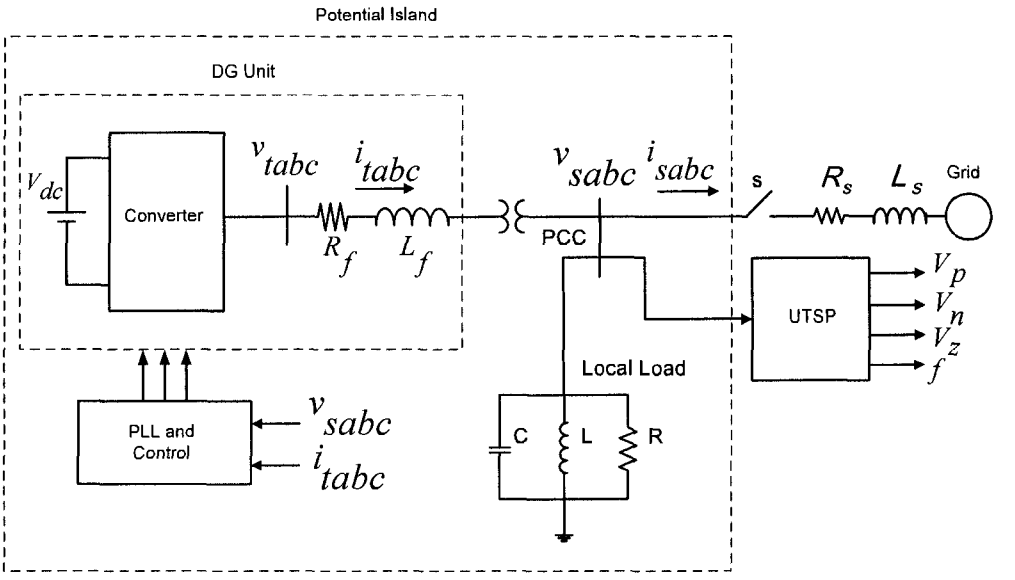

Figure 4.1: Schematic diagram of the study system for UL1741 anti-islanding test

enables small (e.g. 3%) negative-sequence current injection for islanding detection.

4.2 Test System

Either UL1741 [3] or the IEEE1547 [2] anti-islanding standard tests can be used to evaluate specific features of an islanding detection or an anti-islanding method. These two standard tests are very similar and we have adopted the UL1741 test requirements to evaluate specific features of the proposed islanding detection method. Figure 4.1 shows a schematic diagram of the UL1741 test system in which the DG unit is represented by a DC voltage source, a VSC interface unit, and a series filter. R_f and L_f represent the VSC filter for each phase. A step-up transformer connects the DG to the utility grid at the Point of Common Coupling (PCC) and its parameters can be represented as part of R_f and L_f. According to UL1741, the local load at the PCC is a parallel RLC, tuned at resonance frequency of 60 ± 0.1 Hz. At 60 Hz, the local load appears as a pure resistance, R, which is adjusted to absorb the rated power of the DG unit at the rated PCC voltage. The study system parameters are given in Table 4.1.

Table 4.1: Parameters of the study system of Figure 4.1 based on UL1741 standard

Quantity	Value	P.U.	Comment
R_f	1.5 mΩ	0.010 pu	Resistance of VSC filter
L_f	300 μH	0.785 pu	Inductance of VSC filter
VSC rated power	2.5 MW	1 pu	
VSC terminal voltage (line-line)	600 V (rms)	1 pu	
f_{sw}	1,980 Hz		PWM carrier frequency
R	76 Ω	1 pu	Load nominal resistance
L	111.9 mH	0.554 pu	Load nominal inductance
C	62.86 μF	1.805 pu	Load nominal capacitance
$Q = R\sqrt{\frac{C}{L}}$	1.8		Load quality factor
$f_{res} = \frac{1}{2\pi\sqrt{LC}}$	60 Hz		Load resonant frequency
R_s	1 Ω	0.013 pu	Grid line resistance
L_s	10 mH	0.049 pu	Grid line inductance
SCR	19.5		Grid short circuit ratio at PCC
f_0	60 Hz		System nominal frequency
Grid nominal voltage (line-line)	13.8 kV (rms)	1 pu	
Step-up transformer voltage ratio	0.6/13.8 kV		Wye/Delta
Step-up transformer rating	2.5 MVA		
V_{dc}	1500 V		DC bus voltage

4.3 VSC Control System

To control the power-exchange between the VSC and the grid of Figure 4.1, a dq-frame current-control scheme is adopted [1]. Figure 4.2(a) shows a block diagram of the VSC d- and q-axis current controllers, the decoupling stage, and a model of the VSC system for positive-sequence voltage/current components [86,87]. As shown in Figure 4.2(b), feedback signals I_d^+ and I_q^+, and feed-forward signals V_{sd}^+ and V_{sq}^+ are obtained through abc- to dq-frame transformations of VSC currents i_{tabc} and PCC voltage v_{sabc} (See Figure 4.1). Figure 4.2(b) also indicates that the angle for the abc- to dq-frame transformations, $\widehat{\theta}$, is provided by a PLL mechanism which fulfills $V_{sq}^+ = 0$, to ensure that the q-axis of the positive-sequence dq-frame is aligned with the positive-sequence voltage of the PCC [88]. Thus, the exchanged real- and reactive-power components of the VSC are proportional to the positive-sequence direct- and quadrature-axis current components [1].

Practically, PCC voltages v_{sabc} and VSC currents i_{tabc} (Figure 4.1) are unbalanced and thus include both positive- and negative-sequence components. Therefore, each variable in the dq-frame

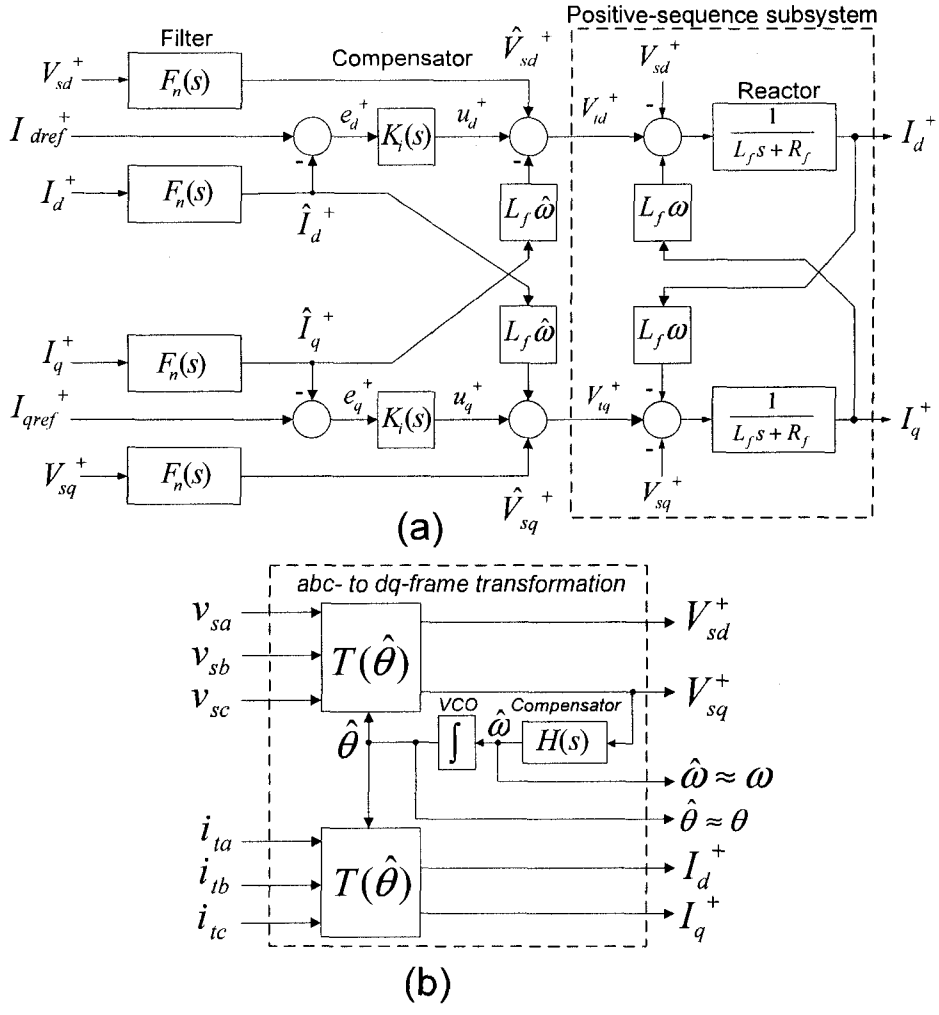

Figure 4.2: Block diagrams of (a) positive-sequence current controller and the corresponding sub-system (outlined), and (b) positive-sequence voltage/current resolver with embedded PLL [89]

includes a double power-frequency ripple, in addition to its DC component. The DC component is due to the positive-sequence component of the variable, whereas the double power-frequency ripple results from the negative-sequence component of the variable. Thus, to attenuate the double power-frequency components, notch filters $F_n(s)$ are used in Figure 4.2(a). Compensator $H(s)$ also embeds a notch filter to attenuate the double power-frequency component of V_{sq}^+ and to eliminate distortions of $\widehat{\theta}$, Figure 4.2(b). Both $K_i(s)$ and $H(s)$ include integral terms to reject steady-state error. The design procedure of the transfer functions $F_n(s)$, $H(s)$, and $K_i(s)$ are discussed in detail

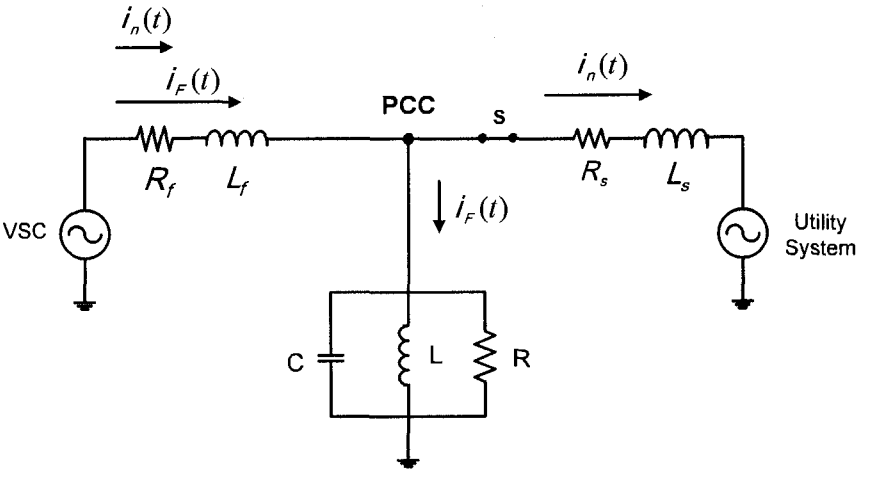

Figure 4.3: Schematic diagram of the test system illustrating positive- and negative-sequence current injection

in [89]. These transfer functions are given by:

$$H(s) = 90.63\frac{(s+30)(s^2+754^2)}{s(s+599)(s^2+126s+754^2)},$$

$$F_n(s) = \frac{s^2+754^2}{s^2+602s+754^2}, \qquad K_i(s) = 0.24\frac{s+8.33}{s}.$$

4.4 Principle of Negative-Sequence Current Injection for Islanding Detection

Figure 4.3 shows a schematic representation of the system of Figure 4.1 under the UL1741 test conditions in which the grid imposes a balanced, 60-Hz voltage at PCC. The RLC load tank draws the rated, positive-sequence fundamental current component, $i_F(t)$, supplied by VSC at unity power factor. If a 60 Hz negative-sequence current component, $i_n(t)$, is also injected by the converter current controller, it flows into the grid through the low-impedance path provided by the stiff utility grid, Figure 4.3. However, subsequent to an islanding event, i.e. when switch S is open, both injected current components flow into the load resistor. $i_F(t)$ results in the rated positive-sequence voltage component, and $i_n(t)$ results in a negative-sequence voltage component, across the load resistor at PCC. Thus under islanding conditions, the net PCC voltage is an unbalanced

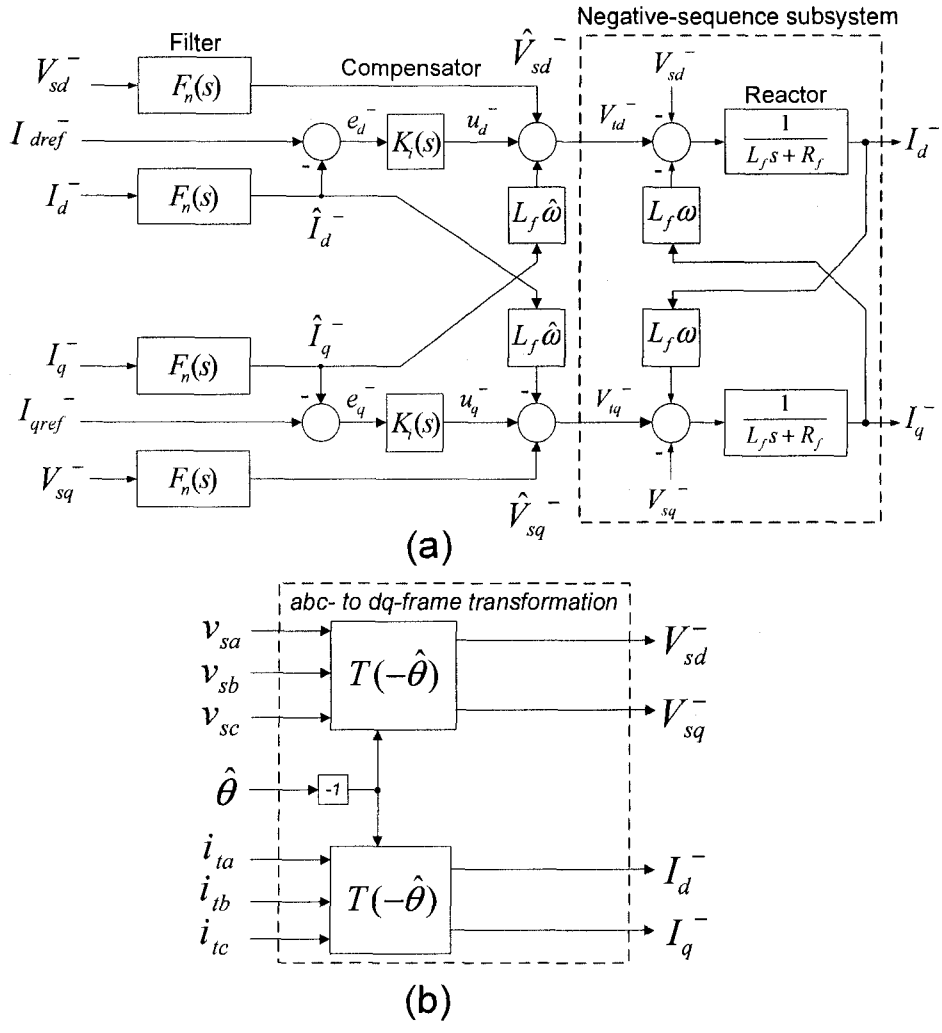

Figure 4.4: Block diagrams of (a) negative-sequence current controller and the corresponding subsystem (outlined), and (b) negative-sequence voltage/current resolver [89]

voltage. The level of voltage imbalance at PCC is detected and quantified. If the level of unbalance is beyond a permissible value, e.g. 2% [90], it indicates that islanding has occurred. Percentage of Voltage Imbalance (VI) is defined as

$$VI = \frac{V_n}{V_p} 100\%, \tag{4.1}$$

where V_p and V_n are the magnitudes of instantaneous positive- and negative-sequence voltage components (in abc reference frame), respectively. During an islanded condition, V_p and V_n are

proportional to the magnitudes of the corresponding current components, i.e. I_F and I_n, thus:

$$VI = \frac{V_n}{V_p}100\% = \frac{I_n}{I_F}100\%. \tag{4.2}$$

Thus, the proposed islanding detection is based on detection/estimation and quantification of V_p and V_n as described in Chapter 2 and Chapter 3. The following section describes the methodology to inject $i_n(t)$ through the VSC current–control for the purpose of islanding detection.

4.5 Negative-Sequence Current Injection

To inject negative–sequence current $i_n(t)$ in the system, Figure 4.3, and to generate $v_n(t)$ during islanding conditions, the conventional positive-sequence current controller of the VSC, Figure 4.2, is augmented with the negative-sequence current controller of Figure 4.4 [86,87]. Instantaneous negative-sequence feedback current and feed–forward voltage signals, i.e. I_d^-, I_q^-, V_{sd}^-, and V_{sq}^-, are obtained from *abc*- to *dq*-frame transformation of i_{tabc} and v_{sabc} (Figure 4.1) as shown in Figure 4.4(b). It should be noted that in contrast to the positive–sequence transformation of Figure 4.2(b), the transformation angle in Figure 4.4(b) is $-\widehat{\theta}$ [86,87]. Then signals I_d^-, I_q^-, V_{sd}^-, and V_{sq}^- are provided to the negative-sequence controller, Figure 4.4(a). Output signals of the negative-sequence controller of Figure 4.4(a), i.e. V_{td}^- and V_{tq}^-, and the corresponding positive-sequence components from Figure 4.2(a), i.e. V_d^+ and V_q^+, are transformed into the *abc*-frame, Figure 4.5, and used for Sinusoidal PWM (SPWM) switching of the converter. The SPWM switching strategy of Figure 4.5 generates both positive-sequence current $i_F(t)$ and the negative-sequence current $i_n(t)$, [86].

It is worth to mention that, as compared with dq0-based PLL of Chapter 3, Section 3.3, the UTSP system:

- Provides a noticeably higher degree of immunity to noise and harmonics, and thus can be used for reliable detection of small magnitudes of instantaneous negative-sequence voltage for islanding detection.

- Has a longer transient response, and thus is not used in the control path, e.g. control systems of Figures 4.2 and 4.4. However, the time response of the UTSP is well within the range for

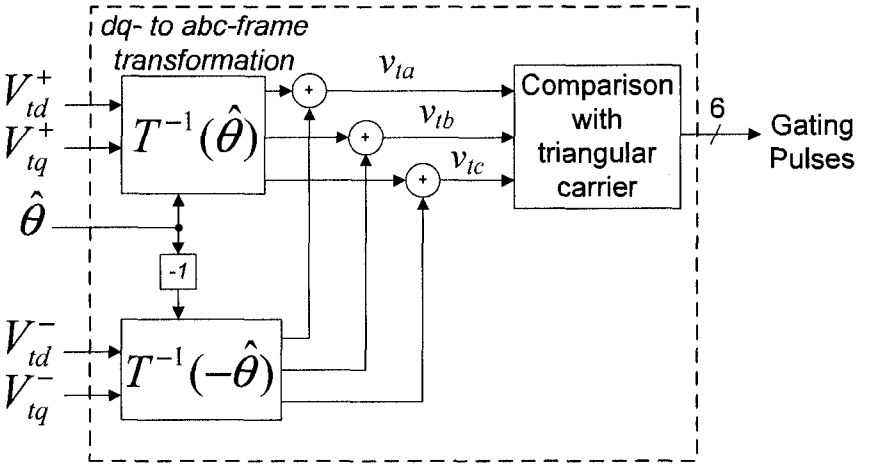

Figure 4.5: Block diagram of the converter PWM signal generator [89]

fast (within 60 ms) islanding detection [10].

Therefore, in the reported studies in this chapter, the conventional dq0-based PLL is used for the current control systems, and the UTSP system is used for islanding detection.

4.6 Performance Evaluation

This section investigates the performance of the proposed islanding detection scheme based on digital time-domain simulation of the study system of Figure 4.1 in the PSCAD/EMTDC software environment.

4.6.1 Performance Under UL1741 Test Conditions

The operating point and parameters of the study system of Figure 4.1 are adjusted based on the UL1741 test conditions [3]. Islanding detection is based on the PCC voltage signals as the input of the UTSP system. The system is islanded at time t=3.012 s by opening switch S, Figure 4.1. Prior to the islanding event, in addition to fundamental positive-sequence current, the VSC also injects 0.04 pu negative-sequence current by means of the negative-sequence current controller of Figure 4.4.

Figures 4.6(a) and (b) show instantaneous PCC voltage and grid current (i_{sabc}) signals. Figures 4.6(c) and (d) show instantaneous positive- and negative-sequence voltage signals of PCC

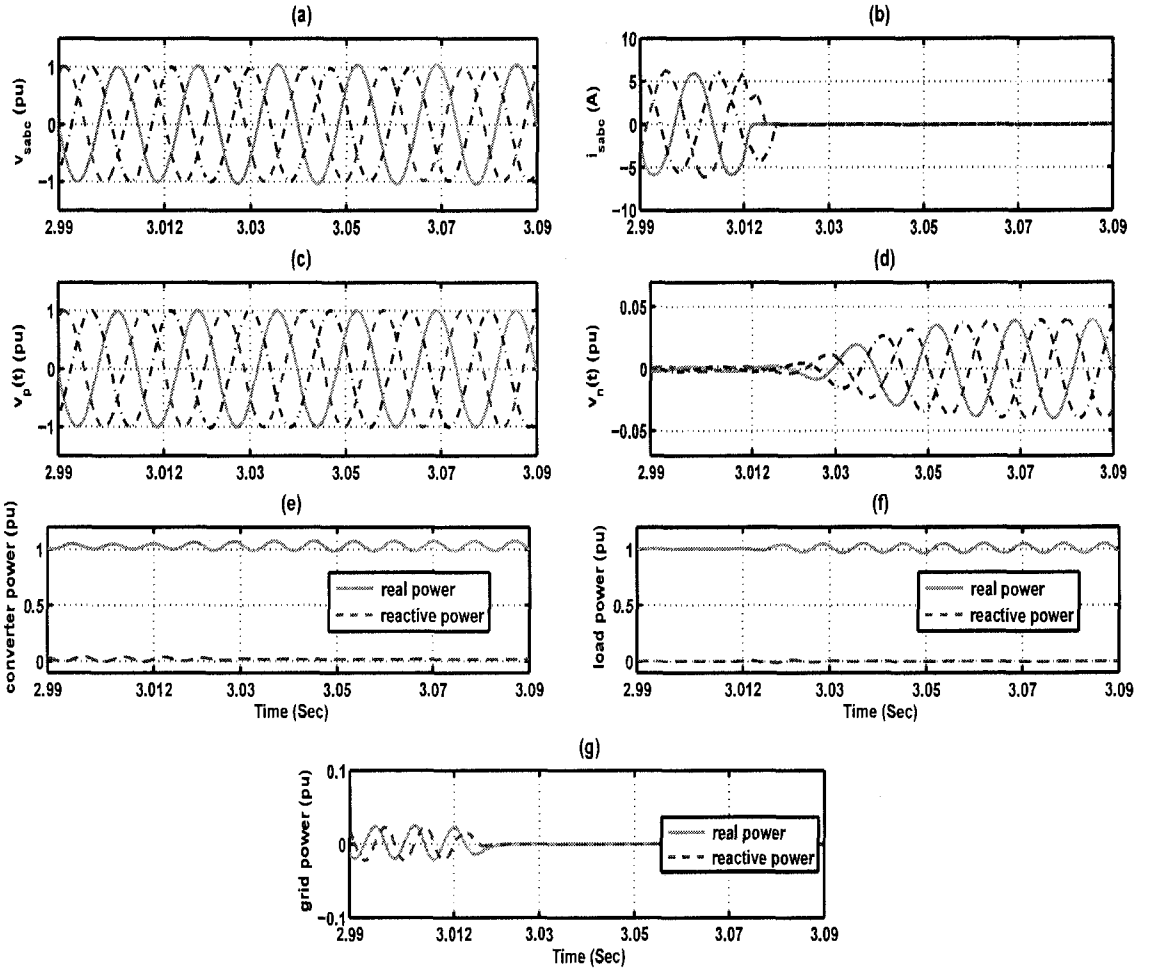

Figure 4.6: UTSP and the test system signals under UL1741 test conditions (a) PCC voltages, (b) grid currents, (c,d) instantaneous positive-, and negative-sequence voltages at PCC, and (e,f,g) instantaneous power components of converter, load, and grid

which are extracted by the UTSP, before and after the islanding instant. Figures 4.6(e) to (g) show instantaneous active and reactive power components of the converter, load, and the grid prior and subsequent to the islanding instant.

Figure 4.7(a) shows the system frequency at PCC which is extracted by the UTSP. Figure 4.7(a) indicates that frequency remains within the limit of 60 ± 0.1 Hz after islanding, and cannot be used for islanding detection within the presented time interval. Figures 4.7(b) and (c) show magnitudes of positive- and negative-sequence PCC voltage signals. Figure 4.7(c) clearly identifies the islanding event within 3.5 cycles (60 ms) while changes in the (i) instantaneous voltage of Figure 4.6(a), and (ii) amplitude of positive-sequence voltage of Figure 4.7(b) are not usable

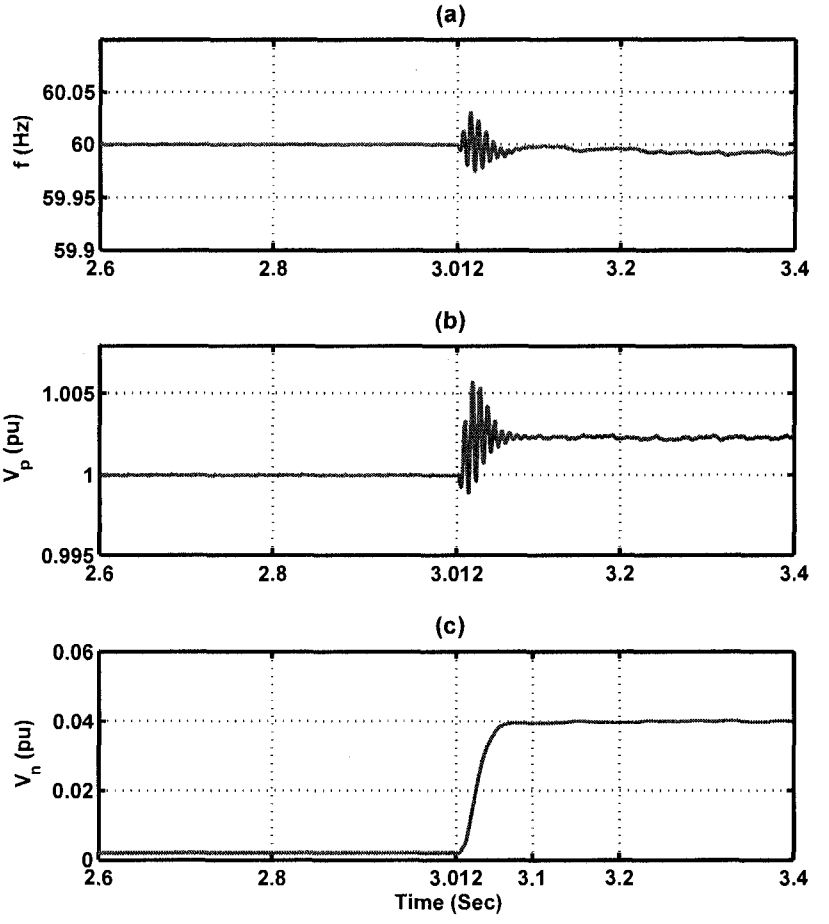

Figure 4.7: UTSP output signals under UL1741 test conditions (a) estimated frequency, and (b,c) estimated magnitudes of positive-, and negative-sequence PCC voltages

for islanding detection.

4.6.2 Sensitivity of UTSP Output Signals to Noise

The UTSP output signals, illustrated in Figures 4.6(b), (c), and 4.7, are deduced based on ideal measurement, i.e. without any noise pollution. Figure 4.8 shows the same signals of Figure 4.7, while the measured (PCC voltage) signals are polluted with a Gaussian White Noise of 30 dB Signal-to-Noise Ratio (SNR). The noise represents imperfections in measurement devices and noise in the system. SNR=30 dB is a typical value for a relatively highly polluted power system environment [78]. Figure 4.8 shows that due to noise pollution at the UTSP input signals, a small amount of ripple error is introduced in the UTSP output signals. However, comparison

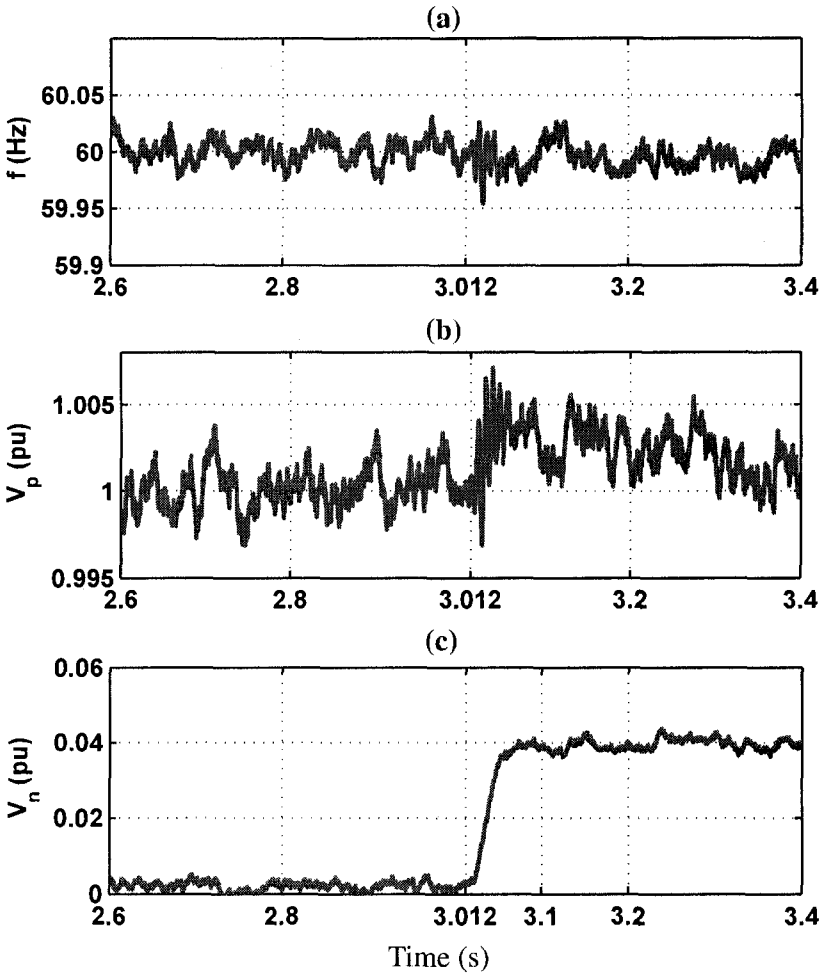

Figure 4.8: UTSP output signals under UL1741 test conditions (polluted PCC voltages) (a) estimated frequency, and (b,c) estimated magnitudes of positive-, and negative-sequence PCC voltages

between Figure 4.7 and Figure 4.8 shows that islanding detection is not adversely affected by the measurement noise. This is due to the high immunity of UTSP to noise and pollution which is its main advantage comparing to the conventional PLL, as observed in Chapter 3, Sections 3.2.4 and 3.3.

4.6.3 Response of Islanding Detection Method to Different Values of Injected Negative-Sequence Current

Figure 4.9 shows the detected negative-sequence voltage at PCC, after islanding, corresponding to injected negative-sequence current components with amplitudes of 0.5% to 5%. Figure 4.9

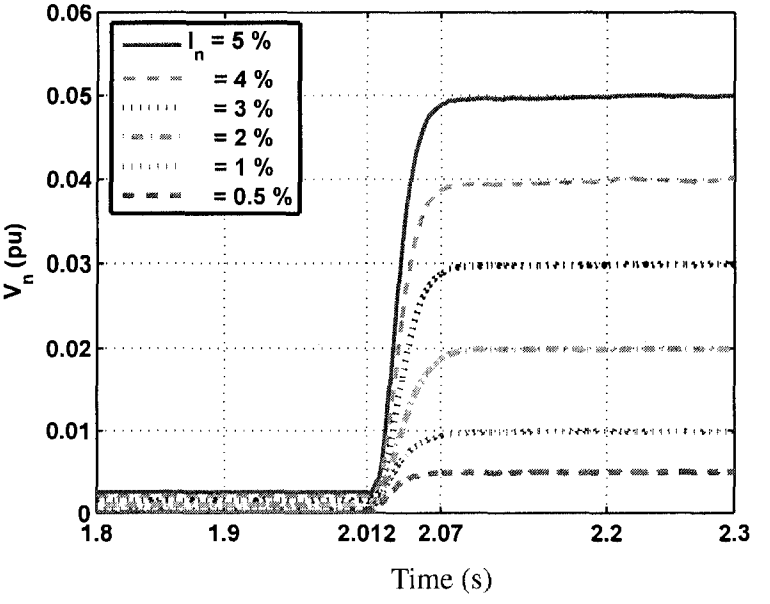

Figure 4.9: Estimated magnitude of the negative-sequence of PCC voltage for different levels of injected negative-sequence current

indicates that the negative-sequence voltage is proportional to the corresponding injected current and can be readily detected for even 1% current injection.

4.6.4 Sensitivity to Changes in Load Resistance

In this case study, while the load inductor and capacitor are kept constant at their rated values, the load resistance is changed from 97% to 103% of its rated value. For each value of R, the VSC injects 1%, 2.5%, and 5% negative-sequence current. Figure 4.10 shows the UTSP output signals when the load resistance is equal to 97% of its rated value. In this case, in addition to the power delivered by the VSC, the grid also delivers a small component of real power to the local load prior to islanding. Therefore, after the islanding event, the magnitude of positive-sequence voltage of PCC drops to 97% which is not large enough to detect the islanding event. However, the magnitude of negative-sequence voltage at PCC is readily detectable for all injection levels.

Figure 4.11 shows the UTSP outputs when the load resistance is 103% of its rated value. In this case, the grid absorbs a small component of real power prior to the islanding instant. Therefore, after islanding event, magnitude of the positive-sequence PCC voltage rises to 103% which is not

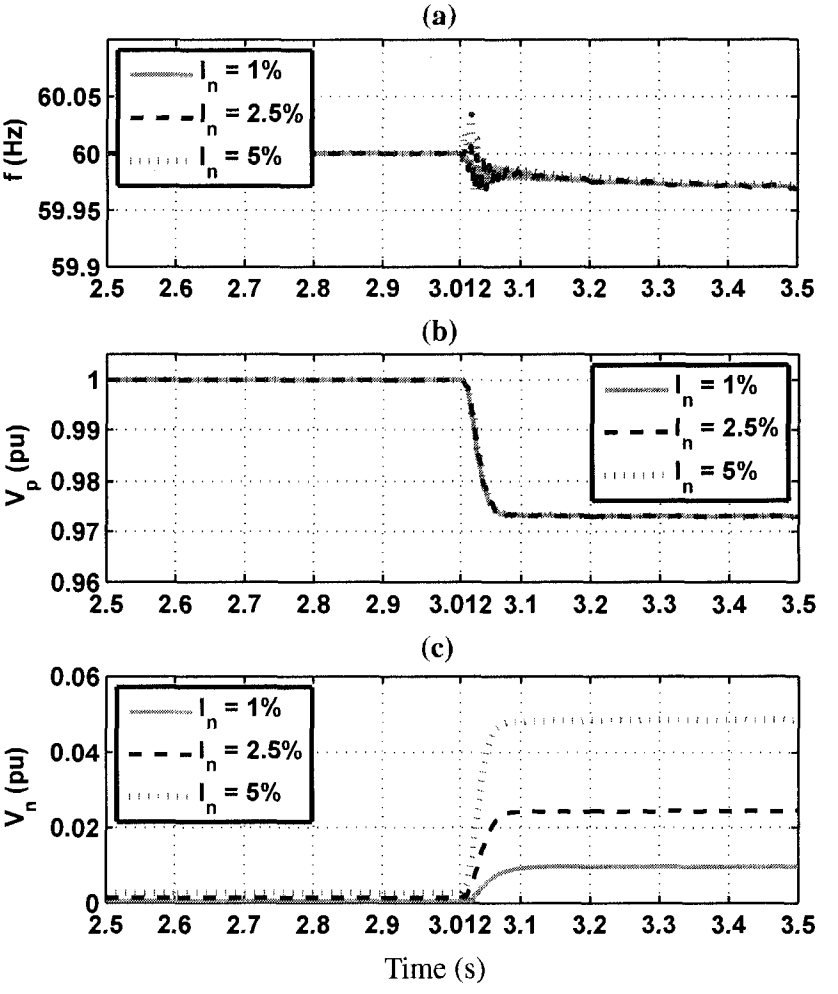

Figure 4.10: UTSP output signals corresponding to different levels of injected current (R=97% of rated value) (a) estimated frequency, and (b,c) estimated magnitudes of positive-, and negative-sequence PCC voltages

large enough to detect the islanding event. In this case, magnitude of the negative-sequence PCC voltage is detectable for all current injection levels and can be used for islanding detection. It should be noted that for both case studies of Figures 4.10 and 4.11, the system frequency exhibits small changes after islanding operation which cannot be used for islanding detection.

4.6.5 Sensitivity to Load Inductance and Capacitance

In this case study, while the load resistor and capacitor are kept constant at their rated values, the load inductance L varies from 95% to 105% of its rated value. The VSC current controller injects 4% negative-sequence current and the system is islanded at t=3.012 s. The grid exchanges a small

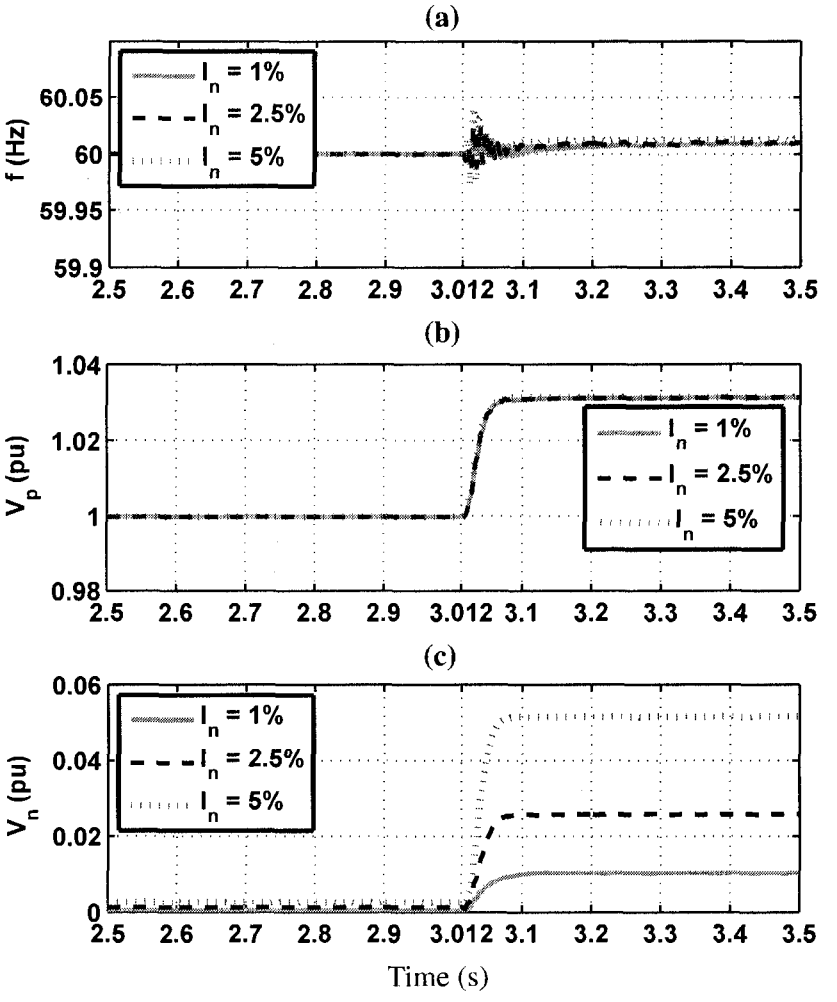

Figure 4.11: UTSP output signals corresponding to different levels of current injection (R=103% of rated value) (a) estimated frequency, and (b,c) estimated magnitudes of positive-, and negative-sequence PCC voltages

component of reactive power with the potential island since L and C are not tuned for resonance at the power system frequency. Therefore, subsequent to an islanding event, the island frequency deviates from its rated value. Figure 4.12 shows the UTSP output signals for different values of load inductance L. Figure 4.12 clearly shows that a larger deviation of L from its rated value results in a larger frequency deviation. However, based on the negative-sequence current injection, the measured negative-sequence voltage provides a reliable signal for islanding detection. If variation of L is small enough such that the resonance frequency is within 60 ± 0.1 Hz, the injected negative-sequence current still provides a reliable islanding detection signal.

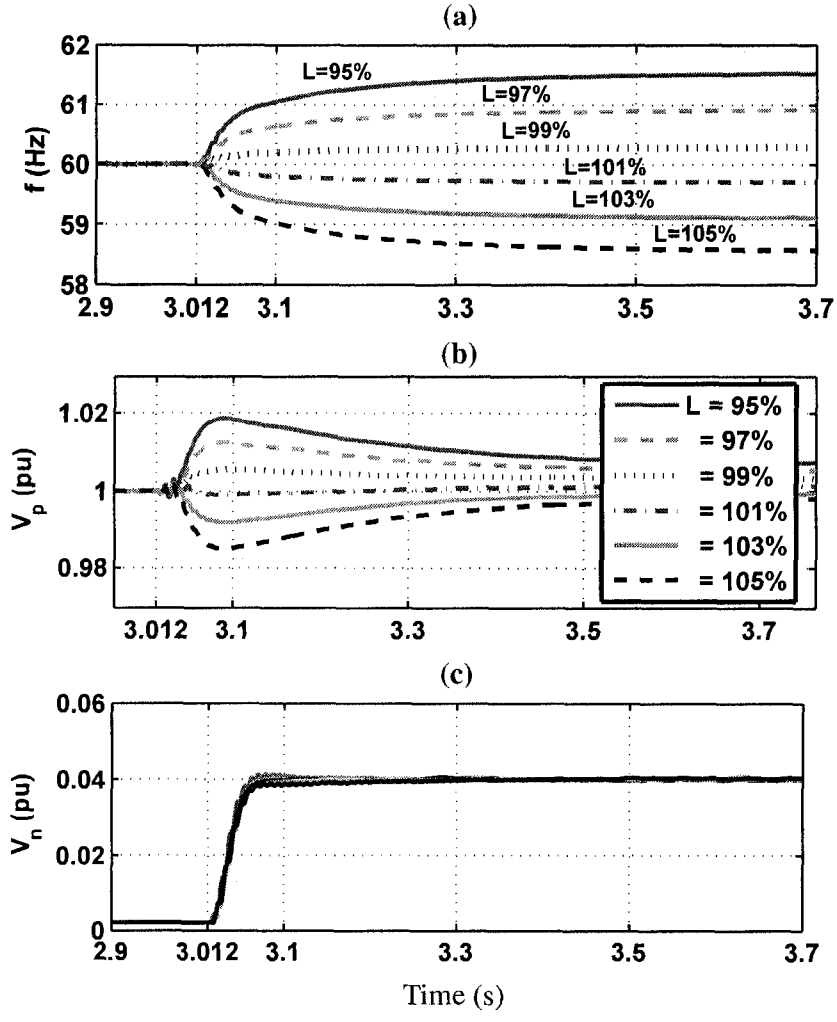

Figure 4.12: UTSP output signals when L changes from 95 to 105% of rated value (a) estimated frequency, and (b,c) estimated magnitudes of positive-, and negative-sequence PCC voltages

4.6.6 Effect of Grid SCR

This case study evaluates performance of the proposed islanding detection method for different grid Short-Circuit-Ratio (SCR) values. Prior to the islanding instant at t=3.005 s, the VSC injects 100% and 4% positive- and negative-sequence current components, respectively. Figure 4.13 shows amplitudes of negative-sequence PCC voltages corresponding to five different SCR values. For a weak grid, e.g. at SCR value of 1, even prior to islanding, the injected negative-sequence current results in a relatively significant negative-sequence voltage component at PCC. This can result in an erroneous islanding detection, if a 2% negative-sequence voltage is considered as the acceptable threshold. Figure 4.13 shows that for SCR values larger than 2, the proposed method

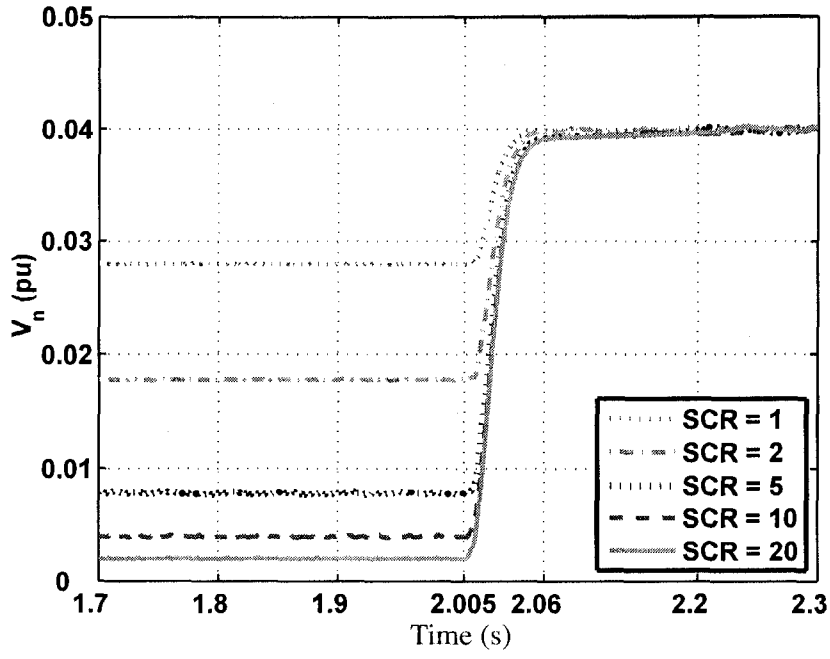

Figure 4.13: Estimated magnitude of the negative-sequence of PCC voltage for different values of short circuit ratio

can correctly detect the islanding event.

4.6.7 Effect of Source Imbalance

Figure 4.14 shows performance of the proposed islanding detection method when the grid is fairly stiff (SCR=17) but its voltage is not balanced. In case 1 (and case 2) voltage imbalance is due to 2% (and 5%) negative-sequence voltage component. Since the grid is stiff, the level of voltage imbalance of the grid source almost equally appears at the PCC voltage as well. Initially, the VSC is injecting 4% negative-sequence current, and at t=1.002 s the system is subjected to an islanding event.

Figure 4.14(c) indicates that even with 2% voltage imbalance of the grid (case 1), the PCC negative-sequence voltage, due to the injected negative-sequence current, can correctly provide an islanding detection signal. The proposed detection method cannot be used for islanding detection when the grid voltage imbalance is 5% (case 2). Figures 4.14(a) and (b) show that deviations in V_p and frequency are not usable for islanding detection within the given time frame.

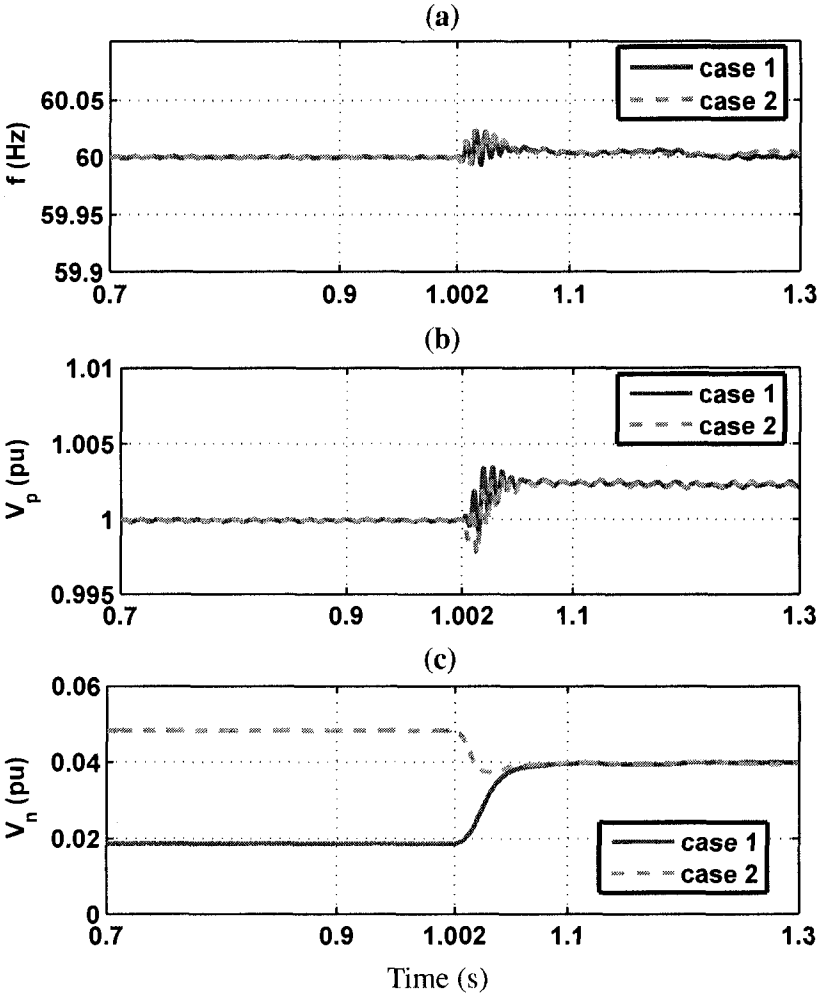

Figure 4.14: UTSP output signals under grid imbalance conditions (a) estimated frequency, and (b,c) estimated magnitudes of positive-, and negative-sequence PCC voltages

4.6.8 Effect of Load (R) Imbalance

In this case study, all conditions comply with the UL1741 test conditions except that the load resistance is not balanced. Two cases are considered: in case 1 only the resistance of phase-a is set to 97% of its rated value, in case 2 resistances of phase-a and phase-c are set at 97% and 103% of the rated value. Islanding occurs at t=3.012 s and 4% negative-sequence current is injected by the VCS negative-sequence current controller.

Figures 4.15(a) and (b) show that frequency and positive-sequence voltage at PCC do not provide reliable information for fast islanding detection. However, Figure 4.15(c) clearly shows that the PCC negative-sequence voltage due to 4% negative-sequence current injection can provide

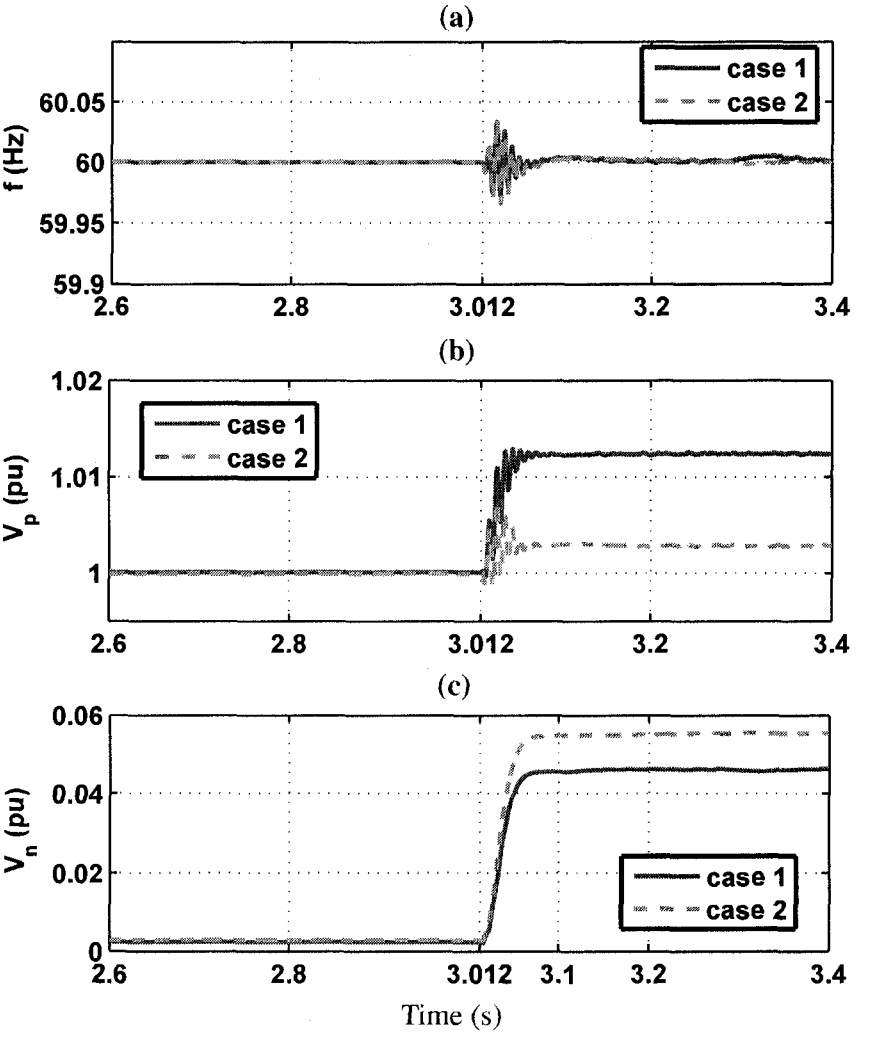

Figure 4.15: UTSP output signals under load (R) imbalance conditions (a) estimated frequency, and (b,c) estimated magnitudes of positive-, and negative-sequence PCC voltages

islanding detection within 3.5 cycles (60 ms). Figure 4.15(c) also indicates that higher degree of load imbalance (case 2) results in a higher level of negative-sequence voltage at PCC, after islanding.

4.7 Discussion

In a practical scenario, e.g. subsequent to unbalanced transients due to a load change or a rotating machine inrush-currents, the PCC voltages may transiently include negative sequence components that exceed the detection threshold of the proposed method and result in false islanding detection.

Since such negative sequence voltage components at the PCC are experienced transiently, a logic can be added to the proposed detection method to monitor the rate of change of the negative sequence voltage and indicate islanding detection, if the negative sequence signal is either a "steady-state" or a "quasi steady-state" signal. Inevitably this increases the islanding detection time of the proposed method, however, still it remains much faster than the existing islanding detection methods.

The proposed islanding detection method also can be augmented with another logic to prevent false trips. This logic is based on monitoring the grid current (in addition to the converter current) at the grid side of the PCC, Figure 4.1. When the system is subjected to the transient conditions, there will be a power exchange between the utility grid and the potential island. Thus, there exists a measurable current flowing through the grid line (which is not the same as the converter current) and indicates that the system is still operating in the grid-connected mode. Therefore, a more elaborate logic for the proposed islanding detection method is based on measurement of the grid line currents and the negative-sequence voltage estimated at the PCC.

The reported studies in this research only deal with a single DG unit and do not investigate feasibility of the proposed islanding detection method for multiple DG units. In the case of multiple DG units, one of the following two scenarios exists.

- In the first scenario all DG units are in parallel, i.e. all units are connected to the same PCC. In this case, since each DG unit is equipped with its own islanding detection platform and the required signals (and synchronization reference) of each platform are deduced from the voltage of the common PCC, the injected negative sequences currents of the DG units are approximately in-phase and do not cancel each other. Thus each DG unit can detect an islanding event independently and irrespective of the other DG units.

- In the second scenario, the DG units are not in parallel and interfaced to the host grid at different PCCs. In this case, depending on the grid topology, i.e. ring or radial configuration and electrical distances among PCCs, the injected negative sequence current components of DG units, subsequent to an islanding event, at some PCCs can interact with each other. For a radial feeder, particularly when the DG units are in relative electrical proximity of each other, this interaction is not significant. It should be noted that this interaction phenomenon

is an inherent nature of all active islanding detection methods and not limited only to the proposed detection method.

The two main criteria to compare the proposed islanding detection method with other existing active resident islanding detection methods [4,14,15] are:

- speed of detection or run-on time which is defined as the time interval between the actual islanding instant and the islanding detection instant,
- non-detection zone (NDZ) which is a region (or space) specified by the system parameters, in which islanding detection fails [8].

In comparison with the existing islanding detection methods, that have run-on times of even up to about 120 cycles [8], the proposed method is significantly faster and detects an islanding event within a few cycles, e.g. maximum of four cycles for the reported study cases. The proposed islanding detection method has no NDZ while the other active methods [4,14,15] exhibit NDZs depending on the strategy and parameters they adopt for islanding detection.

4.8 Conclusions

This chapter proposed a new active islanding detection method for a VSC-coupled Distributed Resource (DR) unit. Islanding signal is deduced based on detection and quantification of the instantaneous negative-sequence voltage at the Point of Common Coupling (PCC) of the DR unit. The negative-sequence voltage is actively generated by injecting a small negative-sequence current through a negative-sequence VSC current controller which is introduced as a supplement to the conventional VSC current controllers.

The Unified Three-phase Signal Processor (UTSP) introduced in Chapter 2 was used for detection and quantification of the PCC negative-sequence voltage as the islanding detection signal. Based on time-domain simulation in the PSCAD/EMTDC software environment, the proposed islanding detection method was evaluated under UL1741 test conditions. The studies conclude that the proposed islanding detection method:

- detects an islanding event within 60 ms (3.5 cycles) under UL1741 test conditions,

- is highly immune to noise and accurately performs its task even when the PCC voltage is polluted with a Gaussian White Noise of SNR=30 dB,
- requires 2 to 3% negative-sequence current injection for islanding detection,
- can correctly detect an islanding event for the grid short-circuit ratio of 2 or higher,
- is insensitive to variations of the load parameters of UL1741 test system.

Chapter 5

Control of an Islanded Electronically-Coupled DR Unit under Balanced Conditions

5.1 Introduction

The expected high depth of penetration of distributed generation (DG) units in the utility distribution grid [91] have brought about concepts of "microgrid" [21] and "smart grid" [92]. Although full benefits of high depth of penetration of DG units are gained if a microgrid or a smart grid can be operated in both grid-connected and islanded (autonomous) modes [20,21], the current utility practice and the existing standards [2,3] do not permit such islanded operations. The main reason is the safety concerns associated with that portion of the utility grid that remains energized at part of the island [4]. However, there are provisions to permit islanded operation of a DG unit and its dedicated load, if the island does not include any portion of the utility grid. In this context, the DG unit operates analogous to an Un-interruptible Power Supply (UPS) for the load.

A technical challenge to enable an electronically-coupled DG unit and its local load to remain operational in both grid-connected and islanded modes is to equip the coupling Voltage-Sourced Converter (VSC) with controllers that can accommodate both modes of operation and the transition process between the two modes. The conventional control strategy for an interface VSC, in a grid-connected mode, is based on current-controlled operation of the VSC [1]. Based on this control

strategy, the grid dominantly dictates frequency and voltage at the Point of Common Coupling (PCC) of the DG unit and the VSC controls its exchanged real and reactive power components with the grid based on the controlled dq-current components.

In this chapter, autonomous operation of an islanded single DG system which is under balanced conditions is investigated. The islanded system includes a DG unit and a passive RLC load. The objective is to design a robust controller for the DG unit to regulate voltage magnitude and frequency of the island, despite unknown load parameters. To provide a fixed frequency in the islanded mode, a crystal oscillator whose frequency equals the system nominal frequency is used in the control system of the DG unit. Therefore, the island frequency is controlled/dictated in an open-loop manner at the pre-specified frequency. To robustly regulate voltage magnitude at the PCC, a feedback control system must be come into play. Since the voltage magnitude at PCC is the only control quantity and also the islanded system is assumed to be under a balanced condition, the rotating reference frame (dq-frame) is used to obtain dynamic models for the islanded system.

In this chapter, depending on the selection of the reference phase-angle, two distinct mathematical models for the islanded system in the dq-frame are presented. In the first model, phase-angle of the PCC voltage is used as the reference phase-angle for the dq-frame transformation. In this case, the obtained model represents a multiple-input single-output (MISO) nonlinear system. However, by making the simplifying assumption that the rate of change of reference phase-angle, i.e. frequency, is constant, the MISO nonlinear system is converted to a single-input single-output (SISO) linear time invariant (LTI) system. Then, using the classical control approach, a controller which is structurally simple is designed. The proposed controller (i) guarantees stability of the islanded system, and (ii) provides desired performance characteristics, e.g. fast transient response and zero steady-state error, for the islanded system. However, the proposed SISO controller cannot cope with a wide range of load parameter uncertainties and is appropriate for a pre-specified load with a relatively small range of parameter variations.

In the second formulation, phase-angle of the VSC internal oscillator is used as a reference to obtain an exact model for the islanded system in the dq-frame. In this case, the model obtained corresponds to a multivariable LTI system with structured uncertainties [48,93]. The parametric structured uncertainties result from the local load parameters which can vary about their rated values. Based on this dynamic model of the islanded system, a multiple-input multiple-output

(MIMO) servomechanism controller for the nominal plant is designed to guarantee robust stability, and to provide desired high performance for the islanded system despite load parameters uncertainty. To the best of our knowledge, this is the first time that such a controller design has been carried out to achieve these objectives in the context of an islanded DG unit.

It should be noted that the SISO controller is structurally simple and can only be used for the applications where the local load is fixed, and cannot compensate large perturbations about the nominal load. For the applications for which the local load is highly uncertain, the MIMO servomechanism controller is preferred, since it is strongly robust with respect to load parameters uncertainty. However, the MIMO servomechanism is a high-order controller and its hardware realization demands more resources.

In this chapter, PSCAD/EMTDC software is used to simulate both SISO and MIMO control systems. Simulation case studies provide a performance evaluation of both control systems under various operational scenarios.

In addition to the simulation case studies, a laboratory test system is also mounted to experimentally validate the performance of both control systems. The experimental results of the test system are given in Appendix A, Section A.4 and Section A.5.

5.2 System Description

Figure 5.1 provides a schematic, single-line diagram of a DG unit which is interfaced to a utility grid through its interface VSC. A local load is connected to the PCC where the DG unit and the main grid are coupled. The DG unit is represented by a DC voltage source, the interface VSC, and a series filter specified by R_t and L_t in each phase. The pre-specified DC source indicates that the DG unit is a dispatchable unit. A step-up transformer connects the DG to the utility grid at the PCC. The transformer parameters can be assumed as parts of R_t and L_t. According to the UL1741 and IEEE1547 standard tests [2,3], the local load is modeled by a three-phase parallel RLC network. A parallel RLC network is the worst type of load for most islanding detection methods when the load inductance and capacitance are tuned to the system frequency and its total power is delivered by the DG [2,3]. Parameters of the DG unit, the utility system, and the rated values of the local load which are used in this study are summarized in Table 5.1.

Table 5.1: Parameters of the system studied in Figure 5.1

Quantity	Value	P.U.	Comment
R_t	1.5 mΩ	0.010 pu	Resistance of VSC filter
L_t	300 μH	0.785 pu	Inductance of VSC filter
VSC rated power	2.5 MW	1 pu	
VSC terminal voltage (line-line)	600 V (rms)	1 pu	
f_{sw}	1,980 Hz		PWM carrier frequency
V_{dc}	1500 V		DC bus voltage
R	76 Ω	1 pu	Load nominal resistance
L	111.9 mH	0.554 pu	Load nominal inductance
C	62.86 μF	1.805 pu	Load nominal capacitance
$Q = R\sqrt{\frac{C}{L}}$	1.8		Load quality factor
$f_{res} = \frac{1}{2\pi\sqrt{LC}}$	60 Hz		Load resonant frequency
$q_l = \frac{L\omega_0}{R_l}$	120		Inductor quality factor
R_s	1 Ω	0.013 pu	Grid line resistance
L_s	10 mH	0.049 pu	Grid line inductance
SCR	19.5		Grid short circuit ratio at PCC
f_0 ($\omega_0 = 2\pi f_0$)	60 Hz		System nominal frequency
Grid nominal voltage (line-line)	13.8 kV (rms)	1 pu	
Step-up transformer voltage ratio	0.6/13.8 kV		Wye/Delta
Step-up transformer rating	2.5 MVA		

The system of Figure 5.1 is required to operate in both grid-connected and islanded modes. In a grid-connected mode, the interface VSC operates as a current-controlled VSC. Voltage magnitude and frequency of the local load (PCC) are regulated by the grid. Based on the methods discussed in [1,86,87], a dq-frame current-control scheme is designed to control the power-exchange between the DG unit and the grid of Figure 5.1. The grid may exchange real and reactive power with the potential island. Under the conditions that both real and reactive power exchange between the potential island and the grid are zero, the system operates in a matched-power state. Otherwise, the system is in a mismatched-power condition.

In an islanded DG-load, without voltage and frequency controls, the voltage magnitude and the island frequency deviate from their rated values. This occurs due to the power mismatch between the DG unit and load. Thus, voltage and frequency of the load can vary significantly and result in the system collapse if the DG unit does not provide voltage and frequency control. Therefore, to

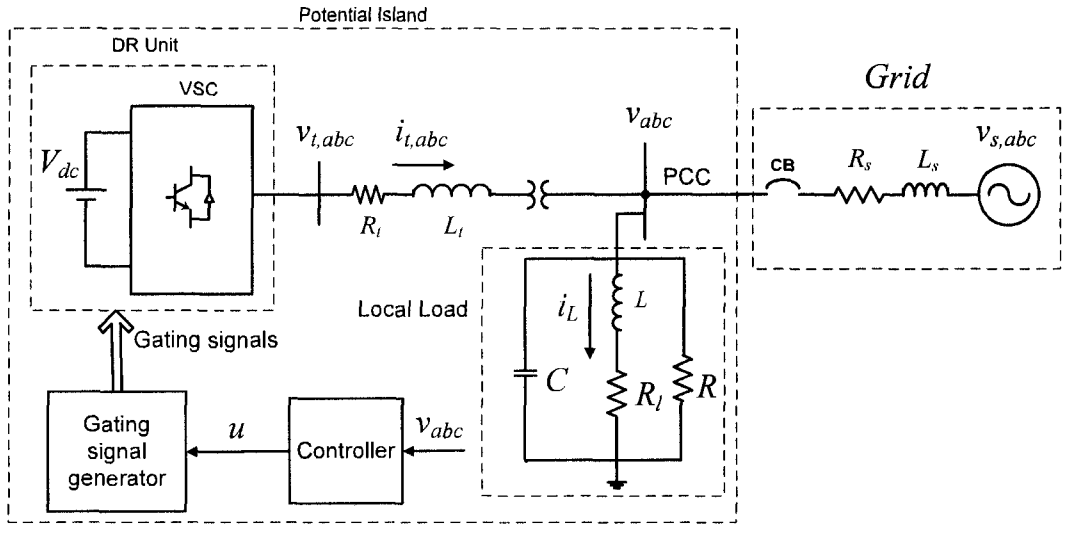

Figure 5.1: Schematic diagram of a grid-interfaced DG unit and its controller

achieve uninterruptible, autonomous, operation of the island, the islanding event must be detected and subsequently voltage and frequency must be controlled. In this case, the new controllers to be developed should regulate voltage magnitude and frequency of the load, and the design of the new controllers is to be based on dynamic models of the islanded system which are discussed in Section 5.3.1 and Section 5.4.1. Frequency of the islanded system is controlled using an internal oscillator in an open-loop manner. Frequency of the internal oscillator is set at the system nominal frequency ω_0. Thus, the frequency of voltage and current signals within the islanded system is at ω_0. It should be noted that the islanding event is detected by the proposed method and procedures of Chapter 4.

5.3 SISO System

In this section, first a mathematical model for the islanded system of Figure 5.1 in the stationary reference frame ($\alpha\beta$-frame) is derived. Then using the load voltage as a reference vector, the model obtained in the $\alpha\beta$-frame is transferred into a dq-frame system. In this case, the dq-frame model represents a MISO nonlinear system with structured uncertainties. Controller design for a nonlinear system with structured uncertainties is not a straightforward task [50,94,95]. Therefore, by imposing the assumption that frequency of the load voltage is constant, we simplify the MISO

model to obtain a SISO LTI system. Such an assumption is realistic since the load is a passive RLC network and we are using an internal oscillator to control the island frequency. Based on the simplified model (SISO model) of the islanded system and the classical control approaches, a controller for the nominal plant is designed to guarantee stability, and to provide desired performance for the islanded system. To verify performance of the proposed SISO control system, various simulation case studies in the PSCAD/EMTDC software environment are performed.

5.3.1 Mathematical Model of Islanded System

This section provides a state space mathematical model for the islanded system of Figure 5.1. It is assumed that the DG unit and the local load are balanced three-phase subsystems within the island. The state-space model of the islanded system of Figure 5.1 in the abc-frame is

$$\begin{cases} v_{t,abc} = L_t \dfrac{di_{t,abc}}{dt} + R_t i_{t,abc} + v_{abc} \\ i_{t,abc} = \dfrac{1}{R} v_{abc} + i_{L,abc} + C \dfrac{dv_{abc}}{dt} \\ v_{abc} = L \dfrac{di_{L,abc}}{dt} + R_l i_{L,abc}. \end{cases} \tag{5.1}$$

In (5.1), $v_{t,abc}$, $i_{t,abc}$, $i_{L,abc}$, and v_{abc} are 3×1 vectors comprising the individual phase quantities, Figure 5.1. Under balanced conditions, each set of three-phase variable x_{abc} of (5.1) can be transferred to a stationary $\alpha\beta$ reference frame system by applying the following abc to $\alpha\beta$ transformation:

$$x_{\alpha\beta} = x_a e^{j0} + x_b e^{j\frac{2\pi}{3}} + x_c e^{j\frac{4\pi}{3}}, \tag{5.2}$$

where $x_{\alpha\beta} \triangleq x_\alpha + j x_\beta$. Therefore, a dynamic model of the islanded system in the $\alpha\beta$-frame is

$$\begin{cases} \dfrac{di_{t,\alpha\beta}}{dt} = -\dfrac{R_t}{L_t} i_{t,\alpha\beta} - \dfrac{v_{\alpha\beta}}{L_t} + \dfrac{v_{t,\alpha\beta}}{L_t} \\ \dfrac{dv_{\alpha\beta}}{dt} = \dfrac{1}{C} i_{t,\alpha\beta} - \dfrac{1}{RC} v_{\alpha\beta} - \dfrac{1}{C} i_{L,\alpha\beta} \\ \dfrac{di_{L,\alpha\beta}}{dt} = \dfrac{1}{L} v_{\alpha\beta} - \dfrac{R_l}{L} i_{L,\alpha\beta}. \end{cases} \tag{5.3}$$

We transfer (5.3) to a rotating reference frame (dq-frame) based on

$$x_{\alpha\beta} = X_{dq}e^{j\theta} = \left(X_d + jX_q\right)e^{j\theta}, \tag{5.4}$$

where $\theta(t) \triangleq \int_0^t \omega(\zeta)d\zeta + \theta_0$ is the phase-angle of an arbitrary reference vector $x_\alpha^{ref} + jx_\beta^{ref}$ in the $\alpha\beta$-frame, i.e.,

$$\theta = \arctan\left(\frac{x_\beta^{ref}}{x_\alpha^{ref}}\right). \tag{5.5}$$

Substituting for $\alpha\beta$ variables from (5.4) in (5.3), we deduce

$$\begin{cases} \dfrac{dI_{t,dq}}{dt} + j\omega I_{t,dq} &= -\dfrac{R_t}{L_t}I_{t,dq} - \dfrac{V_{dq}}{L_t} + \dfrac{V_{t,dq}}{L_t} \\ \dfrac{dV_{dq}}{dt} + j\omega V_{dq} &= \dfrac{1}{C}I_{t,dq} - \dfrac{1}{RC}V_{dq} - \dfrac{1}{C}I_{L,dq} \\ \dfrac{dI_{L,dq}}{dt} + j\omega I_{L,dq} &= \dfrac{1}{L}V_{dq} - \dfrac{R_l}{L}I_{L,dq}. \end{cases} \tag{5.6}$$

$v_{\alpha\beta}$ is selected as a reference vector such that $V_q = 0$, and therefore $\dot{V}_q = 0$. The d- and q-axis components of the state variables are deduced from (5.6) as

$$\begin{cases} \dfrac{dI_{td}}{dt} &= -\dfrac{R_t}{L_t}I_{td} + \omega I_{tq} - \dfrac{V_d}{L_t} + \dfrac{V_{td}}{L_t} \\ \dfrac{dI_{tq}}{dt} &= -\omega I_{td} - \dfrac{R_t}{L_t}I_{tq} + \dfrac{V_{tq}}{L_t} \\ \dfrac{dI_{Ld}}{dt} &= -\dfrac{R_l}{L}I_{Ld} + \omega I_{Lq} + \dfrac{1}{L}V_d \\ \dfrac{dI_{Lq}}{dt} &= -\omega I_{Ld} - \dfrac{R_l}{L}I_{Lq} \\ \dfrac{dV_d}{dt} &= \dfrac{1}{C}I_{td} - \dfrac{1}{C}I_{Ld} - \dfrac{1}{RC}V_d \\ \omega C V_d &= I_{tq} - I_{Lq} \\ \dot{\theta} = \omega & \end{cases} \tag{5.7}$$

where V_d is the only output, and V_{td} and V_{tq} are the input signals. Dynamical equations of (5.7) represent a multi-input single-output (MISO) nonlinear system. In addition, since the load parameters R, L, C are not fixed values, the plant has structured uncertainties. Controller design for such

systems are not straightforward and therefore we simplify the model to obtain a SISO LTI system.

In an islanded mode of operation, the VSC can employ an internal oscillator with a constant frequency $\omega_0 = 2\pi f_0$ to generate the modulating signals. Thus, the islanded system frequency is controlled in an open-loop manner by the internal oscillator and the VSC generates a set of three-phase voltages at the system nominal frequency, i.e. ω_0. Moreover, since the local load is passive, all voltage and current signals in a steady state condition are at frequency ω_0. Therefore, assuming $\omega = \omega_0$, the last equation of (5.7) is a linear combination of the state variables, and leads to redundancy of one state variable. Substituting $I_{Lq} = I_{tq} - \omega_0 C V_d$ in (5.7) yields

$$\begin{cases} \dfrac{dI_{td}}{dt} = -\dfrac{R_t}{L_t} I_{td} + \omega_0 I_{tq} - \dfrac{1}{L_t} V_d + \dfrac{1}{L_t} V_{td} \\ \dfrac{dI_{tq}}{dt} = \omega_0 I_{td} - \dfrac{R_l}{L} I_{tq} - 2\omega_0 I_{Ld} + \left(\dfrac{R_l C \omega_0}{L} - \dfrac{\omega_0}{R}\right) V_d \\ \dfrac{dI_{Ld}}{dt} = \omega_0 I_{tq} - \dfrac{R_l}{L} I_{Ld} + \left(\dfrac{1}{L} - \omega_0^2 C\right) V_d \\ \dfrac{dV_d}{dt} = \dfrac{1}{C} I_{td} - \dfrac{1}{C} I_{Ld} - \dfrac{1}{RC} V_d \\ V_{tq} = L_t \left[2\omega_0 I_{td} + \left(\dfrac{R_t}{L_t} - \dfrac{R_l}{L}\right) I_{tq} - 2\omega_0 I_{Ld} + \left(\dfrac{R_l \omega_0 C}{L} - \dfrac{\omega_0}{R}\right) V_d \right]. \end{cases} \tag{5.8}$$

In (5.8), V_{td} and V_{tq} are the input signals and V_d is the only output signal which should be regulated. It should be noted that V_{tq} does not explicitly appear in (5.8), and is a function of state variables and parameters of the system. As all state variables are not accessible and the load parameters are uncertain, we cannot readily calculate control signal V_{tq}. In such a case, V_{tq} is assumed as a disturbance signal and set to zero. Therefore, to control the only output variable V_d, one of the two inputs suffices.

The state space equations of the islanded system of Figure 5.1, i.e. (5.8), in the standard state space form are

$$\begin{cases} \dot{x}(t) &= Ax(t) + bu(t) \\ y(t) &= cx(t) \\ u(t) &= V_{td}, \end{cases} \tag{5.9}$$

where

$$A = \begin{bmatrix} -\frac{R_t}{L_t} & \omega_0 & 0 & -\frac{1}{L_t} \\ \omega_0 & -\frac{R_l}{L} & -2\omega_0 & \frac{R_l C\omega_0}{L} - \frac{\omega_0}{R} \\ 0 & \omega_0 & -\frac{R_l}{L} & \frac{1}{L} - \omega_0^2 C \\ \frac{1}{C} & 0 & -\frac{1}{C} & -\frac{1}{RC} \end{bmatrix} \quad b = \begin{bmatrix} \frac{1}{L_t} \\ 0 \\ 0 \\ 0 \end{bmatrix} \quad c = \begin{bmatrix} 0 \\ 0 \\ 0 \\ 1 \end{bmatrix}^T \quad x = \begin{bmatrix} I_{td} \\ I_{tq} \\ I_{Ld} \\ V_d \end{bmatrix} \tag{5.10}$$

Dynamical equations (5.9) describe a SISO control system in the dq-frame. To design a controller for the potential island of Figure 5.1 in s-domain, a transfer function of the system is obtained from (5.9) as

$$g(s) = \frac{Y(s)}{U(s)} = c(sI - A)^{-1}b = \frac{N(s)}{D(s)}, \tag{5.11}$$

where

$$\begin{aligned} N(s) &= RL^2\left(s^2 + \frac{2R_l}{L}s + \frac{w_0^2L^2 + R_l^2}{L^2}\right), \\ D(s) &= a_4s^4 + a_3s^3 + a_2s^2 + a_1s + a_0, \end{aligned} \tag{5.12}$$

and $a_i,\ i = 0, 1, 2, 3$, are functions of the system parameters and expressed as

$$\begin{aligned} a_0 &= R_tR_lR + \omega_0{}^2RL^2 + R_t\omega_0{}^2L^2 + R_l{}^2R + R_tR_l{}^2 + \omega_0{}^2L_tRL - \omega_0{}^2L_tR_l{}^2RC - \omega_0{}^4L_tRL^2C \\ a_1 &= R_tRL + 2R_lRL + R_tR_l{}^2RC + R_lL_tR + 2R_tR_lL + R_t\omega_0{}^2RL^2C + R_l{}^2L_t + \omega_0{}^2L_tL^2 \\ &\quad -2\omega_0{}^2L_tR_lRLC \\ a_2 &= L_tRL + RL^2 + R_tL^2 + 2R_tR_lRLC + 2R_lL_tL + R_l{}^2L_tRC \\ a_3 &= L_tL^2 + R_tRL^2C + 2R_lL_tRLC \\ a_4 &= L_tRL^2C \end{aligned}$$

Transfer function $g(s)$ has the following features:

- $g(s)$ has two stable zeros at $z_{1,2} = -\frac{R_l}{L} \pm j\omega_0$ and consequently is minimum phase.
- $g(s)$ represents a fourth-order system which can be unstable for a specific range of values of load parameters R, L, and C.
- Since R, L, and C are uncertain, transfer function $g(s)$ has structured uncertainty of polynomic uncertainty type [48].

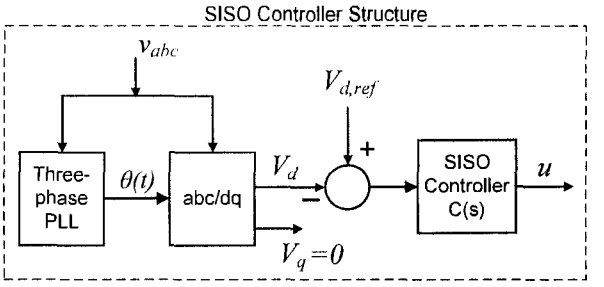

Figure 5.2: Structure of SISO controller for the islanded system

Design of a robust controller for this type of system is not straightforward [48] since the coefficients of variable "s" in plant $g(s)$ are nonlinear functions of load parameters R, L, C. In the following section we design a controller for nominal plant $g_n(s)$ and based on simulation results verify robustness of the control system with respect to load parameter uncertainties. The nominal plant $g_n(s)$ is obtained by substituting rated values of the load and the system parameters from Table 5.1 in (5.12) and (5.13), and is expressed as

$$g_n(s) = \frac{33150s^2 + 208300s + 4.711e9}{s^4 + 220.6s^3 + 177700s^2 + 3.094e7s + 4.868e9}.$$

5.3.2 Control Strategy

Using the classical control approaches [71,96], a controller based on the transfer function of the nominal plant, i.e. $g_n(s)$, is designed. The controller should guarantee stability of the closed-loop system and provide pre-specified desired performance characteristics, e.g. time response, acceptable disturbance rejection capability, and zero steady-state error to a step command input.

Figure 5.2 shows a controller structure for the islanded mode. In the islanded mode of operation, load voltages v_{abc} are measured and transferred to a dq-frame. A three-phase PLL [72-75] is used to provide the reference angle for the abc/dq block and thus the q component of the load voltages is set to zero, i.e., $V_q = 0$. In such a case, the d component of the load voltages, V_d, should be regulated to the desired peak value of load voltages. To regulate V_d, it is compared with reference signal $V_{d,ref}$ and the resultant error signal is applied to designed controller $C(s)$, Figure 5.2. Controller outputs $u = V_{td}$ and $V_{tq} = 0$ are applied to the gating signal generator for the VSC, Figure 5.1.

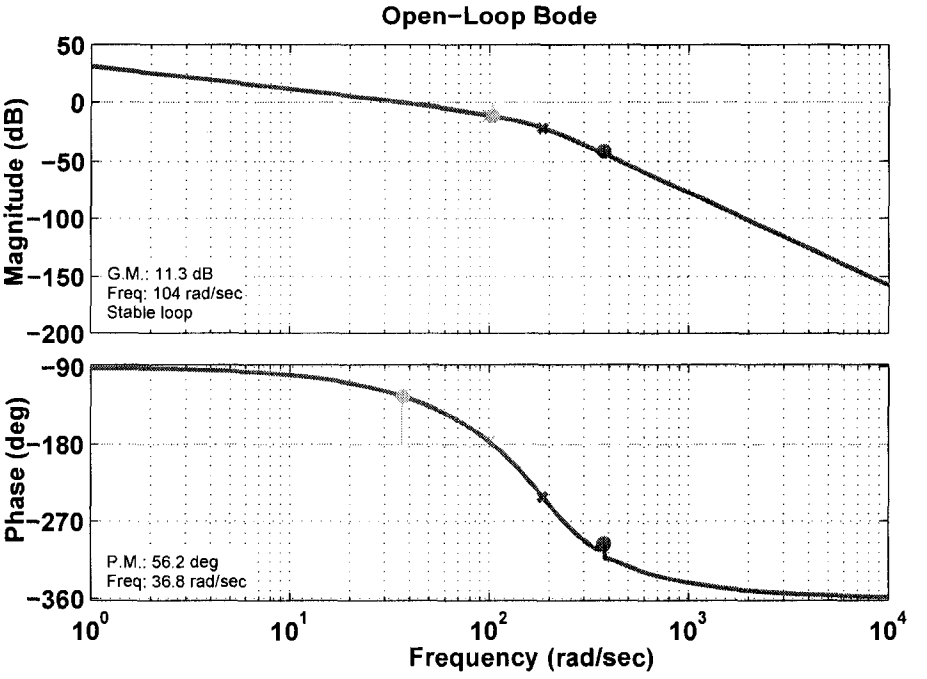

Figure 5.3: Bode diagrams for the compensated system

To obtain zero steady-state error ($e_{ss} = 0$) to a step reference signal, a simple pole is assigned at the origin of s-plane. By adding another simple pole at $s = -100$ and adjusting the controller gain, the desired speed of response, overshoot, and robust stability margins are obtained. The transfer function of designed controller $C(s)$ is

$$C(s) = \frac{4000}{s(s + 100)}. \tag{5.13}$$

The designed controller is structurally simple and has a limited bandwidth which results in acceptable noise and disturbance rejection properties. Figures 5.3 and 5.4 show the bode diagrams and the step response of the compensated closed-loop system, respectively. Figure 5.3 shows that the designed controller provides gain and phase margins of 11.3 dB and 56.2 deg, respectively, and guarantees robust stability of the closed-loop system for the load parameter uncertainties within limits. Zero steady-state error and fast step response of the controller and the closed-loop system are observed in Figure 5.4. The step response of the closed-loop system demonstrates 44 ms rise-time.

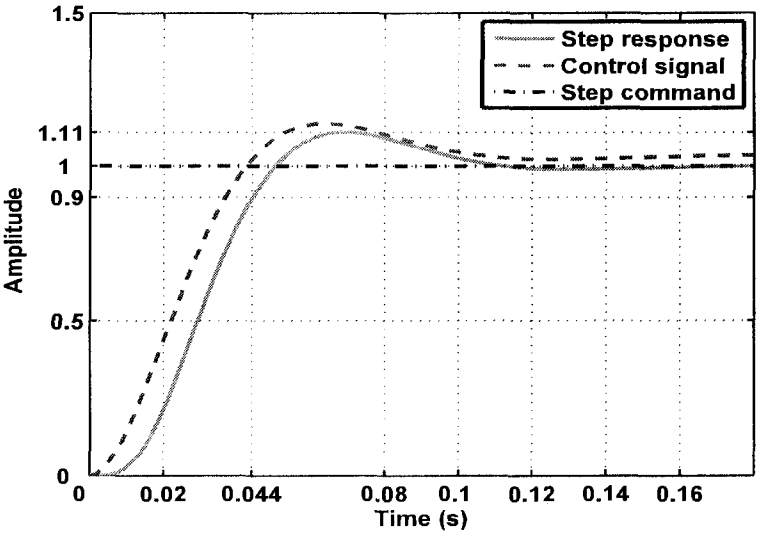

Figure 5.4: Response of the controller and the closed-loop system to a step command signal

5.3.3 Performance evaluation of SISO System

This section evaluates performance of the system of Figure 5.1 during and subsequent to an islanding event, based on the proposed SISO controller of (5.13). The reported case studies demonstrate that the SISO controller of (5.13) is (i) capable of maintaining the magnitude of the PCC voltage in the islanded mode, and (ii) robust with respect to small perturbations in the load parameters. In the presented studies of this section, the islanding event is detected based on the proposed method of Chapter 4, and upon detection the control strategy is changed from the conventional grid-connected control to the proposed SISO control of Figure 5.2. The UTSP system presented in Chapter 2 is also used to estimate the sequence components of the PCC voltage and the system frequency. The studies are performed based on digital time-domain simulation in the PSCAD/EMTDC software environment.

A. Matched Power

The system of Figure 5.1 initially operates in a grid-connected mode, where real and reactive power components of the RLC load are supplied by the DG unit. The load and the DG parameters are set at their rated values as given in Table 5.1. The system is islanded at t=1.000 s by opening CB of Figure 5.1, and the event is detected by the proposed method of Chapter 4 at t=1.060 s. The control

strategy is changed from the grid-connected strategy, i.e. the conventional I_{dq} control [1,86], to the proposed SISO control strategy of Figure 5.2 at t=1.060 s. Figure 5.5 shows the dynamic response of the system prior, during and subsequent to the islanding event.

Figure 5.5(a) shows the instantaneous voltage of phase-*a* at PCC and its estimated magnitude by the UTSP system. Figure 5.5(a) confirms that the proposed SISO controller maintains the load voltage after the islanding event. Figure 5.5(b) shows the control signal in response to the islanding event. Figure 5.5(c) shows the magnitude of negative-sequence component of the PCC voltages which is estimated by the UTSP and used for the islanding detection. The system frequency at PCC is also estimated by the UTSP system and depicted in Figure 5.5(d). Figure 5.5(d) indicates that the internal oscillator provides a constant frequency for the islanded system. However, the system frequency is distorted for a short time during the islanding event.

Figures 5.5(e), (f), and (g) show variations of real and reactive power components of the converter, load, and the grid. In the grid-connected mode, real and reactive power components of the VSC and the grid exhibit a 120 Hz ripple component, since the VSC injects a small component of negative-sequence current which is absorbed by the grid. Based on the instantaneous real and reactive power concepts [69], if a set of three-phase voltages and/or currents are unbalanced, i.e. contain negative-sequence components, instantaneous real/reactive power components are not constant values and contain double frequency ripple components. Figure 5.5(f) shows phase-*a* current of the load and demonstrates that it does not undergo a significant variations due to transition from the grid-connected mode to the islanded mode and change of controllers.

To guarantee stability and desirable performance of the islanded system, transition from the grid-connected mode to the islanded mode must be carried out smoothly and without a long interruption. In other words, the control signals and all state variables of the new system (islanded system) should be initialized with those of the grid-connected mode system, prior to the islanding event. This requires that the phase-angles of the internal oscillator and the *dq*-current controller be in a synchronous condition when the proposed SISO controller is activated, and the *dq*-current controller disabled. This can be achieved by using the instantaneous control signals of the *dq*-current controller, at the control transfer instant, as the initial conditions for the proposed SISO controller. Our studies show that the lack of smooth transition can result in a long period of transients or even instability of the island.

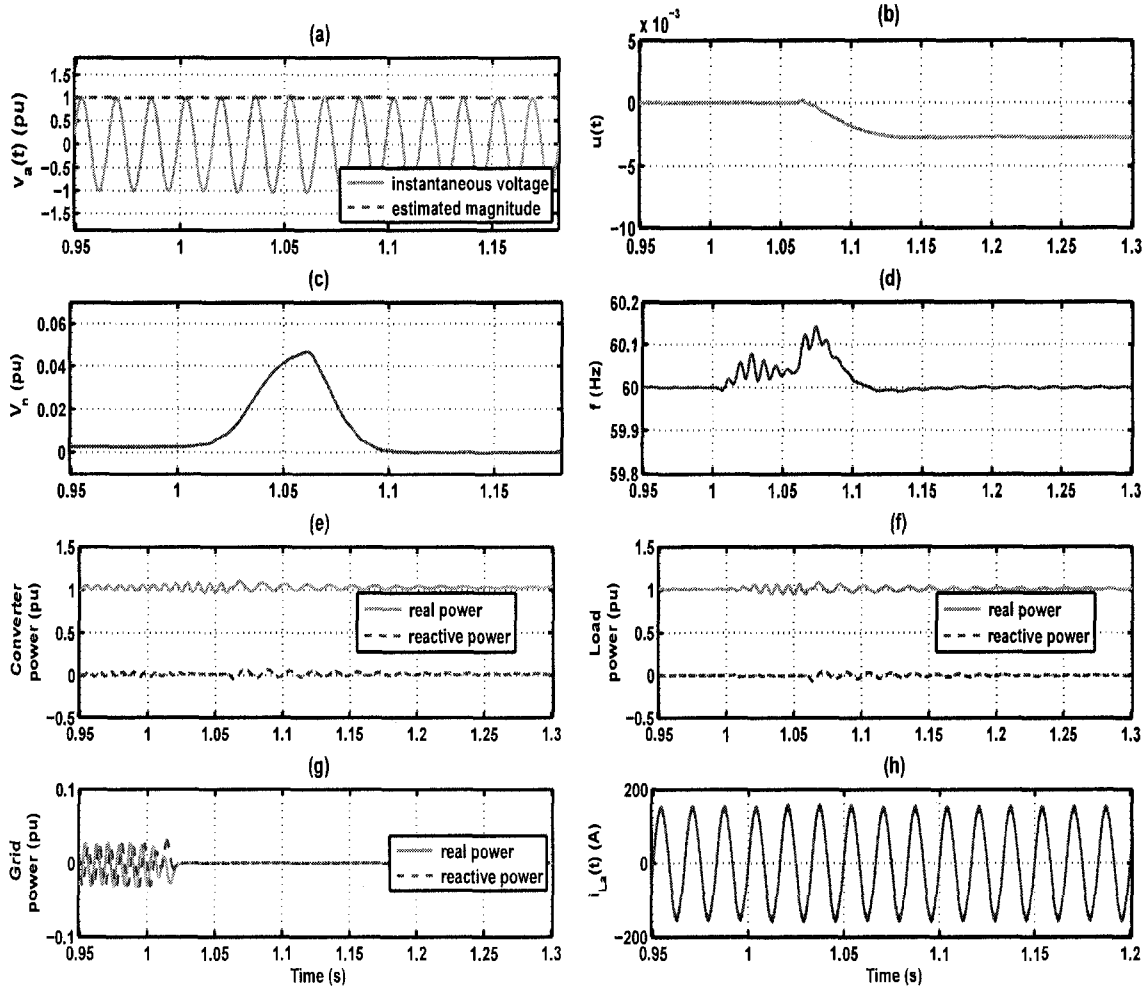

Figure 5.5: Dynamic response of the system of Figure 5.1 to a pre-planned islanding event (a) instantaneous voltage of phase-a at PCC and its estimated magnitude by the UTSP, (b) control signal, (c,d) estimated magnitude of negative-sequence component of PCC voltages and estimated frequency at PCC by the UTSP, (e,f,g) real and reactive power components of the converter, load, and the grid, and (h) phase-a current of the load

B. Mismatched Power

The system of Figure 5.1 initially operates in a grid-connected mode. The grid absorbs 1.43 MW (0.57 pu) real power from the converter and 710 kVAr (0.28 pu) reactive power from the load. The DG unit delivers real power to the system at unity power factor. The load parameters are given in Figure 5.6 (S_a is open). An accidental islanding event occurs at t=1.200 s and is detected by the UTSP at t=1.208 s. The islanding detection time is shorter than the previous case study since power components of the DG unit and the RLC load are not matched prior to the islanding instant

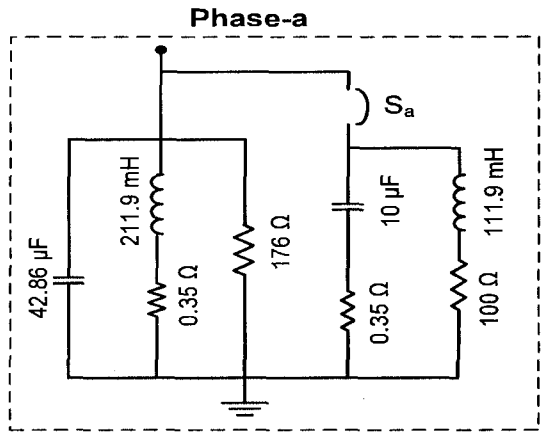

Figure 5.6: Single-line diagram of the local load

and therefore the voltage magnitude at PCC and/or the islanded system frequency rapidly deviate from their acceptable limits.

Dynamic response of the system of Figure 5.1 to the islanding event is shown in Figure 5.7. Instantaneous voltage of phase-*a* at the PCC and its estimated magnitude by the UTSP are shown in Figure 5.7(a). It is observed that after three cycles of transients the load voltage is regulated at the desired reference value of 1.0 pu by the control system of Figure 5.2. The voltage transients are as a result of power mismatch condition prior to the islanding event. Figure 5.7(b) shows the control signal in response to the islanding event. Estimated magnitude of negative-sequence component of the PCC voltages and estimated system frequency by the UTSP are shown in Figures 5.7(c) and (d), respectively. Figures 5.7(e), (f), and (g) show variations of real and reactive power components of the converter, load, and the grid, respectively. Figure 5.7(h) shows the load current of phase-*a* prior, during and subsequent to the islanding event, and demonstrates that the proposed SISO controller can readily adjust the current to its pre-islanding steady-state condition within 2.5 cycles.

C. Change of Load Parameters

This study case verifies robust stability and performance of the proposed SISO controller with respect to the load parameter uncertainties. While the system is operating in an islanded mode and under balanced conditions, the load parameters, in the three phases, are equally changed such that the resultant load remains balanced. The load change is imposed by closing switch S_a of

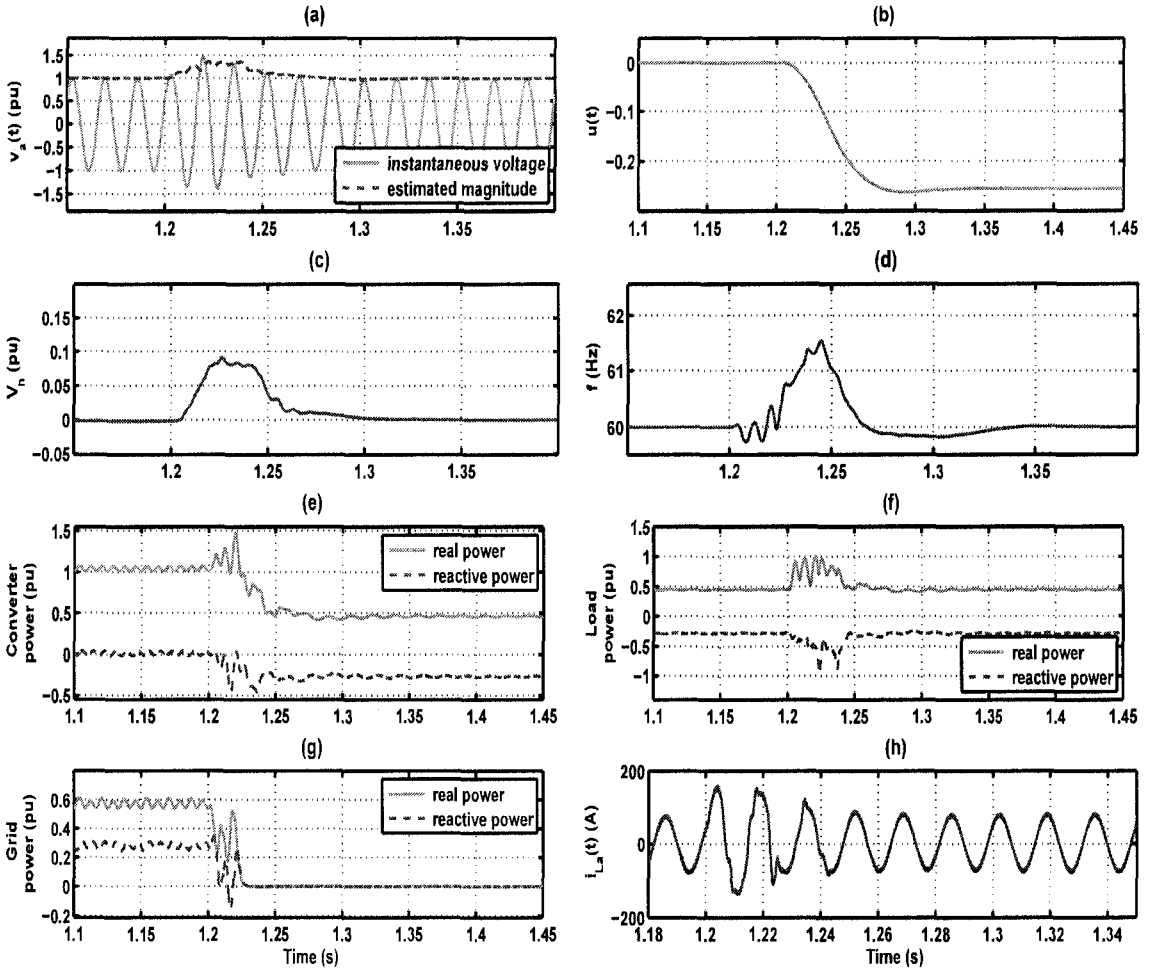

Figure 5.7: Dynamic response of the system of Figure 5.1 to an accidental islanding event (a) instantaneous voltage of phase-*a* at PCC and its estimated magnitude by the UTSP, (b) control signal, (c,d) estimated magnitude of negative-sequence component of PCC voltages and estimated frequency at PCC by the UTSP, (e,f,g) real and reactive power components of the converter, load, and the grid, and (h) phase-*a* current of the load

Figure 5.6 at t=1.600 s.

Figure 5.8 shows the simulated system response to the load change. Figure 5.8(a) shows the instantaneous voltage of phase-*a* and its estimated magnitude at PCC by the UTSP. Figure 5.8 shows that the designed SISO controller is robust with respect to this change in the load parameters, and within three cycles retains magnitude of the load voltage at its desired value. Figure 5.8(b) shows the control signal in response to the load change. The islanded system frequency which is extracted by the UTSP is shown in Figure 5.8(c). A transient error in the estimated frequency is observed which is introduced by the UTSP system. The load power components and phase-

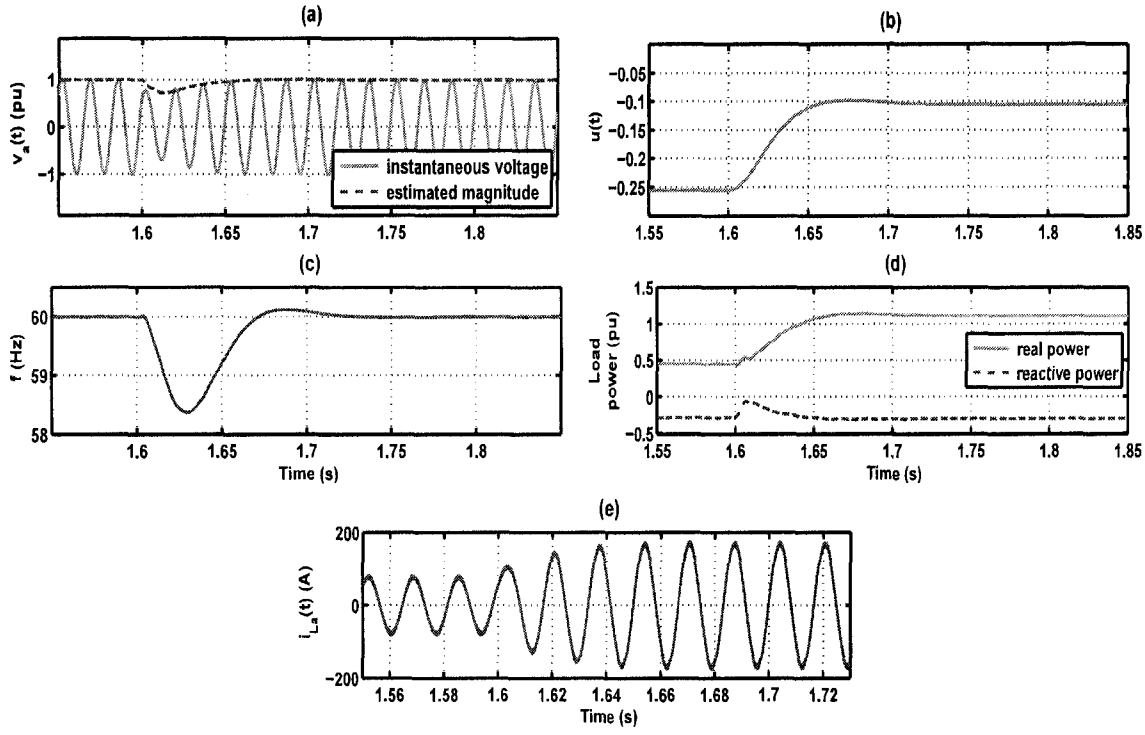

Figure 5.8: Performance of the islanded system to a balanced change in load parameters (a) instantaneous voltage of phase-a at PCC and its estimated magnitude by the UTSP, (b) control signal, (c) estimated frequency at PCC by the UTSP, (d) real and reactive power components of the load, and (e) phase-a current of the load

a current are shown in Figure 5.8(d) and (e), respectively. This case study demonstrates that the proposed SISO controller is robust if the load perturbations about their nominal values are small. However, the proposed controller cannot necessarily accommodate large perturbations of the load parameters. For example, our studies show that the load resistances larger than 300 Ω result in a large rise-time (0.2 s) and poor performance. Therefore, the proposed SISO controller is appropriate only for those applications that the local is almost fixed and pre-determined.

D. Voltage Tracking

This case study demonstrates the performance of the SISO controller under an islanded condition in terms of reference signal tracking. While the system is operating in the islanded mode, the voltage reference signal is stepped down from 1 pu to 0.82 pu at t=2.500 s. The load parameters are set at their rated values as given in Table 5.1. Figure 5.9 shows the system response to the

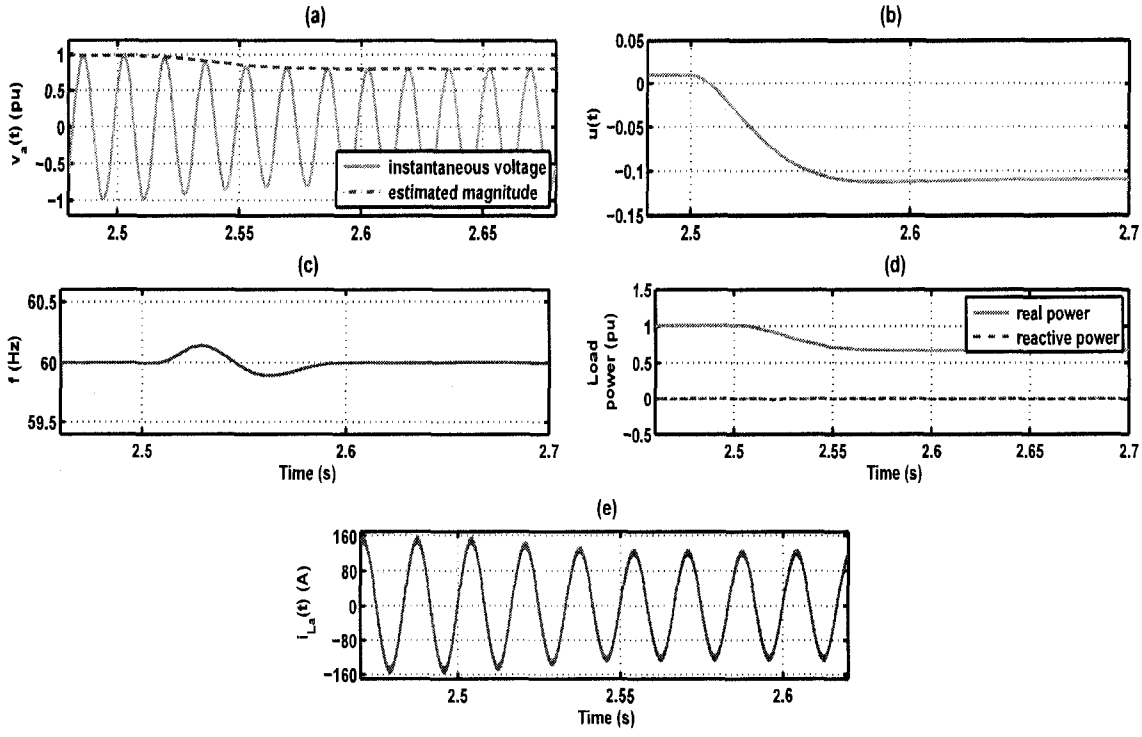

Figure 5.9: Dynamic performance of the islanded system to a step voltage command (a) instantaneous voltage of phase-a at PCC and its estimated magnitude by the UTSP, (b) control signal, (c) estimated frequency by the UTSP, (d) real and reactive power components of the load, and (e) phase-a current of the load

reference change. Figure 5.9(a) shows the instantaneous voltage of phase-a and its estimated magnitude at PCC by the UTSP. Figure 5.9(a) demonstrates that the load voltage is regulated at the new reference value of 0.82 pu by the designed control system within four cycles. Figures 5.9(b) and (c) show the control signal and the estimated frequency by the UTSP system in response to the step voltage change. Power components and phase-a current of the load are shown in Figures 5.9(d) and (e), respectively. Figure 5.9 verifies that the proposed SISO control system is capable of tracking the reference signal, with zero steady-state error.

E. Load Imbalance

In this case study, while the system is initially operating in an islanded mode as a balanced system, the load parameters are changed such that the islanded system becomes unbalanced. Figure 5.10 shows the unbalanced load diagram, where the rated load is a parallel RLC network as given in Figure 5.1 with the nominal values given in Table 5.1. Switches S_a, S_b, and S_c are initially

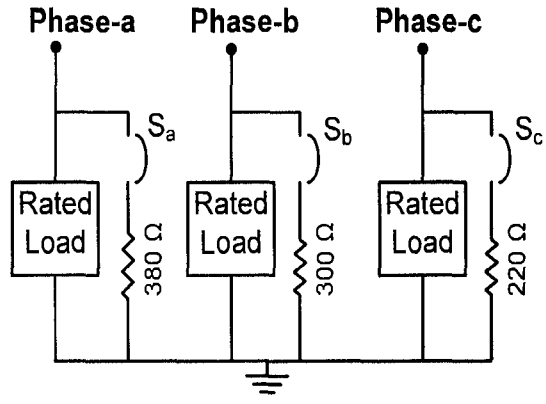

Figure 5.10: Three-phase unbalanced load

open and simultaneously closed at t=1.500 s and the load becomes resistively unbalanced. This switching event results in $R_b = \%95R_a$ and $R_c = \%89R_a$. Magnitudes of sequence components of the load voltage are estimated based on the UTSP system as described in Chapter 2.

Dynamic response of the islanded system to the unbalanced condition is depicted in Figure 5.11. Figures 5.11(a), (b) show instantaneous load voltages and the control signal, respectively. Figure 5.11(a) indicates that the designed controller maintains the load voltage (line-line) at the desired reference value of 1.0 pu within three cycles after the switching event. Figures 5.11(c), and (d) show the estimated magnitudes of positive- and negative-sequence components of the PCC. Figure 5.11(d) shows that the load voltages exhibit a negative-sequence component of 2.25% which is acceptable in terms of power quality requirements [90]. The reason that the load voltages becomes imbalance is that the DG unit generates a set of balanced three-phase voltages and cannot compensate the unbalanced condition introduced by the load. The control signal $u(t)$ is also polluted by a small-amplitude, 120 Hz ripple component. The ripple component in the control signal is the result of the load voltage imbalance which appears in the dq-frame as a double-frequency, 120 Hz component. The estimated frequency by the UTSP and the instantaneous three-phase currents of the load are depicted in Figures 5.11(e) and (f), respectively. This case study verifies that the proposed SISO controller is capable of partially compensating unbalanced conditions, however, it necessarily cannot cope with large unbalanced load conditions. A control strategy, which can accommodate large unbalanced load conditions, is proposed in the next chapter.

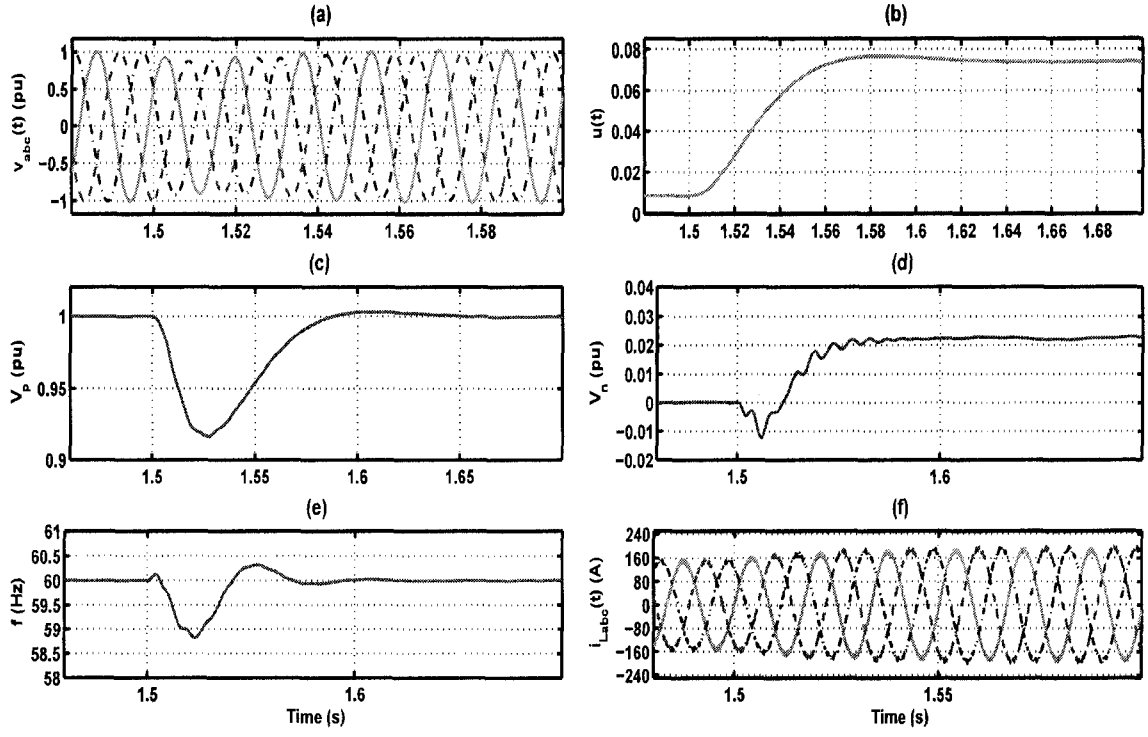

Figure 5.11: Performance of the islanded system to an unbalanced condition (a) instantaneous load voltages, (b) control signal, (c,d) estimated magnitude of positive-, and negative-sequence components of PCC voltages, (e) estimated frequency by the UTSP, and (f) instantaneous currents of the load

5.4 MIMO System

In Section 5.3, we observed that the islanded system of Figure 5.1 is modelled by a MISO nonlinear system. Then, a simplifying assumption is made which results in a SISO LTI model. Based on the simplified model, a structurally simple SISO controller is designed. However, our studies show that the designed controller cannot accommodate large perturbation of load parameters. The reason is that the plant model itself can be unstable for large load perturbations and therefore the resultant closed-loop system becomes unstable. Nevertheless, for those applications in which the local load is pre-specified and fairly fixed, the SISO controller is a good choice. To overcome the shortcomings of the SISO model, a more precise LTI model is proposed in this section.

To obtain a more precise LTI model for the islanded system of Figure 5.1 in a dq-frame, phase-angle of the internal oscillator, as shown in Figure 5.12, is used as the reference phase-angle. In this case, the model obtained corresponds to a multivariable LTI system. Based on this

dynamic model of the islanded system, a multiple-input multiple-output (MIMO) servomechanism controller for the nominal plant is designed to guarantee robust stability, and to provide desired high performance, e.g. fast transient response and zero steady-state error, for the islanded system despite load parameters uncertainty. It is shown, based on simulation results, that the proposed MIMO controller is robust for a wide range of load parameter uncertainties.

5.4.1 Mathematical Model of Islanded System

This section provides a more precise model for the islanded system given in Figure 5.1. If the transformation angle θ in (5.4) is produced by the internal oscillator of the converter, as shown in Figure 5.12, and the frequency of the internal oscillator is set at the system nominal frequency ω_0, then $\theta(t) = \omega_0 t + \theta_0$. On substituting the $\alpha\beta$ variables from (5.4) into (5.3), we obtain

$$\begin{cases} \dfrac{dI_{t,dq}}{dt} + j\omega_0 I_{t,dq} &= -\dfrac{R_t}{L_t} I_{t,dq} - \dfrac{V_{dq}}{L_t} + \dfrac{V_{t,dq}}{L_t} \\ \dfrac{dV_{dq}}{dt} + j\omega_0 V_{dq} &= \dfrac{1}{C} I_{t,dq} - \dfrac{1}{RC} V_{dq} - \dfrac{1}{C} I_{L,dq} \\ \dfrac{dI_{L,dq}}{dt} + j\omega_0 I_{L,dq} &= \dfrac{1}{L} V_{dq} - \dfrac{R_l}{L} I_{L,dq}, \end{cases} \tag{5.14}$$

where each equation in (5.14) can be expressed by two scalar equations in terms of the d- and q-axis components of the state variables. In this case, the set of scalar equations obtained from (5.14) can be represented in the following standard form:

$$\begin{cases} \dot{x}(t) &= Ax(t) + B\tilde{u}(t) \\ y(t) &= C_m x(t) \\ e(t) &= y(t) - y_{ref}(t) \end{cases} \tag{5.15}$$

where $x = [V_d \;\; V_q \;\; I_{td} \;\; I_{tq} \;\; I_{Ld} \;\; I_{Lq}]^T \in \mathbf{R}^6$ is the vector of state variables, $\tilde{u} = [V_{td} \;\; V_{tq}]^T \in \mathbf{R}^2$ is the input vector, $y = [V_d \;\; V_q]^T \in \mathbf{R}^2$ is the output vector, $y_{ref} \in \mathbf{R}^2$ are the reference inputs, $e \in \mathbf{R}^2$ is the error in the system, and A, B, C_m are constant matrices of appropriate dimensions. Matrices A, B, and C_m are given by:

$$A = \begin{bmatrix} -\frac{1}{RC} & \omega_0 & \frac{1}{C} & 0 & -\frac{1}{C} & 0 \\ -\omega_0 & -\frac{1}{RC} & 0 & \frac{1}{C} & 0 & -\frac{1}{C} \\ -\frac{1}{L_t} & 0 & -\frac{R_t}{L_t} & \omega_0 & 0 & 0 \\ 0 & -\frac{1}{L_t} & -\omega_0 & -\frac{R_t}{L_t} & 0 & 0 \\ \frac{1}{L} & 0 & 0 & 0 & -\frac{\omega_0}{q_l} & \omega_0 \\ 0 & \frac{1}{L} & 0 & 0 & -\omega_0 & -\frac{\omega_0}{q_l} \end{bmatrix}, \quad B = \begin{bmatrix} 0 & 0 \\ 0 & 0 \\ \frac{1}{L_t} & 0 \\ 0 & \frac{1}{L_t} \\ 0 & 0 \\ 0 & 0 \end{bmatrix}, \quad C_m = \begin{bmatrix} 1 & 0 \\ 0 & 1 \\ 0 & 0 \\ 0 & 0 \\ 0 & 0 \\ 0 & 0 \end{bmatrix}^T. \tag{5.16}$$

It should be noted that input signal $\tilde{u}(t)$ is generated based on a sinusoidal pulse-width modulation (SPWM) method, and therefore polluted by high frequency harmonics. These harmonics can be considered as disturbance signals in the system. Therefore, we replace $\tilde{u}$ in (5.15) with $u + w$ and obtain:

$$\begin{cases} \dot{x}(t) &= Ax(t) + Bu(t) + Ew(t) \\ y(t) &= C_m x(t) \\ e(t) &= y(t) - y_{ref}(t) \end{cases} \tag{5.17}$$

where $E = B$, $w \in \mathbf{R}^2$ denotes the disturbance signals, and u the control signal. The open-loop system (5.17) includes two control inputs and two outputs to be controlled, i.e. $r = m = 2$, and reference signal y_{ref} and disturbance signal w belong to the class of step and sinusoidal signals, respectively. In (5.16), load parameters R, L, and C are uncertain parameters and perturbed about their nominal rated values. Other parameters are assumed to be fixed and known, as given in Table 5.1.

5.4.2 Control Strategy

In this section, some features of the open-loop system are initially studied. Then, a robust servomechanism controller, using the parameter optimization methods of [47,97-99], is designed for the system of Figure 5.1. Finally, a robust stability analysis and evaluation of the resulting closed-loop system is performed.

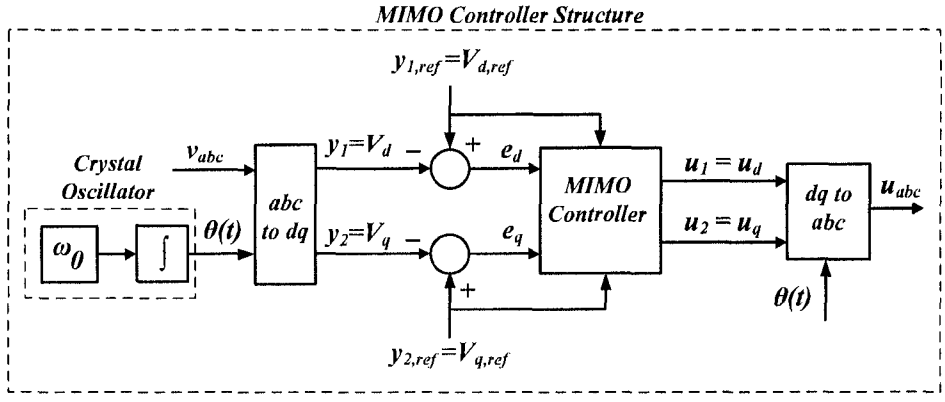

Figure 5.12: Structure of MIMO controller for the islanded system

Figure 5.12 shows the proposed controller structure for the islanded mode. In an islanded mode of operation, load voltages v_{abc} are measured and transferred to a dq-frame, and the internal oscillator is used to provide reference angle $\theta(t)$ for the abc/dq and dq/abc blocks. The d and q components of the load voltages, i.e. V_d and V_q, should be regulated to their desired values such that the magnitude of the load voltage, i.e. $\sqrt{V_d^2 + V_q^2}$, satisfies power quality requirements. To regulate V_d and V_q, these components are compared with the corresponding reference signals, i.e. $V_{d,ref}$ and $V_{q,ref}$, and the resultant error signals e_d, e_q are applied to designed MIMO (robust servomechanism) controller of Figure 5.12. Finally, control signals u_d and u_q are transferred to the abc-frame and applied to the gating signal generator for the converter, as depicted in Figure 5.1.

A. Open-Loop System Properties

The following result is obtained:

Theorem 5.4.1 *Given the open-loop system (5.17); then:*

(*a*) *The open-loop system is asymptotically stable for all positive values of plant and load parameters.*

(*b*) *The open-loop system with input u and output y is minimum phase for all positive values of plant and load parameters, and has transmission zeros [100] given by:*

$$t_z = -\frac{\omega_0}{q_l} \pm j\omega_0. \tag{5.18}$$

(c) *The open-loop system is stabilizable and detectable for all positive values of plant and load parameters.*

Proof 1 See Appendix A, Section B.1.

Remark 5.4.1 Based on the numerical parameters of Table 5.1, the transmission zeros and poles of the system (5.17) are given by:

$$t_z = -3.1416 \pm j376.99 \tag{5.19}$$

$$poles = \left\{ -106.42 \pm j782.86, \quad -106.42 \pm j28.877, \quad -4.648 \pm j376.99 \right\} \tag{5.20}$$

Remark 5.4.2 (*i*) In the plant model (5.16), load parameters R, L, C are not fixed values, since the electric load applied to the system can vary. This implies that the plant has structured uncertainties R, L, C, which based on parameters of Table 5.1, can be explicitly observed in the transfer function of the system $G(s) = C_m(sI - A)^{-1}B = \frac{1}{P(s)}\tilde{G}(s)$, where $P(s)$ and $\tilde{G}(s) = \begin{pmatrix} g_{11}(s) & g_{12}(s) \\ g_{21}(s) & g_{22}(s) \end{pmatrix}$ are given by:

$$\begin{aligned} P(s) = \frac{1}{R^2L^2C^2}[&s^6R^2C^2L^2 + (16.28R^2C^2L^2 + 2L^2RC)s^5 + (32.57L^2RC + L^2 + 4.2R^2CL^2 \\ &+426464R^2C^2L^2 + 2LR^2C)s^4 + (4.63e6R^2C^2L^2 + 16.28L^2 + 2RL + 47.4R^2CL^2 + 4.2RL^2 \\ &+568684L^2RC + 26.28LR^2C)s^3 + (173.4R^2CL^2 + 2.8e5L^2 + 4.63e6L^2RC + R^2 + 47.4RL^2 \\ &+112.8LR^2C + 6e10R^2C^2L^2 + 26.28RL + 4.2R^2L + 4.42R^2L^2)s^2 + (2.3e6L^2 \\ &+34.2R^2L + 4e10L^2RC + 27.72R^2L^2 - 7.66e5R^2CL^2 + 3.3e11R^2C^2L^2 - 1.95e6LR^2C \\ &+284357RL + 5.98e5RL^2 + 10R^2)s + (893136RL + 2.87e15R^2C^2L^2 - 4e10LR^2C \\ &+627041R^2L^2 + 5.97e5R^2L - 8.49e10R^2CL^2 + 2.99e6RL^2 + 2e10L^2 + 142147R^2)], \end{aligned} \tag{5.21}$$

$$
\begin{aligned}
g_{11} = g_{22} &= \frac{1}{RLC^2}[2.1RLCs^4 + (23.7RLC + 2.1L)s^3 + (86.72RLC + 4.41RL \\
&+2.1R + 23.7L)s^2 + (27.72RL - 3.83e5RLC + 17.1R + 2.99e5L)s \\
&+(6.27e5RL - 4.24e10RLC + 2.99e5R + 1.49e6L)], \\
g_{12} = -g_{21} &= \frac{1}{RLC^2}[1583.66RLCs^3 + 791.83(17.57RLC + L)s^2 \\
&+791.83(2.84e5RLC + 6.28L)s \\
&+(5.63e8RLC - 1471.55R + 1.13e8L)].
\end{aligned}
\tag{5.22}
$$

(*ii*) As it is observed from (5.21) and (5.22), the type of uncertainty in the plant model is polynomic [48], which results in a difficult robust stability analysis for the system when it is in closed-loop.

B. Controller Design Requirements

It is desired to design a controller for plant (5.16) using the nominal parameters of Table 5.1, such that:

1. The resultant closed-loop system is asymptotically stable.
2. Asymptotic tracking and regulation occur for all constant set points in $y_{ref} = \begin{bmatrix} V_{d,ref} & V_{q,ref} \end{bmatrix}^T$ and all constant disturbances in w.
3. It is desired that the dominant harmonic frequency $\omega^* = 1.244e4$ rad/s which exists in the SPWM signal, should not be excited, i.e. the converter generates a SPWM signal which contains harmonics centered at integer multiples of the switching frequency $f_{sw} = 33\times60$ Hz, and the controller should reject this dominant harmonic frequency.
4. It is desired that the controller be robust, i.e. conditions 2 and 3 must hold for any perturbations of plant model (5.16) (including dynamic perturbations) which do not destabilize the resultant perturbed closed-loop system.
5. It is desired that the controller should be "fast" with smooth non-peaking transients, i.e. in particular, it should be able to respond to set point changes and disturbance changes within about three cycles of 60 Hz.

6. It is desired that "low interactions", and ideally "no interactions", should occur between channels for both cases of tracking and regulation [47].

7. It is desired that the above requirements be satisfied for as wide as possible range of R, L, C parameters of the load.

These objectives can be achieved by designing a controller to solve the robust servomechanism problem (RSP) [47,97-99] for the case of constant signals, and sinusoidal signals with a frequency of ω^* rad/s given above. Since the plant is minimum phase, in principle, we can achieve "perfect control" [102] for the system, ignoring robust constraints and non-linear effects, as is indicated in the following existence results:

C. Existence Conditions

Lemma 5.4.2 [97-99,102], Given plant (5.16) with parameters of Table 5.1, there exists a solution to the RSP such that requirements 1, 2, 3, 4 of Section 5.4.2-B are all satisfied *if and only if* the following conditions all hold:

a) the plant is stabilizable and detectable,

b) $m \geq r$,

c) the transmission zeros of the plant exclude 0 and $\pm j\omega^* = \pm j12440.7$,

d) output signals y are measurable,

and there exists a solution to the RSP, such that requirements 1, 2, 3, 4 of Section 5.4.2-B together with additional requirements 5, 6 of Section 5.4.2-B, are satisfied if the following conditions all hold:

a') the plant is stabilizable and detectable,

b') the plant is minimum phase,

c') $m \geq r$, and

d') output signals y are measurable.

It should be noted from Theorem 5.4.1 that the plant satisfies all conditions a'), b'), c'), d') for all load parameters R, L, C, so that there exists a solution to the RSP to satisfy all of requirements 1 to 6 of Section 5.4.2-B.

D. Controller Design

Given plant (5.17), the controller design method of [47,97-99] was adopted in which the following "cheap control" performance index:

$$J_\epsilon = \int_0^\infty (e^T e + \epsilon v^T v) d\tau, \qquad \epsilon > 0 \tag{5.23}$$

where $e = y - y_{ref}$, $v = \dddot{u} + \omega^2 \dot{u}$ [104] and $\omega = 12440.7$, is to be minimized for the system:

$$\begin{aligned} \dot{\tilde{x}} &= \begin{bmatrix} A & 0 \\ \mathscr{B}_c C_m & \mathscr{A}_c \end{bmatrix} \tilde{x} + \begin{bmatrix} B \\ 0 \end{bmatrix} v, \\ e &= \begin{bmatrix} 0 & \mathscr{C}_c \end{bmatrix} \tilde{x}, \end{aligned} \tag{5.24}$$

where $\tilde{x} = \begin{bmatrix} \bar{x} \\ \bar{\eta} \end{bmatrix}$, $\bar{x} = \dddot{x} + \omega^2 \dot{x}$ and where

$$\dot{\bar{\eta}} = \mathscr{A}_c \bar{\eta} + \mathscr{B}_c e, \tag{5.25}$$

is the servo-compensator [97] for the system, where

$$\mathscr{A}_c = \begin{bmatrix} 0 & I & 0 \\ 0 & 0 & I \\ 0 & -\omega^2 I & 0 \end{bmatrix}, \quad \mathscr{B}_c = \begin{bmatrix} 0 \\ 0 \\ I \end{bmatrix}, \quad \mathscr{C}_c = \begin{bmatrix} I & 0 & 0 \end{bmatrix}.$$

In this case, it follows from the existence conditions of *Lemma* 5.4.2 that since plant (5.16) is stabilizable and detectable and conditions a'), b'), c'), d') all hold, (5.24) is stabilizable and detectable. Hence the optimal controller which minimizes (5.23), subject to (5.24), is a stabilizing controller. It also follows from [102] that as $\epsilon \to 0$, the obtained controller is "perfect" [102], in the sense that $\int_0^\infty e^T(t)e(t)dt \to 0$ as $\epsilon \to 0$. This implies that a standard observer can be used to implement

the optimal state feedback controller obtained in minimizing (5.23) given by:

$$v = K_0\bar{x} + K_1\bar{\eta} \tag{5.26}$$

where K_0 and K_1 are constant gain matrices [104]. In particular, as $\epsilon \to 0$, zero channel interaction and arbitrary fast speed of response occur, while no unbounded peaking occurs in the error response. These desirable characteristics are achieved for all constant tracking and disturbance signals and all sinusoidal tracking and disturbance signals of frequency $\omega = 12440.7$ rad/sec, under all initial conditions of plant (5.17), assuming that $\eta(0) = 0$, i.e. the initial conditions of servo-compensator (5.25) are zero. The last requirement $\eta(0) = 0$ can be easily implemented, and corresponds to the controller "reset-windup problem", i.e. if $\eta(0) \neq 0$, then controller reset windup occurs in the response of the closed-loop system [102], which is undesirable.

Assume now that the controller (5.26) is implemented by using an observer so that controller (5.26) becomes:

$$v = K_0\bar{\xi} + K_1\bar{\eta}, \tag{5.27}$$

where

$$\dot{\bar{\xi}} = (A - \Lambda C_m + BK_0)\bar{\xi} + \Lambda C_m\bar{x} + BK_1\bar{\eta}, \tag{5.28}$$

is the observer. The closed-loop system then becomes:

$$\begin{aligned}
\begin{bmatrix} \dot{\bar{x}} \\ \dot{\bar{\eta}} \\ \dot{\bar{\xi}} \end{bmatrix} &= \begin{bmatrix} A & BK_1 & BK_0 \\ \mathscr{B}_c C_m & \mathscr{A}_c & 0 \\ \Lambda C_m & BK_1 & A - \Lambda C_m + BK_0 \end{bmatrix} \begin{bmatrix} \bar{x} \\ \bar{\eta} \\ \bar{\xi} \end{bmatrix}, \\
e &= \begin{bmatrix} 0 & \mathscr{C}_c & 0 \end{bmatrix} \begin{bmatrix} \bar{x} \\ \bar{\eta} \\ \bar{\xi} \end{bmatrix},
\end{aligned} \tag{5.29}$$

or alternatively, since the controller represented by (5.27) and (5.28) can be implemented by using

controller:

$$\begin{aligned} u &= K_0\xi + K_1\eta, \\ \dot{\eta} &= \mathscr{A}_c\eta + \mathscr{B}_c e, \\ \dot{\xi} &= (A - \Lambda C_m + BK_0)\,\xi + \Lambda y + B\,K_1\eta, \end{aligned} \tag{5.30}$$

the closed-loop system becomes:

$$\begin{aligned} \begin{bmatrix} \dot{x} \\ \dot{\eta} \\ \dot{\xi} \end{bmatrix} &= \begin{bmatrix} A & BK_1 & BK_0 \\ \mathscr{B}_c C_m & \mathscr{A}_c & 0 \\ \Lambda C_m & BK_1 & A - \Lambda C_m + BK_0 \end{bmatrix} \begin{bmatrix} x \\ \eta \\ \xi \end{bmatrix} + \begin{bmatrix} E \\ 0 \\ 0 \end{bmatrix} w + \begin{bmatrix} 0 \\ -\mathscr{B}_c \\ 0 \end{bmatrix} y_{ref}, \\ y &= \begin{bmatrix} C_m & 0 & 0 \end{bmatrix} \begin{bmatrix} x \\ \eta \\ \xi \end{bmatrix}. \end{aligned} \tag{5.31}$$

All of the controller design requirements 1 to 6 of Section 5.4.2-B can therefore be achieved by implementing controller (5.30).

Thus, the "dominant" design feature which needs attention is requirement 7, which is to satisfy previous requirements 1 to 6 for "as large a range as possible for R, L, C parameters of the load". This will be done by using the CAD approach of [47], i.e. by carrying out a 1-D minimization search on parameter "ϵ" of (5.23), subject to the constraint that perturbed parameters of the nominal load R, L, C should satisfy a certain closed-loop stability constraint [103].

E. Structured Robust Stability Constraint [103]

Given the open-loop asymptotically stable plant (5.16), matrices B and C_m are independent of the load parameters R, L, C, and only the following elements of A are functions of R, L, C:

$$A = \begin{bmatrix} -\theta_1 & 0 & \theta_2 & 0 & -\theta_2 & 0 \\ 0 & -\theta_1 & 0 & \theta_2 & 0 & -\theta_2 \\ 0 & 0 & 0 & 0 & 0 & 0 \\ 0 & 0 & 0 & 0 & 0 & 0 \\ \theta_3 & 0 & 0 & 0 & 0 & 0 \\ 0 & \theta_3 & 0 & 0 & 0 & 0 \end{bmatrix}. \tag{5.32}$$

Now assume that $A \rightarrow A + \Delta A$, where parameters $\theta_i \rightarrow \theta_i + \Delta\theta_i$, $i = 1, 2, 3$ where:

$$\Delta\theta_1 = \frac{1}{RC}\delta_1\,,$$
$$\Delta\theta_2 = \frac{1}{C}\delta_2\,,$$
$$\Delta\theta_3 = \frac{1}{L}\delta_3\,.$$

R, L, C are the nominal parameters of the load given in Table 5.1, and δ_1, δ_2, δ_3 are perturbation parameters.

Now, define matrix U:

$$U = \begin{bmatrix} u_{11} & 0 & u_{13} & 0 & u_{15} & 0 \\ 0 & u_{22} & 0 & u_{24} & 0 & u_{26} \\ 0 & 0 & 0 & 0 & 0 & 0 \\ 0 & 0 & 0 & 0 & 0 & 0 \\ u_{51} & 0 & 0 & 0 & 0 & 0 \\ 0 & u_{62} & 0 & 0 & 0 & 0 \end{bmatrix}, \tag{5.33}$$

and assuming the nominal load parameters of Table 5.1 are used, let

$$u_{11} = u_{22} = \frac{1}{RC} = 210\,,$$
$$u_{13} = u_{15} = u_{24} = u_{26} = \frac{1}{C} = 1.590 \times 10^4\,,$$
$$u_{51} = u_{62} = \frac{1}{L} = 8.9\,,$$

and let the elements of matrix A, given in (5.16), be perturbed so that $A \rightarrow A + \Delta A$, where the elements of perturbation matrix ΔA are given by:

$$\begin{aligned} &|\Delta A_{11}| \le u_{11}\bar{\epsilon}, \quad |\Delta A_{13}| \le u_{13}\bar{\epsilon}, \quad |\Delta A_{15}| \le u_{15}\bar{\epsilon}, \quad |\Delta A_{22}| \le u_{22}\bar{\epsilon}, \\ &|\Delta A_{24}| \le u_{24}\bar{\epsilon}, \quad |\Delta A_{26}| \le u_{26}\bar{\epsilon}, \quad |\Delta A_{51}| \le u_{51}\bar{\epsilon}, \quad |\Delta A_{62}| \le u_{62}\bar{\epsilon}, \end{aligned} \tag{5.34}$$

where $\bar{\epsilon} > 0$. Now given (5.31), let

$$\mathscr{A} = \begin{bmatrix} A & BK_1 & BK_0 \\ \mathscr{B}_c C_m & \mathscr{A}_c & 0 \\ \Lambda C_m & BK_1 & A - \Lambda C_m + BK_0 \end{bmatrix}, \tag{5.35}$$

and assume $\mathscr{A}$ is stable. Let $\mathscr{S}_1 = \begin{bmatrix} I \\ 0 \\ 0 \end{bmatrix}$, $\mathscr{S}_2 = \begin{bmatrix} I & 0 & 0 \end{bmatrix}$, and assume that

$$\mathscr{A} \rightarrow \mathscr{A} + \mathscr{S}_1 \Delta A \mathscr{S}_2,$$

where ΔA is given by (5.34). The following bound on $\bar{\epsilon}$ is obtained such that $\mathscr{A} + \mathscr{S}_1 \Delta A \mathscr{S}_2$ remains stable for all perturbations ΔA which satisfy (5.34):

Theorem 5.4.3 *Given the class of perturbations ΔA described in (5.34), then $\mathscr{A} + \mathscr{S}_1 \Delta A \mathscr{S}_2$ remains stable if:*

$$\bar{\epsilon} < rstab := \frac{1}{\sup_{\omega \geq 0} \pi \left[|\mathscr{S}_2 (j\omega I - \mathscr{A})^{-1} \mathscr{S}_1| U \right]} \tag{5.36}$$

where U is defined in (5.33), $|(.)|$ denotes a matrix whose elements are all equal to their respective absolute values, and $\pi(.)$ denotes eigenvalue of $(.)$ which has the largest moduli of all other eigenvalues of $(.)$.

Proof 2 See [103].

1. **Design of Controller:** The following value of *rstab* is obtained from (5.36) for the case when $\epsilon = 10^{10}$ in (5.23), which corresponds to the case when controller gains K_0 and K_1 of (5.30) are equal to zero, corresponding to an open-loop plant:

   $$rstab^* = 0.1707,$$

   i.e. the open-loop plant remains stable for all perturbations ΔA given by (5.34) for $\bar{\epsilon} < 0.1707$ which corresponds to a perturbation of 17%. The following one-dimensional optimization problem is then solved:

2. **1-D Optimization Problem:**

$$\min_{\epsilon \geq 0} J_\epsilon \mid rstab \geq 0.1$$

where J_ϵ is given by (5.23), for system (5.24), i.e. it is desired to find a "high performance" controller for (5.24) which has the property that it has a robust stability measure (5.36) of 10%. It is to be noted that always exists a solution to this problem, given that with no control applied $rstab = 17\%$. It is also to be noted that there is a trade off of the robust properties of the closed-loop system versus speed of response in choosing the constraint $rstab \geq 0.1$.

3. **Controller Design Obtained:** In this case, on carrying out the 1-D optimization problem, an optimal value of $\epsilon = 10^{-2}$ is obtained to produce the 12^{th}-order strictly proper controller:

$$\begin{aligned} \dot{\beta} &= \overline{\mathscr{A}}_c\beta + \overline{\mathscr{B}}_c(y - y_{ref}) + \overline{\mathscr{E}}_c y_{ref}, \\ u &= \overline{\mathscr{C}}_c\beta, \end{aligned} \tag{5.37}$$

where a standard observer, with poles $\{-5107 \pm j\,14490, -5107 \pm j\,13730, -4.175 \pm j\,376.9\}$, was used to implement the final controller for the system. A listing of matrices $\overline{\mathscr{A}}_c$, $\overline{\mathscr{B}}_c$, $\overline{\mathscr{E}}_c$, $\overline{\mathscr{C}}_c$ is given in Appendix A, Section B.2. The eigenvalues of this controller are given by:

$$\begin{matrix} controller \\ eigenvalues \end{matrix} = \left\{ \begin{matrix} 0, 0, \pm j\,12441, \pm j\,12441, -5214.6 \pm j\,14526, \\ -4.159 \pm j\,377.59, -5220.3 \pm j\,13773 \end{matrix} \right\}, \tag{5.38}$$

of which $\{0, 0, \pm j\,12441, \pm j\,12441\}$ are the servo-compensator (5.25) modes, and the remaining modes correspond to the observer modes.

F. Properties of Closed-Loop System

Consider the following augmented system which is obtained by applying controller (5.37) to plant (5.16):

$$\begin{cases} \begin{bmatrix} \dot{x} \\ \dot{\beta} \end{bmatrix} = \begin{bmatrix} A & B\overline{\mathscr{C}}_c \\ \overline{\mathscr{B}}_c C_m & \overline{\mathscr{A}}_c \end{bmatrix} \begin{bmatrix} x \\ \beta \end{bmatrix} + \begin{bmatrix} 0 \\ \overline{\mathscr{E}}_c - \overline{\mathscr{B}}_c \end{bmatrix} y_{ref} + \begin{bmatrix} E \\ 0 \end{bmatrix} w \\ y = \begin{bmatrix} C_m & 0 \end{bmatrix} \begin{bmatrix} x \\ \beta \end{bmatrix} \end{cases} \tag{5.39}$$

The eigenvalues of this closed-loop system are asymptotically stable and are given by:

$$\begin{matrix} closed-loop \\ eigenvalues \end{matrix} = \left\{ \begin{array}{lll} -5106.7 \pm j\,14487\,, & -5106.7 \pm j\,13733\,, & -0.0113 \pm j\,12441\,, \\ -0.009997 \pm j\,12441\,, & -106.51 \pm j\,782.92\,, & -107.78 \pm j\,29.537\,, \\ -220.05 \pm j\,0.59592\,, & -4.1759 \pm j\,376.99\,, & -4.6459 \pm j\,376.99 \end{array} \right\} \tag{5.40}$$

In this case, the closed-loop poles $\{-0.0113 \pm j\,12441\,, -0.009997 \pm j\,12441\}$ correspond to the servo-compensator poles $\{0 \pm j\,12441, 0 \pm j\,12441\}$, and there is an approximate pole-zero cancellation of the plant and observer closed-loop poles $\{-4.176 \pm j\,376.99\,, -4.6459 \pm j\,376.99\}$ with the transmission zeros of the plant $\{-3.1416 \pm j\,376.99\}$. This implies that the dominant time constant of the closed-loop system is associated with the closed-loop poles $\{-106.51 \pm j\,782.92\,, -107.78 \pm j\,29.537\}$. Therefore, the dominant time constant of the closed-loop system is approximately 10 ms.

G. Robustness Properties of closed-loop System

The closed-loop system has the following robustness properties.

Result G1

- The system is asymptotically stable for all simultaneous perturbations of the following elements of matrix A as given in (5.16): ΔA_{11}, ΔA_{13}, ΔA_{15}, ΔA_{22}, ΔA_{24}, ΔA_{26}, ΔA_{51}, ΔA_{62} which satisfy (5.34) with $\bar{\epsilon} = 0.1$.

Let $|(.)|$ denote the two norm of (.), the following definition is made:

Definition [105]: Given a plant $\dot{x} = Ax + Bu$, $y = Cx$ controlled by a controller $\dot{\eta} = \mathscr{A}_c\eta + \mathscr{B}_c y$, $u = \mathscr{C}_c\eta + \mathscr{D}_c y$, assume that the closed-loop system is asymptotically stable. Let $y = Cx$ be replaced by $y = (I + \mathcal{K}_y)Cx$; then if the closed-loop system remains stable $\forall \mathcal{K}_y$ with $|\mathcal{K}_y| < \ell_y$, the system is said to have an *output gain margin* of $(1 + \ell_y)$. Also let Bu be replaced by $B(I + \mathcal{K}_u)u$; then if the closed-loop system remains stable $\forall \mathcal{K}_u$ with $|\mathcal{K}_u| < \ell_u$, the system is said to have an *input gain margin* of $1 + \ell_u$.

Such a gain margin (GM) can be calculated from real stability radius [106] of the system; in this case the following result is obtained:

Result G2

- The closed-loop system (5.39) has output and input gain margins of 2 and 1.707, respectively.

Definition: Given a plant $\dot{x} = Ax + Bu$, $y = Cx$ controlled by the controller $\dot{\eta} = \overline{\mathscr{A}}_c\eta + \overline{\mathscr{B}}_c y$, $u = \overline{\mathscr{C}}_c\eta$, assume that the closed-loop system is asymptotically stable, and let $u(t)$ be replaced by $u(t-\beta)$. Then if the closed-loop system remains stable $\forall\beta \in [0\ \ \overline{\beta}]$, the closed-loop system is said to have an *input time delay tolerance* of $\overline{\beta}$. Such a tolerance can be determined from [106], [107]; in this case, the following result is obtained:

Result G3

- The closed-loop system (5.39) has an input delay tolerance of 1.0×10^{-3} sec. Since the converter switching frequency is 1980 Hz, this delay tolerance is quite acceptable.

Definition: Given a plant $\dot{x} = Ax + Bu$, $y = Cx$ controlled by a controller $\dot{\eta} = \overline{\mathscr{A}}_c\eta + \overline{\mathscr{B}}_c y$, $u = \overline{\mathscr{C}}_c\eta$, assume that the closed-loop system is asymptotically stable, and let A and B have the following perturbations:

$$(A, B) \rightarrow (A, B)(I + \Delta),$$

where Δ is real. Then if the resultant closed-loop perturbed system remains stable $\forall\Delta$ with the property of $\|\Delta\| < \overline{rstab}$, the system is said to have a *real stability radius* of $100 \times \overline{rstab}$ % stability perturbation. This stability radius can be calculated using the development of [106].

Result G4

- The closed-loop system (5.39) has a 0.410% real stability radius perturbation. It is to be noted that the results obtained in G2, G3 and G4 are exact, i.e. if the perturbation bounds are exceeded, then there exist real perturbations which destabilize the system.

5.4.3 Performance evaluation of MIMO System

This section evaluates the performance of the islanded system given in Figure 5.1, based on the proposed robust servomechanism controller of (5.37). The MATLAB/SimPowerSystems software is used to simulate the proposed MIMO control system, since it is an appropriate platform for simulation of high order controllers. All nonlinearities resulting from the switching devices and time delay of the converter are also considered in the Simulink model of the controlled system.

The reported case studies are to demonstrate that the designed controller is robustly capable of maintaining the magnitude of the PCC voltage. The studies also show that the proposed control system is robust with respect to load parameter uncertainties, and to unmodelled load dynamics.

A. Voltage Tracking

This case study demonstrates the performance of the designed robust servomechanism controller in terms of reference signal tracking. While the system is operating in an islanded mode, the d component of the reference signals, i.e. $y_{1,ref} = V_{d,ref}$, is stepped up from 0.8 pu to 0.98 pu at t=1.0 s, and the q component of the reference signal, i.e. $y_{2,ref} = V_{q,ref}$, is stepped down from 0.44 pu to 0.18 pu at t=1.5 s. In this case, the load parameters are set at their rated values as given in Table 5.1. Figure 5.13 shows the system step responses. In particular, Figure 5.13(a) shows the d and q components of the load voltage at PCC, and demonstrates that based on the designed control system, the output signals V_d and V_q are regulated to their reference values within three cycles. Moreover, Figure 5.13(a) indicates that the controlled closed-loop system is decoupled, i.e. there is no interaction between the d and q channels. Figure 5.13(b) shows the step response of the controller. Figures 5.13(a) and (b) verify that the proposed control system is capable of providing excellent reference signal tracking.

The d and q components of the load current, and power components of the load are shown in Figures 5.13(c) and (d), respectively. The load current demonstrates a longer transient response than the load voltage does, since the quality factor of the load is large ($Q = 1.8$) or equivalently the damping factor of the load is small. Figure 5.13(e) shows instantaneous voltages of the load and their magnitudes. The control signals in the abc-frame are shown in Figure 5.13(f). The time responses verify that the proposed servomechanism controller is able to regulate the load voltages at the reference signals with zero steady-state error.

B. Change of Load Parameters

This case study investigates robust stability and performance of the islanded system with respect to load parameter uncertainties. While the system is operating in an islanded mode and under balanced conditions, the load parameters undergo sudden changes such that the resultant load remains balanced. Three different scenarios, which are sudden changes in the load resistance, load

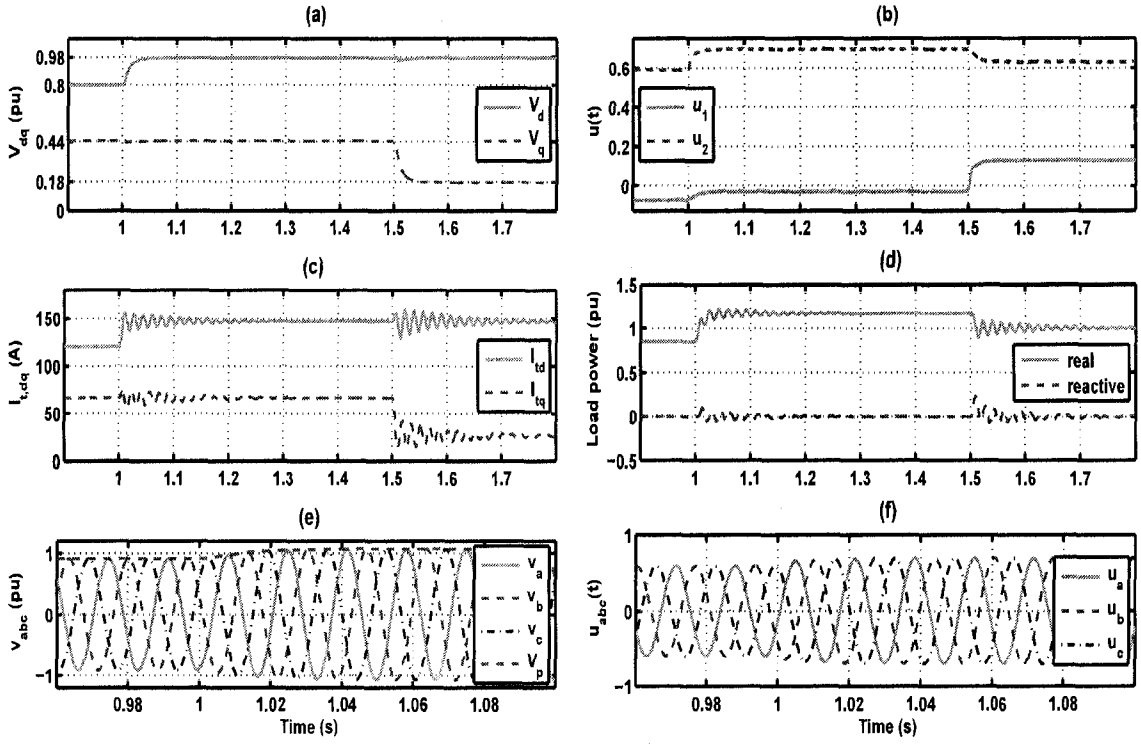

Figure 5.13: Dynamic performance of the islanded system in terms of reference signal tracking (a,b,c) d and q components of load voltage at PCC, control signals and load current, (d) real and reactive power components of load, and (e,f) instantaneous voltages of load and control signals in abc-frame

inductance, and load capacitance, are studied. In all case studies, the reference signals are selected as $V_{d,ref} = 0.9$ and $V_{q,ref} = 0.45\ pu$. It should be noted that although some of these sudden changes in the load parameters are not realistic, the objective here is to verify the robustness properties of the proposed robust servomechanism controller.

1. Change in Load Resistance

In this case study, while the load inductance and capacitance are set at their rated values as given in Table 5.1, the load resistance undergoes step changes from 76 Ω to 50 Ω, 152 Ω, and 760 Ω. Figure 5.14 shows dynamic responses of the islanded system when the load resistance is stepped down from its rated value (76 Ω) to 50 Ω at t=1.0 s. Figure 5.14(a) shows the d and q components of the load voltage and demonstrates that the proposed controller successfully regulates the load voltage within about two cycles. Figures 5.14(b), (c) and (d) show the control signals, load

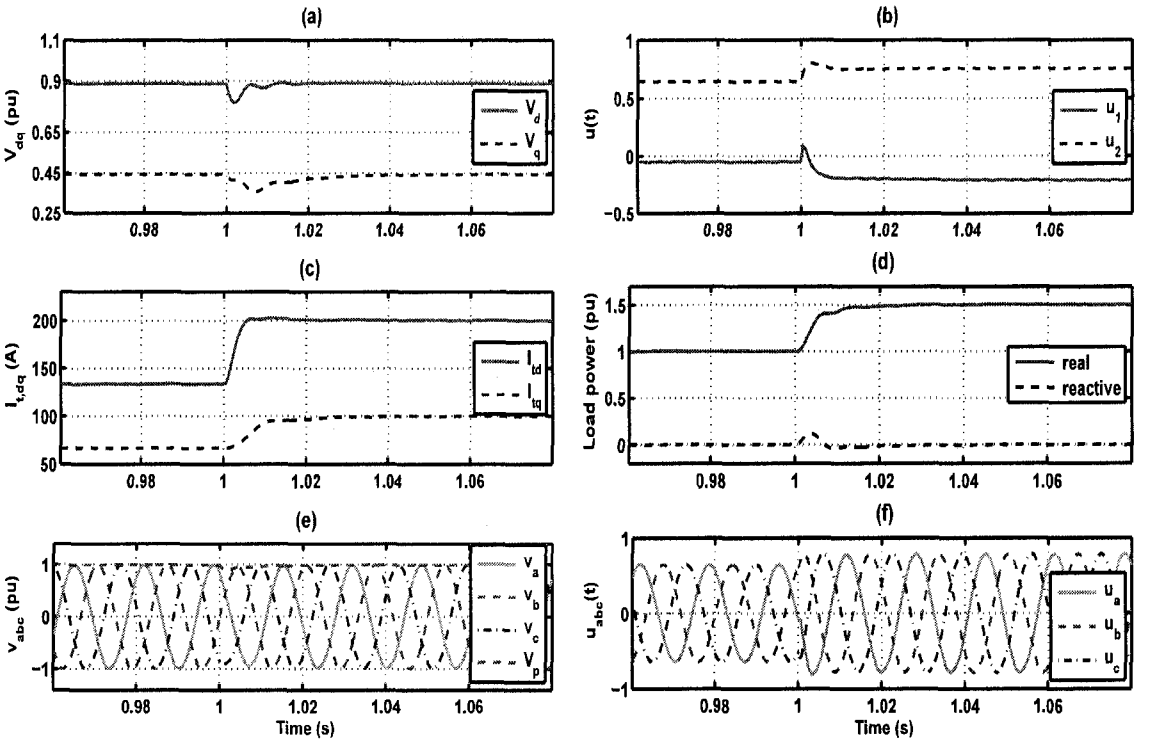

Figure 5.14: Performance of the islanded system when the load resistance is changed from 76 Ω to 50 Ω (a,b,c) d and q components of load voltage, control signals, load current, (d) instantaneous power components of load, and (e,f) instantaneous voltages of load and control signals in abc-frame

current, and power components of the load, respectively. It should be noted that since only the load resistance is changed/stepped down, the VSC has to deliver more real power to the load and reactive power remains unchanged.

Instantaneous voltages of the load and their magnitudes, and the control signals in the abc-frame are demonstrated in Figures 5.14(e) and (f), respectively. Fast transient response of the resultant closed-loop system is also observed from Figures 5.14(e) and (f). Figure 5.15 shows the performance of the islanded system when the load resistance undergoes a step change from 76 to 152 Ω. The d and q components of the load voltage are depicted in Figure 5.15(a), and indicate that the proposed controller is capable of maintaining the load voltage despite uncertainties in the load resistance. Figures 5.15(b), (c) and (d) show the control signals, real and reactive current of the load, and power components of the load, respectively. Instantaneous voltages of the load and the control signals in the abc-frame are depicted in Figures 5.15(e) and (f), respectively. Figure 5.15

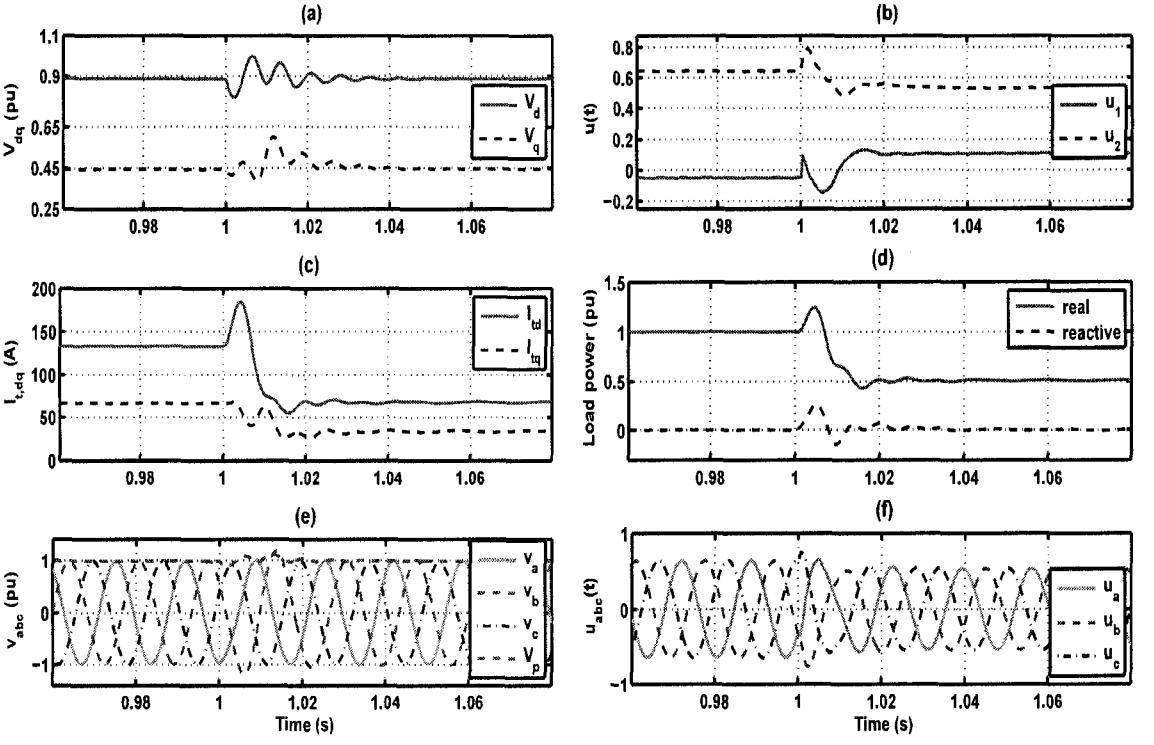

Figure 5.15: *Performance of the islanded system when the load resistance is changed from 76 Ω to 152 Ω (a,b,c) dq components of load voltage, control signals, load currents, (d) instantaneous power components of load, and (e,f) instantaneous voltages of load and control signals in abc-frame*

indicates a transient period of less than three cycles.

Dynamic responses of the islanded system, when the load resistance is suddenly switched from 76 to 760 Ω at t=1.0 s, are shown in Figure 5.16. Similar to the previous cases, this case study also shows the robustness of the proposed controller with respect to the uncertainties in the load resistance. The results show that the closed-loop system is robustly stable and presents excellent performance for all load resistances larger than 50 Ω. The results obtained from all cases such as sudden load changes from 76 Ω to 380 Ω, 1520 Ω, and 10 *k*Ω, and even disconnecting the load resistance, are similar to those of the last case, i.e. the step change in the load resistance from 76 Ω to 760 Ω. It should be noted that a load resistance less than 50 Ω results in over-modulation of the VSC and therefore is not permissible.

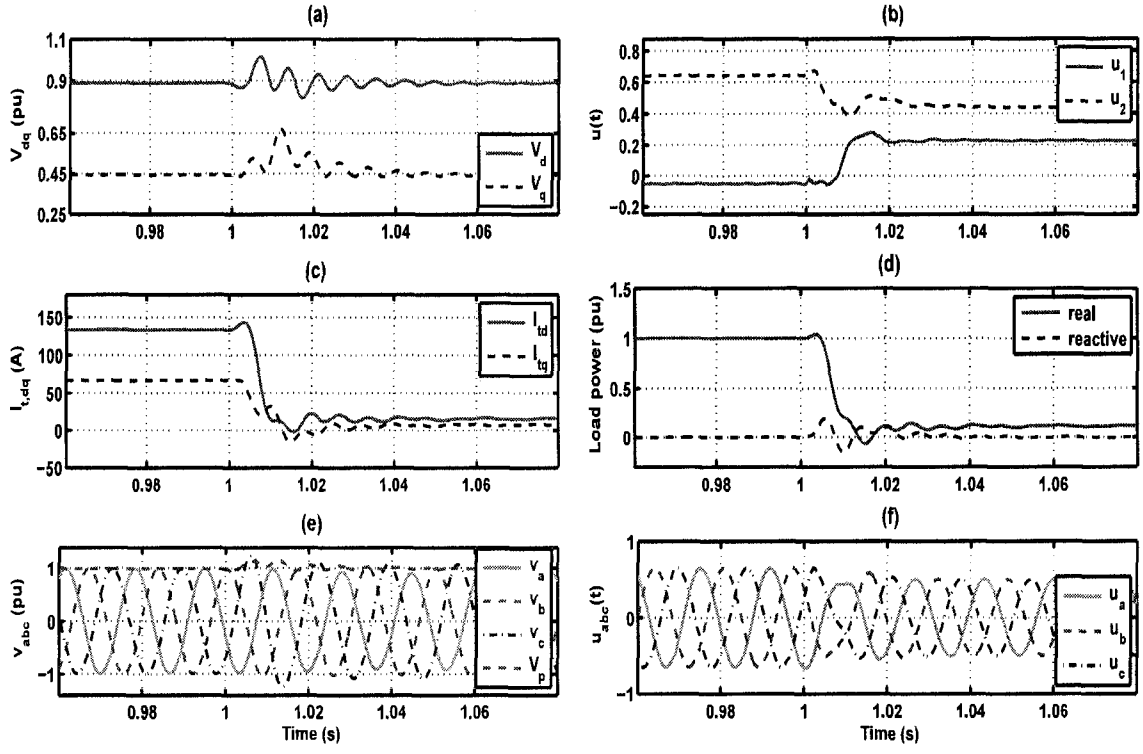

Figure 5.16: Performance of the islanded system when the load resistance is changed from 76 Ω to 760 Ω (a,b,c) dq components of load voltage, control signals, load currents, (d) instantaneous power components of load, and (e,f) instantaneous voltages of load and control signals in abc-frame

2. Change in Load Inductance and Load Capacitance

Simulation results for these two cases are given in Appendix A, Section B.3. In the first case, while the load resistance and capacitance are kept fixed at their rated values, as given in Table 5.1, the load inductance undergoes sudden changes from its rated value of $L = 111.9\ mH$ to $0.7L$ and $2L$. The results show that the resultant closed-loop system is robustly stable and presents a superb performance for all load inductance greater than $0.7L$. It should be noted that a load inductance less than $0.7L$ results in over-modulation of the VSC and therefore is not permitted.

In the second case, while the load resistance and inductance kept fixed at their rated values, as given in Table 5.1, the load capacitance assumes sudden changes from its rated value of $C = 62.86\ \mu F$ to $0.5C$ and $2C$. Our studies show that the closed-loop system is robustly stable for all values of the load capacitance $C \leq 160\ \mu F$. However, due to the kVA limitation of the VSC, any value of capacitance less than $C = 30\ \mu F$ or larger than $C = 160\ \mu F$ results in over-modulation of

Table 5.2: Induction motor parameters

Nominal Power	$S_n = 250\ kVA$
Nominal voltage	$V_n = 575\ V$ (line-line)
Nominal frequency	$f_n = 60\ Hz$
Stator resistance and inductance	$R_s = 14.77\ m\Omega$, $L_{ls} = 169.5\ \mu H$
Rotor resistance and inductance	$R'_r = 7.94\ m\Omega$, $L'_{lr} = 169.5\ \mu H$
Mutual inductance	$L_m = 8.5\ mH$
Inertia constant, friction factor and pairs of poles	$H = 0.5\ s$, $F = 0.015\ pu$, $p = 2$

the VSC and is thus not permitted.

C. Unmodeled Uncertainties

To investigate the impact of unmodeled modes of the plant on performance of the closed-loop system, an induction motor load, described by a sixth-order system, is incorporated in parallel with the *RLC* load. An induction motor inherently has low speed dynamics due to its mechanical system which can be modelled by a second-order mechanical system. Dynamics of the mechanical system are relatively slow compared with those of the motor's fourth-order electrical system. The induction motor is assumed to be at zero state conditions prior to t=0.5 s, when it is energized by connecting it in parallel with the *RLC* load. The motor reaches its steady-state condition within two seconds and then a mechanical load of 1 pu (250 kW) is connected to its shaft at t=2.5 s. Parameters of the *RLC* load are $R = 200\ \Omega$, $L = 111.9\ mH$ and $C = 62.86\ \mu F$, and those of the induction motor are given in Table 5.2.

Performance of the islanded system in response to the motor energization is illustrated in Figures 5.17 and 5.18. Figures 5.17(a) to (d) show variation of the d and q components of the load voltage, control signals, converter current, and real/reactive power components of the converter, respectively. Figures 5.17(c) and (d) indicate that the converter injects more current and real/reactive power during the motor start-up. Figure 5.17(e) shows variations of instantaneous voltages of the load when the induction motor is paralleled to the *RLC* load. The motor currents, during various time intervals, are demonstrated in Figures 5.17(f) to (h). It is observed that the motor inrush current is about eight times its normal steady-state current level and lasts from t=0.5 s to t=1.5 s. Due to inrush current characteristic of the motor, the controller has to apply more effort during the start-up process, e.g. see Figure 5.17(b). Despite the start-up characteristics of the motor, i.e. an

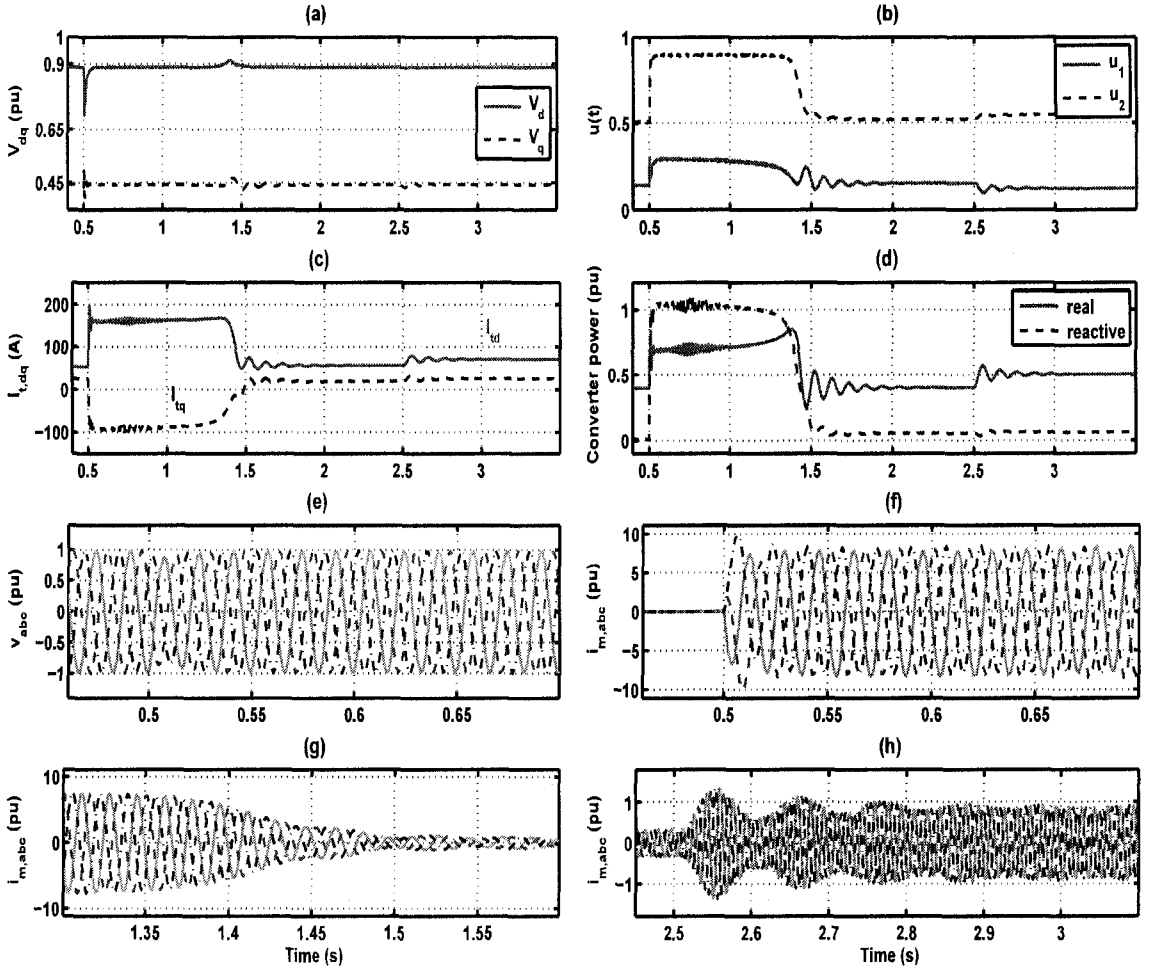

Figure 5.17: Dynamic response of the islanded system to induction motor energization at t=0.5 s (a,b,c) dq components of load (PCC) voltage, control signals, converter currents, (d) instantaneous power components of converter, (e) instantaneous voltages of load, and (f,g,h) motor currents during different time intervals

inrush current and a step change in its mechanical load, the proposed controller successfully regulates the d and q components of the load voltage at their reference values of 0.9 pu and 0.45 pu, as shown in Figure 5.17(a).

Figures 5.18(a) and (b) demonstrate the mechanical speed and electrical torque of the motor, respectively. Real and reactive power components of the motor, during various time intervals, are shown in Figures 5.18(c) and (d). The results obtained from this case study verify robust stability and robust performance of the closed loop system with respect to unmodeled uncertainties due to the inclusion of an induction motor.

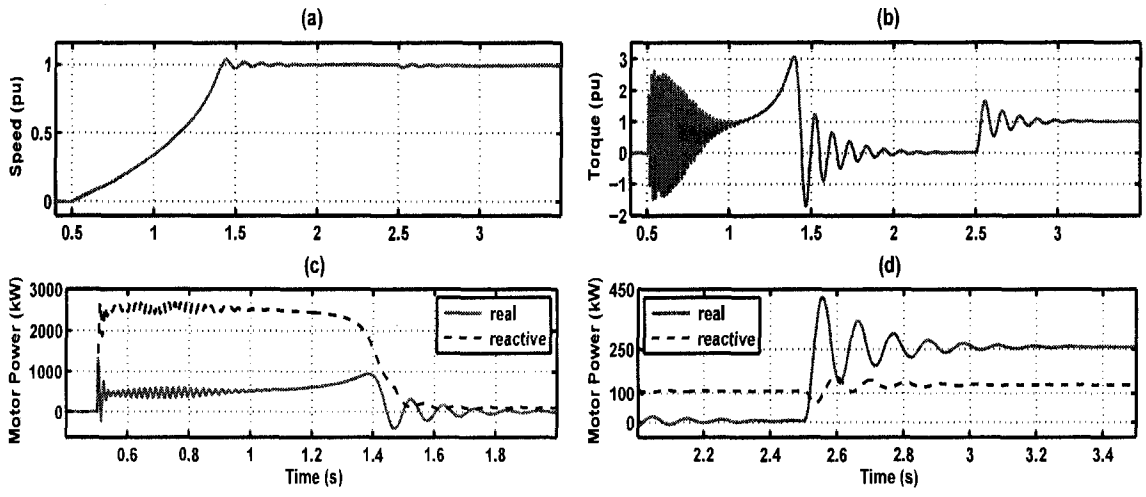

Figure 5.18: Dynamic response of the islanded system to induction motor energization at t=0.5 s (a) mechanical speed, (b) electrical torque, and (c,d) instantaneous power components of motor

5.5 Conclusions

Two dynamic models and corresponding to each model a controller for autonomous operation of an electronically-coupled DG unit and its local load are presented in this chapter. Both dynamic models are obtained based on a state space representation of the DG unit and the load in a dq-frame. The first model which represents a SISO LTI system, indeed, is a simplified version of the more general MISO nonlinear system. In this case, the classical control approach is adopted to design a second-order controller for the VSC of the DG unit. In the grid-connected mode, based on the conventional dq-current control strategy, the VSC controls real- and reactive-power components of the DG unit. Subsequent to an islanding event, the dq-current controller is disabled and the proposed SISO controller is activated. The proposed islanding detection method of Chapter 4 is used to detect the islanding event.

Performance of the proposed SISO controller under (i) accidental and planned islanding events, (ii) uncertainties in the load parameters, (iii) step changes in the set point signal, and (iv) unbalanced load conditions are reported. The studies are carried out based on time-domain simulations in the PSCAD/EMTDC software environment. The simulation results verify that the proposed SISO controller is able to regulate the voltage magnitude of the islanded system within three cycles of transients, even in the worst case scenarios. However, our studies also show that the SISO controller is not robust with respect to large perturbation of load parameters. Nevertheless, for

those applications in which the local load is pre-specified and fairly fixed, the SISO controller is a good choice.

To overcome the shortcomings of the SISO system, a more precise LTI model is also proposed in this chapter. This model for the islanded system corresponds to a MIMO LTI system with structured uncertainties [48,93]. The robust servomechanism approach of [97]-[107] is adopted to design a 12^{th}-order MIMO controller for the VSC of the DG unit. The proposed MIMO controller guarantees robust stability and desired performances, e.g. fast transient response and zero steady-state error, despite uncertainties in the load parameters.

Performance of the proposed MIMO controller under (i) step changes in the set point signals, (ii) uncertainties in the load parameters, and (iii) unmodeled uncertainties are investigated and reported. The studies are carried out based on time-domain simulations in the MATLAB/SimPowerSystems software environment. The studies conclude that the proposed 12^{th}-order controller maintains voltage magnitude of the islanded system within a transient period of less than three cycles, and provides such a performance over the following uncertainty bounds:

- The load resistance is greater than 50 Ω and the load inductance and capacitance do not assume large perturbations about their nominal values.
- The load inductance is larger than 75 mH and the load resistance and capacitance do not assume large perturbations about their nominal values.
- The load capacitance is $30\ \mu F \leq C \leq 160\ \mu F$ and the load resistance and inductance do not assume large perturbations about their nominal values.

Chapter 6

Control of an Islanded Electronically-Coupled DR Unit under Unbalanced Conditions

6.1 Introduction

Autonomous operation of an islanded system is discussed in Chapter 5. The islanded system is modeled in a dq-frame, and the system is assumed to be under balanced conditions. The main advantage of transformation into the dq-frame is that a set of balanced three-phase signals is transformed to two dc components. The dq-frame has no specific merits when the three-phase system is unbalanced. An unbalanced condition in a power system usually results from asymmetry of the loads, asymmetry in lines, and/or abnormal system conditions, e.g. phase-to-ground, phase-to-phase and open conductor faults [90].

Representation of a set of unbalanced signals, in a dq-frame, contains double frequency components. In such a case, one cannot take advantage of the dq-frame transformation to reduce sinusoidal signals to time invariant quantities. Nevertheless, dynamical equations of such systems in a dq-frame still can be expressed by a set of LTI differential equations, assuming a constant frequency for the system. However, if an unbalanced condition results from asymmetry of three-phase loads, the model of such a system in a dq-frame represents a highly nonlinear multiple-input multiple-output (MIMO) system. Robust stability analysis and controller synthesis of a nonlinear

MIMO system is not a simple task, particularly when there are parametric uncertainties in the plant model [50,94,95].

Therefore, for an autonomous DG unit with an unbalanced load, transformation to a dq-frame does not offer any particular advantage, and we propose to use the abc-frame to model such a system. The main advantage of the abc-frame over the dq-frame is that a three-phase, four-wire system can be decomposed into three independent single-phase systems, assuming there are no mutually coupled elements in the three phases. Thus, the abc-frame results in a simpler dynamic model than that of the dq-frame. Moreover, the model obtained by the abc-frame represents an LTI system.

It should be noted that if there are mutually coupled elements in the three phases of a three-phase system, or the three-phase system is a three-wire apparatus which does not permit flow of zero-sequence current, we cannot decompose the system into three independent single-phase systems using the abc-frame. Moreover, since the zero-sequence current is not permitted, it is not possible to balance the phase-to-neutral voltages of the load. In such a case, one can balance the phase-to-phase voltages of the load based on a unified dynamic model for the three-phase system. Appendix C discusses the mathematical model and controller design for an islanded system, with no neutral connection between the load and the voltage-sourced converter (VSC).

In this chapter, autonomous operation of an islanded single DG system which is under unbalanced conditions is investigated. The imbalance results from asymmetry of the three-phase load. The objective of this chapter is to design a controller for the DG unit to provide a set of balanced voltages at the load terminals. Moreover, voltage magnitude and frequency of the system must be controlled despite the load parameters uncertainties.

In this chapter, first a mathematical model for the islanded system, in an abc-frame, is derived. Then, based on the model, a controller is designed and robust stability of the resultant closed-loop system is analyzed. It is shown that the closed-loop system is robustly stable over a wide range of load parameter uncertainties. It is also shown that the closed-loop system satisfied the pre-specified robust performance characteristics, e.g. fast response to load changes, and zero steady-state error. To demonstrate the performance of the proposed controller, various case studies based on digital time-domain simulation in the PSCAD/EMTDC software environment are carried out. The simulation results show effectiveness of the designed control system in terms of maintaining

voltage magnitude and frequency of the islanded system under both balanced and unbalanced conditions.

To experimentally verify the performance of the proposed controller, the test system of Appendix A is implemented and the proposed controller is digitally realized using an RT-Linux system. The detail of the RT-Linux system and the experimental results of the test system are given in Appendix A, Section A.6. The test results validate the performance of the proposed controller in terms of reference signal tracking and robustness with respect to load parameter uncertainties.

6.2 Study System

A single-line diagram of the study system is depicted in Figure 6.1, where the DG unit is represented by a DC voltage source, a VSC, a series filter, and a step-up transformer. Phase-x, $x = a, b, c$, of the local load is represented by a parallel RLC network which can be generally unbalanced and its parameters can be uncertain within a range. Nominal parameters of the study system of Figure 6.1 are the same as those of the system of Figure 5.1 as summarized in Table 5.1.

Similar to the system of Figure 5.1, the study system of Figure 6.1 must remain in service in both grid-connected and islanded modes. In a grid connected mode, voltage magnitude and frequency of the local load, at the PCC, are dictated by the grid and the control strategy of the VSC is identical to that of the system of Figure 5.1. Moreover, assuming a stiff and balanced grid, the load voltage at the PCC is almost balanced, despite asymmetry of the load. In a grid-connected mode, when the local load is unbalanced, the grid provides a set of unbalanced currents for the local load and the interfaced VSC operates under balanced conditions, based on the conventional dq-current control strategy.

Subsequent to an islanding event, due to power mismatch prior to the islanding instant and/or lack of control over voltage and frequency, frequency and voltage of the island drift and the island eventually becomes unstable [21,23]. In addition, from the studies carried out in Chapter 5, Section 5.3.3-E, we conclude that the proposed controllers of Chapter 5 cannot cope with large unbalanced load conditions. Therefore, a new control strategy should be designed (i) to regulate voltage magnitude and frequency of the island, and (ii) to provide a set of balanced voltages at the PCC despite asymmetry and uncertainties of the load. It should be mentioned that to obtain

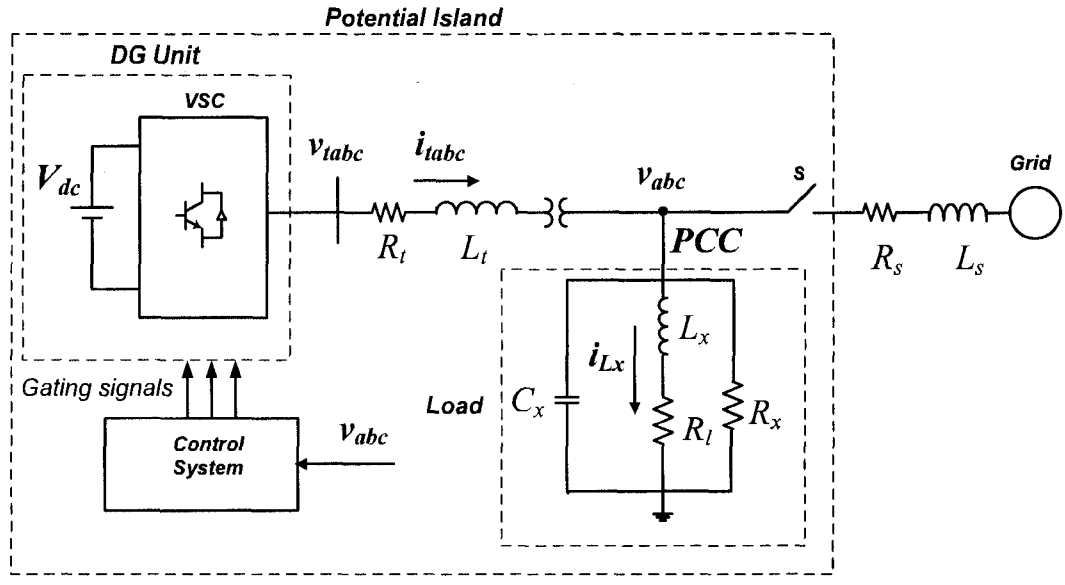

Figure 6.1: Schematic representation of a single-DG island

seamless transition from the grid-connected mode to the islanded mode, the islanding event should be detected as fast as possible, e.g. by the proposed method of Chapter 4.

6.3 Control System Structure

Figure 6.2 shows a block diagram of the control system strategies for both grid-connected and islanded modes. In the grid-connected mode, the dq-frame controller provides a set of balanced three-phase control signals u_a, u_b, and u_c. Then, the control signals are compared with the triangular carrier signals and produce the gating pulses for the VSC. Subsequent to an islanding event, the proposed islanding detection method of Chapter 4 detects the event, and upon detection S_a, S_b, and S_c are switched to the control signals produced by the abc-frame controller. The control signals are then applied to the gating signal generator unit to produce the gating pules for the VSC.

Based on Figure 6.2, the control strategy of the islanded system consists of three identical SISO control subsystems in the abc-frame. If the reference signals $v_{ref,a}$, $v_{ref,b}$, and $v_{ref,c}$ are pure sinusoidal and balanced with a constant frequency, and the proposed controllers are capable of perfect tracking of the reference signals, the load voltage at PCC will remain balanced at the same frequency. Therefore, autonomous operation of the islanded system can be maintained.

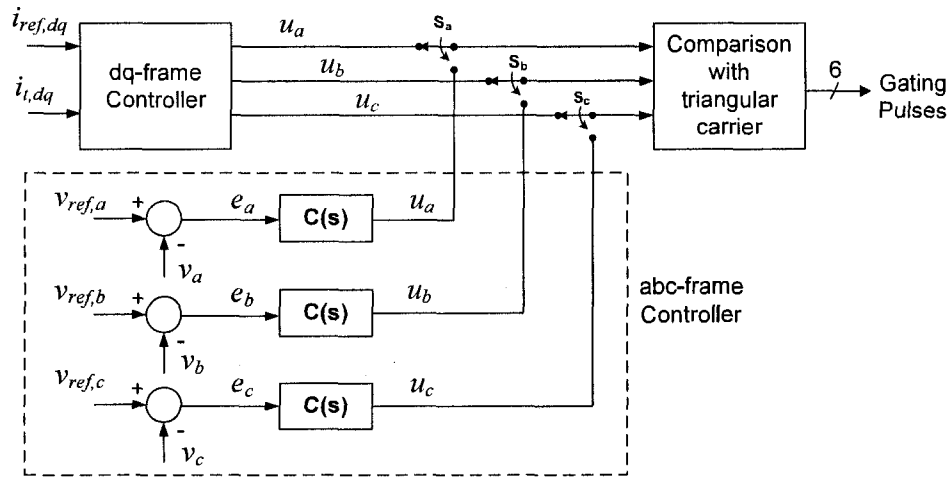

Figure 6.2: Control system structure

6.4 Mathematical Model and Stability Analysis of Islanded System

In this section, a mathematical model of the islanded system in the Laplace domain is derived, and a stability analysis for the plant (open-loop system) is carried out.

6.4.1 Transfer Function of Open-loop System

Based on Figure 6.1, control and output signals are the instantaneous voltages of phase-x, $x = a, b, c$, of the VSC and the load, respectively. Therefore, the open-loop system can be described by a transfer function from the VSC terminal voltage at phase-x, v_{tx}, to the load terminal voltage at phase-x, v_x, Figure 6.1. Three decoupled transfer functions are derived corresponding to each phase of the islanded system. $Z_t(s)$ and $Z_{load}(s)$ denote the series filter impedance and the impedance of phase-x of the load in the Laplace domain, respectively:

$$\begin{aligned} Z_t(s) &= R_t + L_t s \\ Z_{load}(s) &= \left(\tfrac{1}{R_x} + \tfrac{1}{L_x s} + C_x s\right)^{-1} \end{aligned} \tag{6.1}$$

Transfer function of the open-loop system for each phase (phase-x) is then

$$G(s) = \frac{v_x}{v_{tx}} = \frac{Z_{load}}{Z_{load} + Z_t}. \tag{6.2}$$

Substituting for $Z_t(s)$ and $Z_{load}(s)$ from (6.1) in (6.2), we deduce

$$G(s) = \frac{R_x L_x s + R_x R_l}{a_3 s^3 + a_2 s^2 + a_1 s + a_0}, \tag{6.3}$$

where

$$\begin{aligned} a_3 &= R_x L_x C_x L_t \\ a_2 &= R_x L_x C_x R_t + R_x C_x R_l L_t + L_t L_x \\ a_1 &= R_x C_x R_t R_l + R_t L_x + R_l L_t + R_x L_t + R_x L_x \\ a_0 &= R_x R_t + R_x R_l + R_t R_l. \end{aligned} \tag{6.4}$$

The open-loop system of (6.3) is a third order LTI and SISO system. If a vector comprising the load parameters is defined as $q = [R_x \ L_x \ C_x]$, then the open-loop system of (6.3) can be expressed as a function of both variable "s" and vector q, i.e.

$$G = G(s, q) = \frac{N(s, q)}{D(s, q)} \tag{6.5}$$

where $N(s, q)$ and $D(s, q)$ are polynomial functions with respect to "s". Since the load parameters (components of vector q) are assumed to be uncertain positive real numbers, plant (6.3) represents a system with structured real parametric uncertainties [48]. Moreover, as it is observed from (6.3) and (6.4), plant $G(s, q)$ has a *multilinear uncertainty structure* [48], i.e. all coefficients of variable "s" in plant (6.3) are linear with respect to each parameter of vector q.

6.4.2 Stability Analysis of Open-Loop System

To analyze stability of the open-loop system, we use the Routh-Hurwitz stability criterion. The Routh-Hurwitz table for plant $G(s, q)$ is [71]

s^3	a_3	a_1
s^2	a_2	a_0
s^1	$b_1 = a_1a_2 - a_3a_0$	
s^0	a_0	

in which

$$\begin{aligned} b_1 &= a_1a_2 - a_0a_3 \\ &= L_tL_x{}^2R_t + L_tL_x{}^2R_x + L_t{}^2L_xR_x + 2L_tL_xR_tC_xR_xR_l + L_t{}^2L_xR_l + R_t{}^2C_xR_xL_x{}^2 + \\ &\quad R_tC_xR_x{}^2L_x{}^2 + R_t{}^2C_x{}^2R_x{}^2L_xR_l + L_t{}^2C_xR_x{}^2R_l + L_tC_x{}^2R_x{}^2R_l{}^2R_t + L_t{}^2C_xR_xR_l{}^2 \end{aligned}$$

a_i, $i = 0, 1, 2, 3$ and b_1 are positive real numbers. Thus, open-loop system $G(s, q)$ is stable for all load parameter uncertainties. This is clearly obvious from the fact that any passive and LTI open-loop circuit represents a stable system. Moreover, the plant is minimum-phase since it has one stable zero at $z = \frac{-R_l}{L_x}$.

6.5 Control Strategy

In this section, first based on the classical control approaches, we design a robust controller for the nominal plant. Then, with the aid of robust stability tools for the linear systems, a robust analysis of the resultant closed-loop system is performed. The nominal plant $G(s, q^0)$ is obtained by substituting for the parameters of the system from Table 5.1 in (6.3), as expressed by

$$G(s, q^0) = \frac{3.315e4s + 1.041e5}{s^3 + 217.5s^2 + 1.77e5s + 8.183e5}, \tag{6.6}$$

where $q^0 = [76\Omega \;\; 111.9\, mH \;\; 62.86\, \mu F]$ contains the nominal parameters of the load.

6.5.1 Controller Design

In this section, using classical control methods and Matlab/Robust Control Toolbox, an optimum controller for (6.6) is designed to meet the following desired characteristics.

- The resultant closed-loop system must be asymptotically stable.

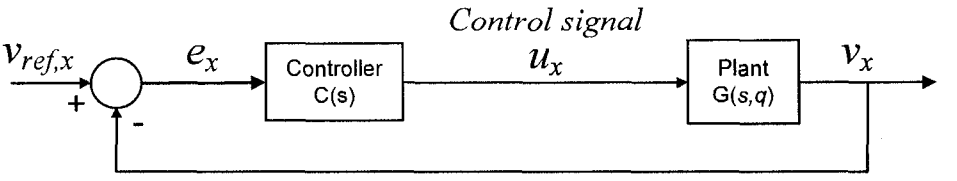

Figure 6.3: Block diagram of the closed-loop system

- The steady-state error with respect to a sinusoidal reference signal with constant frequency $\omega_0 = 2\pi 60$ should be zero.
- The closed-loop system must be robust with respect to disturbance signals, measurement noise, and uncertainties in the load parameters.

Figure 6.3 shows a block diagram of the resultant closed-loop system including the plant model and the controller. The controller receives error signal e_x and produces control signal u_x for the VSC system. To obtain zero steady-state error ($e_{ss} = 0$) with respect to sinusoidal reference signal, a pair of complex poles is assigned to the imaginary axis at $p = \pm j\omega_0$. In other words, the gain of the loop transfer function $G(s, q^0)C(s)$ at the reference signal frequency ω_0 must be very high. This pole assignment destabilizes the resultant closed-loop system. To stabilize the closed-loop system, one real and two complex stable zeros are assigned at $z = -40$, and $z = -200 \pm j400$, respectively. The controller is not a proper transfer function and thus its bandwidth is not limited. Thus, the present controller is not capable of suppressing the measurement noise and high frequency disturbances. Therefore, a pair of stable complex poles are assigned at $p = -2000 \pm j2000$ which limits the controller bandwidth. Therefore, transfer function of the final controller is obtained as

$$C(s) = \frac{N_C(s)}{D_C(s)} = \frac{(71,060\,s + 2,842,000)\left(s^2 + 400\,s + 200,000\right)}{(s^2 + 142,100)\,(s^2 + 4,000\,s + 8,000,000)}. \tag{6.7}$$

Figure 6.4 shows the bode plots of controller $C(s)$ and loop transfer function $G(s, q^0)C(s)$. It is observed from the bode magnitude plots that controller $C(s)$ and loop transfer function $G(s, q^0)C(s)$ have narrow bands at the system frequency ω_0 and roll off as frequency increases. The designed controller provides gain and phase margins of $G.M. = 21.3$ dB and $P.M. = 47.4°$, respectively.

(a)

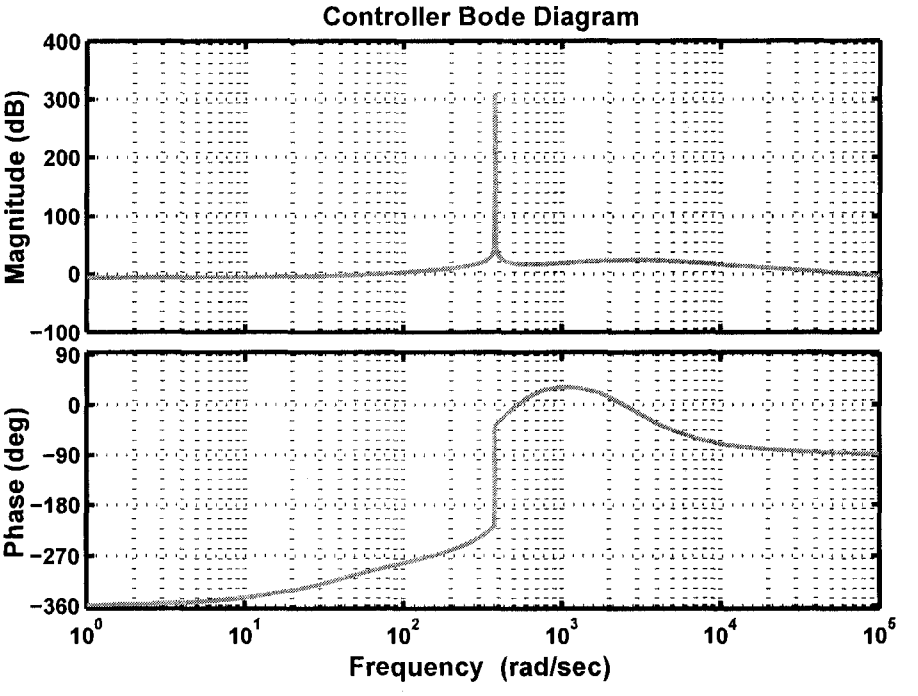

(b)

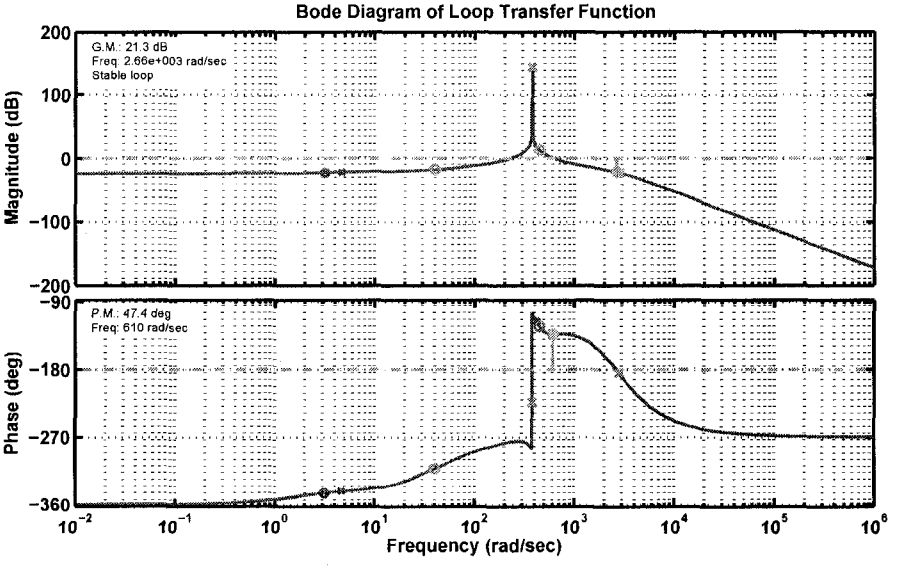

Figure 6.4: Bode plots of (a) controller $C(s)$, and (b) loop transfer function $C(s)G(s, q^0)$

6.5.2 Robust Stability Analysis

Robustness analysis of the closed-loop system of Figure 6.3 is discussed in this section. The robustness analysis approach adopted here primarily relies on the "Zero Exclusion Condition" and the "Mapping Theorem" [48,93]. A brief explanation of the Mapping Theorem and Zero Exclusion Condition are given in Appendix A. Appendix A also provides basic definitions, e.g. *Value Set, Uncertainty Bounding Set, Convex Hull, and Uncertainty Structure*, which are used for robust analysis of LTI systems.

The problem of robustness analysis is first converted into a polynomial problem with coefficients that structurally depend on the vector of load parameters q. This polynomial is the characteristic equation of the closed-loop system. Transfer function of the closed-loop system of Figure 6.3 is

$$G_{CL}(s,q) = \frac{G(s,q)C(s)}{1+G(s,q)C(s)} = \frac{N(s,q)N_C(s)}{D(s,q)D_C(s)+N(s,q)N_C(s)}. \tag{6.8}$$

Therefore, characteristic equation of the closed-loop system, i.e. $P(s,q)$, is

$$P(s,q) = D(s,q)D_C(s) + N(s,q)N_C(s). \tag{6.9}$$

The algebraic expression of $P(s,q)$ is

$$\begin{aligned}
P(s,q) &= 0.4761R_xL_xC_xs^7 \\
&+(1907R_xL_xC_x + 0.1674R_xC_x + 0.4761L_x)s^6 \\
&+(3886\times10^3R_xL_xC_x + R_xL_x + 670.3R_xC_x + 0.4761R_x + 1907L_x + 0.1674)s^5 \\
&+(29\times10^7R_xL_xC_x + 75060R_xL_x + 1366\times10^3R_xC_x \\
&+1907R_x + 3886\times10^3L_x + 670.3)s^4 \\
&+(5427\times10^8R_xL_xC_x + 3941\times10^4R_xL_x + 102\times10^6R_xC_x \\
&+3912\times10^3R_x + 29\times10^7L_x + 1366\times10^3)s^3 \\
&+(2707\times10^9R_xL_xC_x + 1592\times10^7R_xL_x + 1908\times10^8R_xC_x \\
&+3039\times10^5R_x + 5427\times10^8L_x + 102\times10^6)s^2 \\
&+(1705\times10^9R_xL_x + 9515\times10^8R_xC_x \\
&+5483\times10^8R_x + 2707\times10^9L_x + 1908\times10^8)s \\
&+(3306\times10^9R_x + 9515\times10^8).
\end{aligned} \tag{6.10}$$

It is observed from (6.10) that characteristic polynomial $P(s,q)$ has a *multilinear uncertainty structure*; i.e., the coefficients of $P(s,q)$ depend multilinearly on the vector of uncertain parameters q [48].

We also assume that set Q is a box in $\mathbb{R}^3$ and contains the load parameters $q = [R_x \;\; L_x \;\; C_x]$. The goal is to determine the maximal uncertainty bounding set Q under which the stability of the closed-loop system or equivalently stability of the characteristic polynomial $P(s,q)$ is satisfied. In other words, the objective is to find the largest uncertainty box Q such that the family of polynomials $\mathcal{P} = \{P(.,q) : q \in Q\}$ is stable for all $q \in Q$; that is, for all $q \in Q$, all roots of $P(s,q)$ lie in the strict left half plane. In such a case, set Q represents a *Robustness Margin* for the stability of the closed-loop system. A recursive calculation is required to solve the robustness margin problem. Robust stability analysis carried out in this section is summarized in the following theorem.

Theorem 6.5.1 *The family of polynomials $\mathcal{P} = \{P(.,q) : q \in Q\}$, as described by (6.10), with uncertainty bounding set Q given by*

$$Q = \begin{cases} 50\,\Omega \le R_x \le 2000\,\Omega \\ 40\,mH \le L_x \le 400\,mH \\ 10\,\mu F \le C_x \le 80\,\mu F \end{cases} \quad or \quad \begin{cases} 0.66\,pu \le R_x \le 26.26\,pu \\ 0.2\,pu \le L_x \le 1.98\,pu \\ 0.29\,pu \le C_x \le 2.3\,pu, \end{cases} \tag{6.11}$$

is robustly stable.

Proof 3 The proof can be performed in the following three steps.

I: Necessary Condition

First, we verify that the critical precondition for application of the Zero Exclusion Condition (see Appendix A) holds. Substituting $q^0 = [76\Omega \;\; 111.9\,mH \;\; 62.86\,\mu F] \in Q$ in (6.10), we obtain

$$\begin{aligned} P(s,q^0) \;&= 2.545\times10^{-4}s^7 + 1.073s^6 + 2339s^5 + 1.38\times10^6 s^4 + 9.569\times10^8 s^3 \\ &\quad +2.217\times10^{11}s^2 + 5.667\times10^{13}s + 2.522\times10^{14} \end{aligned} \tag{6.12}$$

which is a stable member of the family of polynomials $\mathcal{P} = \{P(.,q) : q \in Q\}$.

II: Cutoff Frequency

It can be shown that there exists some frequency $\omega_c \geq 0$ which has the property that $0 \notin P(j\omega, Q)$ for all $\omega > \omega_c$. This frequency is called cutoff frequency and its existence is established using the invariant degree condition (Appendix A); that is, the degree of polynomial $P(s, q)$ is 7 for all $q \in Q$. Suppose that $P(s, q) = \sum_{i=0}^{n} a_i(q)s^i$ and, without loss of generality, assume that $min\{a_i(q)\} > 0$ for all $q \in Q$ and $i = 0, 1, ..., n$. Then, given any $q \in Q$, it can be seen that for $\omega \geq 0$,

$$|P(j\omega, q)| \geq \left(\min_{q\in Q} |a_n(q)|\right)\omega^n - \sum_{i=0}^{n-1}\left(\max_{q\in Q} |a_i(q)|\right)\omega^i. \tag{6.13}$$

Since the right-hand side tends to $+\infty$ as $\omega \to \infty$, it follows that for any $\beta > 0$ there exists an $\omega_c > 0$ such that $|P(j\omega, q)| \geq \beta$ for all $\omega > \omega_c$. Hence, $0 \notin P(j\omega, Q)$ for all $\omega > \omega_c$.

We can select ω_c to be the largest real root of the test polynomial

$$f(\omega) = min\{a_n(q)\}\omega^n - \sum_{i=0}^{n-1} max\{a_i(q)\}\omega^i. \tag{6.14}$$

For the given uncertainty box of (6.11), the test polynomial $f(\omega)$ is

$$\begin{aligned} f(\omega) \;&= 9.522 \times 10^{-6}\,\omega^7 - 122.3\,\omega^6 - 2.513 \times 10^5\omega^5 - 8.42 \times 10^7\omega^4 \\ &\quad -7.422 \times 10^{10}\omega^3 - 1.376 \times 10^{13}\,\omega^2 - 2.462 \times 10^{15}\,\omega - 6.611 \times 10^{15}. \end{aligned} \tag{6.15}$$

Therefore, we obtain $\omega_c \simeq 12.84 \times 10^8$ rad/s as an acceptable cutoff frequency for the required Mapping Theorem plot, i.e. when applying the Mapping Theorem, we can terminate the frequency sweep at the $\omega = \omega_c$.

III: Value Set Synthesis

Finally, we need to find the "true" value set of $P(s, q)$, as defined in Appendix A, for all $\omega \geq 0$. To the best of our knowledge, there exists no analytical tool in the technical literature to calculate the true value set for polynomials with multilinear uncertainty structure. However, using the Mapping Theorem [48], we can obtain the tightest possible polytopic overbound for the value sets of such polynomials. Based on the Mapping Theorem, we can obtain the convex hull of the true value set

at each positive frequency ω. This indicates that first for all $\omega \geq 0$, $P(j\omega, \{q^i\})$ is calculated, where $\{q^i\}$ is the set of extreme points or vertexes of the uncertainty box Q. The uncertainty bounding set Q, which is a box in $\mathbb{R}^3$, has eight vertices. Therefore, based on the Mapping Theorem we conclude that

$$P(j\omega, Q) \subseteq conv\ \ P(j\omega, Q) = conv\{P(j\omega, \{q^i\})\} \quad i = 1, 2, 3, ..., 8 \tag{6.16}$$

where "conv" denotes the convex hull. Using the Matlab software, a code is developed to synthesize an overbounding convex hull approximation of the true value sets.

Figures 6.5, 6.6, and 6.7 show the convex hull of the true value set for the characteristic polynomial $P(s, q)$ for $0 \leq \omega \leq 1000$, $1000 \leq \omega \leq 10^6$ and $10^6 \leq \omega \leq \omega_c$, respectively. Figures 6.5(b), 6.6(b), and 6.7(b) are the zoomed version of the value sets and show that the origin of the complex plane is excluded from the computed value set, i.e., $0 \notin P(j\omega, Q)$ for all $\omega \geq 0$. Moreover, polynomial family $\mathcal{P} = \{P(., q) : q \in Q\}$ has an invariant degree of n=7. Hence, by the Zero Exclusion Condition, family $\mathcal{P}$ is robustly stable. ■

Any uncertainty set $\hat{Q}$ larger than the set Q of (6.11) results in a value set that includes the origin of the complex plane. Therefore, the uncertainty set of (6.11) could represent the robustness margin box for the closed-loop system. It should be noted that the robustness margin of (6.11) is conservative, since the Mapping Theorem is a sufficient condition.

6.6 Performance evaluation

This section investigates performance of the system of Figure 6.1 during and subsequent to an islanding event, based on the proposed controller of (6.7). In the presented studies, the islanding event is detected based on the proposed method of Chapter 4 and upon its detection, the control strategy is switched from the conventional dq-frame controller to the proposed abc-frame controller of Figure 6.2. In each case study, the UTSP system of Chapter 2 is also used to estimate the sequence components of the PCC voltage and to measure the system frequency. The studies are performed based on digital time-domain simulation method in the PSCAD/EMTDC software environment. The reported case studies demonstrate that the designed controller is (i) capable of

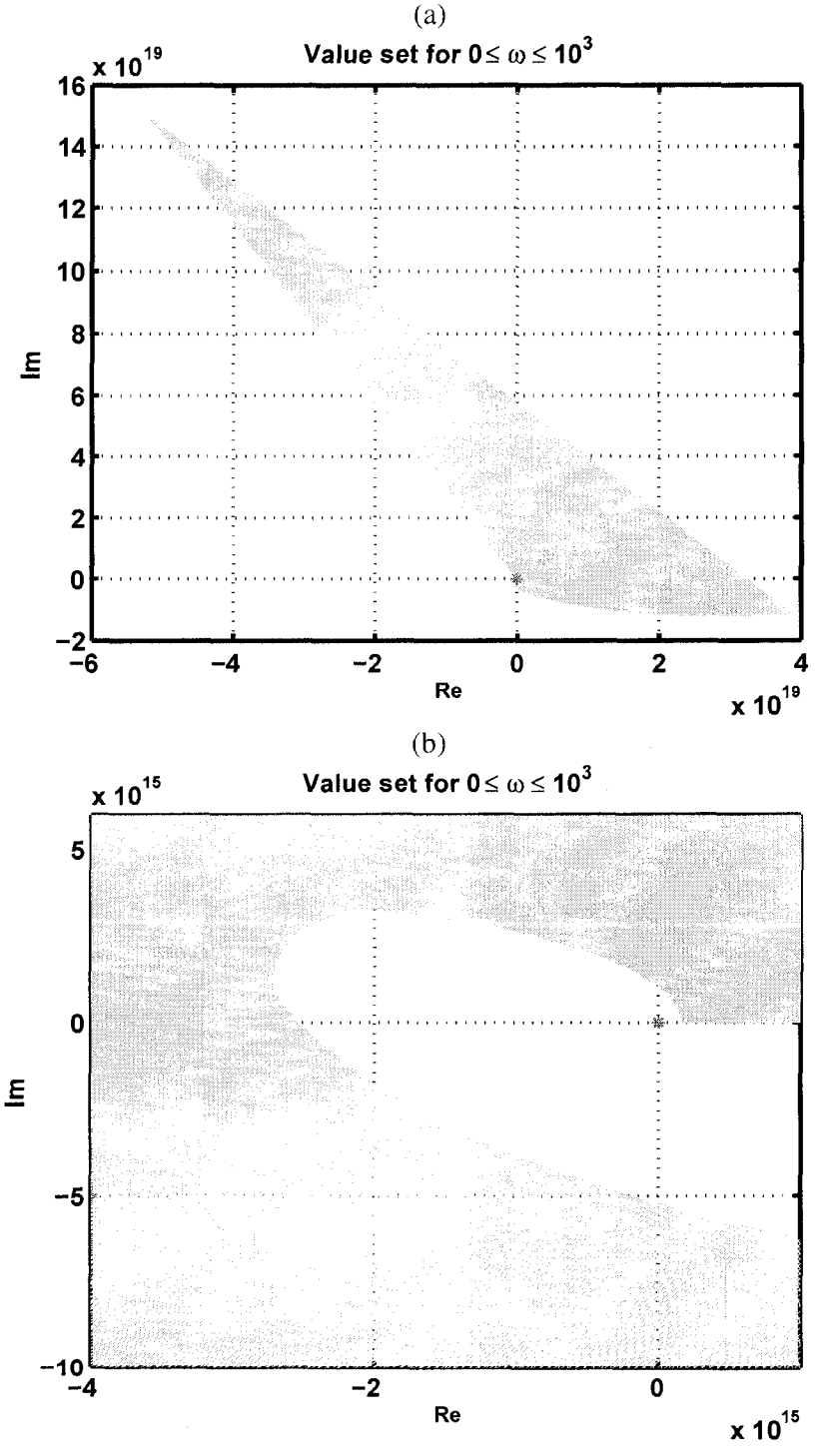

Figure 6.5: (a) Convex hull of the value set for $P(s,q)$ for $0 \leq \omega \leq 10^3$ rad/sec, (b) zoomed version

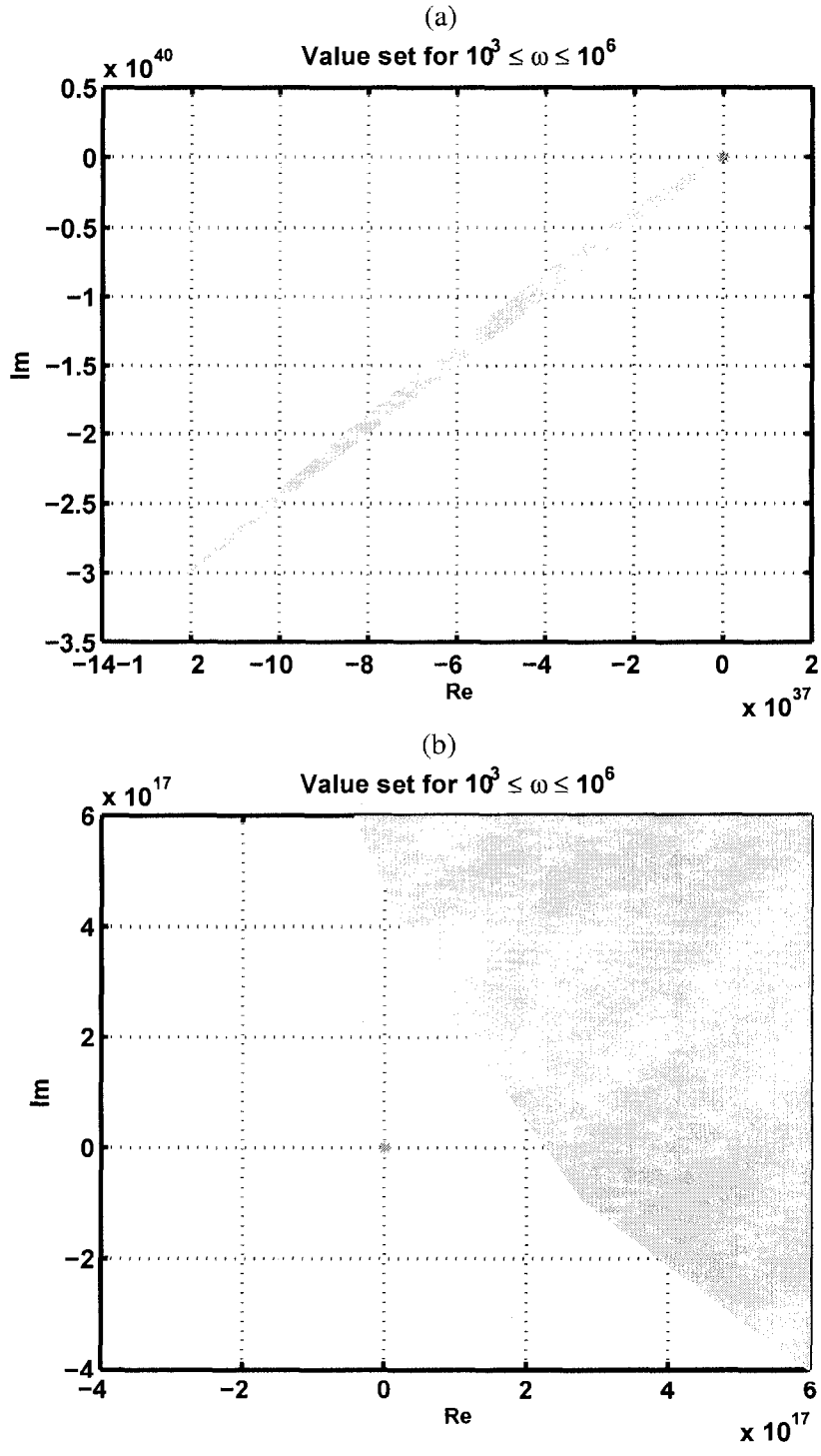

Figure 6.6: (a) Convex hull of the value set for $P(s,q)$ for $10^3 \leq \omega \leq 10^6$ rad/sec, (b) zoomed version

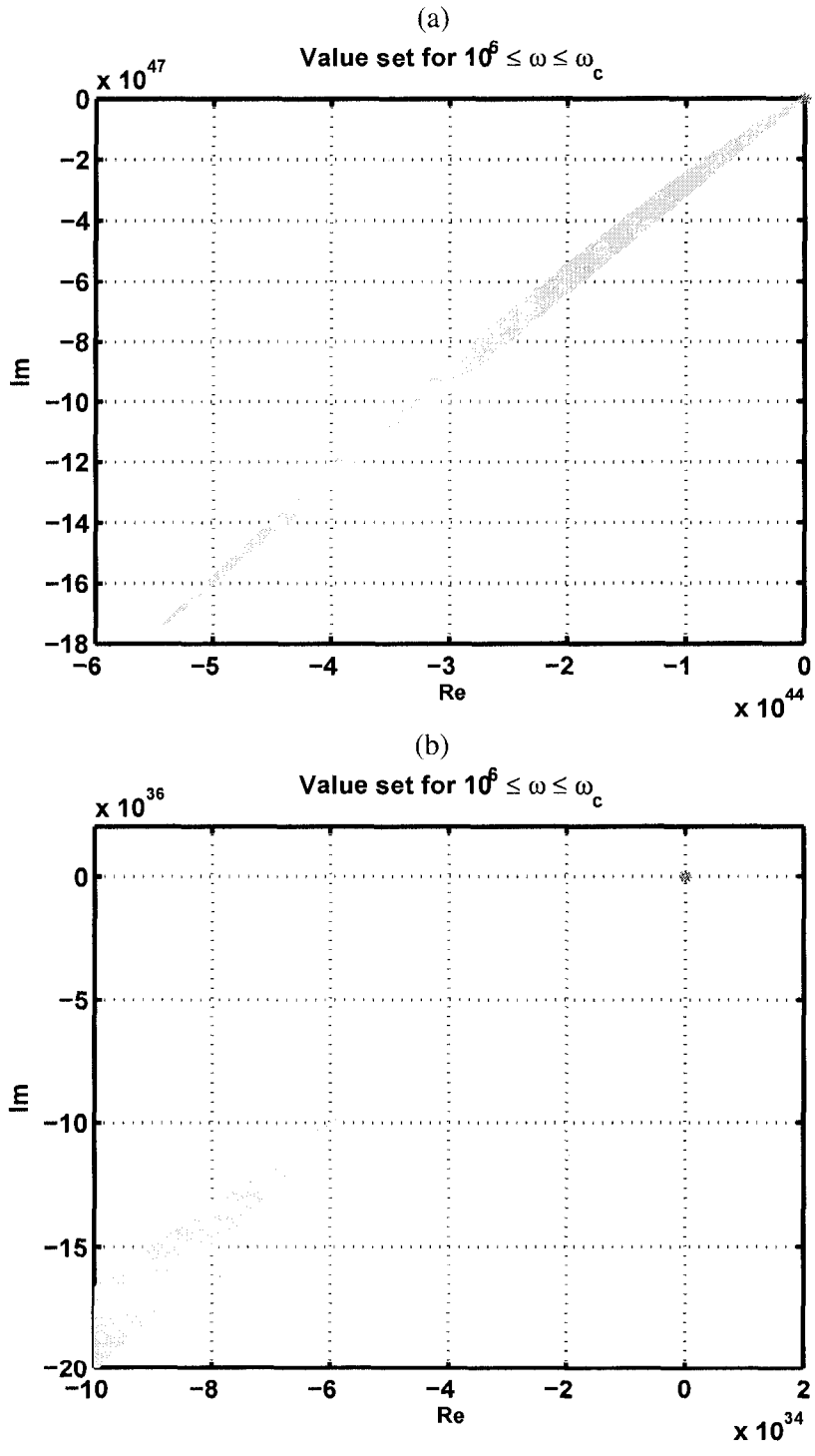

Figure 6.7: (a) Convex hull of the value set for $P(s, q)$ for $10^6 \leq \omega \leq \omega_c$, (b) zoomed version

maintaining the voltage magnitude at the PCC in the islanded mode, and (ii) robust with respect to uncertainties in the load parameters provided that the load uncertainties remain within set Q of (6.11). Moreover, the proposed control system provides a set of balanced three-phase voltages at the load terminals despite the asymmetry and the uncertainties of the load.

6.6.1 Transition from Grid-connected to Islanded Mode

In this section, transition from a grid-connected to an islanded mode is considered. Three case studies are considered. In the first case study, the system of Figure 6.1 is in a matched power condition, i.e. real and reactive power components of the RLC load are supplied by the DG unit. In the second case study, the whole system is under a balanced condition; however, there is real and reactive power mismatch between the DG unit and the local load. In the third case study, the local load is unbalanced at the time of islanding event.

Case1: Matched Power

The system of Figure 6.1 initially operates in a grid-connected mode in which real and reactive power components of the RLC load are supplied by the DG unit. The whole system is in a balanced condition. The load and the DG parameters are set at their nominal values as given in Table 5.1. The system is islanded at t=0.940 s by opening switch S of Figure 6.1, and the event is detected at t=1.000 s. The control strategy is changed from the grid-connected strategy, i.e. the conventional dq-current controller [1] to the proposed abc-frame controller of Figure 6.2, at t=1.000 s. Figure 6.8 shows the dynamic response of the system prior, during and subsequent to the islanding event.

Figure 6.8(a) shows the instantaneous voltages of the load at the PCC. Figure 6.8(a) shows that the proposed controller maintains the load voltage after the islanding event. Figures 6.8(b), (c) and (d) show the control signals, error signals and the load currents in response to the islanding event, respectively. Figure 6.8(c) indicates that the error signals approach zero within a transient time of three cycles of 60 Hz. It should be noted that since the system is in a matched power condition, both the load voltages and control signals do not undergo significant transients due to transition from the grid-connected mode to the islanded mode and change of controllers. Figures 6.8(e) to (g) show instantaneous real and reactive power components of the converter, load, and the grid

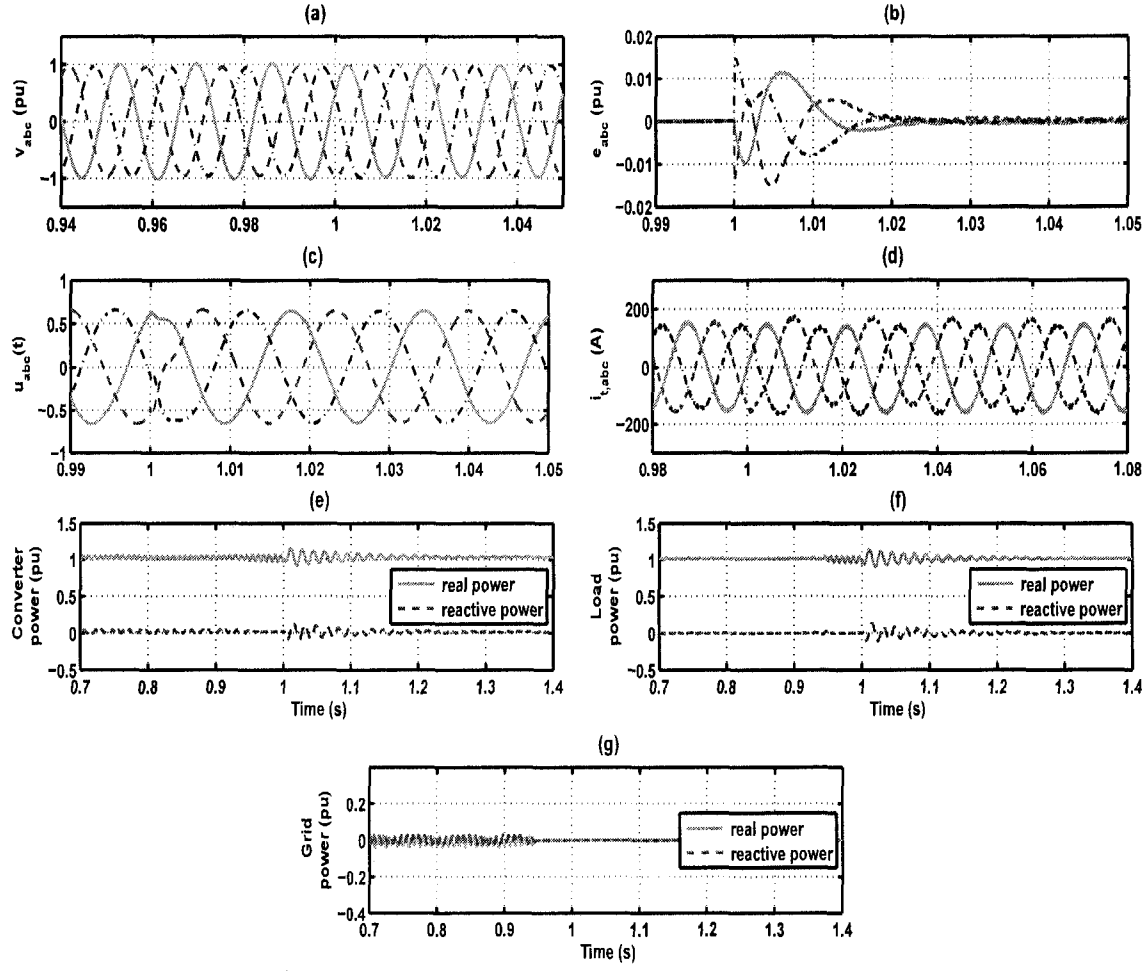

Figure 6.8: Dynamic response of the system of Figure 6.1 to a pre-planned islanding event (a) instantaneous voltages of the load, (b) error signals, (c) control signals, (d) load currents, and (e,f,g) real and reactive power components of the converter, load, and the grid

prior and subsequent to the islanding instant. Figures 6.8(e) to (g) confirm that the system is in a matched power condition at the time of islanding event.

Magnitudes of sequence components of the load voltages and the system frequency are estimated by the UTSP system. Figures 6.9(a) and (b) show the estimated magnitudes of positive- and negative-sequence components of the PCC voltages. Figures 6.9(a) and (b) verify that the proposed controller regulates magnitudes of the load voltages at 1 pu and provides a set of balanced three-phase voltages at PCC. The estimated system frequency is shown in Figure 6.9(c) which undergoes a small transient subsequent to the islanding event.

As discussed in Chapter 5, Section 5.3.3, to guarantee robust stability and desirable perfor-

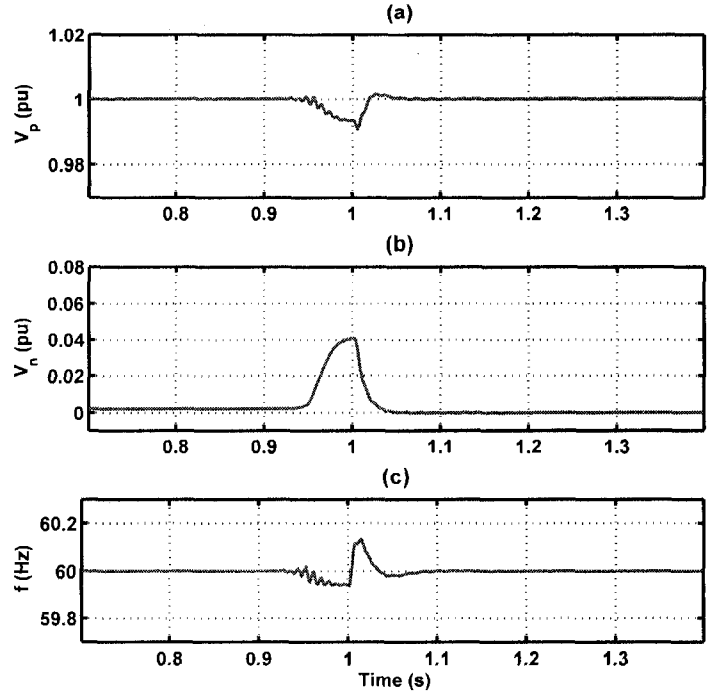

Figure 6.9: UTSP output signals to a pre-planned islanding event (a,b) estimated magnitudes of positive-, and negative-sequence components of PCC voltages, and (c) estimated frequency

mance of the islanded system, transition from the grid-connected mode to the islanded mode must be done smoothly. In other words, control signals generated by the abc-frame controllers should be equal to those of the grid-connected controllers at the islanding detection instant. This requires that phase-angles of the abc-frame controllers and the dq-frame current controller match when the proposed abc-frame controller is activated and the dq-frame current controller disabled. This can be achieved by using the instantaneous control signals of the dq-frame current controller, at the control transfer instant, as the initial conditions for the proposed abc-frame controller. Lack of smooth transition can result in a long period of transients or even instability of the island.

Case 2: Mismatched Power

The system of Figure 6.1 initially operates in a grid-connected mode and under a balanced condition. The grid absorbs 1.4 MW (0.56 pu) real power from the converter and 750 kVAr (0.3 pu) reactive power from the load. The DG unit delivers real power to the system at unity power factor. The load parameters of Figure 6.1 are set at $R = 176\ \Omega$, $L = 111.9\ mH$, $R_l = 0.35\ \Omega$, and

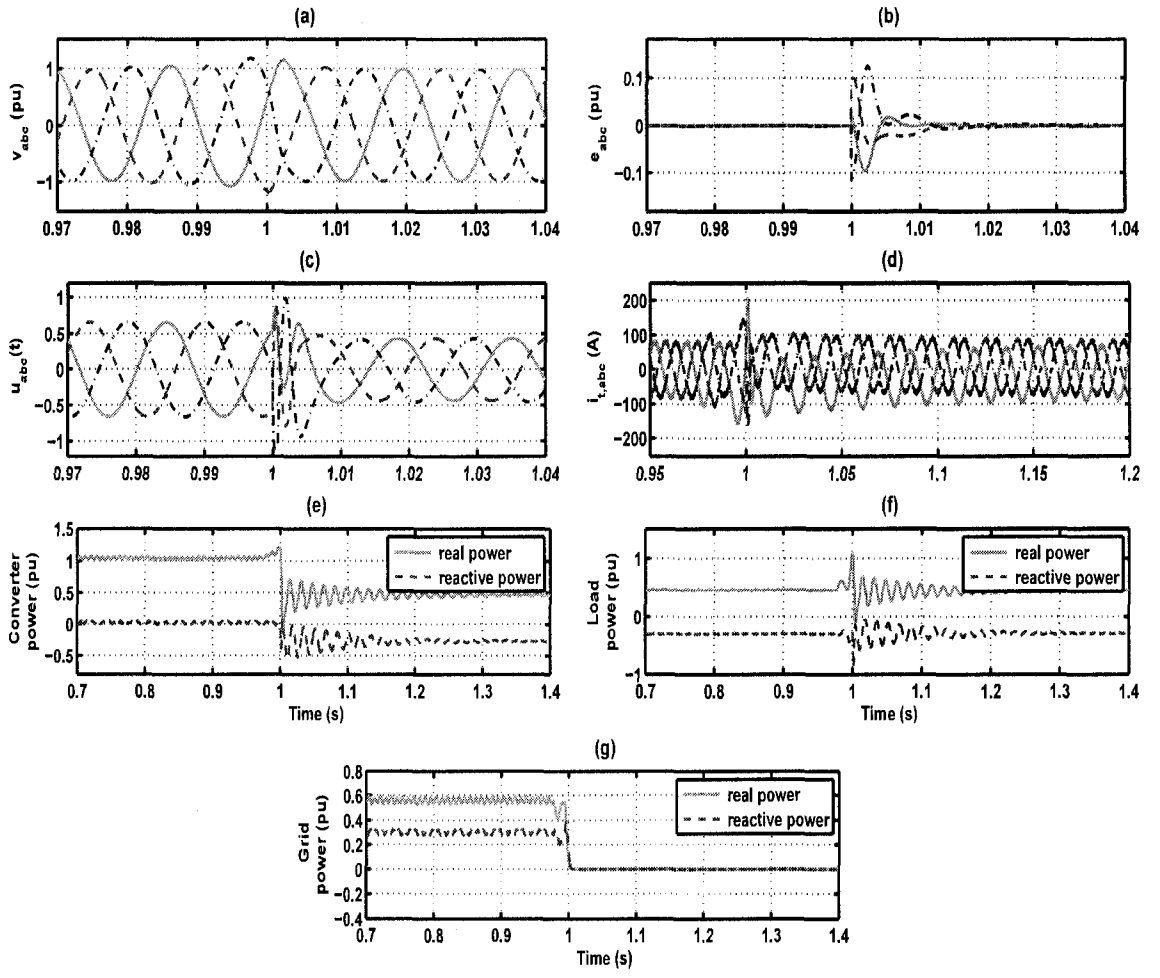

Figure 6.10: Dynamic response of the system of Figure 6.1 to an accidental islanding event (a) instantaneous voltages of the load, (b) error signals, (c) control signals, (d) load currents, and (e,f,g) real and reactive power components of the converter, load, and the grid

$C = 72.86\ \mu F$. An accidental islanding event occurs at t=0.975 s and is detected by the UTSP system at t=1.000 s. The islanding detection time (run-on time) is shorter than the matched power case, since power components of the DG unit and the RLC load are not matched prior to the islanding instant and therefore the voltage magnitude at PCC and/or the islanded system frequency rapidly deviate from their acceptable limits.

Dynamic response of the system of Figure 6.1 to the islanding event is shown in Figure 6.10. Instantaneous voltages of the load at the PCC and the error signals are shown in Figure 6.10(a) and (b), respectively. It is observed that the load voltages are regulated at the desired reference signals by the proposed abc-frame controller, and the error signals approach zero in less than two cycles.

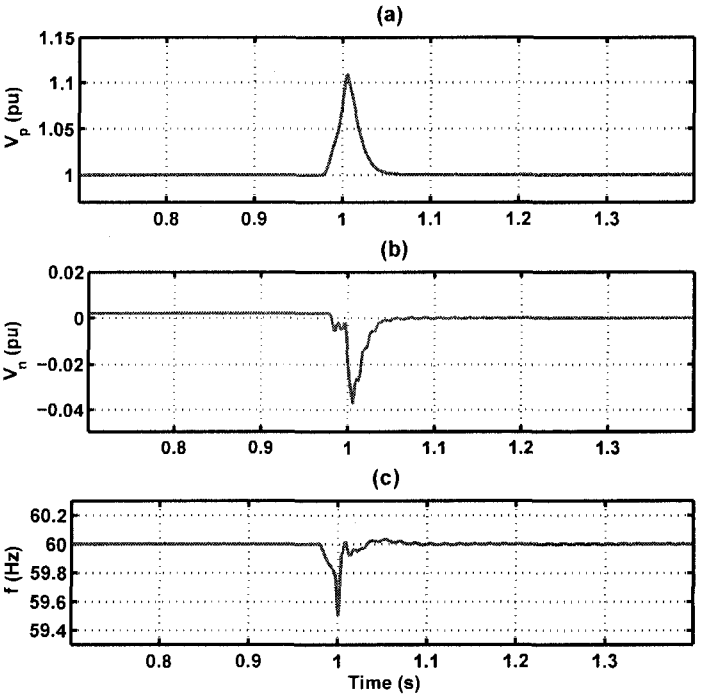

Figure 6.11: UTSP output signals to an accidental islanding event (a,b) estimated magnitudes of positive-, and negative-sequence components of PCC voltages, and (c) estimated frequency

The voltage transients are as a result of a power mismatch condition prior to the islanding event. The control signals, which undergoes a transient of about one cycle, are shown in Figure 6.10(c). Figure 6.10(d) shows the load currents in response to the islanding event. The long transient response observed in the current signals results from the large quality factor of the load, that is $Q = R\sqrt{\frac{C}{L}} = 4.5$. Figures 6.10(e), (f), and (g) show the variations of real and reactive power components of the converter, load, and the grid, respectively.

The UTSP output signals are illustrated in Figure 6.11. Figure 6.11(a) and (b) show the estimated magnitudes of positive- and negative-sequence components of the PCC voltages. Figure 6.11(b) confirms that load voltages are balanced after the islanding event. The estimated system frequency is shown in Figure 6.11(c) which undergoes a short transient subsequent to the islanding event.

Table 6.1: Unbalanced Load Parameters

	$R(\Omega)$	$L(mH)$	$C(\mu F)$	$R_l(\Omega)$
Phase-a	96	111.9	62.86	0.35
Phase-b	876	111.9	72.86	0.35
Phase-c	1576	211.9	42.86	0.35

Case 3: Unbalanced Load

In this case study, the local load is unbalanced prior and subsequent to the islanding event. Each phase of the load is a parallel RLC network and its parameters are summarized in Table 6.1. An islanding event occurs at t=0.980 s and the proposed islanding detection method of Chapter 4 detects the event at t=1.000 s. Upon islanding detection, the control strategy is changed from the dq-current controller to the proposed abc-frame controller at t=1.000 s. The simulation results of this case study are shown in Figures 6.12 and 6.13.

Instantaneous voltages of the load and the error signals are depicted in Figures 6.12(a) and (b), respectively. The error signals are set to zero by the proposed abc-frame controller within two cycles after the islanding event. This implies that the proposed abc-frame controller regulates the load voltages at the reference signals. Control signals and the load currents are shown in Figures 6.12(c) and (d), respectively. Since the load is unbalanced and the proposed controller provides a set of balanced three-phase voltages, the load currents and consequently the control signals are unbalanced. It should be noted that the control signals are balanced prior to the islanding event, since the VSC operates under a balanced condition.

Figures 6.12(e) to (g) show instantaneous active and reactive power components of the converter, load, and the grid prior and subsequent to the islanding instant. In the grid-connected mode, real and reactive power components of the load and grid exhibit a 120 Hz ripple component, since both the load and grid currents are unbalanced. Based on the instantaneous real and reactive power concepts [69], if a set of three-phase voltages and/or currents are unbalanced, instantaneous real/reactive power components are not constant values and contain double frequency ripple components. It should be noted that since the islanded system operates under an unbalanced condition, real and reactive power components of both the load and the VSC exhibit double frequency ripples.

Figure 6.13 shows the magnitudes of the sequence components of the PCC voltages and the system frequency which are extracted by the UTSP. Figure 6.13(b) indicates that the proposed

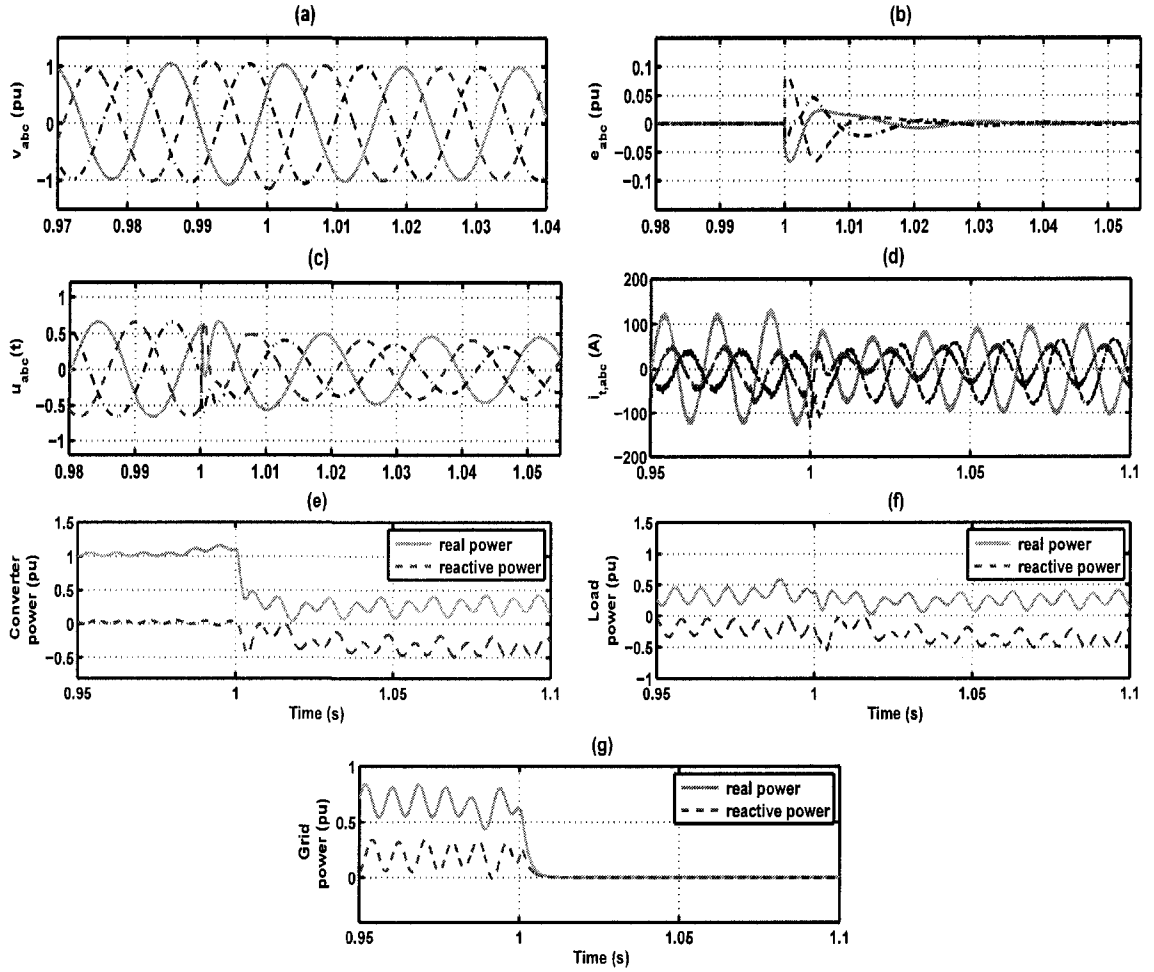

Figure 6.12: Dynamic response of the system of Figure 6.1 to an islanding event when the load is unbalanced at the islanding instant (a) instantaneous voltages of the load, (b) error signals, (c) control signals, (d) load currents, and (e,f,g) real and reactive power components of the converter, load, and the grid

abc-frame controller balances the load voltages despite asymmetry of the three-phase load after the islanding event. The estimated system frequency is shown in Figure 6.13(c) and experiences a short transient subsequent to the islanding event. However, the frequency transient is well within the acceptable limits [80], and also indicates no steady-state error.

6.6.2 Islanded Mode

This section verifies robust stability and performance of the proposed abc-frame controller with respect to the load parameter uncertainties in an islanded mode. Moreover, performance of the

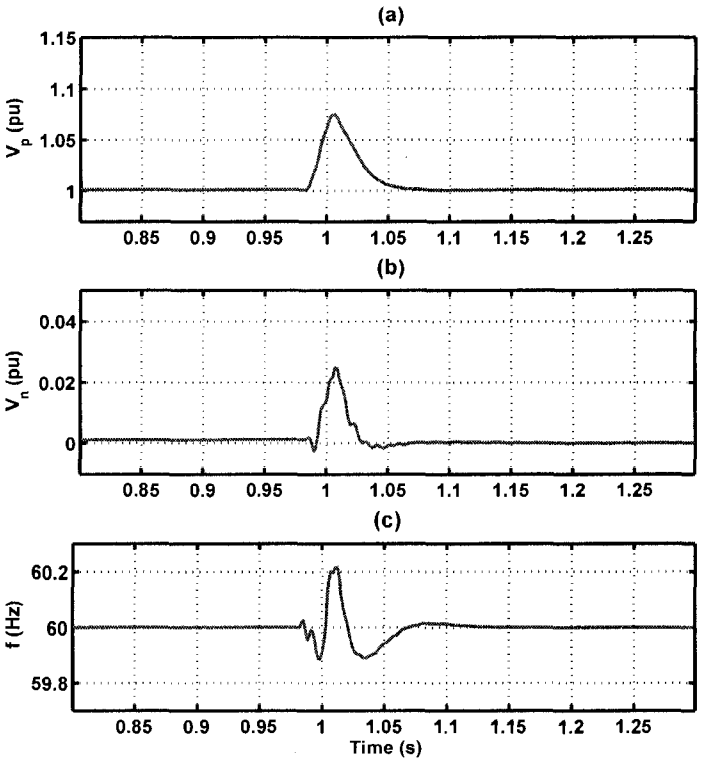

Figure 6.13: UTSP output signals when the load is unbalanced at the islanding instant (a,b) estimated magnitudes of positive-, and negative-sequence components of PCC voltages, and (c) estimated frequency

designed abc-frame controller, in terms of reference signal tracking, is also presented.

Case 1: Change in Load Parameters

Robust stability of the proposed control system with respect to the load parameter uncertainties is verified in this case study. The islanded system is initially operating under a balanced condition, i.e., the three-phase load is balanced. The load parameters and configuration are shown in Figure 6.14. Prior to t=1.500 s, switches S_{a1}, S_{b1}, and S_{c1} are open and S_{a2}, S_{b2}, and S_{c2} are closed, Figure 6.14. Three load changes at three different instants are imposed. The first load change is imposed by closing switch S_{a1} and opening switches S_{a2} and S_{b2} at t=1.500 s. Thus, the resistance of phase-*a* of the load is halved and the resistance of phase-*b* of the load is almost fully disconnected. The results obtained from this study are demonstrated in Figure 6.15.

The load voltages and error signals are shown in Figures 6.15(a) and (b), respectively. Control signals and the load currents are shown in Figures 6.15(c) and (d), respectively. The switching

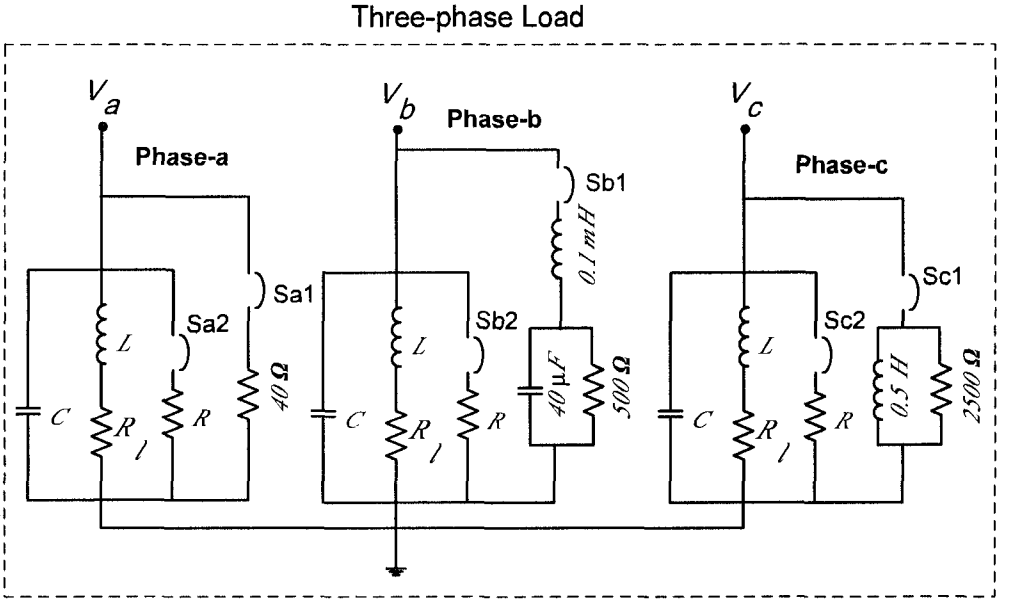

Figure 6.14: Three-phase load: $R = 76\Omega$, $L = 111.9\ mH$, $C = 62.86\mu F$, and $R_l = 0.35\Omega$

events result in unbalanced load currents and control signals. Figure 6.15(e) and (f) show the estimated magnitudes of positive- and negative-sequence components of the load voltages, respectively. Figure 6.15(f) verifies that the load voltages are balanced despite asymmetry of the load. Moreover, the proposed abc-frame controller is robust with respect to changes in the load parameters. The estimated system frequency is shown in Figure 6.15(g). The system frequency exhibits a transient resulting from the load changes.

The second load change occurs at t=2.000 s when switch S_{b1} is closed, and results in a capacitive load with 500Ω resistance at phase-*b* of the load. Figure 6.16 show the instantaneous load voltages, error and control signals, the load currents, estimated sequence components of the load voltages, and the system frequency. The results of this simulation also indicates that the control system is capable of balancing the load voltages and maintaining its magnitude and the frequency with no steady-state error.

The last change in load configuration is imposed at t=2.400 s by opening switch S_{c2} and closing S_{c1}. This change results in a highly inductive load at phase-*c*. The resistance of phase-*c* of the load is 2500Ω which is more than 30 times of its rated value. Figure 6.17 shows the dynamic response of the islanded system to this change in the load parameters. Similar to the previous cases, the control system provides a set of balanced voltages for the load.

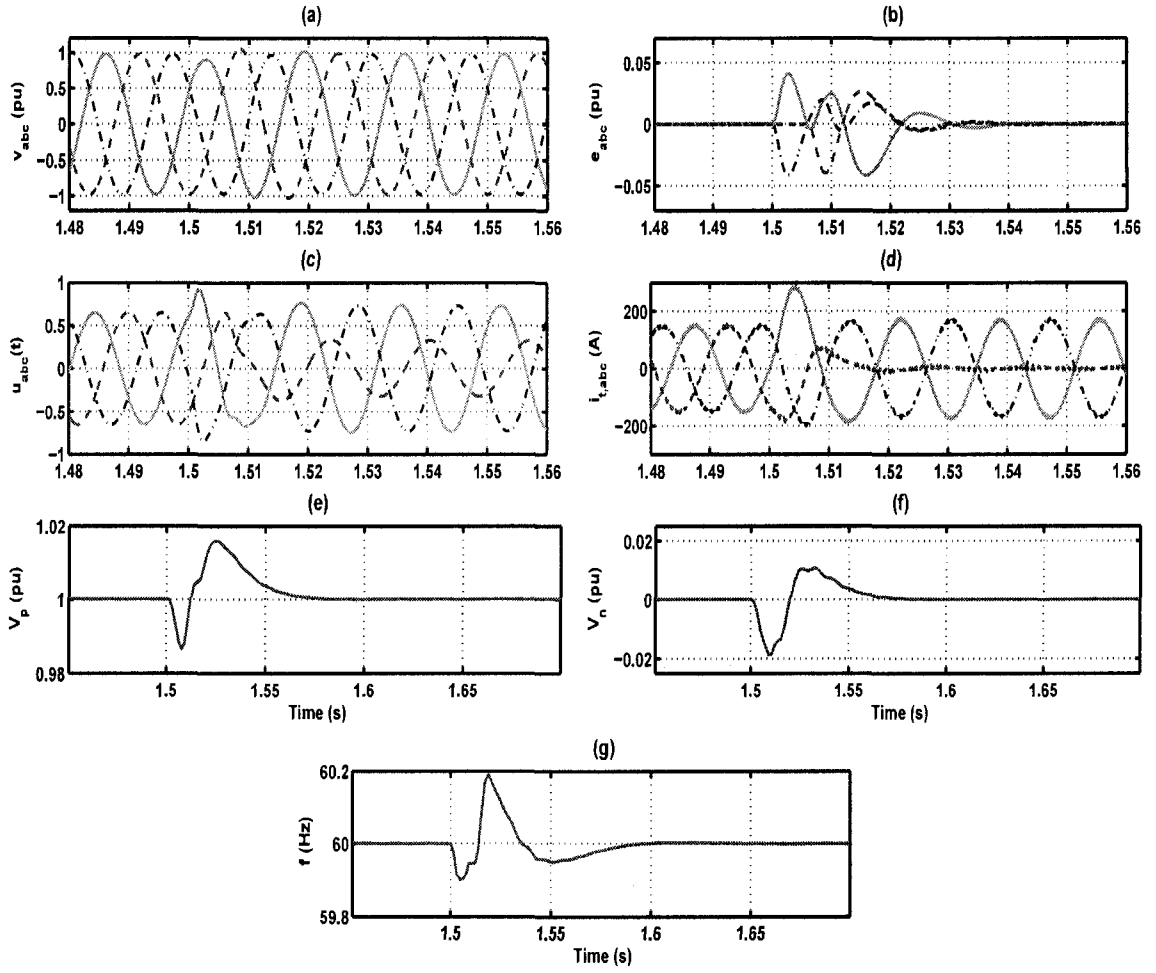

Figure 6.15: Performance of the islanded system to a change in load parameters (changes in phase-*a* and phase-*b*) (a) instantaneous voltages of the load, (b) error signals, (c) control signals, (d) load currents, (e,f) estimated magnitudes of positive-, and negative-sequence components of PCC voltages, and (g) estimated frequency

Case 2: Voltage Tracking

In this case study, the performance of the islanded system controller, in terms of reference signal tracking, is evaluated. While the system is operating in an islanded mode, the magnitude of the reference signal steps up/down to a pre-specified value. The load configuration for this case study is depicted in Figure 6.14, where switches S_{a1}, S_{b1}, and S_{c1} are closed and switches S_{a2}, S_{b2}, and S_{c2} are open.

Magnitudes of the reference signals step up from 1.0 pu to 1.1 pu at t=3.000 s and step down from 1.1 pu to 0.8 pu at t=3.300 s. Figures 6.18 and 6.19 show the simulation results obtained from

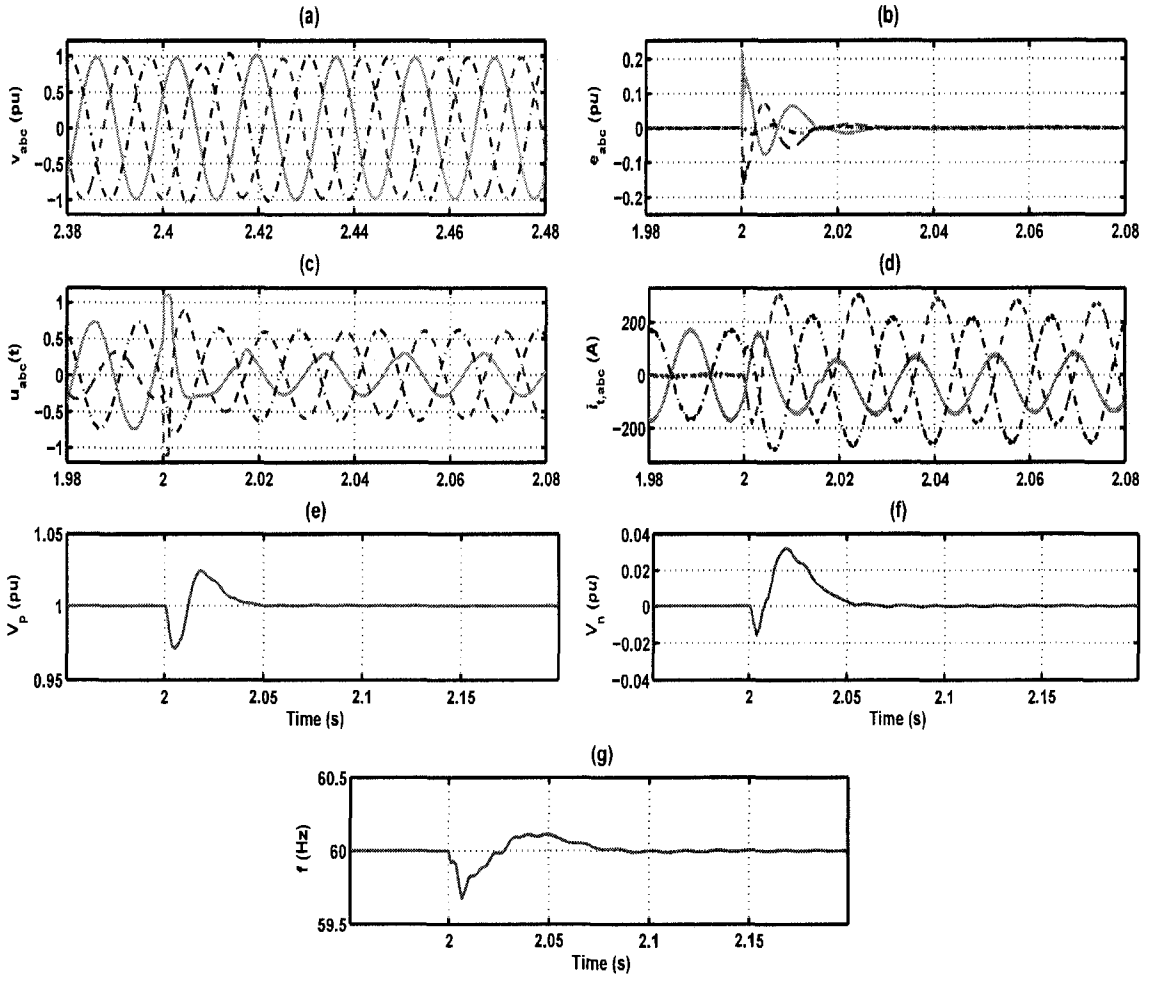

Figure 6.16: Performance of the islanded system to a change in load parameters (change in phase-*b*) (a) instantaneous voltages of the load, (b) error signals, (c) control signals, (d) load currents, (e,f) estimated magnitudes of positive-, and negative-sequence components of PCC voltages, and (g) estimated frequency

this study. It is observed that asymptotic tracking and regulation occur for both step changes in magnitude of the reference signals. Zero steady-state errors are observed in magnitude of sequence components of the load voltages and the system frequency.

6.7 Conclusions

A dynamic model and a control strategy for autonomous operation of an electronically-coupled DG unit and its local load subsequent to islanding from a utility power grid, are presented in

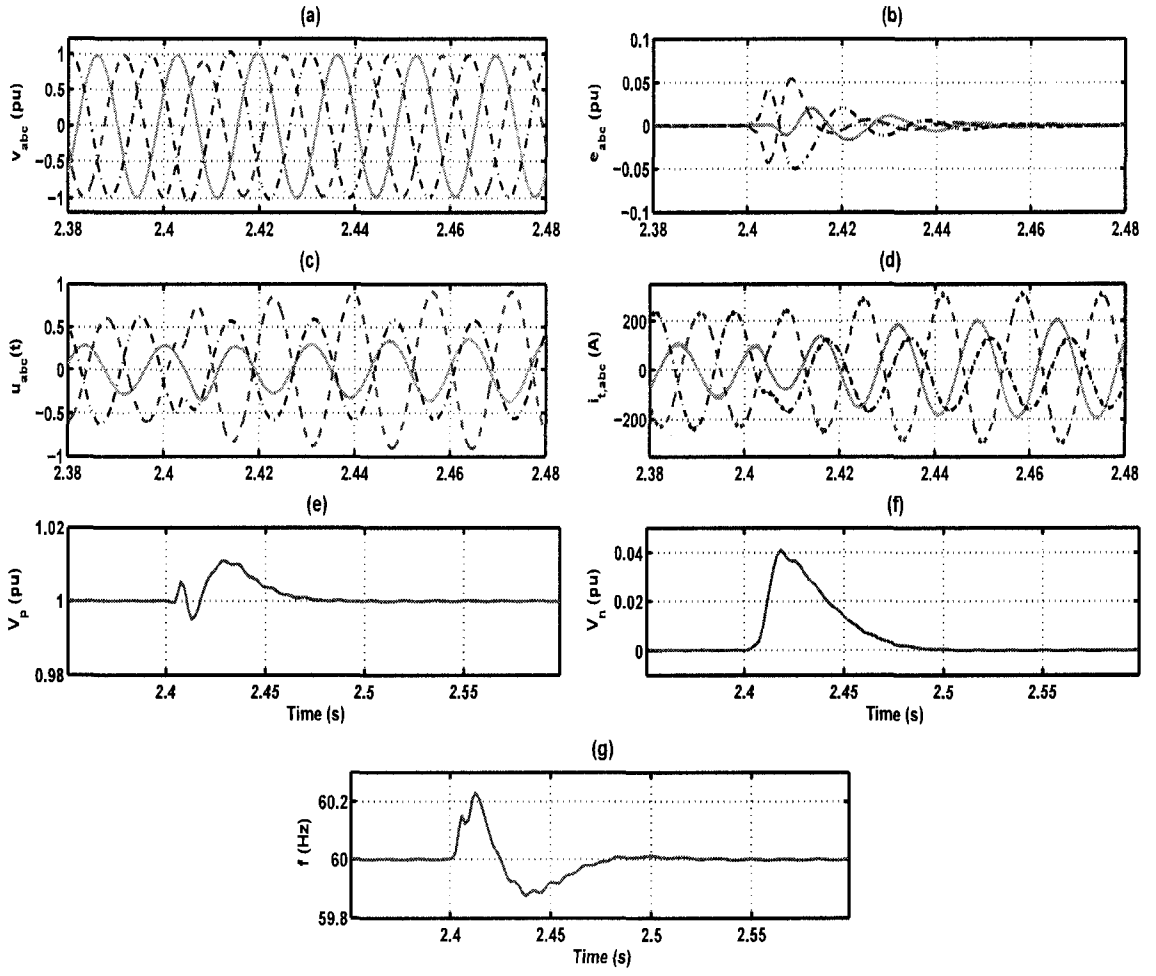

Figure 6.17: Performance of the islanded system to a change in load parameters (change in phase-c) (a) instantaneous voltages of the load, (b) error signals, (c) control signals, (d) load currents, (e,f) estimated magnitudes of positive-, and negative-sequence components of PCC voltages, and (g) estimated frequency

this chapter. In most practical situations, the local load is unbalanced and therefore the islanded system can be unbalanced. A mathematical model representation of an unbalanced system in a dq-frame coordination is a highly nonlinear MIMO system. Controller synthesis and robust analysis of a nonlinear MIMO system is a very demanding task. Therefore, the dynamic model proposed in this chapter is based on a transfer function representation of the DG unit and the load in an abc-frame. The classical control approach is adopted to design a robust controller for the VSC of the DG unit. In the grid-connected mode, based on the conventional dq-current control strategy, the VSC controls real- and reactive-power components of the DG unit. Subsequent to

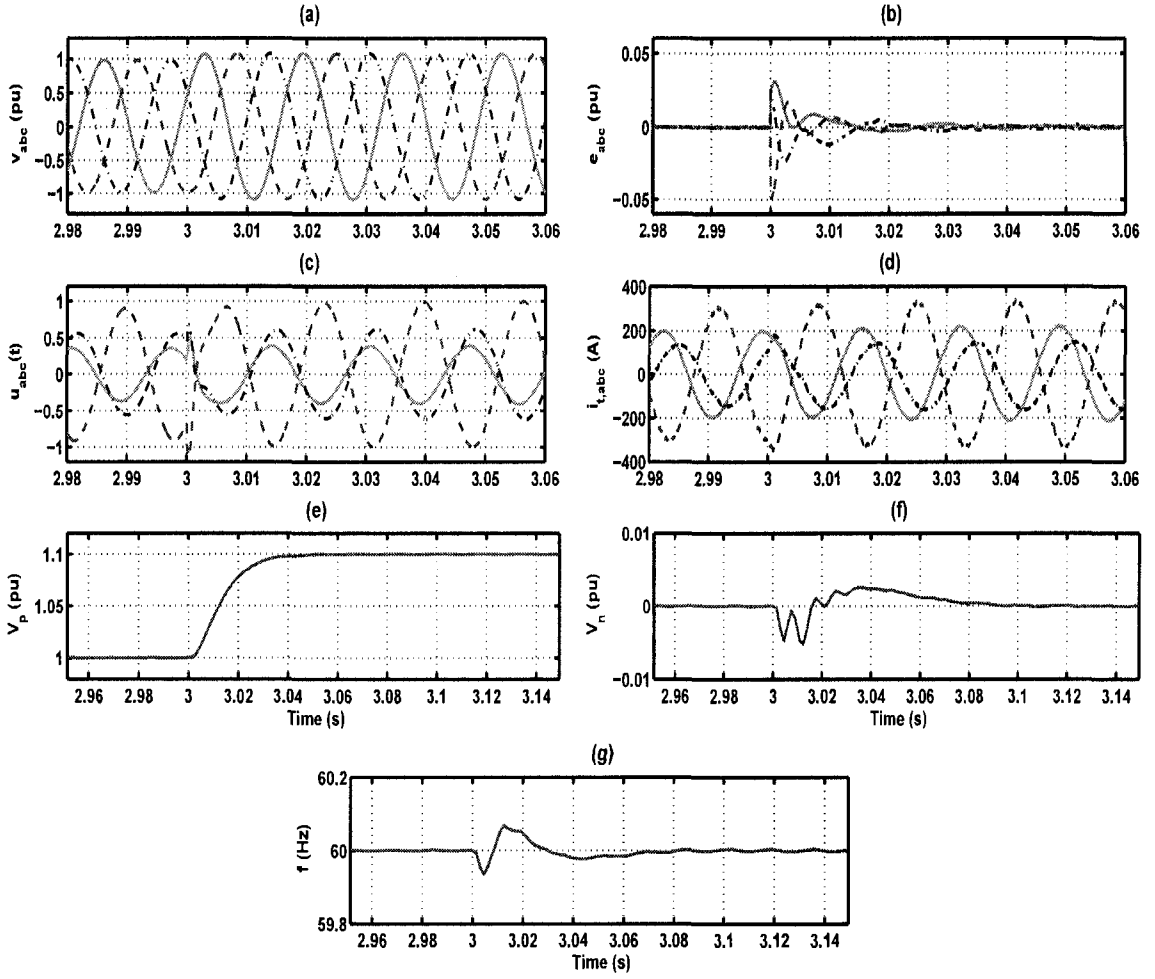

Figure 6.18: Dynamic performance of the islanded system to the reference signal tracking (step-up) (a) instantaneous voltages of the load, (b) error signals, (c) control signals, (d) load currents, (e,f) estimated magnitudes of positive-, and negative-sequence components of PCC voltages, and (g) estimated frequency

an islanding detection and confirmation, the dq-current controller is disabled and the proposed abc-frame controller activated. To provide seamless transition from the grid-connected mode to the islanded mode, the proposed islanding detection method of Chapter 4 is used in this chapter.

The proposed controller uses an internal oscillator to control the frequency, and a voltage feedback signal for each phase to regulate the island voltage. Robust stability analysis of the resultant closed-loop system is carried out, using the Mapping Theorem and the Zero Exclusion

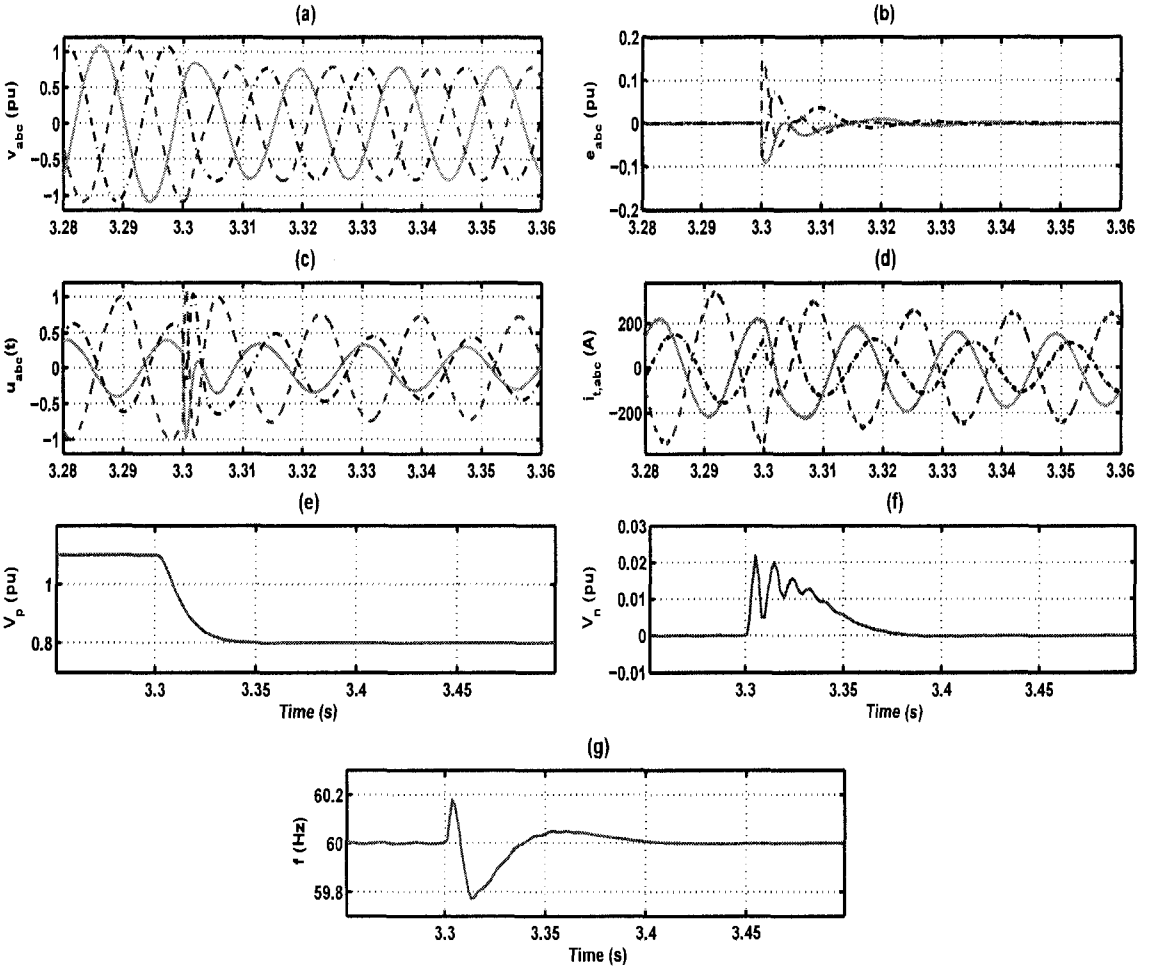

Figure 6.19: Dynamic performance of the islanded system to the reference signal tracking (step-down) (a) instantaneous voltages of the load, (b) error signals, (c) control signals, (d) load currents, (e,f) estimated magnitudes of positive-, and negative-sequence components of PCC voltages, and (g) estimated frequency

Condition, to obtain the following conservative robustness margin (Q):

$$Q = \begin{cases} 50\ \Omega \le R_x \le 2000\ \Omega \\ 40\ mH \le L_x \le 400\ mH \\ 10\ \mu F \le C_x \le 80\ \mu F \end{cases} \quad \text{or} \quad \begin{cases} 0.66\ pu \le R_x \le 26.26\ pu \\ 0.2\ pu \le L_x \le 1.98\ pu \\ 0.29\ pu \le C_x \le 2.3\ pu, \end{cases} \tag{6.17}$$

The proposed controller guarantees robust stability and desired performance, e.g. fast transient response and zero steady-state error, for all uncertainties in the load parameters within the above robustness margin Q.

Performance of the proposed controller under (i) accidental and planned islanding events, (ii) uncertainties in the load parameters, (iii) step changes in the control command, and (iv) unbalanced load conditions are reported. The studies are carried out based on time-domain simulations in the PSCAD/EMTDC software environment. The simulation results conclude that the proposed controller regulates voltage magnitude and frequency of the islanded system in less than three cycles of transients, subsequent to islanding events and/or any load change within the robustness margin Q of (6.17).

Chapter 7

Conclusions

7.1 Conclusions

This thesis presents an active islanding detection method and a control strategy for autonomous (islanded) operation of an electronically-coupled DG unit. The main features of the proposed islanding detection method, and the control strategy are as follows.

7.1.1 Islanding Detection Method

The study results conclude that the proposed islanding detection method:

1. detects an islanding event within 60 ms (3.5 cycles) under UL1741 test conditions,
2. is highly immune to noise and accurately performs islanding detection task even when the PCC voltage is polluted with a Gaussian White Noise of SNR=30 dB, which is a typical value for a relatively highly polluted power system environment [78],
3. requires at least 2 to 3% negative-sequence current injection for islanding detection,
4. can correctly detect an islanding event for a grid short-circuit ratio as low as 2,
5. is insensitive to variations of the load parameters even under UL1741 test conditions.

The Unified Three-phase Signal Processor (UTSP) system introduced in Chapter 2 is used as the main signal processing building block of the proposed islanding detection method. Based

on the studies carried out in Chapter 3, the main features of the UTSP system are (i) structural robustness, (ii) extraction of sequence components, (iii) amplitude and frequency tracking, (iv) noise immunity, and (v) insensitivity to harmonics.

7.1.2 Control Strategies

Depending on the islanded system conditions, two types of control strategies to provide autonomous operation for the island are proposed. The first one is intended for balanced load conditions, and the second one is for unbalanced load conditions.

1. *Balanced Load Conditions*

In Chapter 5, the rotating reference frame (dq-frame) is employed to obtain a state-space model for the islanded system, i.e. the DG unit and its load. Two dynamic models, and corresponding to each model a controller, are presented. In the first model, the phase-angle of the PCC voltage is used as the reference phase-angle for the dq-frame transformation. In this case, the model represents a MISO nonlinear system. However, by assuming that the island frequency is (almost) constant, the MISO nonlinear system is simplified to a SISO LTI system. Then, the classical control approach is adopted to design a structurally simple (second-order) SISO controller for the island. Performance of the proposed SISO controller under (i) accidental and planned islanding events, (ii) small perturbations in the load parameters, (iii) step changes in the set point signal, and (iv) unbalanced load conditions are reported. The studies are carried out based on time-domain simulations in the PSCAD/EMTDC software environment. The simulation results verify effectiveness of the proposed controller in terms of maintaining voltage, frequency and stability of the islanded system during and subsequent to an islanding event. The results show that the proposed SISO controller regulates the island voltage within three cycles of transients even in the worst case scenario, e.g. accidental islanding event. The SISO controller is most appropriate for applications in which the local load is fairly fixed and pre-determined.

In the second modelling approach, the phase-angle of the VSC internal oscillator is used as a reference to obtain an exact model for the islanded system in the dq-frame, and the developed model represents a MIMO LTI system with structured uncertainties. A robust servomechanism approach is adopted to design a 12^{th}-order controller for the interface converter of the DG unit.

The proposed MIMO controller guarantees robust stability and the desired performance indices, e.g. fast transient response and zero steady-state error, despite uncertainties in the load parameters. Performance of the proposed MIMO controller under (i) step changes in the set point signals, (ii) uncertainties in the load parameters, and (iii) unmodelled uncertainties (e.g. motor start-up process) are investigated and reported. The studies are carried out based on time-domain simulations in the MATLAB/SimPowerSystems software environment. The simulation results verify the effectiveness of the proposed controller in terms of maintaining voltage, frequency and robust stability of the islanded system. The proposed robust servomechanism controller robustly regulates the load voltage after a transient period of less than three cycles despite significant changes in the load parameters, e.g. sudden change in the load resistance from its rated value 76 Ω to 10 $k\Omega$ (almost no-load).

2. *Unbalanced Load Conditions*

In Chapter 6, the abc-frame is used to obtain a dynamic model for an islanded DG unit whose load can be unbalanced. Based on the dynamic model and using the classical control approach, a control strategy is designed to regulate voltage magnitude, and to provide a set of balanced voltages at PCC. Robust stability analysis of the closed-loop system is carried out using the Mapping Theorem and the Zero Exclusion Condition. A robustness margin for the load parameters is then obtained. The proposed controller guarantees robust stability and desired performance indices, e.g. fast transient response and zero steady-state error, for all uncertainties in the load parameters within the robustness margin. Performance of the proposed controller under (i) accidental and planned islanding events, (ii) uncertainties in the load parameters, (iii) step changes in the set point signal, and (iv) unbalanced load conditions are reported. The studies are carried out based on time-domain simulations in the PSCAD/EMTDC software environment. The simulation results verify the effectiveness of the proposed controller in terms of maintaining voltage magnitude and frequency of the island, and providing a set of balanced voltages for the load during and subsequent to the islanding events. The studies demonstrate that the proposed controller is capable of maintaining voltage magnitude and frequency of the island in less than three cycles of transients, under both balanced and unbalanced load conditions and despite all uncertainties in the load parameters within the obtained robustness margin.

7.2 Contributions

The main contributions of this thesis are as follows.

1. A new active islanding detection method for an electronically-coupled DG unit, based on negative-sequence current injection, is proposed. The proposed scheme (i) is faster than the existing methods, (ii) has no NDZ, and (iii) is robust to perturbations in the load parameters.

2. A new robust servomechanism controller for autonomous operation of an electronically-interfaced DG unit, under balanced conditions, is proposed. The proposed controller guarantees robust stability, fast transient response, and zero steady-state error, despite uncertainties in the load parameters.

3. A control strategy to provide autonomous operation for an islanded single DG system, under unbalanced load conditions, is proposed. A mathematical model for the islanded system in an abc-frame is derived, and based on the model, a robust controller is designed. Robust stability of the resultant closed-loop system, based on the Mapping Theorem and the Zero Exclusion Condition, is analyzed.

7.3 Future Work

The following topics are suggested for future research in continuation of this work:

- Evaluation of the proposed islanding detection method for a microgrid that includes multiple DG units.

- Development of a robust control strategy for autonomous operation of an islanded microgrid that includes multiple DG units.

Appendices

Appendix A

Experimental Results

A.1 Introduction

This appendix presents several experimental results that validate performance of the unified three-phase signal processor (UTSP) system of Chapter 2, the proposed islanding detection method of Chapter 4, and the control systems proposed in Chapter 5 and Chapter 6. To implement the UTSP and the control systems, a Real Time (RT)-Linux based controller, which provides a C programming environment, is used. Any control and/or signal processing algorithm is first discretized and then developed into the C codes. The RT-Linux system runs the C programming codes for real time realization of the proposed algorithms. It should be noted that, as part of the controllers, the internal oscillator is digitally implemented in the RT-Linux system.

A.2 Experimental Setup

Figure A.1 shows a single-line diagram of the test system in which the distributed generation (DG) unit includes a DC voltage generator (V_{dc}), a voltage sourced-converter (VSC) unit, and a series filter. The VSC filter is represented by inductor L_t for each phase. The load at the PCC is a parallel RLC, tuned at resonance frequency of 60 ± 0.1 Hz. At 60 Hz, the local load appears as a pure resistance, R, which is adjusted to absorb the rated power of the DG unit at the rated PCC voltage. The study system parameters are given in Table A.1.

Data acquisition is carried out by the Yokogawa PZ4000 Power Analyzer [108]. The fea-

Table A.1: Parameters of the system of Figure A.1

Quantity	Value	P.U.	Comment
L_t	3 mH	0.21 pu	Inductance of VSC filter
VSC rated power	2.4 kW	1 pu	S_{base} = 2.4 kVA
VSC terminal voltage (line-line)	115 V (rms)	1 pu	V_{base} = 115 V
f_{sw}	2-3 kHz		PWM carrier frequency
R	5.5 Ω	1 pu	Load nominal resistance
L	7.8 mH	0.53 pu	Load nominal inductance
C	900 μF	1.87 pu	Load nominal capacitance
$Q = R\sqrt{\frac{C}{L}}$	1.87		Load quality factor
$f_{res} = \frac{1}{2\pi\sqrt{LC}}$	60 Hz		Load resonant frequency
f_0	60 Hz		System nominal frequency
V_s (line-line)	115 V (rms)	1 pu	Grid nominal voltage
V_{dc}	230 V		DC bus voltage

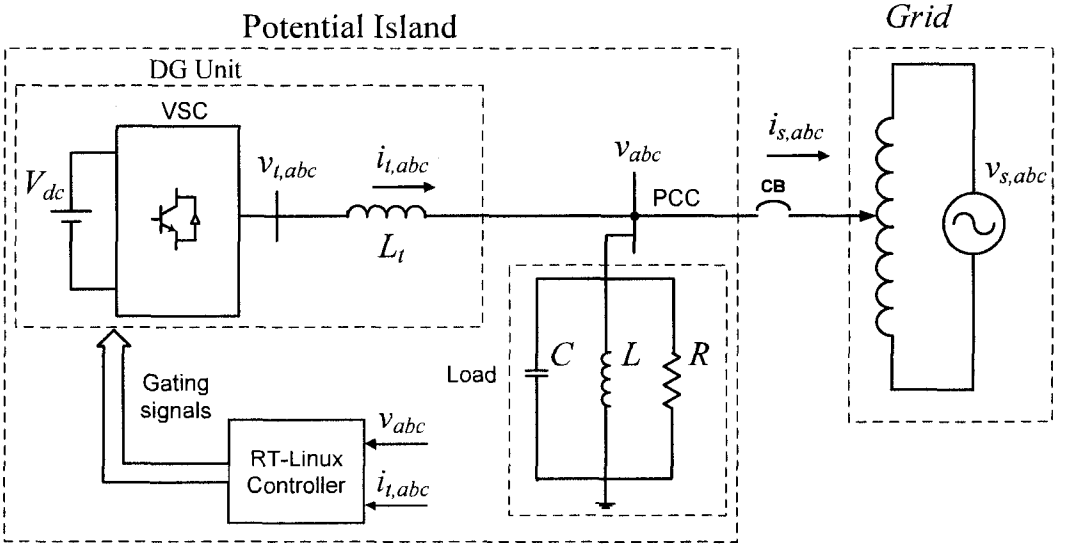

Figure A.1: Schematic diagram of the experimental setup

tures of Yokogawa PZ4000 Power Analyzer includes wide measurement bandwidth (from DC to 2 MHz), high accuracy for capturing input waveforms using high-speed (maximum 5 MS/s) sampling, voltage and current waveform display and analysis functions to enable power calculations on fluctuating inputs, harmonic analysis (up to 500^{th} order), and Fast Fourier Transform (FFT) functions to enable high-frequency power spectrum analysis. The Yokogawa PZ4000 Power Analyzer includes four input elements, each of which has a voltage and a current channel. The data stored on the PZ4000 is then transferred to a PC and plotted/displayed using MATLAB software.

A.3 Islanding Detection Method Based on UTSP System

The following tests experimentally validate the performance of the proposed islanding detection scheme of Chapter 4 and the UTSP system of Chapter 2.

A.3.1 Performance Under UL1741 Test Conditions

The operating point and parameters of the study system of Figure A.1 are adjusted based on the UL1741 test conditions [3]. Islanding detection is based on the PCC voltage signals as the input of the UTSP system. The system is islanded at time t=567.5 ms by opening switch CB, Figure A.1. Prior to the islanding event, the VSC system injects 1 pu fundamental positive-sequence and 0.05 pu negative-sequence current components based on a *dq*-frame current-control scheme.

Figures A.2(a), (b) and (c) show instantaneous PCC voltage, and positive- and negative-sequence voltage signals of PCC which are extracted by the UTSP, before and after the islanding instant. Figures A.2(d) and (e) show converter and grid currents signals, i.e. $i_{t,abc}$ and $i_{s,abc}$, respectively.

Figure A.3(a) shows the system frequency at PCC which is extracted by the UTSP. Figure A.3(a) indicates that frequency remains within the limit of 60 ± 0.3 Hz after islanding, and cannot be used for islanding detection within the presented time interval. Figures A.3(b) and (c) show magnitudes of positive- and negative-sequence PCC voltage signals. Figure A.3(c) clearly indicates that the islanding event is identified within 3.5 cycles (60 ms) while changes in the (i) instantaneous voltage of Figure A.2(a), and (ii) amplitude of positive-sequence voltage of Figure A.3(b) are not usable for islanding detection.

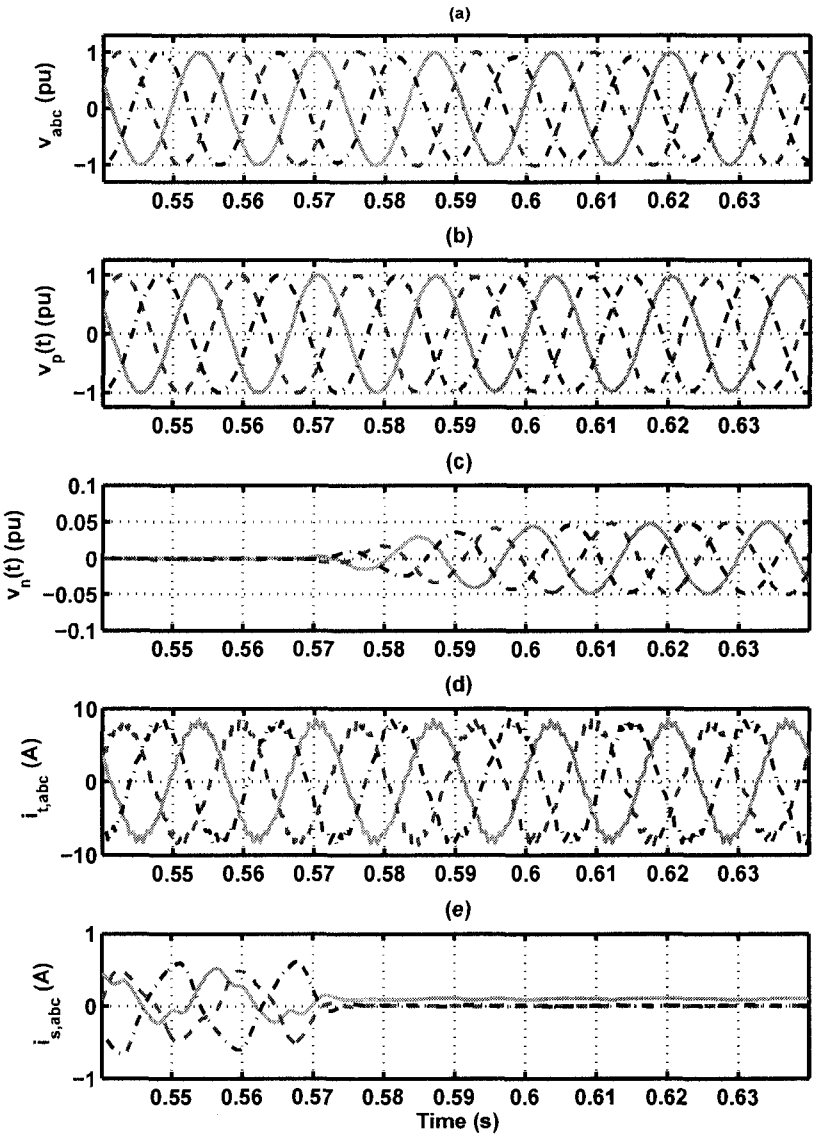

Figure A.2: UTSP and the test system signals under UL1741 test conditions (a) PCC voltages, (b,c) instantaneous positive-, and negative-sequence voltages at PCC, and (d,e) converter and grid currents

A.3.2 Sensitivity to Changes in Load Resistance

In this case study, while the load inductor and capacitor are kept constant at their rated values, the load resistance is changed to 95% and 115% of its rated value (5.5 Ω). The VSC injects almost 5% negative-sequence current. Figure A.4 shows the UTSP output signals when the load resistance is equal to 95% of its rated value. In this case, in addition to the power delivered by the VSC, the

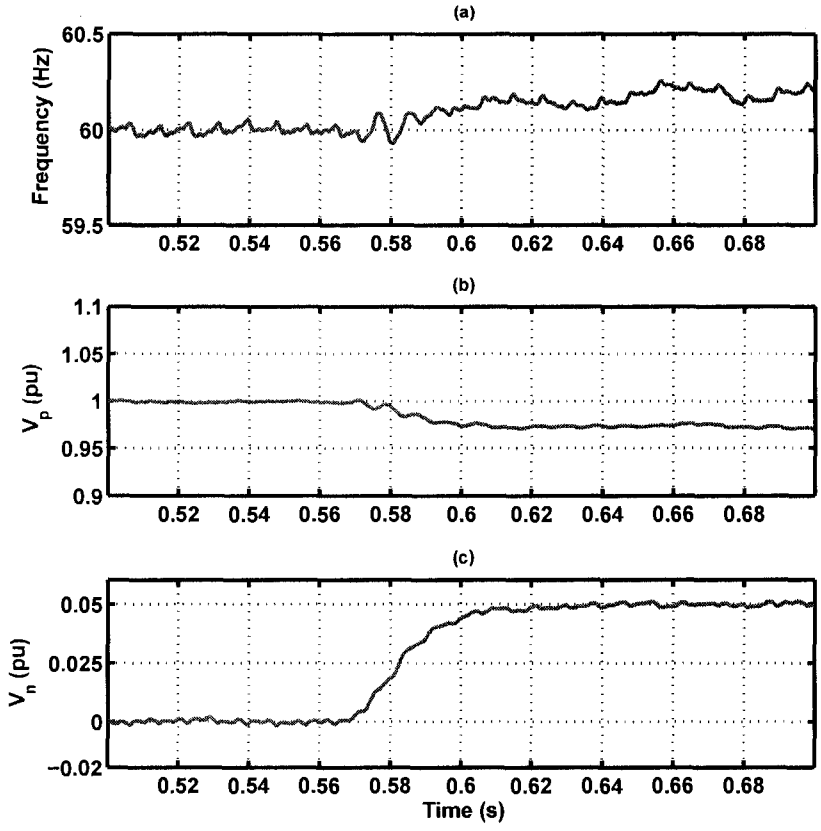

Figure A.3: UTSP output signals under UL1741 test conditions (a) estimated frequency, and (b,c) estimated magnitudes of positive-, and negative-sequence PCC voltages

grid also delivers a small component of real power to the local load prior to islanding. Therefore, after the islanding event, the magnitude of positive-sequence voltage of PCC drops to 92% which is within the acceptable limits of voltage magnitude [80] and cannot be used for the islanding detection. However, the magnitude of negative-sequence voltage at PCC is readily detectable by the UTSP system and is used for islanding detection.

Figure A.5 shows the UTSP outputs when the load resistance is 115% of its rated value. In this case, the grid absorbs a small component of real power prior to the islanding instant. Therefore, after islanding event, magnitude of the positive-sequence PCC voltage rises to 106% which is not large enough to detect the islanding event [80]. In this case, magnitude of the negative-sequence PCC voltage is detectable and can be used for islanding detection. It should be noted that for both case studies of Figures A.4 and A.5, the system frequency exhibits small changes after islanding operation which cannot be used for islanding detection.

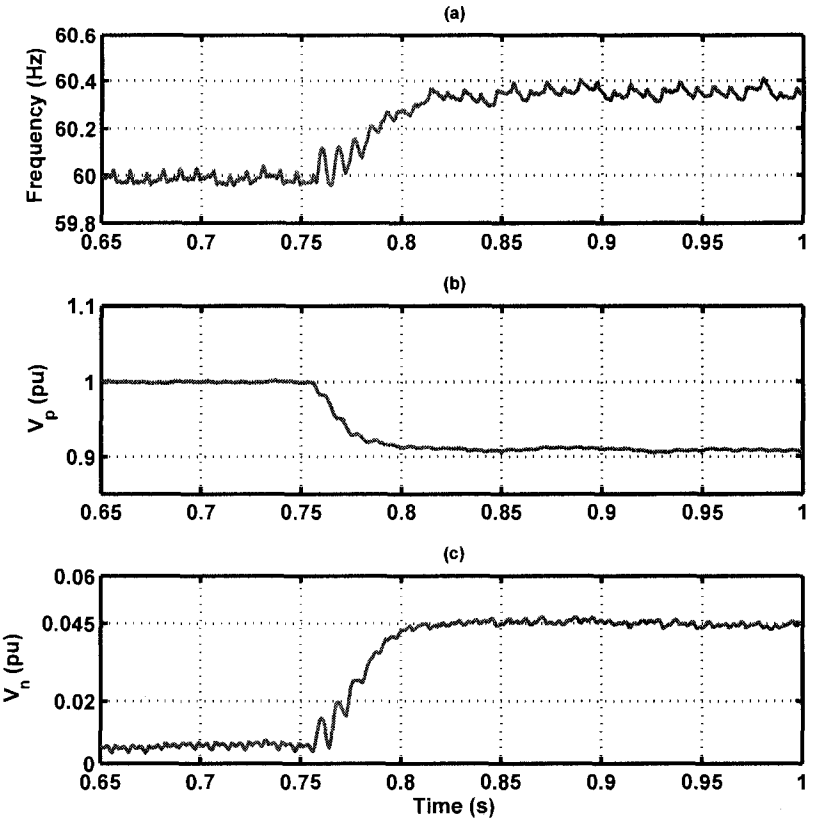

Figure A.4: UTSP output signals corresponding to 95% of rated value (a) estimated frequency, and (b,c) estimated magnitudes of positive-, and negative-sequence PCC voltages

A.3.3 Sensitivity to Load Inductance and Capacitance

In this case study, while the load resistor and capacitor are kept constant at their rated values, the load inductance L slightly (101.35% of its rated value) deviates from of its rated value. The VSC current controller injects 4% negative-sequence current and the system is islanded at t=0.510 s. The grid exchanges a small component of reactive power with the potential island since L and C are not tuned for resonance at the power system frequency. Therefore, subsequent to an islanding event, the island frequency deviates from its rated value. Figure A.6 shows the UTSP output signals and clearly shows that the deviation of L from its rated value results in a frequency deviation. However, based on the negative-sequence current injection, the measured negative-sequence voltage provides a reliable signal for islanding detection. If variation of L is small enough such that the resonance frequency is within 60 ± 0.5 Hz, the injected negative-sequence current still provides a reliable islanding detection signal.

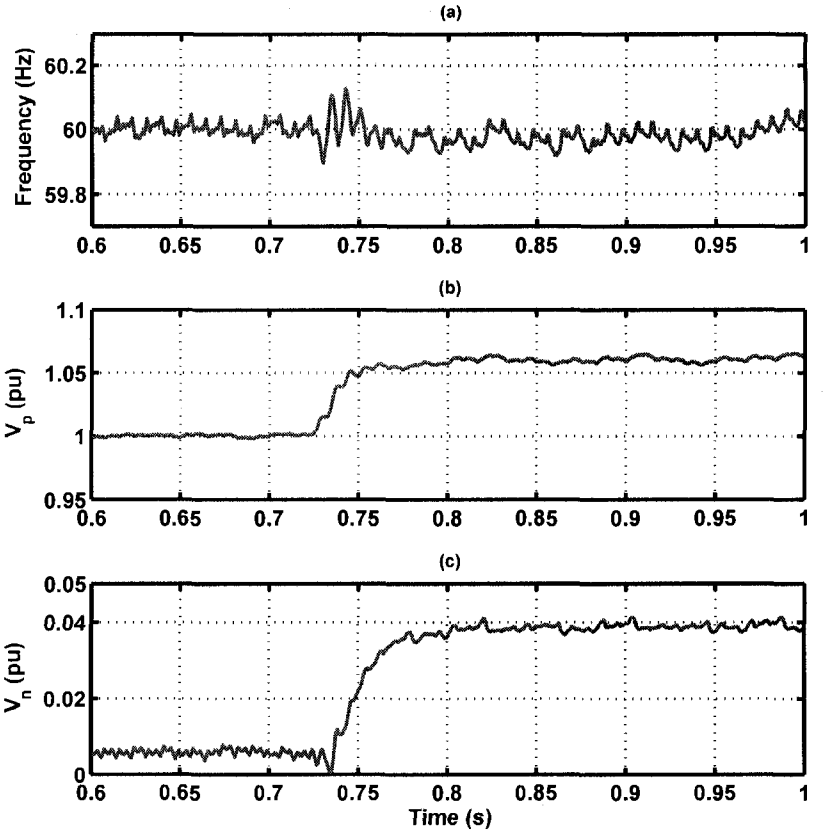

Figure A.5: UTSP output signals corresponding to 115% of rated value (a) estimated frequency, and (b,c) estimated magnitudes of positive-, and negative-sequence PCC voltages

A.4 SISO Controller

This section experimentally evaluates the performance of the proposed SISO controller of Chapter 5, Section 5.3.2. The reported test results demonstrate that the proposed SISO controller is (i) capable of maintaining the voltage magnitude at the PCC of Figure A.1 in the islanded mode, and (ii) robust with respect to perturbations in the load parameters. The UTSP system is also used, as part of the setup system, to estimate the sequence components of the PCC voltage and the system frequency.

A.4.1 Voltage Tracking

This experimental result demonstrates performance of the SISO controller under an islanded condition in terms of reference signal tracking. While the test system of Figure A.1 is operating in the

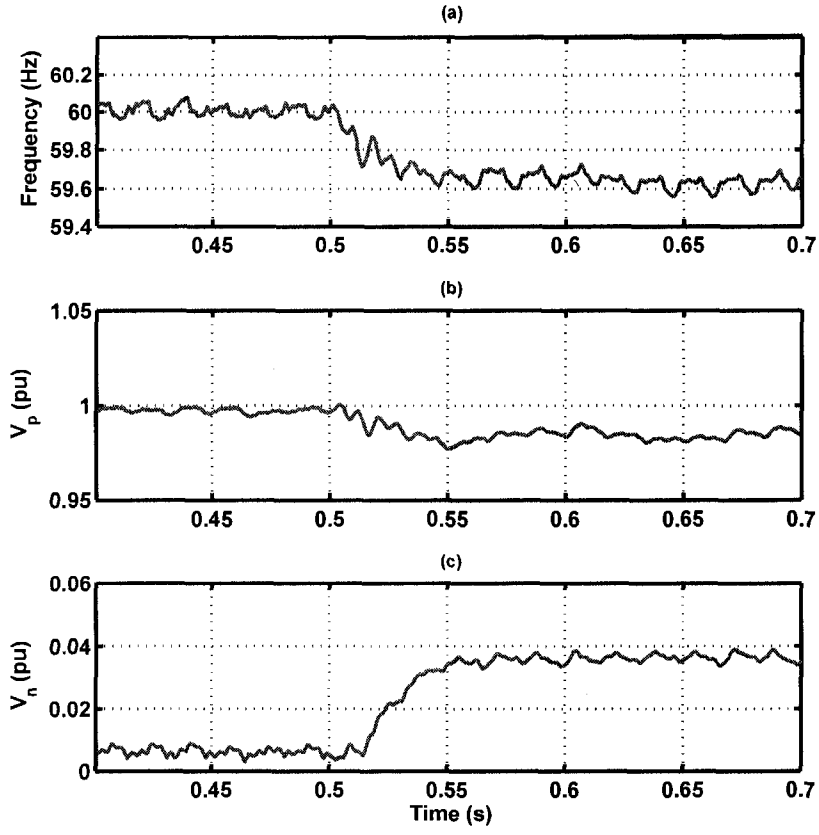

Figure A.6: UTSP output signals when inductance L deviates from its rated value (a) frequency, and (b,c) magnitudes of positive-, and negative-sequence PCC voltages

islanded mode, the voltage reference signal is stepped down from 40 V (0.35 pu) to 20 V (0.17 pu) at t=0.478 s and stepped up from 20 V to 40 V at t=0.910 s. The load parameters are set at their rated values as given in Table A.1. Figure A.7 shows the system response to these reference changes. Figures A.7(a) and (b) show variations of load voltages and converter currents to the first step change. Figure A.7(a) demonstrates that the load voltages are regulated at the new reference value of 20 V by the designed SISO control system within three cycles. Figures A.7(c), (d) and (e) show the control signal, and the estimated frequency and magnitude of positive-sequence component of the PCC voltages by the UTSP system in response to the step voltage change. Figure A.7 validates capability of the proposed SISO control system in tracking the reference signal.

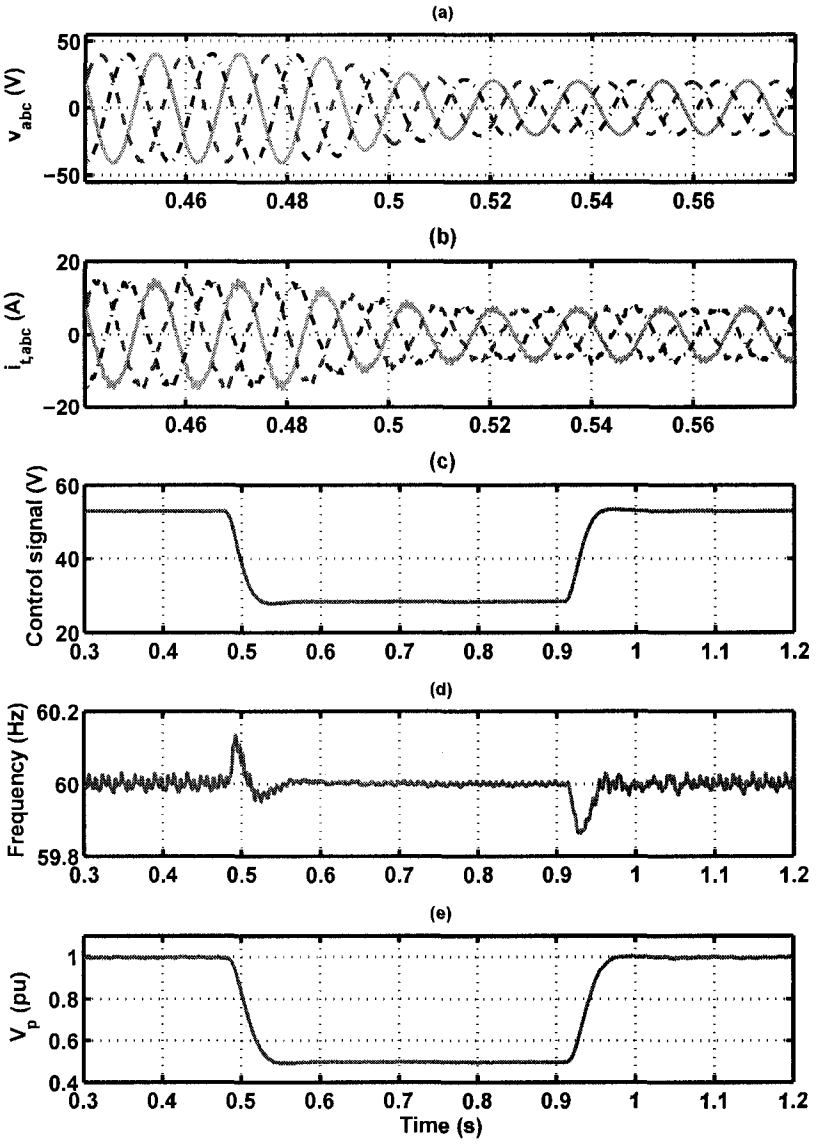

Figure A.7: Dynamic performance of the islanded system in terms of set point tracking (a) instantaneous voltages of the load at PCC, (b) converter currents, (c) control signal, and (d,e) frequency and magnitude of positive-sequence of PCC voltages deduced by the UTSP

A.4.2 Change of Load Resistance

This test verifies robust stability and performance of the proposed SISO controller with respect to the load parameter uncertainties. While the system is operating in an islanded mode and under balanced conditions, the load resistance, in the three phases, are equally changed such that the resultant load remains balanced. In this case, the load resistance is suddenly stepped up from

5.6 Ω (1 pu) to 16.2 Ω (2.9 pu) at t=0.655 s and stepped down to 5.6 Ω at t=0.990 s.

Figure A.8 shows the system response to these load changes. Figures A.8(a) and (b) show instantaneous voltages of the load and the converter currents prior and subsequent to the first resistance change. Figure A.8 shows that the designed SISO controller is robust with respect to the imposed changes, and within three cycles retains magnitude of the load voltage at its desired value. Figure A.8(c) shows the control signal in response to the load changes. The islanded system frequency and the magnitude of positive-sequence component of the PCC voltages which are extracted by the UTSP are shown in Figures A.8(d) and (e), respectively. A transient error in the estimated frequency is observed which is introduced by the UTSP system. This experiment demonstrates that the proposed SISO controller is robust if the resistance perturbations are small. The test results also show that the proposed controller can also accommodate small perturbations of the load inductance and capacitance. Therefore, the proposed SISO controller is appropriate only for those applications that the local is almost fixed and pre-determined.

A.5 MIMO Controller

This section presents a set of experimental results that validate performance of the islanded system given in Figure A.1, based on the proposed robust servomechanism controller of Chapter 5, Section 5.4.2. The reported results are to demonstrate that the designed controller is robustly capable of maintaining the magnitude of the PCC voltage. The test results also show that the proposed MIMO control system is robust with respect to load parameter uncertainties.

A.5.1 Voltage Tracking

This test demonstrates the performance of the designed robust servomechanism controller in terms of reference signal tracking. While the system is operating in an islanded mode, the q component of the reference signals, i.e. $y_{1,ref} = V_{d,ref}$, is stepped up from 30 V (0.26 pu output voltage) to 50 V (0.43 pu output voltage) at t=0.340 s, and the d component of the reference signal, i.e. $y_{2,ref} = V_{q,ref}$, is stepped down from 60 V (0.52 pu) to 40 V (0.35 pu) at t=1.464 s. In this case, the load parameters are set at their rated values as given in Table A.1. Figure A.9 shows the system step responses. In particular, Figure A.9(a) shows the d and q components of the load voltage

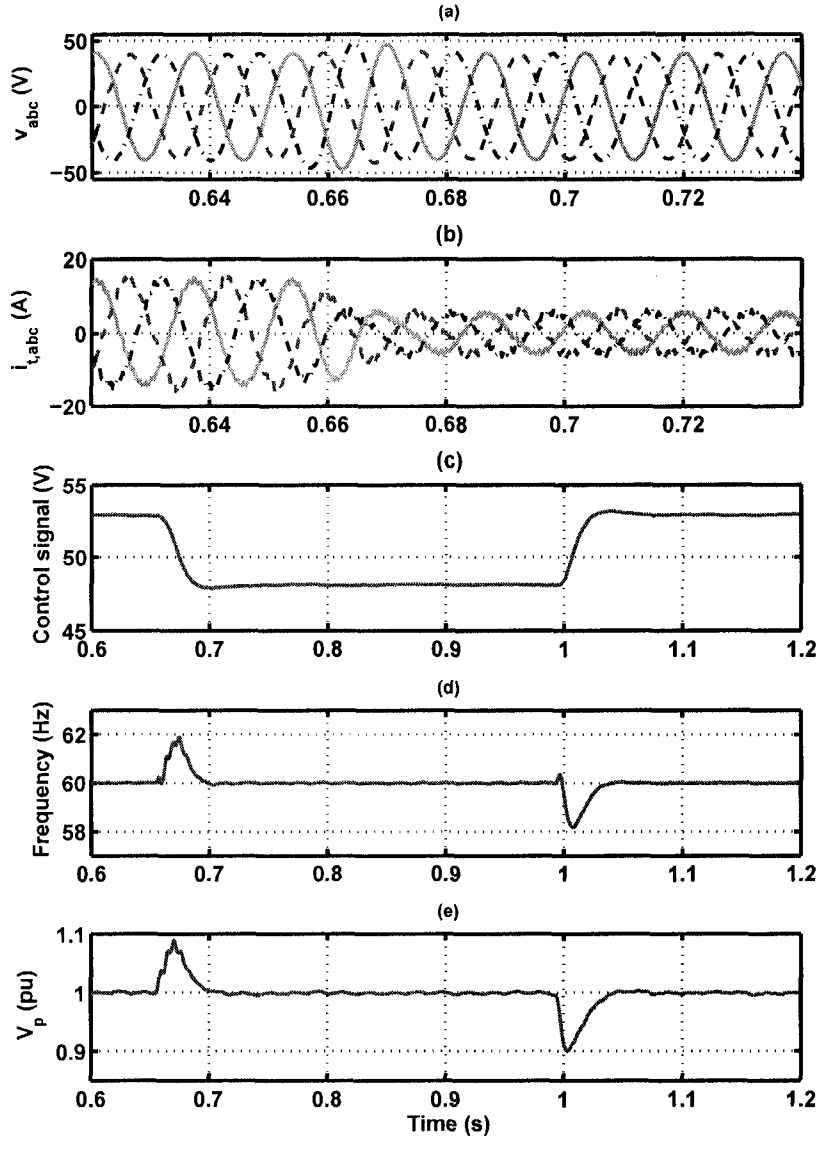

Figure A.8: Dynamic performance of the islanded system to the sudden changes in the load resistance (a) instantaneous voltages of the load at PCC, (b) converter currents, (c) control signal, and (d,e) estimated frequency and magnitude of positive-sequence of PCC voltages by the UTSP

at PCC, and demonstrates that based on the designed MIMO control system, the output signals V_d and V_q are regulated to their reference values within three cycles. Moreover, Figure A.9(a) indicates that the controlled closed-loop system is decoupled, i.e. there is no interaction between the channels. Figure A.9(b) shows the step response of the controller. Figures A.9(a) and (b) verify that the proposed control system is capable of providing reference signal tracking.

Figure A.9(c) shows instantaneous voltages of the load and their magnitude to the first step

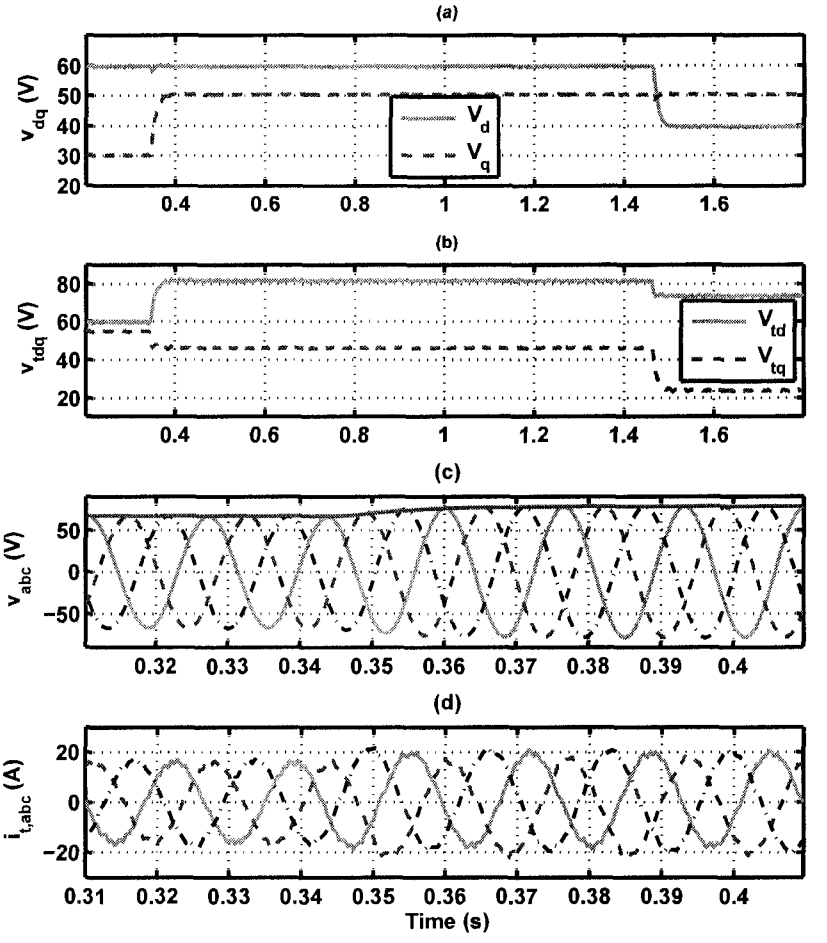

Figure A.9: Dynamic performance of the islanded system in terms of reference signal tracking (a,b) d and q components of the load voltage at PCC and control signals, (c) instantaneous voltages of the load and their magnitude, and (d) converter currents

change. The converter currents, $i_{t,abc}$, are also shown for the first change in Figure A.9(d). The time responses verify that the proposed servomechanism controller is able to regulate the load voltages at the reference signals with zero steady-state error.

A.5.2 Change of Load Resistance

This test verifies robust stability and performance of the proposed MIMO controller with respect to the load parameter uncertainties. While the system is operating in an islanded mode and under balanced conditions, the load resistance, in the three phases, are equally changed such that the resultant load remains balanced. In this case, the load resistance is suddenly stepped down from

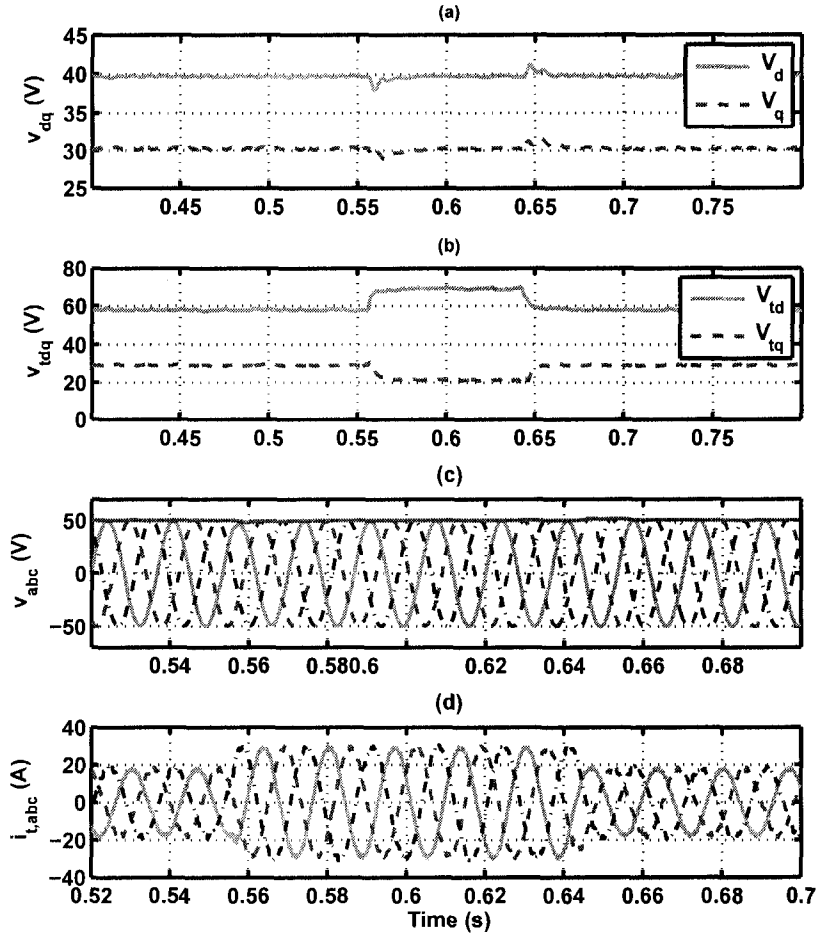

Figure A.10: Dynamic performance of the islanded system to a change in load parameters (a,b) d and q components of load voltage at PCC and control signals, (c) instantaneous voltages of the load and their magnitude, and (d) converter currents

5.5 Ω (1 pu) to 3.5 Ω (0.64 pu) at t=0.555 s and stepped up to 5.5 Ω (1 pu) at t=0.642 s. Figure A.10 shows dynamic responses of the islanded system the two load changes. Figure A.10(a) shows the d and q components of the load voltage and demonstrates that the proposed controller successfully regulates the load voltage within about two cycles. Figures A.10(b), (c) and (d) show the control signals, instantaneous voltages of the load and their magnitude, and the converter currents, respectively. Figure A.10(a) indicate that the proposed controller is capable of maintaining the load voltage despite uncertainties in the load resistance.

A.6 abc-Frame Controller

Performance validation of the proposed abc-frame controller of Chapter 6, Section 6.5.1, is provided in this section. The test results verify robustness and capability of the proposed abc-frame controller in maintaining the voltage magnitude at the PCC of the islanded system, Figure A.1, in the presence of uncertainties in the load parameters. Moreover, it is shown that the proposed abc-frame controller provides a set of balanced three-phase voltages at the load terminals of Figure A.1, despite asymmetries in the load. In each test, the UTSP system of Chapter 2 is also used to extract the sequence components of the PCC voltage and to measure the system frequency.

A.6.1 Voltage Tracking

In this test, performance of the abc-frame controller, in terms of reference signal tracking, is shown. While the system is operating in an islanded mode, magnitudes of reference signals are stepped down from 80.0 V (0.70 pu output voltage) to 50.0 V (0.43 pu output voltage) at t=0.364 s and stepped up from 50.0 V to 80.0 V at t=0.876 s. Figures A.11(a), (b) and (c) show the load voltages, the control signals, and the converter currents in response to the first step change (step-down). The UTSP output signals in response to these step changes are shown in Figure A.12. The estimated frequency and magnitudes of positive- and negative-sequence components of the PCC voltage are shown in Figures A.12(a), (b) and (c). It is observed that asymptotic tracking and regulation occur for both step changes in the magnitudes of reference signals. Moreover, zero steady-state errors are observed in magnitudes of sequence components of the load voltages and the system frequency.

A.6.2 Change in Load Parameters

Robust stability of the proposed control system with respect to the load parameter uncertainties is verified in this test. The load parameters are set at the rated values, as given in Table A.1, except for the capacitance of phase-b which is set at $C_b = 700\ \mu F$, i.e. the three-phase load is capacitively unbalanced. Three sudden changes at three different time instants in the load parameters are imposed. First, a 2.2 Ω (0.4 pu) resistance is paralleled with phase-a of the load at t=0.495 s and therefore the load becomes resistively unbalanced. Then, the capacitance of phase-b of the load is

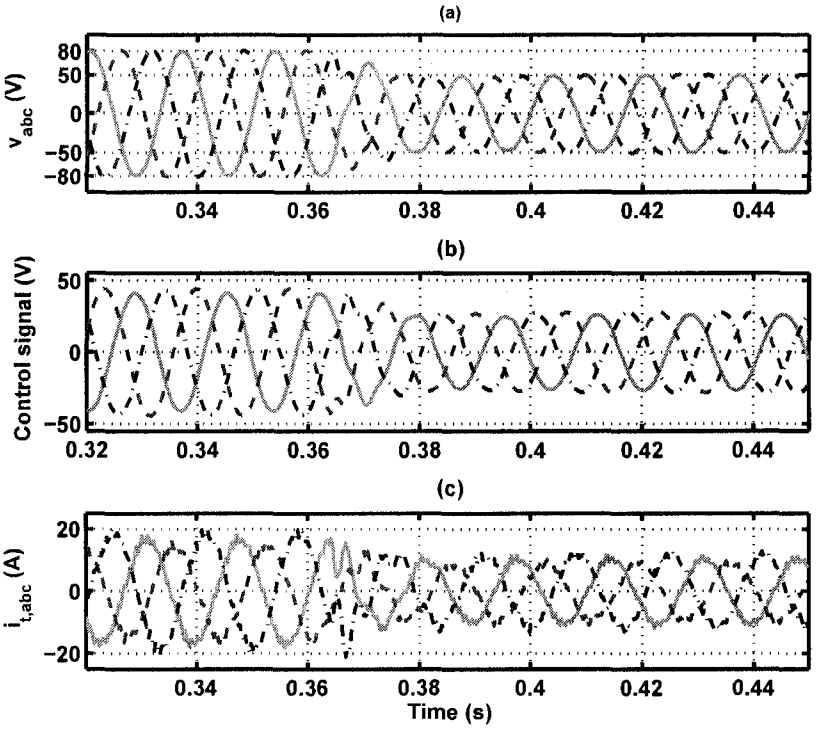

Figure A.11: Dynamic performance of the islanded system to the reference signal tracking (a) instantaneous voltages of the load, (b) control signals, and (c) load currents

stepped up from $700\mu F$ to $900\mu F$ at t=0.900 s. Eventually, the single-phase resistance paralleled with phase-a of the load is disconnected at t=1.570 s.

Figures A.13(a), (b) and (c) show the load voltages, the control signals, and the converter currents subsequent to the last change (resistance disconnection). The transient responses of the load voltages, the control signals, and the converter currents for the other two changes are similar to those of the last change and are not shown here. The UTSP output signals, in response to these load changes, are shown in Figure A.14. The estimated frequency and magnitudes of positive- and negative-sequence components of the PCC voltage are shown in Figures A.14(a), (b) and (c). Figure A.14(c) verifies that the load voltages remain balanced despite asymmetry of the load. The results of this test also indicates that the control system is capable of maintaining the load voltage magnitude and the frequency with no steady-state error. Moreover, the proposed abc-frame controller is robust with respect to changes in the load parameters.

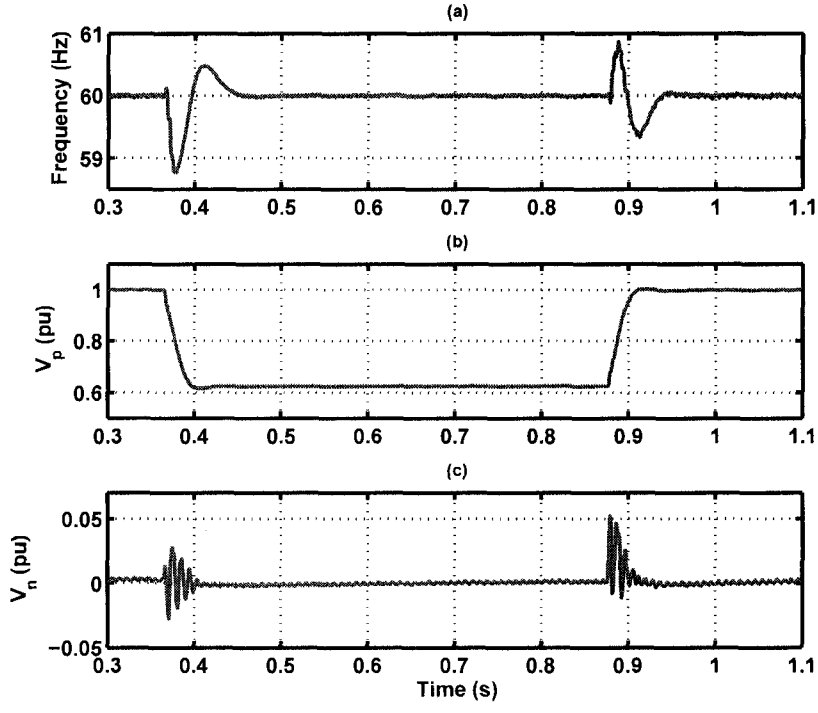

Figure A.12: UTSP response to the reference signal tracking (a) estimated frequency, and (b,c) estimated magnitudes of positive-, and negative-sequence components of PCC voltages

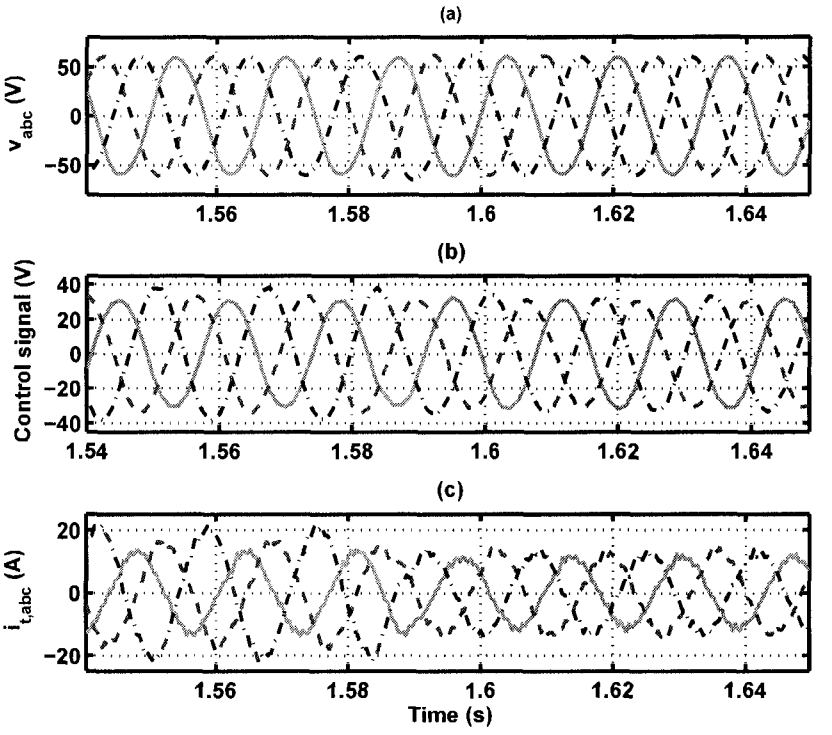

Figure A.13: Performance of the islanded system to a change in load parameters (a) instantaneous voltages of the load, (b) control signals, and (c) load currents

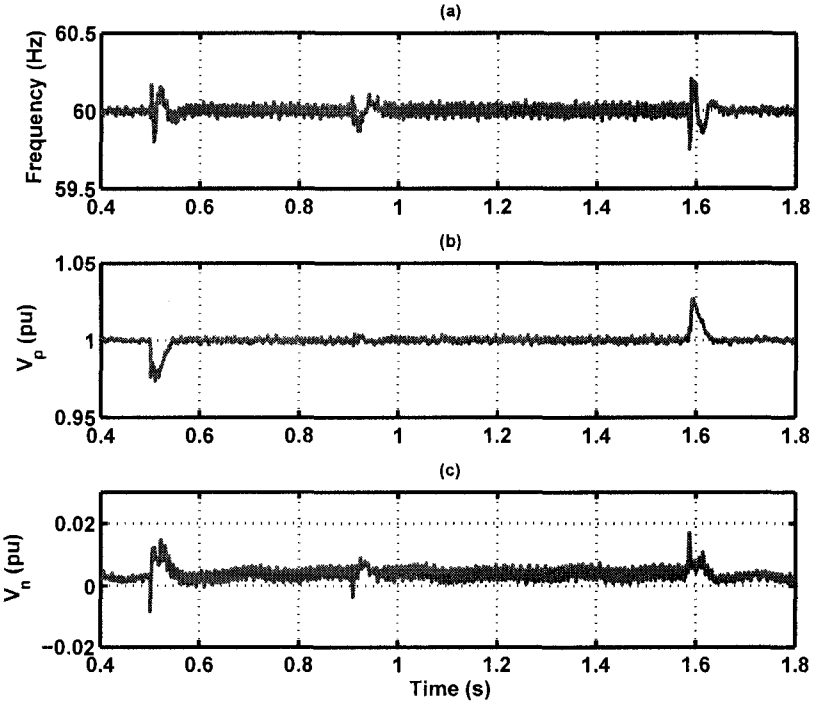

Figure A.14: UTSP output signals to the load changes (a) estimated frequency, and (b,c) estimated magnitudes of positive-, and negative-sequence components of PCC voltages

Appendix B

MIMO System

B.1 Proof of Theorem 5.4.1

(*a*) The proof follows on noting that a similarity transformation may be applied to matrix A in (5.16) to obtain $\tilde{A} = \begin{bmatrix} \bar{A} & X \\ -X & \bar{A} \end{bmatrix}$, where

$$\bar{A} := \begin{bmatrix} -\frac{1}{RC} & \frac{1}{C} & -\frac{1}{C} \\ -\frac{1}{L_t} & -\frac{R_t}{L_t} & 0 \\ \frac{1}{L} & 0 & -\frac{\omega_0}{q_l} \end{bmatrix}, \quad X := \begin{bmatrix} \omega_0 & 0 & 0 \\ 0 & \omega_0 & 0 \\ 0 & 0 & \omega_0 \end{bmatrix}.$$

On noting now that $\bar{A}$ is always Hurwitz for all positive plant parameters $R > 0$, $L > 0$, $C > 0$, $R_t > 0$, $L_t > 0$, $\omega_0 > 0$, $q_l > 0$, and that

$$real\left\{sp(\tilde{A})\right\} = \left\{real\left\{sp(\bar{A})\right\}, real\left\{sp(\bar{A})\right\}\right\},$$

where $sp(.)$ denotes the eigenvalue of (.), it is concluded that the matrix $\tilde{A}$ is Hurwitz, which proves the result.

(*b*) The transmission zeros (5.18) are obtained by determining all $\lambda \in \mathbb{C}$ which satisfy the con-

dition:

$$rank\begin{bmatrix} A-\lambda I & B \\ C & D \end{bmatrix} < n + min(r,m) = 8$$

which yields the stable transmission zeros (5.18) and proves the result.

(*c*) This result directly follows from the fact that the plant has equal number of inputs and outputs and is minimum phase [101].

B.2 Model of MIMO Controller

Matrices $\overline{\mathscr{A}}_c$, $\overline{\mathscr{B}}_c$, $\overline{\mathscr{C}}_c$, $\overline{\mathscr{E}}_c$ of the proposed MIMO controller of (5.37), Section 5.4.2-E.3, are:

$$\overline{\mathscr{A}}_c = \begin{bmatrix}
0 & 1.0 & 0 & 0 & 0 & 0 & 0 & 0 & 0 & 0 & 0 & 0 \\
-1.5477e8 & 0 & 0 & 0 & 0 & 0 & 0 & 0 & 0 & 0 & 0 & 0 \\
0 & 0 & 0 & 1.0 & 0 & 0 & 0 & 0 & 0 & 0 & 0 & 0 \\
0 & 0 & -1.5477e8 & 0 & 0 & 0 & 0 & 0 & 0 & 0 & 0 & 0 \\
0 & 0 & 0 & 0 & 0 & 0 & 0 & 0 & 0 & 0 & 0 & 0 \\
0 & 0 & 0 & 0 & 0 & 0 & 0 & 0 & 0 & 0 & 0 & 0 \\
0 & 0 & 0 & 0 & 0 & 0 & -10209 & 377 & 15910 & 0 & -15910 & 0 \\
0 & 0 & 0 & 0 & 0 & 0 & -377 & -10209 & 0 & 15910 & 0 & -15910 \\
90038 & 206.3 & 1400.9 & -0.11248 & -480.1 & 1123.1 & -6275.1 & 5.242 & -226.53 & 377 & 221.55 & 1.1 \\
-1452.3 & 0.11263 & 90037 & 206.3 & -1123.1 & -480.1 & -5.242 & -6275.1 & -377 & -226.53 & -1.1 & 221.55 \\
0 & 0 & 0 & 0 & 0 & 0 & 7875.7 & 0 & 0 & 0 & -3.1416 & 377 \\
0 & 0 & 0 & 0 & 0 & 0 & 0 & 7875.7 & 0 & 0 & -377 & -3.1416
\end{bmatrix}$$

$$\overline{\mathscr{B}}_c = \begin{bmatrix} 0 & 0 \\ 1.0 & 0 \\ 0 & 0 \\ 0 & 1.0 \\ 1.0 & 0 \\ 0 & 1.0 \\ 10000.0 & 0 \\ 0 & 10000.0 \\ 6272.9 & 0 \\ 0 & 6272.9 \\ -7866.7 & 0 \\ 0 & -7866.7 \end{bmatrix} \quad \overline{\mathscr{C}}_c = \begin{bmatrix} 43218 & -697.1 \\ 99.025 & 0.054063 \\ 672.41 & 43218 \\ -0.053992 & 99.025 \\ -230.45 & -539.07 \\ 539.07 & -230.45 \\ -0.040678 & -2.5161 \\ 2.5161 & -0.040678 \\ -106.34 & 0 \\ 0 & -106.34 \\ 106.34 & -0.52317 \\ 0.52318 & 106.34 \end{bmatrix}^T \quad \overline{\mathscr{E}}_c = \begin{bmatrix} 0 & 0 \\ 0 & 0 \\ 0 & 0 \\ 0 & 0 \\ 0 & 0 \\ 0 & 0 \\ 10000 & 0 \\ 0 & 10000 \\ 6272.9 & 0 \\ 0 & 6272.9 \\ -7866.7 & 0 \\ 0 & -7866.7 \end{bmatrix}$$

B.3 Performance Evaluation of MIMO System

B.3.1 Change in Load Inductance

Robust stability and performance of the resultant closed-loop system of (5.39), Section 5.4.2-F, with respect to uncertainty in the load inductance is carried out in this section. While the load resistance and capacitance are fixed at their nominal values, as given in Table 5.1, the load inductance assumes various sudden changes from its nominal value $L = 111.9\ mH$ to $0.7L$, $2L$, $3L$, $6L$, and infinity at t=0.800 s. It should be noted that although these sudden changes in the load inductance may not be realistic, the objective here is to verify the robustness properties of the proposed robust servomechanism controller. In this section, only simulation results corresponding to step changes from L to $0.7L$ and $2L$ are presented. The results of the other cases such as step-up from L to values larger than $2L$ are very similar to those of L to $2L$. Our studies show that a load with an inductance of less than 0.7 of the nominal value $L = 111.9\ mH$ result in a poor performance and even instability of the closed-loop system.

Figures B.1(a) to (d) show the d and q components of the load voltage, control signals, load current, and real/ractive power components of the load when L is step changed to $0.7L$. A voltage transient of about 40 ms (less than three cycle) is observed from Figure B.1(a). The load current

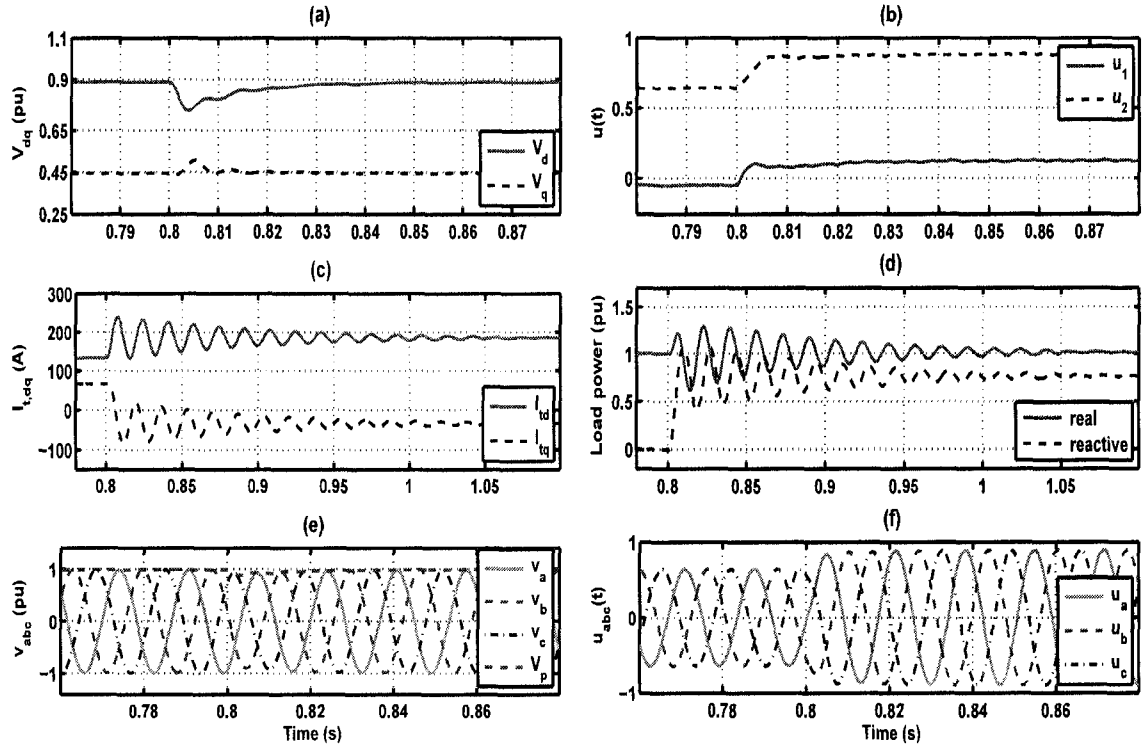

Figure B.1: Performance of the islanded system when the load inductance is changed from L = 111.9 mH to 0.7L (a,b,c) dq components of load voltage, control signals, load currents, and (d) instantaneous power components of load, (d) instantaneous power components of load, and (e,f) instantaneous voltages of load and control signals in abc-frame

and consequently real/reactive power components of the load represent longer transients. The reason is that the load quality factor, at 0.7L, is large (Q = 2.15) and therefore the load current response is slow. It should be noted that the real power of the load remains unchanged, since only the load inductance is changed. Instantaneous voltages of the load and the control signals are depicted in Figures B.1(e) and (f), respectively. The proposed servomechanism controller maintains the load voltage at its reference value within a transient period of about three cycles.

In the next case study, the load inductance steps up from L = 111.9 mH to 2L at t=0.800 s. Simulation results for this case study are presented in Figure B.2. In this case, the load voltage and the controller response undergo transients of about three cycles. Figure B.2(a) shows "fast tracking" of reference signals (2.5 cycles transient response).

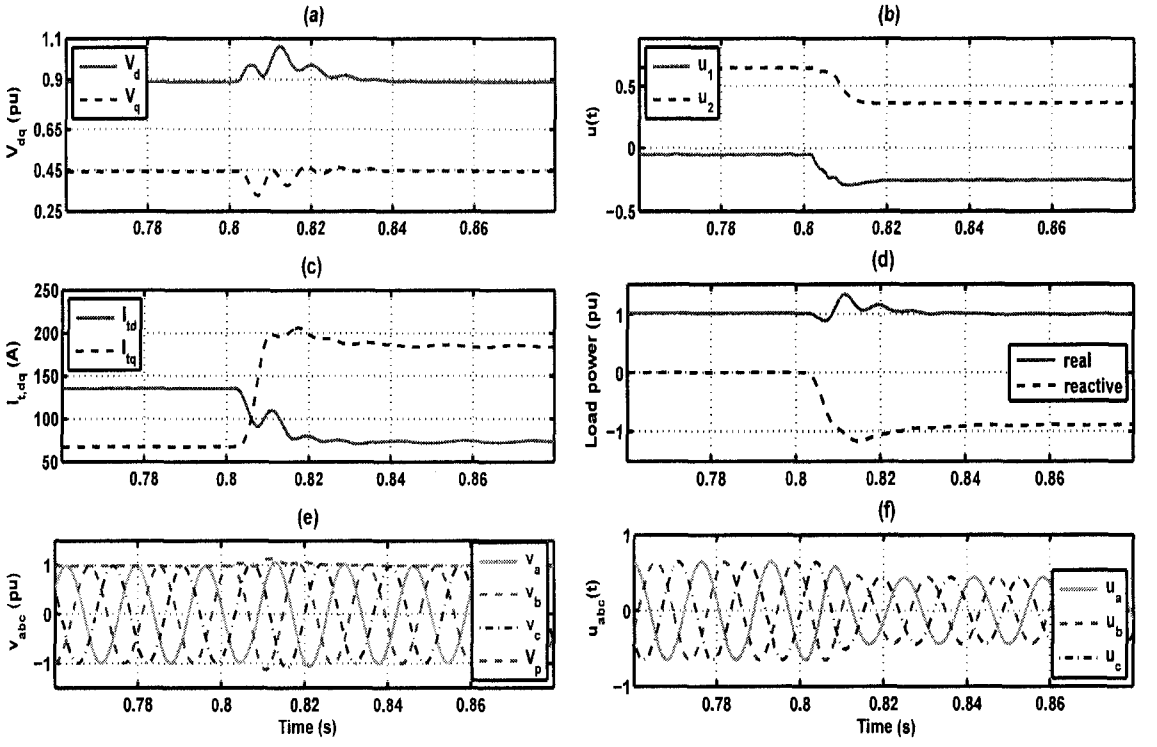

Figure B.2: Performance of the islanded system when the load inductance is changed from L = 111.9 mH to $2L$ (a,b,c) dq components of load voltage, control signals, load currents, and (d) instantaneous power components of load, and (e,f) instantaneous voltages of load and control signals in abc-frame

B.3.2 Change in Load Capacitance

In this section, the effect of load capacitance uncertainty on performance of the closed loop system is evaluated. It is observed that the system cannot accommodate large changes in the load capacitance as were possible for the load resistance and inductance. The reason is the kVA limitation of the VSC, i.e. large as well as small load capacitances result in over-modulation of the VSC and consequently its poor performance. However, our studies show that the closed-loop system is mathematically and robustly stable for all values of the load capacitance $C \leq 160\ \mu F$, assuming that the load resistance and inductance are set at their nominal values.

Initially the load resistance and inductance are set at their nominal values as given in Table 5.1 and the load capacitance undergoes two different step changes from its nominal value $C = 62.86\ \mu F$ to $0.5C$ and $2C$. Dynamic responses of the closed-loop system to these capacitance step changes are shown in Figures B.3 and B.4. Figures B.3(a) to (c) show the d and q components

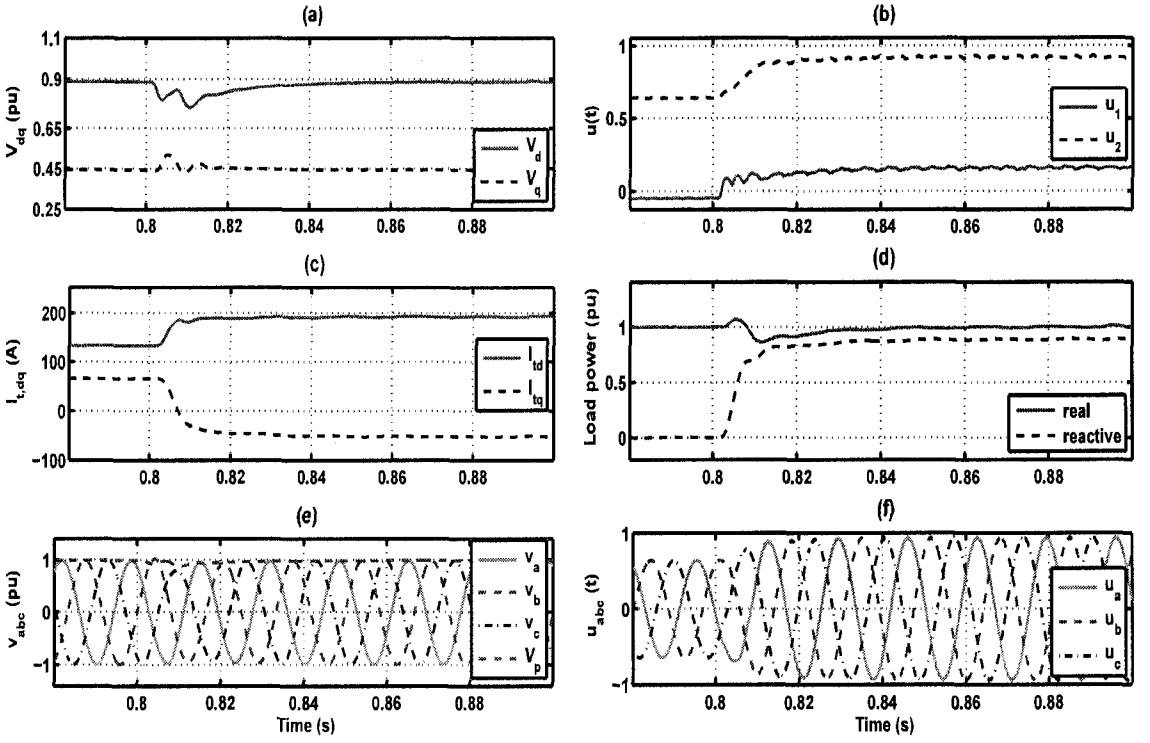

Figure B.3: Performance of the islanded system when the load capacitance is changed from $C = 62.86\ \mu F$ to $0.5C$ (a,b,c) dq components of load voltage, control signals, load currents, (d) instantaneous power components of load, and (e,f) instantaneous voltages of load and control signals in abc-frame

of the load voltage, control signals, and load current when the capacitor is switched from C to $0.5C$ at t=0.800 s. The transient response is about two cycles and well within the acceptable limits. Variations of real and reactive power components of the load are shown in Figure B.3(d). Instantaneous voltages of the load and control signals, in the abc-frame, are depicted in Figures B.3(e) and (f), respectively. Figure B.4 show dynamic performance of the closed-loop system for the case of a step change in the load capacitance from its nominal value of $C = 62.86\ \mu F$ to $2C$. The results are similar to those of the previous case, except for the transient period which is about three cycles. These case studies verify robustness of the proposed servomechanism controller with respect to uncertainties in the load capacitance.

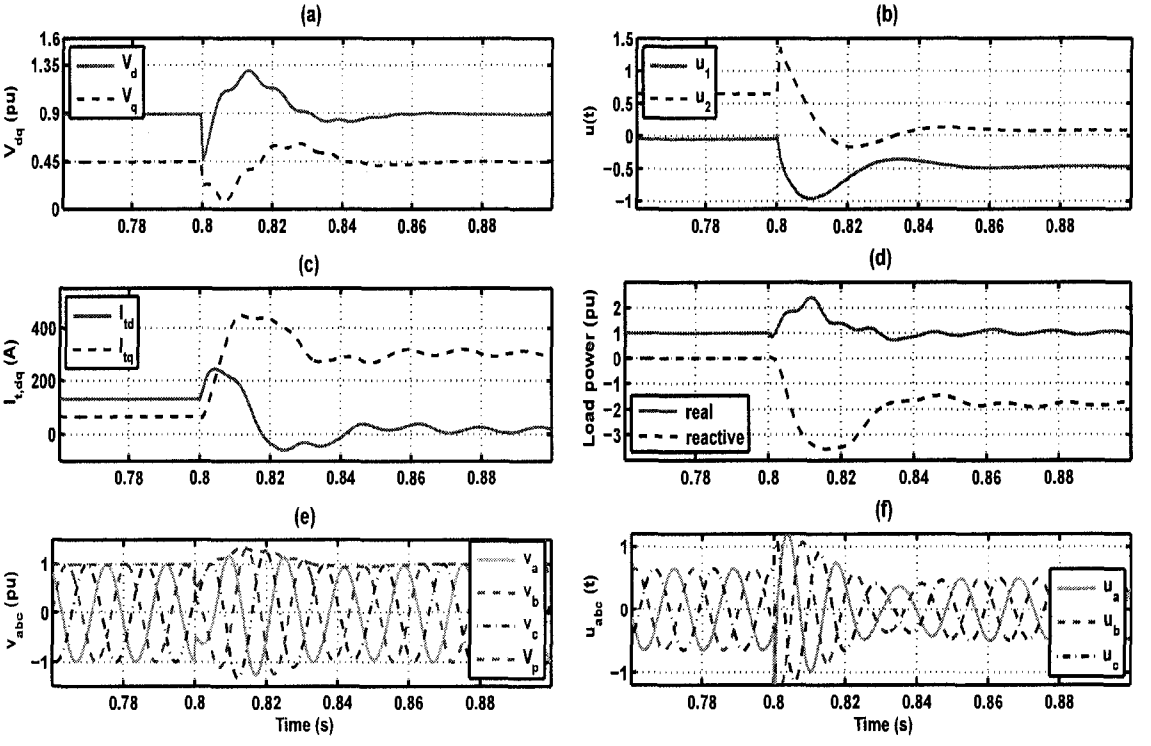

Figure B.4: Performance of the islanded system when the load capacitance is changed from $C = 62.86\ \mu F$ to $2C$ (a,b,c) dq components of load voltage, control signals, load currents, (d) instantaneous power components of load, and (e,f) instantaneous voltages of load and control signals in abc-frame

Appendix C

Control Strategy for an Islanded System under Unbalanced Load Conditions

This appendix provides a control strategy for an islanded system under unbalanced load conditions. A control strategy to provide a set of balanced voltages for the load, despite asymmetry and uncertainties of the load, is proposed in Chapter 6. The proposed controller balances phase voltages of the load and therefore a zero-sequence current should be generated by the voltage-sourced converter (VSC). In this case, the neutral point of the three-phase load should be connected to the DC mid-point of the converter. Moreover, there is a need to actively equalize the two DC voltages of the VSC.

In most practical cases, the VSC is connected to the load as a three-phase, three-wire apparatus and does not permit flow of zero-sequence current. In such cases, phase voltages of the load cannot be balanced. However, it is possible to design a control strategy to generate a set of balanced line-to-line voltages for the load. In the following sections, a mathematical model for an islanded system, with no neutral connection between the load and the converter, is proposed. Depending on the mode of operation of the VSC, two scenarios can be considered. In the first case, the three-phase VSC is represented by three independent voltage sources which are Y-connected. In the second case, the VSC system represents two independent voltage sources and the third voltage source is zero.

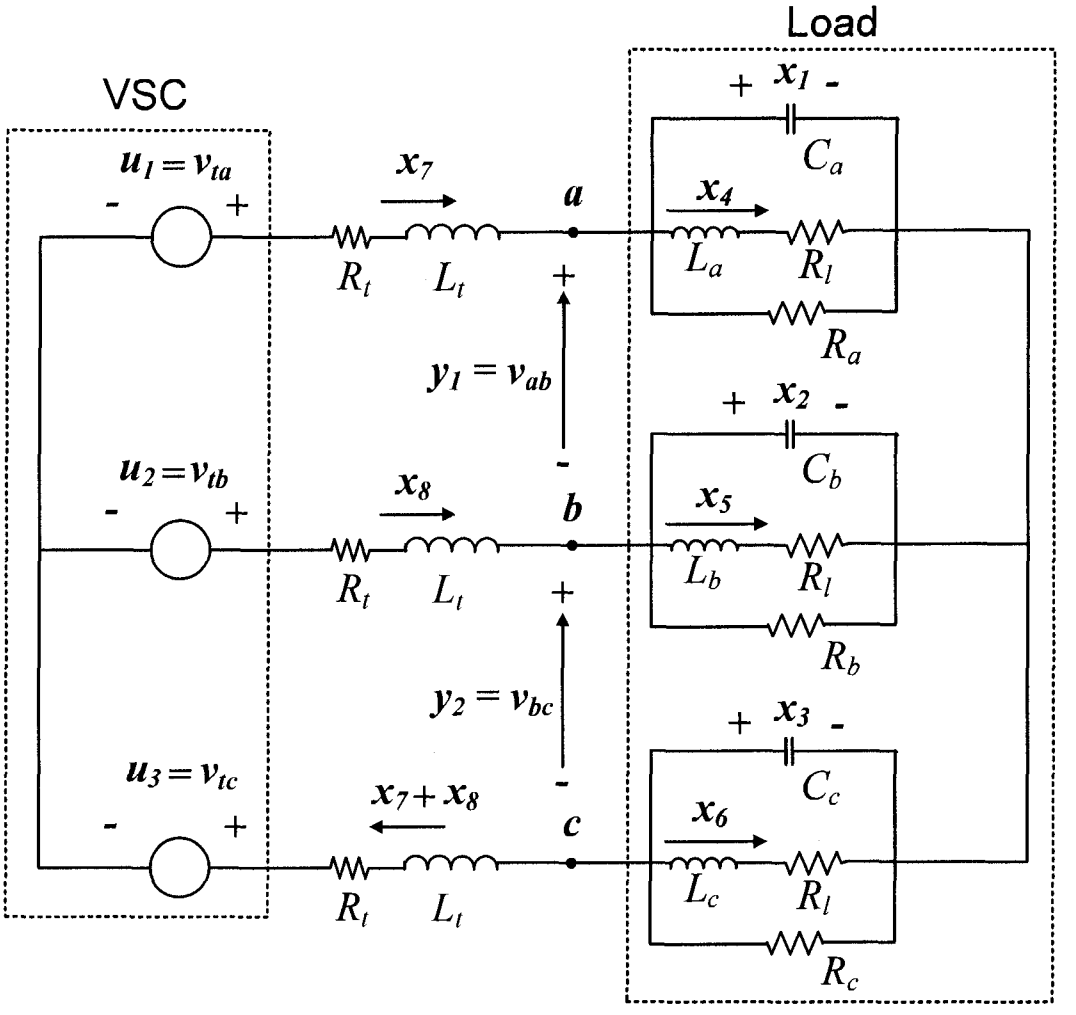

Figure C.1: Schematic representation of a single-DG islanded system consisting of a DG unit and a three-phase load which are connected by series RL branches

C.1 Mathematical Model of Islanded System: Case I

Figure C.1 shows a schematic diagram of an islanded system consisting of a three-phase load and a distributed generation (DG) unit. The three-phase load, which is modeled by a parallel RLC network in each phase, can be unbalanced and parametrically uncertain. The line and the DG unit are represented by series RL branches and a three-phase voltage source, respectively.

The objective is to control the line-to-line voltages of the load, i.e. $y_1 = v_{ab}$ and $y_2 = v_{bc}$. The control signals are phase voltages of the VSC, i.e. v_{ta}, v_{tb}, v_{tc}. As is was discussed in Chapter 6, since the three-phase system is asymmetric, the abc-frame is used to model the islanded system.

The state-space equations of the islanded system of Figure C.1 in the abc-frame are

$$\begin{cases} C_a\dot{x}_1 + \dfrac{x_1}{R_a} + x_4 = x_7 \\ C_b\dot{x}_2 + \dfrac{x_2}{R_b} + x_5 = x_8 \\ C_c\dot{x}_3 + \dfrac{x_3}{R_c} + x_6 = -x_7 - x_8 \\ L_a\dot{x}_4 + R_l x_4 = x_1 \\ L_b\dot{x}_5 + R_l x_5 = x_2 \\ L_c\dot{x}_6 + R_l x_6 = x_3 \\ -v_{ta} + R_t x_7 + L_t\dot{x}_7 + x_1 - x_2 - L_t\dot{x}_8 - R_t x_8 + v_{tb} = 0 \\ -v_{tb} + R_t x_8 + L_t\dot{x}_8 + x_2 - x_3 + L_t\dot{x}_7 + L_t\dot{x}_8 + R_t x_7 + R_t x_8 + v_{tc} = 0 \\ y_1 = x_1 - x_2 \\ y_2 = x_2 - x_3 \end{cases} \tag{C.1}$$

Equations (C.1) in the standard state space form are

$$\begin{cases} \dot{x}(t) &= Ax(t) + Bu(t) \\ y(t) &= C_m x(t) \\ u(t) &= [v_{ta} \;\; v_{tb} \;\; v_{tc}]^T, \end{cases} \tag{C.2}$$

where

$$A = \begin{bmatrix} -\frac{1}{R_a C_a} & 0 & 0 & -\frac{1}{C_a} & 0 & 0 & \frac{1}{C_a} & 0 \\ 0 & -\frac{1}{R_b C_b} & 0 & 0 & -\frac{1}{C_b} & 0 & 0 & \frac{1}{C_b} \\ 0 & 0 & -\frac{1}{R_c C_c} & 0 & 0 & -\frac{1}{C_c} & -\frac{1}{C_c} & -\frac{1}{C_c} \\ \frac{1}{L_a} & 0 & 0 & -\frac{R_l}{L_a} & 0 & 0 & 0 & 0 \\ 0 & \frac{1}{L_b} & 0 & 0 & -\frac{R_l}{L_b} & 0 & 0 & 0 \\ 0 & 0 & \frac{1}{L_c} & 0 & 0 & -\frac{R_l}{L_c} & 0 & 0 \\ -\frac{2}{3L_t} & \frac{1}{3L_t} & \frac{1}{3L_t} & 0 & 0 & 0 & -\frac{R_t}{L_t} & 0 \\ \frac{1}{3L_t} & -\frac{2}{3L_t} & \frac{1}{3L_t} & 0 & 0 & 0 & 0 & -\frac{R_t}{L_t} \end{bmatrix}, \tag{C.3}$$

$$B = \begin{bmatrix} 0 & 0 & 0 \\ 0 & 0 & 0 \\ 0 & 0 & 0 \\ 0 & 0 & 0 \\ 0 & 0 & 0 \\ 0 & 0 & 0 \\ \frac{2}{3L_t} & -\frac{1}{3L_t} & -\frac{1}{3L_t} \\ -\frac{1}{3L_t} & \frac{2}{3L_t} & -\frac{1}{3L_t} \end{bmatrix}, \quad Cm = \begin{bmatrix} 1 & 0 \\ -1 & 1 \\ 0 & -1 \\ 0 & 0 \\ 0 & 0 \\ 0 & 0 \\ 0 & 0 \\ 0 & 0 \end{bmatrix}^T. \tag{C.4}$$

Dynamical equations (C.2) describe a MIMO control system in the abc-frame which has three control inputs and two controlled outputs. Since the load parameters are assumed to be uncertain positive real numbers, plant model (C.2) represents a system with structured real parametric uncertainties [48]. Design of robust controllers for such systems is not straightforward, particularly when the reference signals are time varying functions (sinusoidal in this study).

In Chapter 5, a robust servomechanism controller, using parameter optimization methods of [47,97-99], is designed for the system of Figure 5.1. This approach can also be used to design a robust control strategy for the system of Figure C.1, i.e. plant (C.2).

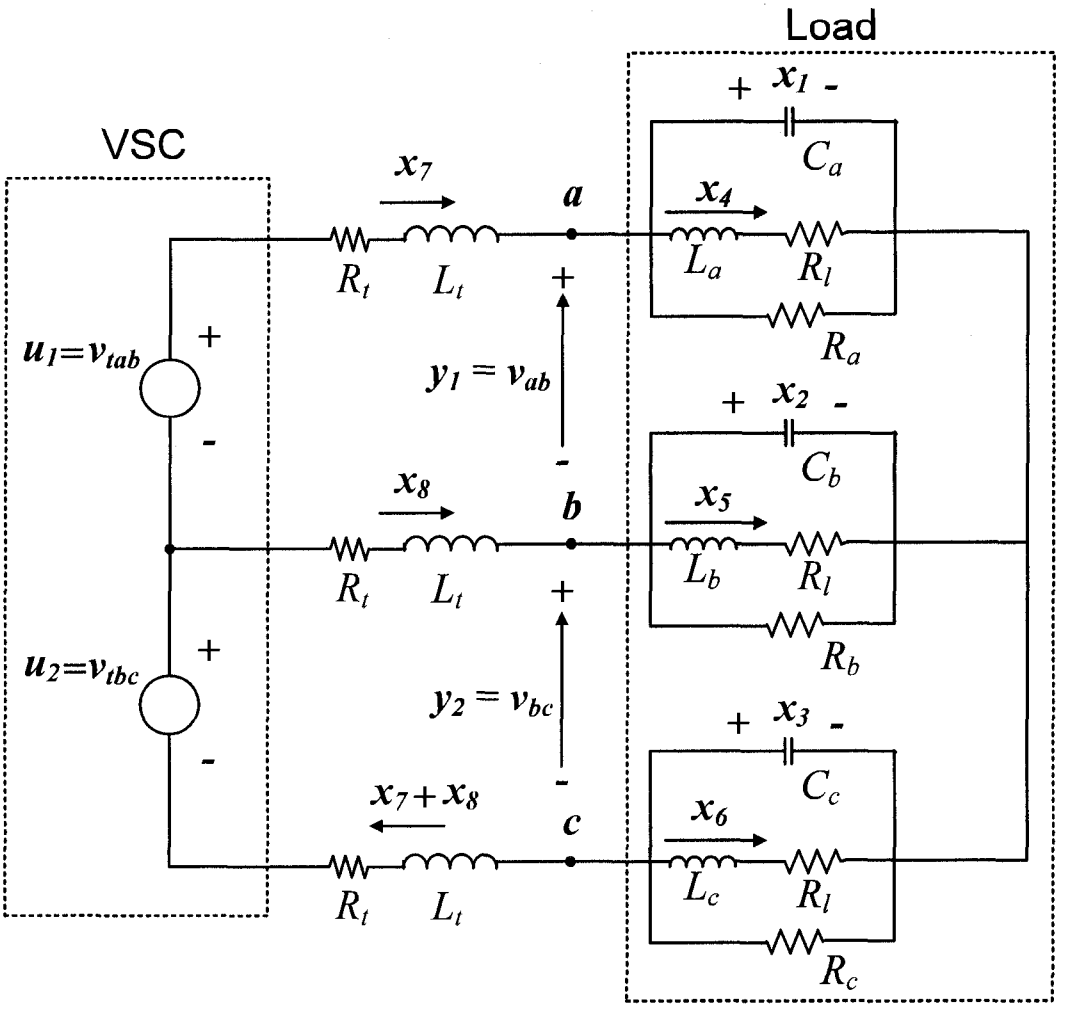

Figure C.2: Schematic representation of a single-DG island comprising a VSC, series filter, and three-phase unbalanced load

C.2 Mathematical Model of Islanded System: Case II

In this case, the VSC system represents two independent voltage sources, as shown in Figure C.2, load voltages v_{ab}, v_{bc} are signals to be controlled, and control signals are v_{tab}, v_{tbc}. It should be noted that case I and case II are equivalent if the control signal v_{tb} of case I is set to zero.

KVL and KCL equations result in the following state space equations for the islanded system

of Figure C.2:

$$\begin{cases} C_a\dot{x}_1 + \dfrac{x_1}{R_a} + x_4 = x_7 \\ C_b\dot{x}_2 + \dfrac{x_2}{R_b} + x_5 = x_8 \\ C_c\dot{x}_3 + \dfrac{x_3}{R_c} + x_6 = -x_7 - x_8 \\ L_a\dot{x}_4 + R_l x_4 = x_1 \\ L_b\dot{x}_5 + R_l x_5 = x_2 \\ L_c\dot{x}_6 + R_l x_6 = x_3 \\ -v_{tab} + R_t x_7 + L_t\dot{x}_7 + x_1 - x_2 - L_t\dot{x}_8 - R_t x_8 = 0 \\ -v_{tbc} + R_t x_8 + L_t\dot{x}_8 + x_2 - x_3 + L_t\dot{x}_7 + L_t\dot{x}_8 + R_t x_7 + R_t x_8 = 0 \\ y_1 = x_1 - x_2 \\ y_2 = x_2 - x_3 \end{cases} \tag{C.5}$$

The state space equations of the islanded system of Figure C.2 in the standard form are

$$\begin{cases} \dot{x}(t) &= Ax(t) + Bu(t) \\ y(t) &= C_m x(t) \\ u(t) &= [v_{tab} \;\; v_{tbc}]^T, \end{cases} \tag{C.6}$$

where

$$A = \begin{bmatrix} -\frac{1}{R_a C_a} & 0 & 0 & -\frac{1}{C_a} & 0 & 0 & \frac{1}{C_a} & 0 \\ 0 & -\frac{1}{R_b C_b} & 0 & 0 & -\frac{1}{C_b} & 0 & 0 & \frac{1}{C_b} \\ 0 & 0 & -\frac{1}{R_c C_c} & 0 & 0 & -\frac{1}{C_c} & -\frac{1}{C_c} & -\frac{1}{C_c} \\ \frac{1}{L_a} & 0 & 0 & -\frac{R_l}{L_a} & 0 & 0 & 0 & 0 \\ 0 & \frac{1}{L_b} & 0 & 0 & -\frac{R_l}{L_b} & 0 & 0 & 0 \\ 0 & 0 & \frac{1}{L_c} & 0 & 0 & -\frac{R_l}{L_c} & 0 & 0 \\ -\frac{2}{3L_t} & \frac{1}{3L_t} & \frac{1}{3L_t} & 0 & 0 & 0 & -\frac{R_t}{L_t} & 0 \\ \frac{1}{3L_t} & -\frac{2}{3L_t} & \frac{1}{3L_t} & 0 & 0 & 0 & 0 & -\frac{R_t}{L_t} \end{bmatrix}, \tag{C.7}$$

$$B = \begin{bmatrix} 0 & 0 \\ 0 & 0 \\ 0 & 0 \\ 0 & 0 \\ 0 & 0 \\ 0 & 0 \\ \frac{2}{3L_t} & \frac{1}{3L_t} \\ -\frac{1}{3L_t} & \frac{1}{3L_t} \end{bmatrix}, \quad Cm = \begin{bmatrix} 1 & 0 \\ -1 & 1 \\ 0 & -1 \\ 0 & 0 \\ 0 & 0 \\ 0 & 0 \\ 0 & 0 \\ 0 & 0 \end{bmatrix}^T. \tag{C.8}$$

The state space model of (C.6) represents a MIMO control system in the abc-frame. Similar to case I, plant model (C.6) represents a control system with structured real parametric uncertainties [48]. The approach of [47,97-99] can be used to design a robust servomechanism controller for the islanded system of Figure C.2.

The main advantage of case II over case I is that its controller is simpler. However, it is not practically efficient to generate a two-phase source from a three-phase VSC.

Appendix D

Polynomial Methods For Robustness of Linear Systems

This appendix is a summary of the book entitled "New Tools for Robustness of Linear Systems" [48][1]. The summary is intended to give the readers an introduction to the robustness of linear systems. The reader is referred to [48] for a comprehensive explanation to the parametric analysis approach of robust control theory.

D.1 Overview

Most problems involving model uncertainty are addressed in the field of modern control theory. A typical scenario begins with a control system whose mathematical model includes uncertain quantities. For example, the mathematical model might contain several physical parameters whose values are specified only within given bounds. Control problems with uncertainty can be categorized into three types [48]:

- Adaptive Problems
- Stochastic Problems
- Robustness Problems

[1] With the permission of Professor B. R. Barmish

This categorization should not be interpreted too literally. For example, fuzzy control and singular perturbation problems do not fit neatly into any of the above categories. The focus of this Appendix is robust stability analysis of linear time invariant (LTI) systems with structured real parametric uncertainty. As far as robust synthesis is concerned, for systems with real parametric uncertainty, many of the most fundamental research questions are as yet unresolved, particularly at the level of multiple-input multiple-output (MIMO) systems.

In general, the results of this Appendix are used for the analysis of the root location of polynomials whose coefficients depend on a set of uncertain parameters. From a control theoretic point of view, the motivation for studying these tools is the fact that many robust control problems can be transformed into equivalent problems involving roots of a polynomial. After converting a robustness analysis problem into a polynomial problem with coefficients depending on uncertain parameters, the issue of uncertainty structure arises. In the discussions to follow, we deal with a vector of uncertain parameters q and a polynomial which is expressed as

$$p(s,q) = \sum_{i=0}^{n} a_i(q)s^i.$$

The uncertainty structure is manifested via the coefficient functions $a_0(q)$, ..., $a_n(q)$. For example, if each component q_i of q enters into only one coefficient, the simplest structure is obtained which is called interval polynomial or Kharitonov polynomial [109]. The next level of complication is the affine linear uncertainty structure. In this case, coefficients depend affine linearly on q and various results on polytopes of polynomials have been developed in the literature [48]. For affine linear uncertainty structures, the highlight is the Edge Theorem of Bartlett, Hollot and Huang given in [110].

To deal with more realistic robust control problems, multilinear and nonlinear uncertainty structures are of paramount importance; e.g., consider $p(s,q)$ above with each coefficient function $a_i(q)$ being nonlinear. At this higher level of difficulty, some authors restrict their attention to analytically tractable special cases, while other authors resort to mathematical programming. This Appendix concentrates on a selected analytical result which is available for multilinear uncertainty structure; a highlight is the Mapping Theorem, which is covered in Section D.6.2.

D.1.1 The Value Set Concept

The main point to note is that we can reformulate many robustness problems in terms of a two-dimensional set which is called *value set*, $V(\delta)$; this set lies in the complex plane. Notice that $V(\delta)$ is parameterized via a real scalar δ, which we call a *generalized frequency variable*. Now, as δ increases, the set $V(\delta)$ typically moves around the complex plane. As we will see later, for many examples, it turns out that the *zero exclusion condition*, [48],

$$0 \notin V(\delta)$$

for all δ is both necessary and sufficient for satisfaction of the stated robustness specification.

In large measure, the power of the value set approach is derived from the fact that it is a two-dimensional set, whereas the uncertain parameter set is typically of higher dimension; i.e., although a robustness problem with an l-dimensional uncertain parameter vector q is initially formulated over $\mathbf{R}^l$, we need only manipulate the two-dimensional value set $V(\delta)$. Furthermore, since $V(\delta)$ is only two-dimensional, we obtain a second advantage. For cases when $V(\delta)$ is readily constructible, we obtain solutions to robustness problems which lend themselves to implementation in graphics. That is, once we have an analytical description of the value set $V(\delta)$, it is often convenient to simply generate this set on a computer and provide a visual display of its motion with respect to δ.

D.1.2 Family

The notion of a *family* $\mathcal{F}$ is fundamental within the framework of uncertain quantities. For example, in the islanded system with the RLC network discussed in Chapter 6, we adopt the point of view that each admissible value of uncertain parameter vector $q = [R \;\; L \;\; C]$ between $q_{min} = [R_{min} \;\; L_{min} \;\; C_{min}]$ and $q_{max} = [R_{max} \;\; L_{max} \;\; C_{max}]$ defines a different system. Hence, we have a *family of system* $\mathcal{F}$ rather than a *fixed* system. The word "family" is used in a wide variety of contexts; e.g., we refer to a family of polynomials, a family of transfer functions or a family of matrices.

D.1.3 Robustness Analysis

Given a family $\mathcal{F}$ and some property **P**, when we say $\mathcal{F}$ is *robust*, we mean the following: Every member $f \in \mathcal{F}$ has property **P**. For example, we are often interested in a family of systems $\mathcal{F}$ with **P** being some aspect of performance. Then, when we say that the family $\mathcal{F}$ is *robust*, the understanding is that the performance specification is satisfied for every system in the family; i.e., for all $f \in \mathcal{F}$. There are numerous other possibilities for $\mathcal{F}$ and **P**. For example, $\mathcal{F}$ can be a family of polynomials and **P** might denote stability, or $\mathcal{F}$ might denote a family of transfer functions and **P** can be a specification on the frequency response.

D.1.4 Robustness Margin

For cases when bounds on the uncertain quantities are not given, we often consider the so-called *Robustness Margin Problem*. The goal is to find the maximal uncertainty bounds under which the performance specification is satisfied. To illustrate, consider the islanded system in Chapter 6 and suppose we know that the vector of parameters $q = [R \;\; L \;\; C]$ is uncertain but we cannot say definitely what variations in R, L, and C might be encountered. Now, if the performance specification (stability) is satisfied at $q_0 = [R_0 \;\; L_0 \;\; C_0]$, one can consider the following problem: Replace $q = q_0$ by $q = q_0 + \Delta q = [R_0 + \Delta R \;\; L_0 + \Delta L \;\; C_0 + \Delta C]$ and determine how large $\Delta q = [\Delta R \;\; \Delta L \;\; \Delta C]$ can be while preserving satisfaction of the performance specification (stability). This maximal value, call it $r_{max} = [\Delta R_{max} \;\; \Delta L_{max} \;\; \Delta C_{max}]$, is called the robustness margin.

D.2 Notation for Uncertain Systems

In most books on control theory, a transfer function $G(s)$ or a polynomial $P(s)$ has "s" as its only argument. Here, however, we use two argument functions; for example, we write $G(s, q)$ instead of $G(s)$ to emphasize dependence of a transfer function on a vector of uncertain parameters q. This is explained below.

D.2.1 Notation for Uncertain Parameters

We use the notation q to represent a vector of real *uncertain parameters* with i-th component q_i. We often refer to q simply as the *uncertainty*. If the uncertainty is l-dimensional, it is often convenient to describe q by writing $q = (q_1, q_2, ..., q_l)$, whereas in other cases, we take q to be a column vector. In either event, we write $q \in \mathbf{R}^l$ and it is clear from the context whether an l-tuple or a column vector is intended.

In the field of robust control theory, we encounter various *uncertain quantities* which depend on q. To emphasize the dependence on q, we include q as an argument of various functions of interest. For example, as mentioned above, to represent a transfer function with uncertain parameters, we write $G(s, q)$ instead of the usual $G(s)$. If numerator and denominator of this transfer function are of concern, we emphasize the dependence by writing

$$G(s, q) = \frac{N(s, q)}{D(s, q)},$$

where $N(s, q)$ and $D(s, q)$ are polynomials in s with coefficients which depend on q. In many cases, we break things down to an even finer level. For example, to denote dependence of the coefficients of $N(s, q)$ and $D(s, q)$ on q, we can write

$$N(s, q) = \sum_{i=0}^{m} a_i(q)s^i$$

and

$$D(s, q) = \sum_{i=0}^{n} b_i(q)s^i.$$

There are dozens of additional examples illustrating q notation in linear systems theory; e.g., if a linear system has a conventional state space representation $\dot{x}(t) = Ax(t)$, we can emphasize the dependance on q by writing

$$\dot{x}(t) = A(q)x(t).$$

Finally, note that we generally append the word "uncertain" to various quantities which depend on q. For example, we refer to an uncertain plant $G(s, q)$, an uncertain polynomial $P(s, q)$ or an uncertain matrix $A(q)$.

D.2.2 Uncertainty Bounding Sets and Norms

For robustness problems, we often assume an apriori bound Q for the vector of uncertain parameters q. We call Q the *uncertainty bounding set.* Motivated by classical engineering considerations, we generally take Q to be a ball in some appropriate norm–usually (but not necessarily) centered at $q = 0$. The two most important norms we consider are l^∞ and l^2. In the l^∞ case, we consider the *max norm*

$$\|q\|_\infty = \max_i |q_i|.$$

We refer to a ball in this norm as a *box.* For example, to describe a box of unit radius with center q^*, we write $\|q - q^*\|_\infty \leq 1$. Often we want to describe such a box via componentwise bounds; e.g., consider

$$Q = \{q \in \mathbf{R}^l : q_i^- \leq q_i \leq q_i^+ \text{ for } i = 1, 2, ..., l\},$$

where q_i^- and q_i^+ are the specified bounds for the i-th component q_i of q.

For the l^2 case, we consider the standard euclidian norm

$$\|q\|_2 = \left(\sum_{i=1}^{l} q_i^2 \right)^{\frac{1}{2}}.$$

Hence, a ball of unit radius and center q^* is described by the inequality $\|q - q^*\|_2 \leq 1$ and is referred to as a *sphere.* On a few occasions, we exploit the l^1 norm

$$\|q\|_1 = \sum_{i=1}^{l} |q_i|.$$

and refer to a ball in this norm as a *diamond.* Analogous to the l^∞ and l^2 cases, the ball of unit radius and center q^* is described by $\|q - q^*\|_1 \leq 1$.

D.2.3 Notation for Families

An uncertain function together with its uncertainty bounding set is called a *family.* To illustrate, suppose that we are given an uncertain plant $G(s, q)$ and uncertainty bounding set Q. Then we denote the resulting family of plants by $\mathcal{G} = \{G(., q) : q \in Q\}$. If $G(s, q) = N(s, q)/D(s, q)$, where

$N(s,q)$ and $D(s,q)$ are uncertain polynomials, then we can write $\mathcal{N} = \{N(.,q) : q \in Q\}$ for the family of numerators and use the notation $\mathcal{D} = \{D(.,q) : q \in Q\}$ for the family of denominators. Finally, if $A(q)$ is a matrix whose entries depend on q, the notation $\mathcal{A} = \{A(q) : q \in Q\}$ is used to describe the family of matrices.

D.2.4 Uncertain Functions Versus Families

It is important to make a distinction between uncertain functions and families. For example, we differentiate between the uncertain polynomial $P(s,q)$ and a family of polynomials $\mathcal{P} = \{P(.,q) : q \in Q\}$. In other words, the uncertain polynomial $P(s,q)$ in combination with the uncertainty bounding set Q defines the family of polynomials $\mathcal{P}$.

D.2.5 Definitions

This subsection provides some basic definitions and powerful theorems which enable us to analyze robust stability of most structured uncertainty problems. For a detailed proof of the theorems, the reader is referred to [48].

Definition D.2.1 (Stability): A fixed polynomial $P(s)$ is said to be *stable* if all of its roots lie in the strict left half plane.

Definition D.2.2 (Robust Stability): A given family of polynomials $\mathcal{P} = \{P(.,q) : q \in Q\}$ is said to be *robustly stable* if, for $q \in Q$, $P(s,q)$ is stable; that is, for all $q \in Q$, all roots of $P(s,q)$ lie in the strict left half plane.

Definition D.2.3 (Invariant Degree): A family of polynomials given by $\mathcal{P} = \{P(.,q) : q \in Q\}$ is said to have *invariant degree* if the following condition holds: Given any $q^1, q^2 \in Q$, it follows that

$$\deg \mathrm{P}(\mathrm{s}, q^1) = \deg \mathrm{P}(\mathrm{s}, q^2).$$

If, for all $q \in Q$, deg P(s, q) = n, then we call $\mathcal{P}$ a *family of n-th order polynomials*. Finally, if $\mathcal{P}$ does not have invariant degree, we say that *degree dropping* occurs.

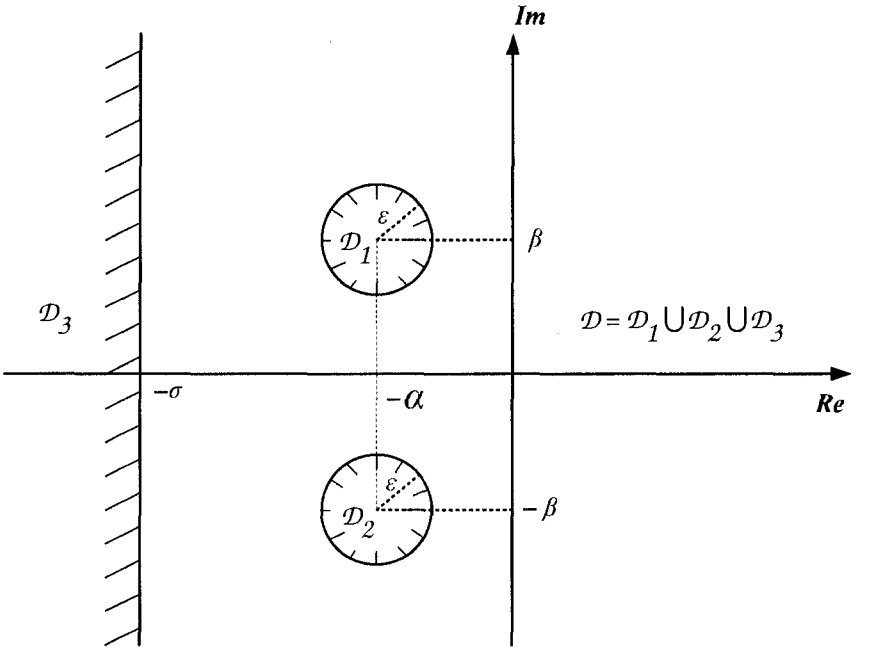

Figure D.1: $\mathcal{D}$ Region for Dominant Roots and Degree of Stability

Definition D.2.4 ($\mathcal{D}$-Stability): Let $\mathcal{D} \subseteq C$ and take $P(s)$ a to be a fixed polynomial. Then $P(s)$ is said to be *$\mathcal{D}$-stable* if all its roots lie in the region $\mathcal{D}$.

Definition D.2.5 (Robust $\mathcal{D}$-Stability): A family of polynomials $\mathcal{P} = \{P(.,q) : q \in Q\}$ is said to be *robustly $\mathcal{D}$-Stable* if, for all $q \in Q$, $P(s,q)$ is $\mathcal{D}$-stable; i.e., all roots of $P(s,q)$ lie in $\mathcal{D}$. For the special case when $\mathcal{D}$ is the open left half plane, $\mathcal{P}$ is simply said to be *robustly stable.*

Example 1 For high order control systems, a typical specification might be as follows: The closed-loop polynomials should have a pair of "dominant roots" in circles of given radius $\epsilon > 0$ centered at $-\alpha \pm j\beta$, and all remaining roots having real part less than $-\sigma$, where $\sigma > 0$. This leads us to consider a $\mathcal{D}$ region as in Figure D.1. In a robustness context, if deg $P(s,q) = n$ for each $q \in Q$, we require 2 roots in $\mathcal{D}_1 \bigcup \mathcal{D}_2$ and $n-2$ roots in $\mathcal{D}_3$.

D.3 Kharitonov's Theorem

In this section first, the theorem of Kharitonov is addressed. Kharitonov's Theorem is a powerful tool for analyzing robust stability of an interval polynomial family. Then, the Kharitonov rectangle which is actually a value set corresponding to a rather specialized uncertainty structure is

introduced. Based on the motion of the Kharitonov rectangle in the complex plane, one can verify robust stability of an interval polynomial.

D.3.1 Independent Uncertainty Structure

Definition D.3.1 (Independent Uncertainty Structure): An uncertain polynomial

$$P(s,q) = \sum_{i=0}^{n} a_i(q)s^i$$

is said to have an *independent uncertainty structure* if each component q_i of q enters into only one coefficient.

Definition D.3.2 (Interval Polynomial Family): A family of polynomials $\mathcal{P} = \{P(.,q) : q \in Q\}$ is said to be an *interval polynomial family* if $P(s,q)$ has an independent uncertainty structure, each coefficient depends continuously on q and Q is a box. For brevity, we often drop the word "family" and simply refer to $\mathcal{P}$ as an *interval polynomial.*

Example 2 Notice that the definition of interval polynomial does not rule out the possibility that some coefficients of $P(s,q)$ are fixed rather than uncertain; e.g., consider $P(s,q) = (5 + q_4)s^4 + 3s^3 + (2 + q_2)s^2 + (4 + q_1)s + 6$ with a given box Q for the uncertainty bounding set.

D.3.2 Shorthand Notation

The uncertainty representation often involves a certain type of redundancy. For example, if $P(s,q) = s^3+(5+q_2+2q_3)s^2+(6+2q_1+5q_4)s+(3+q_0)$ and bounds $|q_i| \leq 0.5$ for $i = 0, 1, 2, 3, 4$, one can "lump" the uncertainty as follows: Define new uncertain parameters $\tilde{q}_2 = 5+q_2+2q_3$, $\tilde{q}_1 = 6+2q_1+5q_4$ and $\tilde{q}_0 = 3+q_0$, a new uncertainty bounding set $\tilde{Q}$ by $2.5 \leq \tilde{q}_0 \leq 3.5$, $2.5 \leq \tilde{q}_1 \leq 9.5$ and $3.5 \leq \tilde{q}_2 \leq 6.5$ and a new uncertain polynomial $\tilde{P}(s,\tilde{q}) = s^3 + \tilde{q}_2 s^2 + \tilde{q}_1 s + \tilde{q}_0$. We call $\tilde{\mathcal{P}} = \{\tilde{P}(.,\tilde{q}) : \tilde{q} \in \tilde{Q}\}$ a *lumped version* of the original family $\mathcal{P}$ and it is easy to verify that $\tilde{\mathcal{P}} = \mathcal{P}$

In view of the discussion of lumping above, we henceforth work with an uncertain polynomial of the form

$$P(s,q) = \sum_{i=0}^{n} q_i s^i$$

when dealing with an interval family. Such a family is completely described by the shorthand notation

$$P(s,q) = \sum_{i=0}^{n} [q_i^- \; q_i^+] s^i$$

with $[q_i^- \; q_i^+]$ denoting the bounding interval for i-th component of uncertainty q_i. We refer to $P(s,q)$ as an *interval polynomial.*

D.3.3 Kharitonov's Theorem

Definition D.3.3 (The Kharitonov Polynomials): Associated with interval polynomial $P(s,q) = \sum_{i=0}^{n} [q_i^- \; q_i^+] s^i$ are the four fixed *Kharitonov polynomials*

$$\begin{aligned}
K_1(s) &= q_0^- + q_1^- s + q_2^+ s^2 + q_3^+ s^3 + q_4^- s^4 + q_5^- s^5 + q_6^+ s^6 + \ldots; \\
K_2(s) &= q_0^+ + q_1^+ s + q_2^- s^2 + q_3^- s^3 + q_4^+ s^4 + q_5^+ s^5 + q_6^- s^6 + \ldots; \\
K_3(s) &= q_0^+ + q_1^- s + q_2^- s^2 + q_3^+ s^3 + q_4^+ s^4 + q_5^- s^5 + q_6^- s^6 + \ldots; \\
K_4(s) &= q_0^- + q_1^+ s + q_2^+ s^2 + q_3^- s^3 + q_4^- s^4 + q_5^+ s^5 + q_6^+ s^6 + \ldots.
\end{aligned}$$

Theorem D.3.1 (Kharitonov's Theorem [109]): *An interval polynomial family $\mathcal{P}$ with invariant degree is robustly stable if and only if its four Kharitonov polynomials are stable.*

D.3.4 The Kharitonov Rectangle

Given an interval polynomial $P(s,q) = \sum_{i=0}^{n} [q_i^- \; q_i^+] s^i$ and a fixed frequency $\omega = \omega_0$, the set of possible values that $P(j\omega_0, q)$ can assume as q ranges over the box Q is of interest. More formally, we want to describe the subset of the complex plane given by

$$P(j\omega_0, Q) = \{P(j\omega_0, q) : q \in Q\}.$$

It is proved that $P(j\omega_0, Q)$ is a rectangle with vertices which are obtained by evaluating the four *fixed* Kharitonov polynomials $K_1(s)$, $K_2(s)$, $K_3(s)$, and $K_4(s)$ at $s = j\omega_0$; i.e., the vertices of $P(j\omega_0, Q)$ are precisely the $K_i(j\omega_0)$. This rectangle is a special type of "value set" and we call it the *Kharitonov rectangle.* When frequency ω sweeps the positive real axis, Kharitonov rectangle moves around the complex plane.

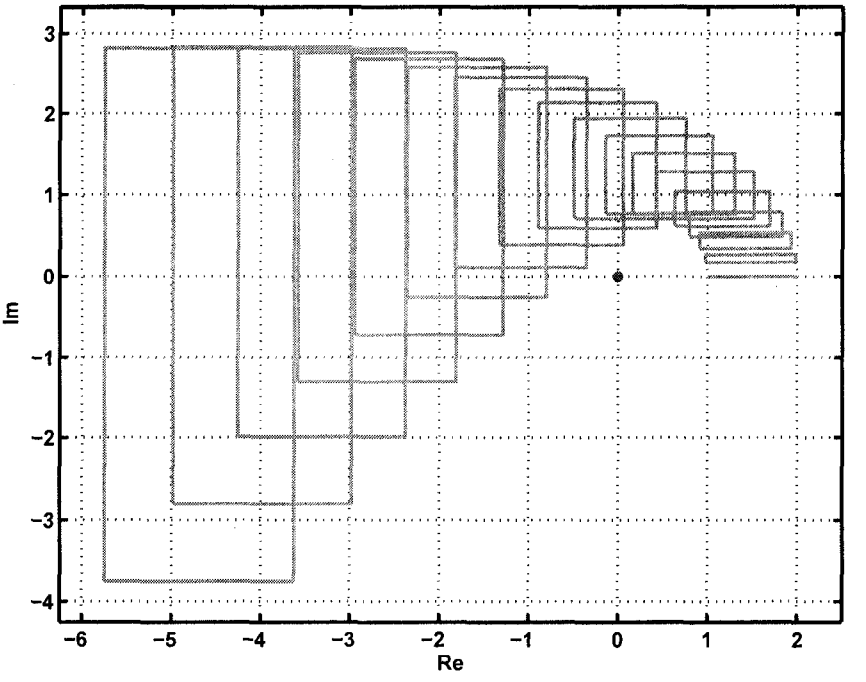

Figure D.2: Motion of Kharitonov rectangle for Example 3

Example 3 (Illustration of Motion): For the interval polynomial

$$P(s, q) = [0.5\ \ 2]s^3 + [2.5\ \ 3]s^2 + [2\ \ 3]s + [1\ \ 2],$$

the motion of the Kharitonov rectangle $P(j\omega, Q)$ is shown in Figure D.2 for 18 frequencies evenly spaced between $\omega = 0$ and $\omega = 1.5$ rad/sec. Notice that this rectangle begins at $\omega = 0$ as an interval on the positive real axis and then moves from the first to the second, and from the second to the third quadrant as ω increases.

D.3.5 The Zero Exclusion Condition

In this section, we introduce the Zero Exclusion Condition. There are several versions of the Zero Exclusion Condition lemmas in the literature. Since we are currently working within the framework of interval polynomials, the lemma below is not stated in full generality; the most general version of the Zero Exclusion Condition is given in Theorem D.4.1.

Lemma 1 (Zero Exclusion Condition): *Suppose that an interval polynomial family* $\mathcal{P} = \{P(.,q) : q \in Q\}$ *has invariant degree and at least one stable member* $P(s,q^0)$. *Then* $\mathcal{P}$ *is robustly stable if and only if* $z = 0$ *is excluded from the Kharitonov rectangle at all nonnegative frequencies; i.e.,*

$$0 \notin P(j\omega, Q)$$

for all frequencies $\omega \geq 0$.

D.3.6 Robust Stability Testing Via Graphics

The Zero Exclusion Condition (Lemma 1) suggests a simple graphical procedure for checking robust stability–watch the motion of the Kharitonov rectangle $P(j\omega, q)$ as ω varies from 0 to $+\infty$ and determine by inspection if the the condition $0 \notin P(j\omega, Q)$ is satisfied. The following question arises: Is there any finite pre-computable *cutoff frequency* $\omega_c > 0$ such that $0 \notin P(j\omega, Q)$ for all $\omega \geq \omega_c$? That is, can we terminate the frequency sweep at the frequency $\omega = \omega_c$?

The existence of ω_c is easily established using the invariant degree condition. Indeed, suppose that $P(s,q) = \sum_{i=0}^{n}[q_i^- \; q_i^+]s^i$ and, without loss of generality, assume that $q_i^- > 0$ for $i = 0, 1, ..., n$. Then given any $q \in Q$, it is easy to see that for $\omega \geq 0$,

$$|P(j\omega, q)| \geq q_n^-\omega^n - \sum_{i=0}^{n-1} q_i^+\omega^i.$$

Since the right-hand side tends to $+\infty$ as $\omega \to \infty$, it follows that for any prescribed $\beta > 0$ there exists an $\omega_c > 0$ such that $|P(j\omega, q)| \geq \beta$ for all $\omega > \omega_c$. Hence, $0 \notin P(j\omega, Q)$ for all $\omega > \omega_c$.

In fact, we can easily compute an appropriate ω_c. For example, one can take ω_c to be the largest real root of the polynomial

$$f(\omega) = q_n^-\omega^n - \sum_{i=0}^{n-1} q_i^+\omega^i.$$

D.3.7 Overbounding via Interval Polynomials

The independent uncertainty structure is restrictive because uncertain parameters typically enter into more than one coefficient. For such "dependent" uncertainty structures, we consider two

alternatives: The first alternative is to develop more general results; this is the topic of the next sections. The second alternative is the so-called *overbounding method*, which is described below. It should be mentioned that although the overbounding method is easy to use, it may lead to unduly conservative results; i.e., we only obtain sufficient conditions for robustness. In short, there is a trade-off between ease of use and degree of conservatism associated with overbounding.

We begin with the uncertain polynomial $P(s,q) = \sum_{i=0}^{n} a_i(q)s^i$ and an uncertainty bounding set Q which is closed and bounded but not necessarily a box. Assuming the coefficient functions $a_i(q)$ depend continuously on q, the following bounds are defined.

$$\bar{q}_i^- = \min_{q \in Q} a_i(q)$$

$$\bar{q}_i^+ = \max_{q \in Q} a_i(q)$$

It is simply observed that the family of polynomials $\bar{\mathcal{P}}$ described by

$$\bar{P}(s,\bar{q}) = \sum_{i=0}^{n} [\bar{q}_i^- \;\; \bar{q}_i^+] s^i$$

is a superset of $\mathcal{P}$. Therefore, any robustness property which holds for the interval polynomial family $\bar{\mathcal{P}}$ must hold for $\mathcal{P}$. In particular, robust stability of $\bar{\mathcal{P}}$ implies robust stability of $\mathcal{P}$. Note, however, that the converse is not true. These points can be simply verified through the examples discussed in [48,93].

D.4 The Value Set Concept

In this section, the value set is defined mathematically. It is observed that the value set is a generalization of the Kharitonov rectangle. The imaginary axis is replaced by the boundary of a desired root location region $\mathcal{D}$. Subsequently, a link is established between robust $\mathcal{D}$-stability and the value set; i.e., a more general Zero Exclusion Condition is established.

D.4.1 Zero Exclusion Condition for Robust $\mathcal{D}$-Stability

It is proved that the zero exclusion concept can be extended to the more general robust $\mathcal{D}$-stability problems. A more general definition of the value set is provided. Instead of calculating an uncertain polynomial along the imaginary axis, an arbitrary point in the complex plane is considered. In other words, instead of sweeping the imaginary axis, we sweep the boundary of $\mathcal{D}$ where $\mathcal{D}$ is a desired root location. Theorem D.4.1 provides the most general version of the Zero Exclusion Condition, which is given in most robust control literatures [48].

Definition D.4.1 (The Value Set at $z \in \mathbf{C}$): Given a family of polynomials $\mathcal{P} = \{P(., q) : q \in Q\}$, the *value set* at $z \in \mathbf{C}$ is defined by

$$P(z, Q) = \{P(z, q) : q \in Q\}.$$

In other words, $P(z, Q)$ is the image of Q under $P(z, .)$.

Definition D.4.2 (Pathwise Connectedness): A set $X \subseteq \mathbf{R}^k$ is said to be *pathwise connected* if given any two points $x^0, x^1 \in X$, there is a continuous function $\Phi : [0,\ 1] \rightarrow X$ such that $\Phi(0) = x^0$ and $\Phi(1) = x^1$.

Theorem D.4.1 (Zero Exclusion Condition): *Let $\mathcal{D}$ be an open subset of the complex plane and suppose that $\mathcal{P} = \{P(., q) : q \in Q\}$ is a family of polynomials with invariant degree, uncertainty bounding set Q which is pathwise connected. Furthermore, assume that the coefficient functions $a_i(q)$ are continuous and that $\mathcal{P}$ has at least one $\mathcal{D}$-stable member $P(s, q^0)$. Then $\mathcal{P}$ is robustly $\mathcal{D}$-stable iff*

$$0 \notin P(z, Q)$$

for all $z \in \partial\mathcal{D}$, where $\partial\mathcal{D}$ denotes the boundary of $\mathcal{D}$.

D.4.2 Boundary Sweeping Functions

The concept of a boundary sweeping function is introduced in this section. The boundary sweeping function facilitates generation of the value set and test of zero exclusion condition. Indeed, since the analysis of robust $\mathcal{D}$-stability using the Zero Exclusion Condition requires sweeping the

boundary $\partial\mathcal{D}$ of $\mathcal{D}$, it is more convenient to parameterize $\partial\mathcal{D}$ by a scalar parameter δ. The parameter δ for robust $\mathcal{D}$-stability analysis plays the same role as ω does in ordinary robust analysis.

Definition D.4.3 (Boundary Sweeping Function): Suppose that $\mathcal{D}$ is an open subset of the complex plane with boundary $\partial\mathcal{D}$. Then, given an interval (perhaps semi-infinite of infinite) $I \subseteq \mathbf{R}$, a mapping $\Phi_{\mathcal{D}} : I \to \partial\mathcal{D}$ is said to be a *boundary sweeping function* for $\mathcal{D}$ if $\Phi_{\mathcal{D}}$ is continuous and onto; i.e., $\Phi_{\mathcal{D}}$ is continuous and for each point $z \in \partial\mathcal{D}$, there exists some $\delta \in I$ such that

$$\Phi_{\mathcal{D}}(\delta) = z.$$

The scalar δ is called a *generalized frequency* variable for $\mathcal{D}$.

Example 4 : When region $\mathcal{D}$ is the interior of the disks centered at $\alpha \pm \beta$ and radius of r, a boundary sweeping function with $I = [0, 2\pi]$ can be

$$\Phi_{\mathcal{D}}(\delta) = \alpha \pm \beta + re^{j\delta}.$$

D.5 Polytopes of Polynomials

Robustness theory for independent uncertainty structures leads to conservative results when applied to more general uncertainty structures. In other words, overbounding using independent uncertainty structures is conservative since only sufficient conditions for robustness are obtained.

In this section, dependent uncertainty structures are addressed in a more direct manner. We consider the systems whose coefficients depend affine linearly on the vector of uncertain parameters q. In this type of systems, polytopes of polynomials are the basic elements to study when the uncertainty bounding set Q is a box. It turns out that the value sets corresponding to such family of polynomials are convex polygons.

D.5.1 Affine Linear Uncertainty Structures

Affine linear uncertainty structures arise in a number of ways such as feedback interconnections. It can easily prove that affine linear uncertainty structures are preserved under large classes of feedback interconnections.

Definition D.5.1 (Affine Linear Uncertainty Structure): An uncertain polynomial $P(s,q) = \sum_{i=0}^{n} a_i(q)s^i$ is said to have an *affine linear uncertainty structure* if each coefficient function $a_i(q)$ is affine linear function of q; i.e., for each $i \in \{0, 1, 2, ..., n\}$, there exists a column vector α_i and a scalar β_i such that

$$a_i(q) = \alpha_i^T q + \beta_i,$$

where $\alpha_i^T(q)$ is the transpose of $\alpha_i(q)$. More generally, an uncertain rational function $G(s,q) = N(s,q)/D(s,q)$ is said to have an *affine linear uncertainty structure* if both polynomials $N(s,q)$ and $D(s,q)$ have affine linear uncertainty structures.

D.5.2 Convex Analysis

In this section, we review some very elementary material from the theory of convex analysis. This theory is required for the robustness analysis of the systems with affine linear uncertainty structures.

Definition D.5.2 (Convex Set and Convex Hull): A set $A \subseteq \mathbf{R}^k$ is said to be *convex* if the line joining any two points a^1 and a^2 in A remains entirely within A; i.e., given any $a^1, a^2 \in A$ and $t \in [0, 1]$, it follows that $ta^1 + (1-t)a^2 \in A$. $ta^1 + (1-t)a^2$ is called a *convex combination* of a^1 and a^2. Figure D.3 shows a convex set and a nonconvex set in $\mathbf{R}^2$.

Given a set $A \subseteq \mathbf{R}^k$ (not necessarily convex), its *convex hull*, conv A, is the "smallest" convex set which contains A. More precisely, if $\mathcal{A}^+$ denotes the collection of all convex sets which contains the set A, then we have

$$conv\ A = \bigcap_{A^+ \in \mathcal{A}^+} A^+.$$

Fig D.4 shows a nonconvex set and its convex hull. Notice that $conv\ A \supseteq A$.

Definition D.5.3 (Polytopes): The convex hull of a finite set of points $\{p^1, p^2, ..., p^m\}$ in $\mathbf{R}^k$ is called a *polytope* $\mathbf{P}$ and it is written as

$$\mathbf{P} = conv\ \{p^1, p^2, ..., p^m\}.$$

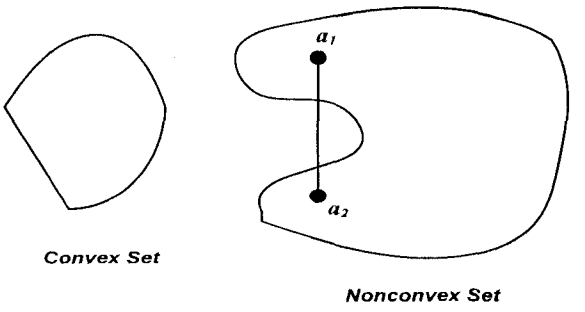

Figure D.3: Examples of convex and nonconvex sets

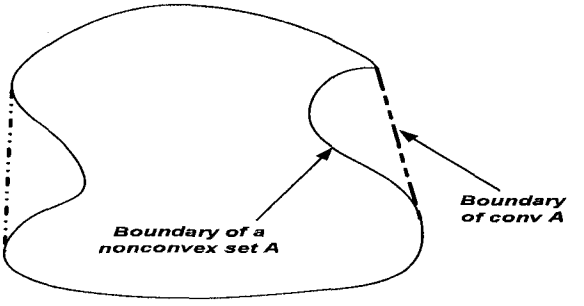

Figure D.4: A nonconvex set and its convex hull

The set of points $\{p^1, p^2, ..., p^m\}$ is called the *set of generators*. It should be noted that the set of generators can be highly nonunique.

Definition D.5.4 (Extreme Points): Assume that $\mathbf{P} = conv\ \{p^i\}$ is a polytope in $\mathbf{R}^k$. Then a point $p \in \mathbf{P}$ is said to be an *extreme point* of $\mathbf{P}$ if it cannot be expressed as a convex combination of two distinct points in $\mathbf{P}$. That is, there does not exist $p^a, p^b \in \mathbf{P}$ with $p^a \neq p^b$ and $t \in (0, 1)$ such that $tp^a + (1 - t)p^b = p$.

Reader can find more material about the other properties of the convex sets such as *convex combination* and direct sum in [48].

D.5.3 Polytopes of Polynomials

Definition D.5.5 (Polytopes of Polynomials): A family of polynomials $\mathcal{P} = \{P(., q) : q \in Q\}$ is said to be a *polytope of polynomials* if $P(s, q)$ has an affine linear uncertainty structure and Q is a polytope. If $Q = conv\ \{q^i\}$, then $P(s, q^i)$ is called the *i-th generator* for $\mathcal{P}$.

Theorem D.5.1 (Value Set for a Polytope of Polynomials): *Let* $\mathcal{P} = \{P(.,q) : q \in Q\}$ *be a polytope of polynomials with uncertainty bounding set* $Q = conv\{q^i\}$. *Then, for fixed* $z \in \mathbf{C}$, *the value set* $P(z, Q)$ *is a polygon with generating set* $\{P(z, q^i)\}$. *That is,*

$$P(z, Q) = conv\ \{P(z, q^i)\}.$$

Furthermore, all edges of the polygon $P(z, Q)$ *are obtained from the edges of* Q *in the following sense: If* z_0 *is a point on an edge of* $P(z, Q)$, *then* $z_0 = P(z, q^0)$ *for some* q^0 *on an edge of* Q.

Example 5 (Polygonal Value Sets for Test of Robust $\mathcal{D}$-Stability): Consider the polytope of polynomials $\mathcal{P}$ described by

$$P(s,q) = (1 - q_0 + q_1)s^3 + (30 + q_0 + 3q_2)s^2 + (88 + q_1 + q_2)s + (160 - 0.5q_0 + q_2)$$

and the uncertainty bounding set Q which is $0.5 \leq q_0 \leq 1.5$, $1.75 \leq q_1 \leq 2.25$, and $1 \leq q_2 \leq 2$. Notice that for $q^0 = [1,\ 2,\ 1.5]$, the *nominal* polynomial $P(s, q^0) = 2s^3 + 35.5s^2 + 91.5s + 161$ has roots $s_1 = -15.0684$ and $s_{2,3} = -1.3408 \pm 1.8827j$. The specification for the system is to have two "dominant" poles remain within circles of radius $r = 0.9$ centered at $s = -2 \pm 2j$ and a third pole with real part less than -9. Therefore, the desired pole location region $\mathcal{D}$ is the interior of the circles and left side of vertical line $\sigma = -9$. By sweeping the boundary of $\mathcal{D}$ using the following functions

$$\Phi_{\mathcal{D}}(\delta) = -2 \pm 2j + 0.9e^{j\delta}, \qquad \delta \in [0, 2\pi]$$

and

$$\Psi_{\mathcal{D}}(\omega) = -9 + j\omega, \qquad 0 \leq \omega \leq 10$$

we generate appropriate value sets $P(\Phi, Q)$ and $P(\Psi, Q)$. Using the Zero Exclusion Condition and polygonal value set depicted in Figure D.5, we deem the family $\mathcal{P}$ to be robustly $\mathcal{D}$-stable.

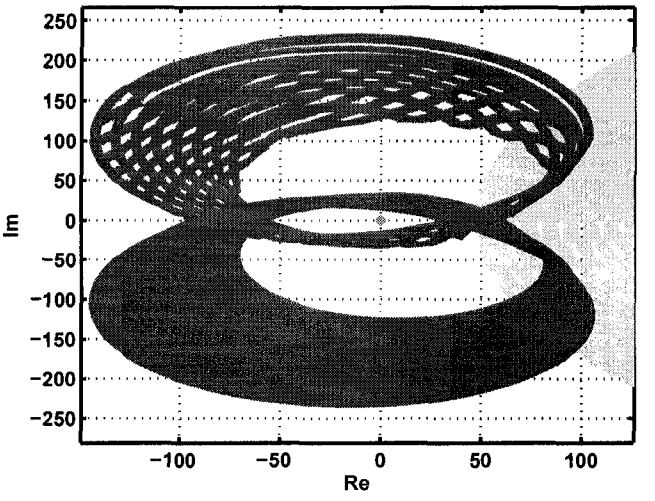

Figure D.5: Polygonal value sets for Example 5

D.6 Multilinear Uncertainty Structure

This section presents robust $\mathcal{D}$-stability of systems with multilinear uncertainty structures. In other words, uncertain polynomials whose coefficients depend multilinearly on the vector of uncertain parameters q are considered. Using the Mapping Theorem, we can often generate the tightest possible polytopic overbound for the value sets and coefficient sets of interest.

Definition D.6.1 (Multilinear and Polynomic Uncertainty Structures): An uncertain polynomial $P(s,q) = \sum_{i=0}^{n} a_i(q)s^i$ is said to have a *multilinear uncertainty structure* if each coefficient $a_i(q)$ is a multilinear function. That is, if one component of vector q is assumed variable parameter and the rest are assumed fixed, then $a_i(q)$ is affine linear in the assumed variable component of q. In general, $P(s,q)$ is said to have a *polynomic uncertainty structure* if each coefficient $a_i(q)$ is a multivariable polynomial function in the components of q.

Example 6 Consider the islanded system discussed in Chapter 6. The transfer function of the

open-loop system is $G(s,q) = N(s,q)/D(s,q)$ in which $q = [R_x\ L_x\ C_x]$ and

$$\begin{aligned} D(s,q) &= (R_xL_xC_xL_t)s^3 \\ &+ (R_xL_xC_xR_t + R_xC_xR_tL_t + L_tL_x)s^2 \\ &+ (R_xC_xR_tR_l + R_tL_x + R_lL_t + R_xL_t + R_xL_x)s \\ &+ (R_xR_t + R_xR_l + R_tR_l). \end{aligned}$$

As it is observed, $D(s,q)$ has a multilinear uncertainty structure, whereas the islanded system discussed in Chapter 5 has a polynomic uncertainty structure.

Remark D.6.1 Thus far, four different types of uncertainty structures have been defined for polynomials. Let $\mathcal{P}_{inter}$, $\mathcal{P}_{aff}$, $\mathcal{P}_{multi}$, and $\mathcal{P}_{poly}$ denote the family of polynomials with independent, affine, multilinear, and polynomic uncertainty structures, respectively. We can obviously deduce the following *hierarchy* on the uncertainty structures

$$\mathcal{P}_{inter} \subset \mathcal{P}_{aff} \subset \mathcal{P}_{multi} \subset \mathcal{P}_{poly}.$$

Lemma D.6.1 (Sideris and Sanchez Pena [111]): *Given a family of polynomials $\mathcal{P} = \{P(.,q) : q \in Q\}$ in which $P(s,q)$ has a polynomic uncertainty structure and the uncertainty bounding set Q is a polytope. Then there exists a second family of polynomials $\tilde{\mathcal{P}} = \{\tilde{P}(.,\tilde{q}) : \tilde{q} \in \tilde{Q}\}$ such that $\tilde{P}(s,\tilde{q})$ has multilinear uncertainty structure, $\tilde{Q}$ is a polytope and*

$$\tilde{\mathcal{P}} = \mathcal{P}.$$

Example 7 Consider the uncertain polynomial

$$P(s,q) = (q_1^3 + q_1^2q_2 + 20)s^3 + s^2 + (q_1^2 + 2q_2^2 + 20)s + (q_1q_2 + q_1 + 14)$$

with uncertainty bounds $-1 \le q_1 \le 2$ and $-2 \le q_2 \le 4$. We "expand" the uncertainty space by defining new uncertain variables $q_1^3 \longmapsto \tilde{q}_1\tilde{q}_2\tilde{q}_3$ and $q_2^2 \longmapsto \tilde{q}_4\tilde{q}_5$. The new family of polynomials

$\tilde{\mathcal{P}}$ is described by $\tilde{q} \in \mathbf{R}^5$, uncertain polynomial with multilinear uncertainty structure given by

$$\tilde{P}(s,\tilde{q}) = (\tilde{q}_1\tilde{q}_2\tilde{q}_3 + \tilde{q}_1\tilde{q}_2\tilde{q}_4 + 20)s^3 + s^2 + (\tilde{q}_1\tilde{q}_2 + 2\tilde{q}_4\tilde{q}_5 + 20)s + (\tilde{q}_1\tilde{q}_4 + \tilde{q}_1 + 14)$$

and polytopic uncertainty bounding set $\tilde{Q}$ described by $-1 \leq \tilde{q}_1 = \tilde{q}_2 = \tilde{q}_3 \leq 2$, and $-2 \leq \tilde{q}_4 = \tilde{q}_5 \leq 4$.

D.6.1 Lack of Extreme Points and Edge Results

We have seen that there is a lack of vertex or extreme points results for affine uncertainty structures. Therefore, we had to develop edge results to overcome this type of problems. Now, this question arises; whether similar results can be used for multilinear uncertainty structures. The following example verifies that the answer is no. In other words, there is a lack of edge results for multilinear uncertainty structures.

Example 8 Consider the family of polynomials described by

$$P(s,q) = (4.1 + 2q_1q_2 + 4q_1 + 4q_2)s^3 + (2 + q_1 + q_2)s^2 + (2 + q_1 + q_2)s + 1$$

and uncertainty bounds $-0.5 \leq q_1 \leq 0.5$ and $-0.5 \leq q_2 \leq 0.5$. The four edges of the uncertainty bounding set Q all lead to stable polynomials. However, for $q = [0\ 0]$, $P(s,q)$ is unstable. Therefore, robust stability cannot be guaranteed by checking extreme points or edges.

D.6.2 The Mapping Theorem

Robust stability analysis for uncertain polynomials with multilinear structures can be quite complicated. However, with the aid of the Mapping Theorem below, we can often establish robust stability using a "special" overbounding family of polynomials. The power of the Mapping Theorem is derived from the fact that this overbounding family turns out to be the convex hull of the original family. Moreover, this convex hull family is seen to be polytope of polynomials. It should be noted that although the Mapping Theorem can be applied to most uncertainty structures, it is a sufficient condition theorem. Unlike the other overbounding methods, the Mapping Theorem

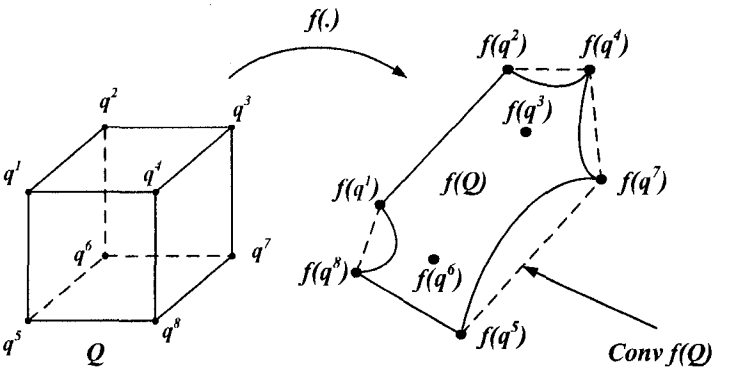

Figure D.6: Geometry associated with the Mapping Theorem

uses the convex hull and this results in the "tightness" of the approximation. Now, we explain the Mapping Theorem and its geometric interpretation.

Theorem D.6.2 (The Mapping Theorem): *Suppose* $Q \in \mathbf{R}^l$ *is a box with extreme points* $\{q^i\}$ *and* $f : Q \to \mathbf{R}^k$ *is a multilinear function. Let*

$$f(Q) = \{f(q) : q \in Q\}$$

denote the range of f. *Then*

$$conv\ f(Q) = conv\{f(q^i)\}.$$

D.6.3 Geometric Interpretation of the Mapping Theorem

The geometry interpretation of the Mapping Theorem is illustrated in Figure D.6 for $l = 3$ and $k = 2$. Notice that we obtain the tightest possible polygon bounding the range set $f(Q)$. Based on the Mapping Theorem, any $f(Q)$ which "curves outward" rather than "inward" is not realizable. For example, since taking the convex hull of the $f(q^i)$ in Figure D.7 does not yield the convex hull of $f(Q)$, it follows that $f(Q)$ cannot be the range of some multilinear function on a box. In particular, the arc joining $f(q^1)$ and $f(q^2)$ is inconsistent with the requirement of inward curvature.

There are also other inconsistencies in Figure D.7. For example, since the straight line joining q^2 and q^3 defines an edge of Q, it must be the case that $f(Q)$ contains the straight line joining $f(q^2)$ and $f(q^3)$; notice that this line is not in $f(Q)$.

Remark D.6.2 (Coefficient Interpretation): Suppose that $P(s, q)$ is an uncertain polynomial with

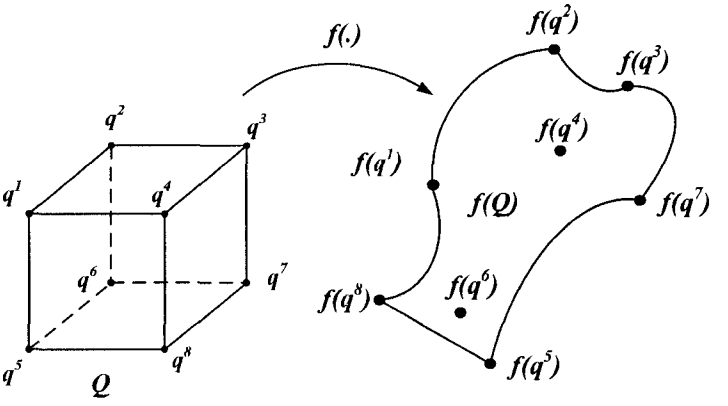

Figure D.7: A geometry which is not realizable

coefficient vector $a(q)$ depending multilinearly on q. Then, if Q is a box with set of extremes $\{q^i\}$, the Mapping Theorem provides a simple description of the convex hull of the coefficient set; i.e.,

$$conv\ a(Q) = conv\{a(q^i)\}.$$

D.6.4 Value Set Interpretation

Suppose $Q \subset \mathbf{R}^l$ is a box with extreme points $\{q^i\}$ and $P(s,q)$ is an uncertain polynomial having a multilinear uncertainty structure. Then, given any $z \in \mathbf{C}$, we consider the mapping $f : Q \to \mathbf{R}^2$ described by

$$q \mapsto (ReP(z,q), ImP(z,q)).$$

Since $ReP(z,q)$ and $ImP(z,q)$ are multilinear with respect to q, the Mapping Theorem tells us that

$$conv\ P(z,Q) = conv\{P(z,q^i)\}.$$

Having this convex hull description available, it is now easy to state a sufficient condition for robust $\mathcal{D}$-stability. The following Lemma is an immediate result of the Zero Exclusion Condition in conjunction with the Mapping Theorem.

Lemma D.6.3 (Robust $\mathcal{D}$-Stability Criterion): *Consider a family of polynomials* $\mathcal{P} = \{P(.,q) : q \in Q\}$ *with invariant degree, multilinear uncertainty structure and at least one* $\mathcal{D}$*-stable member* $P(s,q^0)$. *In addition, assume that* Q *is a box with extreme points* $\{q^i\}$ *and the desired root location*

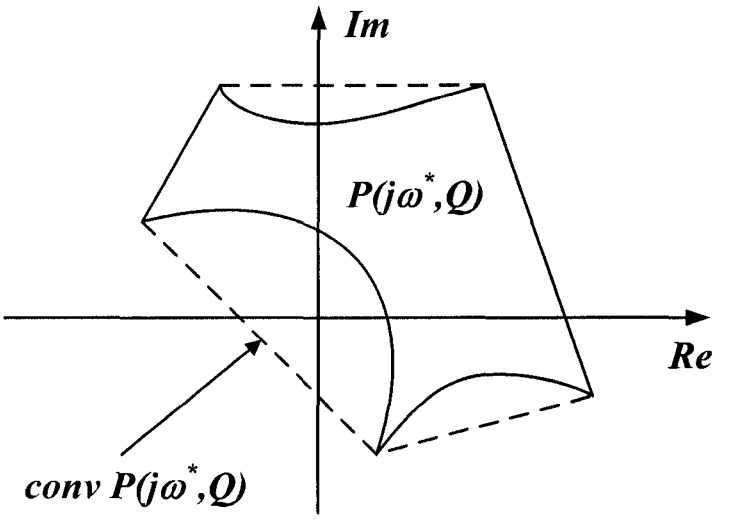

Figure D.8: Inconclusive robust stability test

region $\mathcal{D}$ is open. Then $\mathcal{P}$ is robustly $\mathcal{D}$-stable if the Zero Exclusion Condition

$$0 \notin conv\ \{P(z, q^i)\}$$

is satisfied for all $z \in \partial\mathcal{D}$.

Remark D.6.3 (Conservatism): Based on the above lemma, we now provide a value set interpretation for the fact that the Mapping Theorem only leads to a sufficient condition for robust stability. Suppose $Q \subseteq \mathbf{R}^l$ is a box and the uncertain polynomial $P(s, q)$ has a multilinear uncertainty structure. Then, in a robust $\mathcal{D}$-stability analysis, it is possible that at some frequency $\omega^* > 0$, we have $0 \in conv\ P(j\omega^*, Q)$ but $0 \notin P(j\omega^*, Q)$. This situation is shown in Figure D.8. Notice that if we are applying the polytope stability theory to the overbounding family obtained via the Mapping Theorem, we do not know if stability is lost when $z = 0$ penetrates the set $conv\ P(j\omega, Q)$. Roughly speaking, the Mapping Theorem does not give us the true value set $P(j\omega, Q)$.

References

[1] C. Schauder and H. Mehta, "Vector Analysis and Control of Advanced Static VAR Compensators," *IEE proceedings-C*, Vol. 140, No. 4, pp. 299-306, July 1993.

[2] *Standard Conformance Test Procedures for Equipment Interconnecting Distributed Resources with Electric Power Systems,* IEEE Std. 1547.1, 2005.

[3] *Inverters, Converters, and Controllers for Use in Independent Power Systems,* UL Std. 1741, June 2002.

[4] J. Stevens, R. Bonn, J. Ginn, S. Gonzalez, and G. Kern, "Development and Testing of an Approach to Anti-Islanding in Utility-Interconnected Photovoltaic systems," *Sandia National Laboratories Report SAND 2000-1939,* Sandia National Laboratories, Albuquerque, NM, August 2000.

[5] J. E. Kim and J. S. Hwang, "Islanding detection method of distributed generation units connected to power distribution system," *International Conference on Power System Technology*, Vol. 2, pp. 643-647, 4-7 Dec. 2000.

[6] T. Funabashi, K. Koyanagi, and R. Yokoyama, "A Review of Islanding Detection Methods for Distributed Resources," *IEEE Bologna Power Tech Conference*, Proceedings, Vol. 2, pp. 608-613, June 23-26, 2003.

[7] R. A. Walling, and N. W. Miller, "Distributed Generation Islanding - Implications on Power System Dynamic Performance", *Power Engineering Society Summer Meeting*, 2002 IEEE, Vol. 1, pp. 92-96, 21-25 July 2002.

[8] M. E. Ropp, M. Begovic, A. Rohatgi, G. A. Kern, R. H. Bonn, and S. Gonzalez, "Determining the Relative Effectiveness of Islanding Methods Using Phase Criteria and Nondetection Zones," *IEEE Transactions on Energy Conversion,* Vol. 15, No. 3, pp. 290-296, September 2000.

[9] S. -J. Huang, and F.-S. Pai, "Design and Operation of Grid-connected Photovoltaic System with Power-factor Control and Active Islanding Detection," *IEE Proceedings-Generation, Transmission and Distribution*, Vol. 148, No. 3, pp. 243-250, May 2001.

[10] S.-J. Huang, and F.-S. Pai, "A New Approach to Islanding Detection of Dispersed Generators with Self-commutated Static Power Converters," *IEEE Transactions on Power Delivery,* Vol. 15, No. 2, pp. 500-507, April 2000.

[11] W. Bower, M. Ropp, "Evaluation of Islanding Detection Methods for Utility-Interactive Inverters in Photovoltaic Systems," *Sandia National Laboratories Report SAND2002-3591,* Sandia National Laboratories, Albuquerque, NM, November 2002.

[12] Z. Ye, A. Kolwalkar, Y. Zhang, P. Du, and R. Walling, "Evaluation of Anti-Islanding Schemes Based on Nondetection Zone Concept", *Power Electronics Specialist, PESC 2003*, IEEE 34th Annual Conference on , Vol. 4, 15-19 June 2003, pp. 1735-1741.

[13] H. Kobayashi, K. Takigawa, E. Hashimoto, A. Kitamura, and H. Matsuda, "Method for Preventing Islanding Phenomenon on Utility Grid With a Number of Small Scale PV Systems", *Photovoltaic Specialists Conference, 1991*, Conference Record of the Twenty Second IEEE, 7-11 Oct. 1991, Vol. 1, pp. 695-700.

[14] T. Ambo, "Islanding Prevention by Slip Mode Frequency Shift," *Proceedings of the IEA PVPS Workshop on Grid-interconnection of Photovoltaic Systems*, September 1997.

[15] M. E. Ropp, M. Begovic, and A. Rohatgi, "Prevention of Islanding in Grid-connected Photovoltaic Systems," *Progress in Photovoltaics: Research and Applications*, Vol. 7, No. 1, pp. 39-59, Feb. 1999.

[16] Z. Ye, R. Walling, L. Garces, R. Zhou, L. Li, and T. Wang, "Study and Development of Anti-Islanding Control for Grid-Connected Inverters," *NREL/SR-560-36243,* National Renewable Energy Laboratory, May 2004.

[17] C. M. Riley, B. K. Lin, T. G. Habetler, and G. B. Kliman, "Stator Current Harmonics and Their Causal Vibrations: A Preliminary Investigation of Sensorless Vibration Monitoring Applications", *IEEE Transactions on Industry Applications,* Vol. 35, No. 1, pp. 94-99, January/February 1999.

[18] M. E. Ropp, K. Aaker, J. Haigh, and N. Sabbah, "Using power line carrier communications to prevent islanding," *Photovoltaic Specialists Conference*, 2000. Conference Record of the Twenty-Eighth IEEE, pp. 1675-1678, 15-22 Sept. 2000.

[19] F. Katiraei, and M. R. Iravani, "Power Management Strategies for a Microgrid With Multiple Distributed Generation Units," *IEEE Transactions on Power Systems*, Vol. 21, No. 4, pp. 1821-1831, Nov. 2006.

[20] F. Katiraei, M. R. Iravani, and P. W. Lehn, "Micro-grid Autonomous Operation During and Subsequent to Islanding Process," *IEEE Transactions on Power Delivery*, Vol. 20, No. 1, pp. 248-257, Jan. 2005.

[21] P. Piagi and R. H. Lasseter, "Autonomous control of microgrids," IEEE Power Engineering Society General Meeting, 18-22 June 2006.

[22] C. K. Sao, and P. W. Lehn, "Autonomous Load Sharing of Voltage Source Converters," *IEEE Transactions on Power Delivery,* Vol. 20, No. 2, pp. 1009-1016, April 2005.

[23] M. C. Chandorkar, D. M. Divan, and R. Adapa, "Control of Parallel Connected Inverters in Standalone AC Supply Systems," IEEE Transactions on Industry Applications, Vol. 29, No. 1, pp. 136143, Jan.Feb. 1993.

[24] J. A. Peas Lopes, C. L. Moreira, and A. G. Madureira, "Defining Control Strategies for MicroGrids Islanded Operation," *IEEE Transactions on Power Systems,* Vol. 21, No. 2, pp. 916-924, May 2006.

[25] C. K. Sao, and P. W. Lehn, "Intentional Islanded Operation of Converter Fed Microgrids," *IEEE Power Engineering Society General Meeting*, 2006, 6 pages, 18-22 June 2006.

[26] J. C. Doyle, K. Glover, P. P. Khargonekar, and B. A. Francis, "State Space Solution to Standard H_2 and H_∞ Control Problem," *IEEE Transactions on Automatic Control,* Vol. 34, No. 8, pp. 831-847, Aug. 1989.

[27] D. McFarlane, and K. Glover, "A Loop Shaping Design Procedure Using H_∞ Synthesis," *IEEE Transactions on Automatic Control*, Vol. 37, No. 6, pp. 759-769, June 1992.

[28] Y. Li, D. M. Vilathgamuwa, and P. C. Loh, "Robust Control Scheme for a Microgrid with PFC Capacitor Connected," *IEEE Industry Applications Conference*, Fourtieth IAS Annual Meeting, Vol. 4, pp. 2441-2448, 2-6 Oct. 2005.

[29] P. Mattavelli, G. Escobar, and A. M. Stankovic, "Dissipativity-Based Adaptive and Robust Control of UPS," *IEEE Transactions on Industrial Electronics,* Vol. 48, No. 2, pp. 334-343, April 2001.

[30] J. F. Silva, and S. S. Paulo, "Fixed Frequency Sliding Mode Modulator for Current Mode PWM Inverters," in *Proc. IEEE PESC'93*, Vol. 1, pp. 623-629, 20-24 June 1993.

[31] S. L. Jung, and Y. Y. Tzou, "Discrete Sliding-Mode Control of a PWM Inverter for Sinusoidal Output Waveform Synthesis with Optimal Sliding Curve," *IEEE Transactions on Power Electronics*, Vol. 11, No. 4, pp. 567-577, July 1996.

[32] S. J. Chiang, T. L. Tai, and T. S. Lee, "Variable Structure Control of UPS Inverters," *IEE Proceedings-Electric Power Applications*, Vol. 145, No. 6, pp. 559-567, Nov. 1998.

[33] Y. Ito, and S. Kawauchi, "Microprocessor-based Robust Digital Control for UPS with Three-phase Inverter," *IEEE Transactions on Power Electronics,* Vol. 10, No. 2, pp. 196-204, March 1995.

[34] A. Kawabata, T. Miyashita, and Y. Yamamoto, "Deadbeat Control of Three Phase PWM Inverter," *IEEE Transactions on Power Electronics,* Vol. 5, No. 1, pp. 21-28, Jan. 1990.

[35] C. Hua, "Two-level Switching Pattern Deadbeat DSP Controlled PWM Inverter," *IEEE Transactions on Power Electronics,* Vol. 10, No. 3, pp. 310-317, May 1995.

[36] O. Kukrer, and H. Komurcugil, "Deadbeat Control Method for Single-phase UPS Inverters with Compensation of Computation Delay," *IEE Proceedings-Electric Power Applications,* Vol. 146, No. 1, pp. 123-128, Jan. 1999.

[37] O. Kukrer, "Deadbeat Control of a Three-phase Inverter with an Output LC Filter", *IEEE Transaction on Power Electronics,* Vol. 11, No. 1, pp. 16-23, Jan. 1996.

[38] N. M. Abdel-Rahim, and J. E. Quaicoe, "Analysis and Design of a Multiple Feedback Loop Control Strategy for Single-phase Voltage-Source UPS Inverters," *IEEE Transactions on Power Electronics,* Vol. 11, No. 4, pp. 532-541, July 1996.

[39] S. Buso, S. Fasolo, and P. Mattavelli, "Uninterruptible Power Supply Multiloop Control Employing Digital Predictive Voltage and Current Regulators," *IEEE Transactions on Industry Applications*, Vol. 37, No. 6, pp. 1846-1854, November/December 2001,

[40] K. D. Young, V. I. Utkin, and U. Ozguner, "A Control Engineers Guide to Sliding Mode Control," *IEEE Transactions on Control Systems Technology,* Vol. 7, No. 3, pp. 328-342, May 1999.

[41] H. Asada, and J.-J. E. Slotine, *Robot Analysis and Control,* New York: Wiley, pp. 140-157, 1986.

[42] A. Kawamura, and T. Yokoyama, "Comparison of Five Different Approaches for Real-time Digital Feedback Control of PWM Inverters," *IEEE Industry Applications Society Annual Meeting*, Vol. 2, pp. 1005-1011, Seattle, WA, 7-12 Oct. 1990.

[43] S. Saggini, W. Stefanutti, E. Tedeschi, and Paolo Mattavelli, "Digital Deadbeat Control Tuning for dc-dc Converters Using Error Correlation," *IEEE Transactions on Power Electronics,* Vol. 22, No. 4, pp. 1566-1570, July 2007.

[44] T. -S. Lee, S. -J. Chiang, and J. -M. Chang, "H_∞ Loop-Shaping Controller Designs for the Single-Phase UPS Inverters," *IEEE Transactions on Power Electronics,* Vol. 16, No. 4, pp. 473-481, July 2001.

[45] S. Skogestad, and I. Postlethwaite, *Multivariable Feedback Control: Analysis and Design,* John Wiley & Sons, Chichester, Second Edition, 2005.

[46] T. S. Lee, K. S. Tzeng and M. S. Chong, "Robust Controller Design for a Single-phase UPS Inverter Using μ-synthesis," *IEE Proceedings-Electric Power Applications,* Vol. 151, No. 3, May 2004

[47] E. J. Davison, and I. J. Ferguson, "The Design of Controllers for the Multivariable Robust Servomechanism Problem Using Parameter Optimization Methods," *IEEE Transactions on Automatic Control*, Vol. AC-26, No. 1, pp. 93-110, February 1981.

[48] B. R. Barmish, *New Tools for Robustness of Linear Systems,* MacMillan, New York, 1994.

[49] J. L. Stensby, *Phase-Locked Loops: Theory and Applications,* Bocca Raton, New York, CRC Press, 1997.

[50] H. K. Khalil, *Nonlinear Systems,* Third Edition, Prentice Hall, 2002.

[51] C. L. Fortescue, "Method of Symmetrical Coordinates Applied to the Solution of Polyphase Networks," *Trans. AIEE*, pt. II, Vol. 37, pp. 1027-1140, 1918.

[52] A. M. Stankovic and T. Aydin, "Analysis of Asymmetrical Faults in Power Systems Using Dynamic Phasors," *IEEE Transactions on Power Systems*, Vol. 15, No. 3, pp. 1062-1068 August 2000.

[53] A. M. Stankovic, H. Lev-Ari and M. M. Perisic, "Analysis and Implementation of Model-Based Linear Estimation of Dynamic Phasors," *IEEE Transactions on Power Systems*, Vol. 19, No. 4, pp. 1903-1910, November 2004.

[54] R. A. Flores, I. Y. H. Gu and M. H. J. Bollen, "Positive and Negative Sequence Estimation for Unbalanced Voltage Dips," *IEEE Power Engineering Society General Meeting*, 2003, Vol. 4, pp. 2498-2502, 13-17 July 2003.

[55] G. Andria and L. Salvatore, "Inverter Drive Signal Processing via DFT and EKF," *IEE Proceedings B*, Vol. 137, No. 2, pp. 111-119, March 1990.

[56] M. H. J. Bollen, "Algorithms for Characterizing Measured Three-Phase Unbalanced Voltage Dips," *IEEE Transactions on Power Delivery*, Vol. 18, No. 3, pp. 937-944, July 2003.

[57] W. V. Lyon, *Transient Analysis of Alternating-Current Machinery*, Cambridge and John Wiley, New York: Technology Press, 1954.

[58] G. C. Paap, "Symmetrical Components in the Time Domain and Their Application to Power Network Calculations," *IEEE Transactions on Power Systems,* Vol. 15, No. 2, pp. 522-528, May 2000.

[59] A. Ghosh and A. Joshi, "A New Approach to Load Balancing and Power Factor Correction in Power Distribution System," *IEEE Transactions on Power Delivery,* Vol. 15, No. 1, pp. 417-422, Jan. 2000.

[60] M. Karimi-Ghartemani and H. Karimi, "Processing of Symmetrical Components in Time-Domain," *IEEE Transactions on Power Systems,* Vol. 22, No. 2, pp. 572-579, May 2007.

[61] M. R. Iravani and M. Karimi-Ghartemani, "Online Estimation of Steady State and Instantaneous Symmetrical Components," *IEE Proc.-Gener. Transm. Distrib.*, Vol. 150, No. 5, pp. 616-622, September 2003.

[62] S.-J. Lee, J.-K. Kang, and S.-K. Sul, "A New Phase Detecting Method for Power Conversion Systems Considering Distorted Conditions in Power System," *Proceedings of the Industry Applications Conference, Thirty-Fourth IAS Annual Meeting*, Vol. 4, pp. 2167-2172, 3-7 Oct. 1999.

[63] S. Chen and G. Joós, "A Novel DSP-Based Adaptive Line Synchronization System for Three-Phase Utility Interface Power Converters," *Power Electronics Specialists Conference*, Vol. 2, pp. 528-532, 17-21 June 2001.

[64] K. M. El-Naggar, "A Fast Method for Identification of Symmetrical Components for Power System Protection," *Electrical Power and Energy Systems*, Vol. 23, No. 8, pp. 813-817, Nov. 2001.

[65] M. I. Marei, E. F. El-Saadany and M. A. Salama, "A Processing Unit for Symmetrical Componnets and Harmonics Estimation Based on a New Adaptive Linear Combiner Structure," *IEEE Transactions on Power Delivery*, Vol. 19, No. 3, pp. 1245-1252, July 2004.

[66] H.-S. Song and K. Nam, "Instantaneous Phase-Angle Estimation Algorithm under Unbalanced Voltage-Sag Conditions," *IEE Proc.-Gener. Transm. Distrib.,* Vol. 147, No. 6, pp. 409-415, Nov. 2000.

[67] A. A. Giordano, *Least Square Estimation with Applications to Digital Signal Processing*, New York: John Wiley & Sons, 1985.

[68] R. A. Silverman, *Modern Calculus and Analytic Geometry,* Mineola, New York, Dover Publications, 2003.

[69] H. Akagi, Y. Kanazawa, and A. Nabae, "Generalized Theory of the Instantaneous Reactive Power in Three-phase Circuits," *IPEC'83 Int. Power Electronics Conf.*, Tokyo, Japan, pp. 1375-1386, 1983.

[70] H. Akagi, Y. Kanazawa, and A. Nabae, "Instantaneous Reactive Power Compensators Comprising Switching Devices Without Energy Storage Components," *IEEE Transaction on Industry Application*, Vol. 20, pp. 625-630, May/June 1984.

[71] K. Ogata, *Modern Control Engineering,* Prentice Hall, Englewood Cliffs, NJ, 1990.

[72] V. Kaura and V. Blasko, "Operation of a Phase Locked Loop System under Distorted Utility Conditions," *IEEE Transactions on Industry applications*, Vol. 33, No. 1, pp. 58-63, Jan./Feb. 1997.

[73] S.-K. Chung, "A Phase Tracking System for Three Phase Utility Interface Inverters," *IEEE Transactions on Power Electronics,* Vol. 15, No. 3, pp. 431-438, May 2000.

[74] D. Jovcic, N. Pahalawaththa and M. Zavahir, "Analytical Modelling of HVDC-HVAC Systems," *IEEE Transactions on Power Delivery,* Vol. 14, No. 2, pp. 506-511, April 1999.

[75] W. Leonhard, *Control of Electrical Drives*, Berlin, Germany: Springer Verlag, 1985.

[76] M. Karimi-Ghartemani, *A Synchronization Scheme Based on an Enhanced Phase-Locked Loop System*, Ph.D. Dissertation, Department of Electrical and Computer Engineering, University of Toronto, 2004.

[77] A. G. Phadke, J. Thorp, and M. Adamiak, "A New Measurement Technique For Tracking Voltage Phasors, Local System Frequency and Rate Of Change of Frequency," *IEEE Transactions on Power Apparatus and Systems,* Vol. PAS-102, No. 5, pp. 1025-1038, May 1983.

[78] P. K. Dash, A. K. Pradhan, and G. Panda, "Frequency Estimation of Distorted Power System Signals Using Extended Complex Kalman Filter," *IEEE Transactions on Power Delivery,* Vol. 14, No. 3, pp. 761-766, July 1999

[79] H. S. Black, *Modulation Theory*, Princeton, NJ: Van Nostrand & Co., 1953.

[80] IEEE Std 929-2000, "IEEE Recommended Practice for Utility Interface of Photovoltaic (PV) Systems," 2000.

[81] M. Karimi-Ghartemani and M. R. Iravani, "A Method for Synchronization of Power Electronic Converters in Polluted and Variable-Frequency Environments," *IEEE Transactions on Power Systems,* Vol. 19, No. 3, pp. 1263-1270, August 2004.

[82] R. Aghazadeh, H. Lesani, M. Sanaye-Pasand, and B. Ganji, "New Technique for Frequency and Amplitude Estimation of Power System Signals," *IEE Proc.-Gener. Transm. Distrib.*, Vol. 152, No. 3, pp. 435-440, May 2005.

[83] ANSI/IEEE Std 1001-1988, "IEEE Guide for Interfacing Dispersed Storage and Generation Facilities with Electric Utility Systems," 1989.

[84] G.-K. Hung, C.-C. Chang, and C.-L. Chen, "Automatic Phase-Shift Method for Islanding Detection of Grid-Connected Photovoltaic Inverters," *IEEE Transactions on Energy Conversion,* Vol. 18, No. 1, pp. 169-173, March 2003.

[85] M. E. Ropp, *Design Issues for Grid-Connected Photovoltaic Systems*, Ph.D. dissertation, Georgia Institute of Technology, Atlanta, GA, 1998.

[86] A. Yazdani and R. Iravani, "A Unified Dynamic Model and Control for the Voltage-Sourced Converter Under Unbalanced Grid Conditions," *IEEE Trans. on Power Delivery*, Vol. 21, No. 3, pp. 1620-1629, July 2006.

[87] H. Song and K. Nam, "Dual Current Control Scheme for PWM Converter Under Unbalanced Input Voltage Conditions," *IEEE Trans. on Industrial Electronics*, Vol. 46, No. 5, pp. 953-959, October 1999.

[88] S. Chung, "A Phase Tracking System for Three Phase Utility Interface Inverters," *IEEE Trans. on Power Electronics*, Vol. 15, No. 3, pp. 431-438, May 2000.

[89] A. Yazdani, *Modeling and Control of the Three-Level Neutral Point Diode Clamped (NPC) Converter for High-Power Applications,* Ph.D. Dissertation, Department of Electrical and Computer Engineering, University of Toronto, Toronto, ON, Canada, 2005.

[90] J. Driesen and T. V. Craenenbroeck, "Voltage Disturbances, Introduction to Unbalance," *Power Quality Application Guide, Copper Development Association*, 5.1.3, May 2002.

[91] H. B. Puttgen, P. R. MacGregor, and F. C. Lambert, "Distributed Generation: Semantic Hype or the Dawn of a New Era?", *IEEE Power and Energy Magazine*, Vol. 1, No. 1, pp. 22-29, Jan.-Feb. 2003.

[92] S. M. Amin and B. F. Wollenberg, "Toward a Smart Grid: Power Delivery for the 21st Century" *IEEE Power and Energy Magazine*, Vol. 3, No. 5, pp. 34-41, Sept.-Oct. 2005.

[93] S.P. Bhattacharyya, H. Chapellat, L.H. Keel, *Robust Control - The Parametric Approach,* Prentice Hall, Englewood Cliffs, New Jersey, 1995.

[94] A. Isidori, *Nonlinear Control Systems,* Third Edition, Springer Verlag, 1995.

[95] J. J. E. Slotine, and W. Li, *Applied Nonlinear Control,* Prentice-Hall, 1991.

[96] G. F. Franklin, J. D. Powell, and A. Emami-Naeini, *Feedback control of dynamic systems,* Prentice Hall, Upper Saddle River, NJ, 2002.

[97] E. J. Davison, and A. Goldenberg, "The Robust Control of a General Servomechanism Problem: The Servo Compensator", *Automatica*, Vol. 11, pp. 461-471, 1975.

[98] E. J. Davison, "The Robust Control of a Servomechanism Problem for Linear Time-Invariant Multivariable Systems," *IEEE Transactions on Automatic Control*, Vol. AC-21, No. 1, pp. 25-34, February 1976.

[99] E. J. Davison, "The Robust Decentralized Control of a General Servomechanism Problem," *IEEE Transactions on Automatic Control*, Vol. AC-21, No. 1, pp. 14-24, February 1976.

[100] E. J. Davison, and S. H. Wang, "Properties and Calculation of Transmission Zeros of Linear Multivariable Systems," *Automatica,*, Vol. 10, pp. 643-658, 1974.

[101] E. J. Davison, W. Gesing, and S. H. Wang, "An Algorithm for Obtaining the Minimal Realization of a Linear Time-Invariant System and Determining if a System is Stabilizable-Detectable", *IEEE Transactions on Automatic Control*, Vol. AC-23, No. 6, pp. 1048-1054, Dec. 1978.

[102] E. J. Davison, and B. M. Scherzinger, "Perfect Control of the Robust Servomechanism Problem," *IEEE Transactions on Automatic Control*, Vol. AC-32, No. 8, pp. 689-702, August 1987.

[103] Qiu Li, and E. J. Davison, "New Perturbation Bounds for the Robust Stability of Linear State Space Models," *IEEE Control and Decision Conference*, Athens, pp. 751-755, December 1986.

[104] D. E. Davison, and E. J. Davison, "Optimal Transient Response Shaping of the Servomechanism Problem," *Journal of Optimization Theory and Applications (JOTA)*, Vol. 115, No. 3, pp. 491-515, December 2002.

[105] E. J. Davison, B. R. Copeland, "Gain Margin and Time Lag Tolerance Constraints Applied to the Stabilization Problem and Robust Servomechanism Problem", *IEEE Transactions on Automatic Control*, Vol. AC-30, No. 3, pp. 229-239, March 1985.

[106] Qiu Li, B. Bernhardsson, A. Rantzer, E. J. Davison, P. M. Young, and J. C. Doyle, "A Formulae for Computation of the Real Stability Radius", *Automatica*, Vol. 31, No. 6, pp. 879-890, 1995.

[107] Guangdi Hu, and E. J. Davison, "Real Stability Radius of Linear Time-Invariant Time-Delay Systems", *Systems and Control Letters*, Vol 50, No. 3, pp. 209-219, Oct. 2003.

[108] Yokogawa PZ4000 Power Analyzer Users Manual, 2000.

[109] V. L. Kharitonov, "Asymptotic stability of an equilibrium position of a family of systems of linear differential equations," *Differentsial'nye Uravneniya*, Vol. 14, pp. 2086-2088, 1978a.

[110] A. C. Bartlett, C. V. Hollot, and L. Huang, "Root location of an entire polytope of polynomials: It suffices to check the edges," *Mathematics of Control, Signals and Systems*, Vol. 1, pp. 61-71, 1988.

[111] A. Sideris and R. S. Sanchez Pena, "Fast Computation of the Multivariable Stability Margin for Real Interrelated Uncertain Parameters," *IEEE Transaction on Automatic Control,* Vol. AC-34, pp. 1272-1276, 1989.